NUREG/CR-3689 Vol. IV
ANL-83-85 Vol. IV

NUREG/CR-3689 Vol. IV
ANL-83-85 Vol. IV

MATERIALS SCIENCE AND TECHNOLOGY DIVISION LIGHT-WATER-REACTOR SAFETY RESEARCH PROGRAM: QUARTERLY PROGRESS REPORT

October – December 1983

ARGONNE NATIONAL LABORATORY, ARGONNE, ILLINOIS
Operated by THE UNIVERSITY OF CHICAGO

Prepared for the Office of Nuclear Regulatory Research
U. S. NUCLEAR REGULATORY COMMISSION
under Interagency Agreement DOE 40-550-75

Argonne National Laboratory, with facilities in the states of Illinois and Idaho, is owned by the United States government, and operated by The University of Chicago under the provisions of a contract with the Department of Energy.

NUREG/CR-3689 Vol. IV
ANL-33-85 Vol. IV

(Distribution Codes:
R3 and R5)

ARGONNE NATIONAL LABORATORY
9700 South Cass Avenue
Argonne, Illinois 60439

MATERIALS SCIENCE AND TECHNOLOGY DIVISION LIGHT-WATER-REACTOR SAFETY RESEARCH PROGRAM: QUARTERLY PROGRESS REPORT

October—December 1983

Date Published: August 1984

Previous reports in this series

ANL-82-41 Vol. IV	October—December 1982
ANL-83-85 Vol. I	January—March 1983
ANL-83-85 Vol. II	April—June 1983
ANL-83-85 Vol. III	July—September 1983

Prepared for the Division of Engineering Technology
Office of Nuclear Regulatory Research
U. S. Nuclear Regulatory Commission
Washington, D. C. 20555
Under Interagency Agreement DOE 40-550-75

NRC FIN Nos. A2016, A2017, A2212, A2243

PREFACE

Effective with the January-March 1984 reporting period, progress in the Materials Science and Technology Division Light-Water-Reactor Safety Research Program will be described in two separate quarterly reports, subtitled "Materials Engineering" and "Fuel Element Behavior," respectively. The "Materials Engineering" report will include (1) Environmentally Assisted Cracking in Light Water Reactors, (2) Long-Term Embrittlement of Cast Duplex Stainless Steels in LWR Systems, and (3) NDE of Stainless Steel and On-Line Leak Monitoring of LWRs. The "Fuel Element Behavior" report will include (1) Transient Fuel Response and Fission Product Release and (2) Clad Properties for Code Verification.

MATERIALS SCIENCE AND TECHNOLOGY DIVISION
LIGHT-WATER-REACTOR SAFETY
RESEARCH PROGRAM:
QUARTERLY PROGRESS REPORT

October-December 1983

ABSTRACT

This progress report summarizes the Argonne National Laboratory work performed during October, November, and December 1983 on water reactor safety problems. The research and development areas covered are Environmentally Assisted Cracking in Light Water Reactors, Transient Fuel Response and Fission Product Release, Cla Properties for Code Verification, and Long-Term Embrittlement of Cast Duplex Stainless Steels in LWR Systems.

NRC Fin No.	FIN Title
A2016	Transient Fuel Response and Fission Product Release
A2017	Clad Properties for Code Verification
A2212	Environmentally Assisted Cracking in Light Water Reactors
A2243	Long-Term Embrittlement of Cast Duplex Stainless Steels in LWR Systems

TABLE OF CONTENTS

TABLE OF CONTENTS (Contd.)

TABLE OF CONTENTS (Contd.)

MATERIALS SCIENCE AND TECHNOLOGY DIVISION
LIGHT-WATER-REACTOR SAFETY
RESEARCH PROGRAM:
QUARTERLY PROGRESS REPORT

October-December 1983

EXECUTIVE SUMMARY

I. ENVIRONMENTALLY ASSISTED CRACKING IN LIGHT-WATER REACTORS[a]

Current practice with regard to leak detection has been reviewed and assessed for 74 operating plants, including both BWRs and PWRs. In practice, most reactors presently rely on sump pump monitoring to detect leakage. In most cases, the surveillance periods are too long to detect a 1-gal/min leak in one hour, as suggested by Regulatory Guide 1.45, but it appears that this sensitivity could be achieved if monitoring procedures were modified. Although current leak detection systems are adequate to ensure leak-before-break behavior in the great majority of situations, the possibility of large cracks producing only low leakage rates must be considered. The Duane Arnold cracking incident shows that shortcomings in the existing leak detection systems are not simply a matter of conjecture. However, simply tightening the current leakage limits is not an adequate solution, since this might produce an unacceptably high number of spurious shutdowns owing to the inability of current leak detection systems to identify leak sources.

Acoustic leak detection data from two intergranular stress corrosion cracks, two thermal fatigue cracks, and one mechanical fatigue crack have now been acquired and analyzed. Additional tests have been carried out to help assess the effectiveness of moisture-sensitive tape. The breadboard leak detection system developed by GARD was brought to Argonne for preliminary tests and some modifications have been made.

---

[a]RSR FIN Budget No. A2212; RSR Contact: J. Strosnider.

Low-temperature aging of materials with controlled plastic strains and specimens from weldments prepared with induction heating stress improvement, heat sink welding, last pass heat sink welding, and corrosion resistant cladding is continuing.

The effect of changing frequency and load ratio on crack growth rates in sensitized stainless steels has been investigated. An attempt was made to correlate the resulting data in terms of a crack-tip strain rate, but it was not successful and other approaches will be investigated.

The effect of strain rate on transgranular cracking in Type 316NG stainless steel has been studied in constant extension rate (CERT) tests and correlated with a phenomenological model for stress corrosion cracking based on an estimate of the crack-tip strain rate obtained by use of a J-integral approach, a slip-dissolution model for crack advance, and a J-integral fracture criterion. Good agreement between the predictions of the model and the experimental results is observed.

The residual stresses on the inner surface and the axial throughwall stresses in a minioverlay mockup weldment fabricated by Georgia Power have been measured. The overlay was very successful in inducing compressive residual stresses on the inner surface of the weldment. As expected, the throughwall stresses are strongly compressive on the inner portion of the wall and tensile on the outer portion of the wall.

Additional results have been obtained from CERT tests on a reference heat of Type 304 stainless steel. The influence of the degree of sensitization on the SCC susceptibility has been evaluated in environments containing 0.2 and 1.0 ppm dissolved oxygen with and without sulfate additions. The intergranular and transgranular crack growth rates obtained from the CERT tests have been correlated with the open circuit corrosion potential as well as the dissolved oxygen concentration for a range of conductivities from <0.2 to 70 μS/cm. Fracture mechanics crack growth rate tests are being carried out to determine the effect of water chemistry transients on crack growth rates.

II. TRANSIENT FUEL RESPONSE AND FISSION PRODUCT RELEASE[b]

The theoretical FASTGRASS-VFP model has been used in the interpretation of fission gas, iodine, and cesium release from (1) irradiated high-burnup LWR fuel in a flowing steam atmosphere during high-temperature, in-cell heating tests performed at Oak Ridge National Laboratory and (2) trace-irradiated LWR fuel during severe-fuel-damage (SFD) tests performed in the PBF reactor in Idaho. The results of the analyses demonstrate that intragranular fission product behavior during both types of tests can be interpreted in terms of a grain-growth/grain-boundary-sweeping mechanism that enhances the flow of fission products from within the grains to the grain boundaries. In addition, significant fission product release during the SFD tests depends on fuel fracturing and/or other processes initiated by a requench and on fuel liquefaction initiated by clad melting. The FASTGRASS-VFP predictions, measured release rates from the above tests, and previously published release rates are compared and differences between fission product behavior in trace-irradiated and in high-burnup fuel are highlighted.

[b]RSR FIN Budget No. A2016; RSR Contact: G. P. Marino.

III. CLAD PROPERTIES FOR CODE VERIFICATION[C]

Zircaloy fuel cladding is susceptible to local breach-type failures during power transients in LWRs because of stresses imposed by differential thermal expansion of the fuel and cladding. In this program, the effect of stress state, strain rate, and temperature on the deformation characteristics of irradiated Zircaloy fuel cladding is being investigated to provide mechanical-property information and a failure criterion for the cladding under loading conditions conducive to pellet-cladding interaction (PCI). The information will be used in the development of codes to analyze PCI in fuel rods from power ramp experiments in test reactors, and to evaluate the susceptibility of extended-burnup fuel elements and new fuel element designs in commercial reactors to PCI failures during power transients.

Fracture surfaces of several more H. B. Robinson spent-fuel cladding tubes have been examined by SEM after failure at 325°C by expanding-mandrel loading. Three specimens that contain pseudocleavage in large portions of the fracture surfaces have been identified. The characteristics of the fracture surface morphology are similar to those reported in the literature for fuel rods that failed because of PCI.

Continued efforts in the TEM-HVEM examination of the brittle-type PCI-like failure produced in Big Rock Point fuel cladding by internal gas pressurization at 325°C resulted in direct observations of dark-field images from Zr_3O superlattice reflections. The dark-field morphology shows that the phase forms primarily in association with dislocation substructures and cell walls of the cold-worked material. Closer examination of the dark-field images with a magnifying glass revealed discrete particles of the phase in agglomerations. Individual dislocations decorated by the discrete particles could be observed. There was also evidence that the phase forms to a limited extent on grain boundaries of the partially recrystallized region of the cladding material.

[C]RSR FIN Budget No. A2017; RSR Contact: H. H. Scott.

IV. LONG-TERM EMBRITTLEMENT OF CAST DUPLEX STAINLESS STEELS IN LWR SYSTEMS[d]

Metallographic evaluation of various cast materials is in progress to characterize the chemical composition, ferrite content, hardness, and grain structure. Data on hardness, ferrite content, and morphology are presented. The results indicate some differences in hardness and ferrite content for material from different locations of the castings. The ferrite content is lower and hardness is higher toward the inner surface of the various cast pipes. Variations in the ferrite content of the static cast keel blocks depend on the Cr_{eq}/Ni_{eq} ratio in the material; the ferrite content toward the top of the casting is lower for material with a ratio below 1.13 and higher when the ratio exceeds this value. Orientation of the material, i.e., axial, circumferential, or radial direction of the casting, has little or no effect on hardness or the ferrite content and morphology.

The ferrite morphology in the static cast keel blocks is different from that in centrifugally cast pipes. For the same ferrite content, the islands of ferrite in the keel blocks are smaller and have a finer dispersion than in the pipe material. The ferrite morphology is characterized by a random arrangement of an interfaced network of ferrite islands or fine needle-like ferrite distributed in the austenite matrix.

Material for Charpy impact and 1-T compact tension specimens is being aged at 450, 400, 350, 320, and 290°C. The aging times range from 100 to 50,000 h. Preliminary Charpy impact tests were performed on unaged material to assess the influence of specimen location and orientation on impact strength. Material from two centrifugally cast pipe sections and a static cast pump casing ring was sent to Materials Engineering Associates for J-R curve determination and tensile tests.

Microstructural evaluation has continued on the aged specimens of cast duplex stainless steel obtained from George Fischer Co. of Switzerland. Precipitate phases were not observed in any specimens aged for <10,000 h at 300, 350, or 400°C. An analysis of the aged material by neutron diffraction in the ANL Intense Pulsed Neutron Source (IPNS) is being planned.

---

[d]RSR FIN Budget No. A2243; RSR Contact: J. Muscara.

I. ENVIRONMENTALLY ASSISTED CRACKING IN LIGHT WATER REACTORS

Principal Investigators:
W. J. Shack, T. F. Kassner, D. S. Kupperman, T. N. Claytor,
J. Y. Park, P. S. Maiya, W. E. Ruther,
and F. A. Nichols

The objective of this program is to develop an independent capability for prediction, detection, and control of intergranular stress corrosion cracking (IGSCC) in light-water reactor (LWR) systems. The program is primarily directed at IGSCC problems in existing pla. , but also includes the development of recommendations for plants under construction and future plants. The scope includes the following: (1) development of the means to evaluate acoustic leak detection systems objectively and quantitatively; (2) evaluation of the influence of metallurgical variables, stress, and the environment on IGSCC susceptibility, including the influence of plant operations on these variables; and (3) examination of practical limits for these variables to effectively control IGSCC in LWR systems. The initial experimental work concentrates primarily on problems related to pipe cracking in LWR systems. However, ongoing research work on other environmentally assisted cracking problems involving pressure vessels, nozzles, and turbines will be monitored and assessed, and where unanswered technical questions are identified, experimental programs to obtain the necessary information will be developed to the extent that available resources permit.

The effort is divided into six subtasks: (A) Leak Detection and Nondestructive Evaluation; (B) Analysis of Sensitization; (C) Crack Growth Rate Studies; (D) Evaluation of Nonenvironmental Corrective Actions; (E) Evaluation of Environmental Corrective Actions; and (F) Mechanistic Studies. These subtasks reflect major technical concerns associated with IGSCC in LWR systems, namely: leak and crack detection, the role of materials susceptibility, the role of stress in crack initiation and propagation, and the role of the environment. The program seeks to evaluate potential solutions to IGSCC problems in LWRs, both by direct experimentation (including full-scale welded pipe tests) and through the development of a better basic understanding of the various phenomena.

A. Leak Detection and Nondestructive Evaluation (D. S. Kupperman, T. N. Claytor, R. N. Lanham, and D. Prine*)

1. Introduction

a. Background

No currently available single leak-detection method combines optimal leakage detection sensitivity, leak-locating ability, and leakage measurement accuracy.[1] For example, while quantitative leakage determination is possible with condensate flow monitors, sump monitors, and primary coolant inventory balance, these methods are not adequate for locating leaks and are not necessarily sensitive enough to meet code requirements.

Technology is available to improve leak detection capability at specified sites by use of acoustic monitoring or moisture-sensitive tape. However, current acoustic monitoring techniques provide no source discrimination (i.e., to distinguish between leaks from pipe cracks and valves) and no flow-rate information (a small leak may saturate the system). Moisture-sensitive tape does not provide quantitative leak-rate information and gives no specific location information other than the location of the tape; moreover, its usefulness with "soft" insulation needs to be demonstrated.

Since the issuance of NRC IE Bulletins 83-02 and 82-03 and the training of ultrasonic inspection personnel, the probability of detecting IGSCC under field conditions has increased. However, leak detection techniques need further improvement in the following areas: (1) identifying leak sources through location information and leak characterization, so as to eliminate false calls; (2) quantifying and monitoring leak rates; and (3) minimizing the number of installed transducers in a "complete" system through increased sensitivity.

Many cracks are missed during ultrasonic ISI and detected only because of leakage, thereby raising doubts concerning the capability of ultrasonic ISI to detect cracks. The present ultrasonic testing procedures

*GARD, Inc., Niles, Illinois.

for ferritic weldments (ASME Code Sections V and XI) do not appear to be adequate for the detection and evaluation of IGSCC in austenitic stainless steel (SS) piping. The detection of IGSCC before the cracks have grown large enough to cause a leak, and the detection, location, and sizing of leaks once they occur, are very difficult technical goals to achieve. IGSCC that can be detected by conventional ultrasonic testing under laboratory conditions may be missed during a field examination by even the most skilled operator.

b. Objectives

The program objectives for leak detection are to (a) develop a facility for the quantitative evaluation of acoustic leak detection (ALD) systems; (b) assess the effectiveness and reliability of ALD techniques; (c) evaluate a prototype ALD system; (d) establish the sensitivity, reliability, and decision-making capability of a prototype system through laboratory testing; and (e) assess the effectiveness of field-implementable ALD systems. The program will establish whether meaningful quantitative data on leak rates and location can be obtained from acoustic signatures of leaks due to IGSCC and fatigue cracks in low- and high-pressure lines, and whether these can be distinguished from other types of leaks. It will also establish calibration procedures for acoustic data acquisition and show whether advanced signal processing can be employed to enhance the adequacy of ALD schemes.

The program objectives for ultrasonic nondestructive evaluation are to (a) assess the adequacy of a multielement skew angle probe to distinguish IGSCC from geometrical reflectors, (b) assess methods for characterizing cast SS microstructure to determine ISI reliability, and (c) evaluate new ultrasonic inspection problems (e.g., weld overlays).

c. Review of Current Practice for Leak Detection

Regulatory Guide 1.45 suggests that at least three different detection methods be employed in reactors to detect leakage. Monitoring of both sump-flow and airborne-particulate radioactivity is mandatory. A third method can involve either monitoring of condensate flow rate from air coolers or monitoring of airborne gaseous radioactivity. Although the current methods

used for leak detection reflect the state of the art, other techniques may be developed and used. Regulatory Guide 1.45 also suggests that flow rates from identified and unidentified sources be monitored separately to an accuracy of 1 gal/min,* and that indicators and alarms for leak detection be provided in the main control room.

Since the recommendations of Regulatory Guide 1.45 are not mandatory, the technical specifications for 74 operating plants including PWRs have been reviewed by the present authors to determine the types of leak detection methods employed, the range of limiting conditions for operation, and the surveillance requirements for the leak detection systems.

All plants use at least one of the two systems specified by Regulatory Guide 1.45. All but eight use sump monitoring, and all but three use particulate monitoring. Monitoring of condensate flow rate from drywell air coolers and monitoring of atmospheric gaseous radioactivity are also used in many plants.

The allowed limits on unidentified coolant leakage are shown in Fig. 1.1 (upper panel). The limit for all PWRs is 1 gal/min, while the limit for most BWRs is 5 gpm. The limits on total leakage (Fig. 1.1, lower panel) are generally 10 gal/min for PWRs and 25 gal/min for BWRs. (Regulatory Guide 1.45 does not specify leakage limits, but does suggest that the leakage detection system should be able to detect a 1-gal/min leak in 1 h.) In some cases, limits on rates of increase in leakage are also stated in the plant technical specifications. Two BWRs have a limit of 0.1 gal/min/h; four have a limit of 0.5 gal/min/h.

Surveillance periods for BWRs and PWRs are indicated in Fig. 1.2 (upper panel). Leakage is checked every 12 h in most PWRs, and every 4 or 24 h in most BWRs. One BWR specifies that a continuous monitor with control room alarm shall be operational. The intervals between successive system calibrations and checks are indicated in Fig. 1.2 (lower panel). For BWRs, calibration is generally performed at 18-month intervals; functional tests are performed every month.

---

*Conversion factor: 1 gal/min = 3800 cm^3/min.

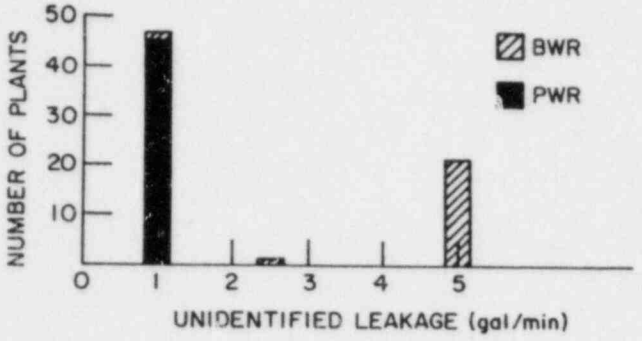

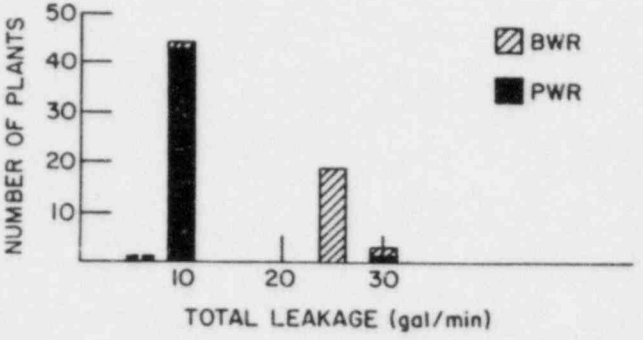

Fig. 1.1. Amounts of Unidentified and Total Coolant Leakage Allowed at BWRs and PWRs. Conversion factor: 1 gal/min = 3800 cm^3/min.

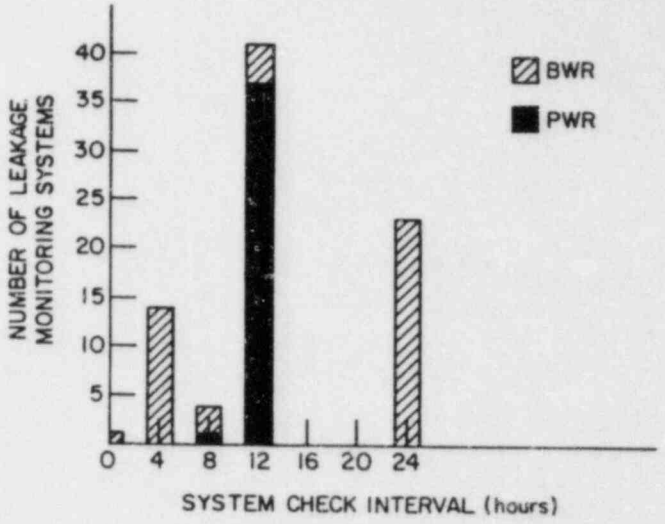

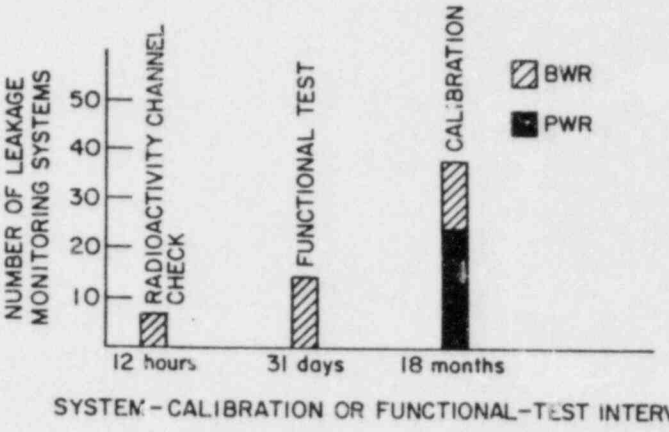

Fig. 1.2. Surveillance Periods (Top) and Test or Calibration Intervals (Bottom) for BWRs and PWRs.

Generally speaking, reactors rely on sump pump monitoring to establish the presence of leaks. Other methods appear to be less reliable or less convenient. In most reactors the surveillance periods are too long to detect a 1-gpm leak in one hour, as suggested by Regulatory Guide 1.45, but it appears that this sensitivity could be achieved if monitoring procedures were modified. None of the systems provides any information on leak location, and leaks must be located by visual examination after shutdown. Since cracks may close when the reactor is shut down, reducing flow rates considerably, it would be desirable to be able to locate cracks during plant operation.

The estimated sensitivity of leakage monitoring systems is occasionally addressed in the technical specifications. For example, one specification indicates that air particulate monitoring can, in principle, detect a 0.013-gal/min leak in 20 min, that the sensitivity of gas radioactivity monitoring is 2-10 gal/min, and that the sensitivity of condensate flow monitoring is 0.5-10 gal/min. Continuous sump pump monitoring appears capable of detecting a 1-gal/min leak in 10-60 min.

The impact of Reactor Coolant Pressure Boundary leakage detection systems on safety was evaluated for eight reactors as part of the Integrated Plant Safety Assessment-Systematic Evaluation Program and described in eight SEP reports (NUREG-0820 through -0827). In four of the eight reactors evaluated, a 1-gal/min leak could not be detected within 1 h; and four of the eight reactors did not have three leakage monitoring systems, contrary to the suggestions in Regulatory Guide 1.45. The fracture mechanics and leak rate calculations in the SEP reports are consistent with other studies which indicate that (1) current leak detection systems will detect throughwall cracks 10-25 cm (4 to 10 in.) long in 12- to 28-in. piping within one day, and (2) current leakage limits will necessitate plant action after such a detection event. Since these cracks are much smaller than those required to produce failure in tough reactor piping, improved leak detection systems may offer little safety benefit for this particular class of flaws when crack growth occurs by a relatively slow mechanism. However, the SEP reports state that local leak detection systems may be necessary for some postulated break locations where separation and/or restraint is not a practical way to mitigate the effects of a high-energy pipe break.

Although current leak detection systems are adequate to ensure a leak-before-break scenario in the great majority of situations, the possibility of large cracks producing only low leakage rates must also be considered. This could arise because of corrosion plugging or fouling of relatively slowly growing cracks or the relatively uniform growth of a long crack before penetration. In such cases the time from a small leak to a significant leak or rupture could be short, depending on crack geometry, pipe loading, and transient loading (a seismic or water hammer event). Furthermore, with existing techniques such as sump pump monitoring, no location information regarding a leak is available.

The shortcomings in existing leak detection systems are not simply a matter of conjecture. The Duane Arnold safe-end cracking incidents and Indian Point Unit 2 fan cooler leakage indicate that the sensitivity and reliability of current leak detection systems are clearly inadequate in some cases. In the Duane Arnold case the plant was shut down on the judgment of the operator when a leak rate of 3 gal/min was detected; however, this leakage rate is below the required shutdown limit for almost all BWRs (see Fig. 1.1). Examination of the leaking safe-end showed that cracking had occurred essentially completely around the circumference. The crack was throughwall over about 20% of the circumference and 50-75% throughwall in the non-leaking area.

Simply tightening the current leakage limits is not an adequate solution to these shortcomings, since this might produce an unacceptably high number of spurious shutdowns owing to the inability of current leak detection systems to identify leak sources.

One other safety-related aspect of improved leak detection systems concerns radiation exposure of plant personnel. Improved systems with leak location capability could reduce the exposure of personnel inside the containment and could present an attractive alternative to augmented ISI. Improved leak detection is consistent with the defense-in-depth philosophy of the NRC and would lead to earlier detection of system degradation.

2. Technical Progress

a. Comparison of Acoustic Leak Data from Different Crack Types

Acoustic leak detection data from two IGSCC specimens, two thermal fatigue cracks (TFCs), and one mechanical fatigue crack (FC) have now been acquired and analyzed. Figure 1.3 shows photographs of these cracks.

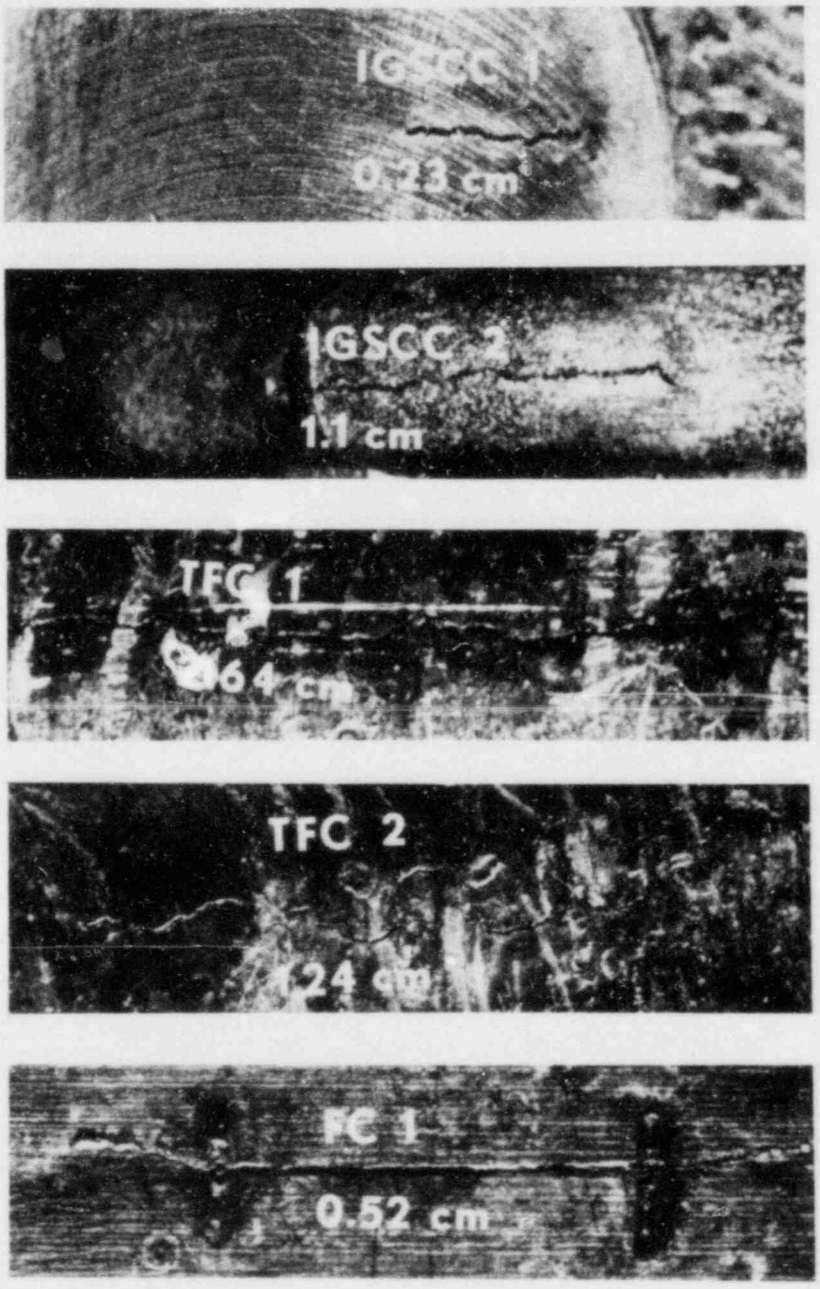

Fig. 1.3. Photographs of Cracks Used in Acoustic Leak Detection Experiments.

The crack widths and lengths at the pipe outer surfaces are indicated in Table 1.1. Figure 1.4 shows acoustic leak data from these five cracks. These data are normalized to an AET-375 transducer on a waveguide with a water temperature of 260°C (500°F) and pressure of 7.7 MPa (1100 psi). The largest correction is for the mechanical fatigue crack FC #1. Corrections for the other data are less than 6 dB. Transducer signals indicated in Fig. 1.4 are for a 300-400 kHz bandwidth and represent the signal after electronic noise levels are subtracted. The acoustic signals from the fatigue cracks vary approximately as $(\text{flow rate})^{0.7}$, whereas the signals from the IGSCC vary approximately as $(\text{flow rate})^{0.37}$. Frequency analysis also indicates less dependence of acoustic signal on frequency for the IGSCC specimens than for the fatigue cracks.[2] An analysis of the frequency spectrum may provide information on the source of acoustic leak signals. The excellent matching of acoustic leak data in the 300-400 kHz range for the two IGSCC specimens, despite their different geometries, suggests that it may be possible to derive flow-rate information from the amplitude of the acoustic leak signal in this frequency range.

TABLE 1.1. Outer-Surface Lengths and Widths of Cracks Shown in Fig. 1.3.

Crack	Length, cm	Width, μm
IGSCC #1	0.23	90
IGSCC #2	1.10	60-80
TFC #1	2.64	75-100
TFC #2	1.24	40-100
FC #1	0.52	150-200

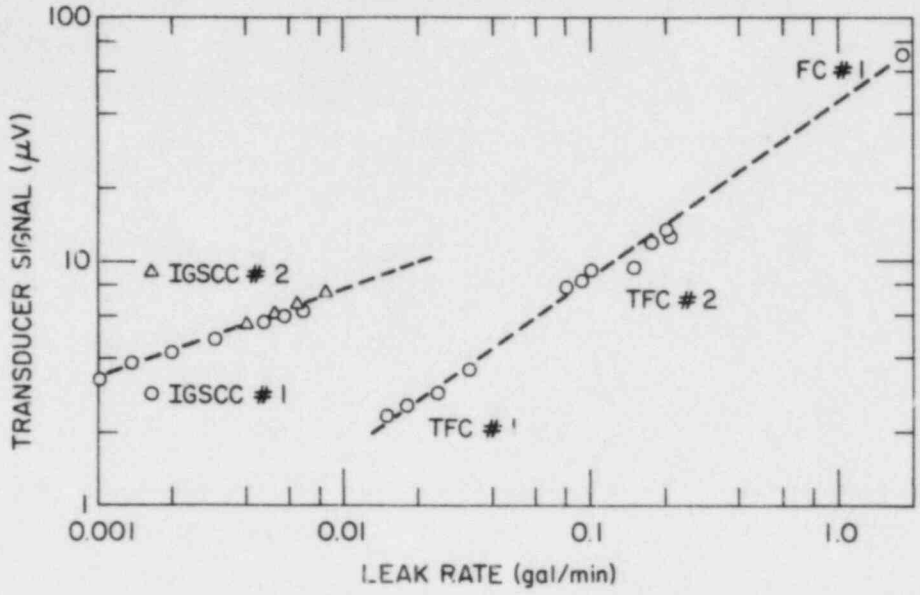

Fig. 1.4. Acoustic Leak Data from the Cracks Shown in Fig. 1.3. Data are normalized as described in text. Signal amplitudes are for a 300-400 kHz bandwidth after electronic background noise is subtracted.

Detection of a leak requires that $S_e = S_1 - T_1 - N_1 + PG > 0$, where S_e = signal excess at detector output, S_1 = source level (affected by waveguide geometry, insulation, and circumferential position), T_1 = transmission loss down pipe, N_1 = background noise level, and PG = system gain (all in dB). The acquisition of acoustic leak data, background noise estimates (from Hatch and Watts Bar), and attenuation data allows a rough estimation of the sensitivity of an ALD system under field conditions. Figure 1.5 shows predicted signal-to-noise ratios (in dB) vs distance along a 10-in. Schedule 80 pipe for three flow rates and three levels of estimated acoustic background noise. The highest level is estimated from the maximum acoustic level obtained during the Watts Bar hot functional test when the reactor was at operating temperature and pressure. The lowest level is obtained from an indirect estimate of background noise from Hatch and the assumptions that the reactor acoustic background level will vary by a factor of 10 in the

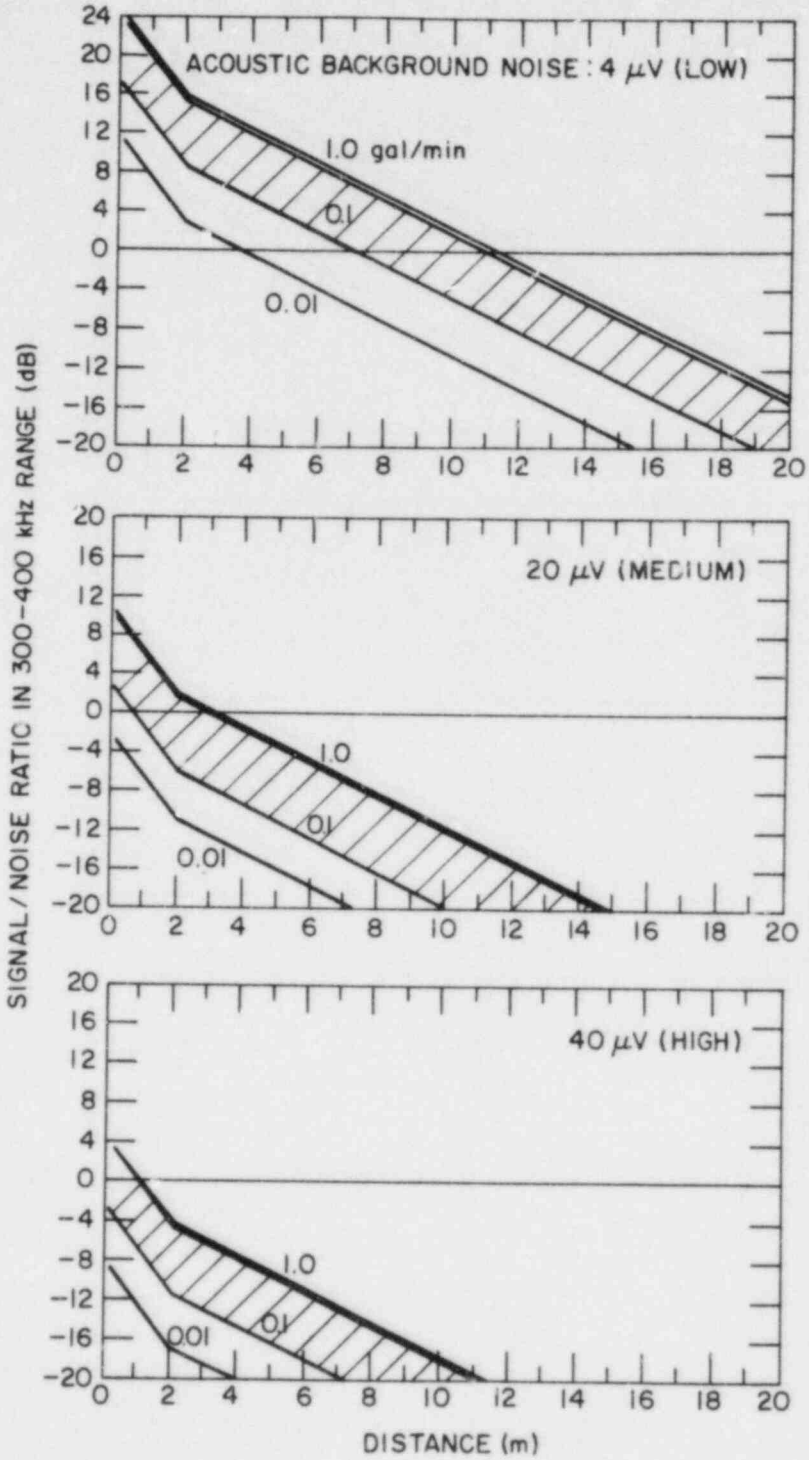

Fig. 1.5. Predicted Acoustic Signal-to-Noise Ratios vs Distance along a 10-in. Schedule 80 Pipe for Three Levels of Estimated Acoustic Background Noise. The shaded area indicates possible enhancement of the signal for the 0.1 gal/min leak because of the presence of reflective insulation.

plant and that the measurement at Watts Bar was an upper-limit value. The striped area suggests possible enhancement of the acoustic signal for a 0.1-gal/min flow rate in a situation where the leak plume strikes the reflective insulation. Results of laboratory experiments suggest that for flow rates greater than 0.02 gal/min but less than 0.2 gal/min, signals could be enhanced significantly, given the correct circumstances. The following equation has been used to generate the curves of Fig. 1.5:

$$S = 20 \log_{10}\left(\frac{70R^{0.32}}{B}\right) - \begin{Bmatrix} 4.5D \text{ for } D < 3 \text{ m} \\ 5.6 + 1.7D \text{ for } D \geq 3 \text{ m} \end{Bmatrix} + \left\{6 \text{ if } 0.01 < R \leq 0.1\right\}, \quad (1.1)$$

where S is the signal-to-noise ratio in dB, R is the flow rate in gal/min, B is the acoustic background level in μV (4, 20, or 40), and D is the distance from the leak in meters. Equation (1.1) assumes a signal loss of 4.5 dB for the first 2 m, followed by a further loss of 1.7 dB/m. The acoustic signal is assumed to vary as $(\text{flow rate})^{0.32}$. A 6-dB signal enhancement is added to the 0.1-gal/min curve to indicate how the presence of reflective insulation could improve the signal-to-noise ratio. For low acoustic background levels, a 1 gal/min leak would be detected at a distance of 11 m. With a high background level, this leak would be detected only at a distance of 1 m.

b. Processing of Acoustic Leak Data

(1) Hardware Accomplishments

Hardware debugging accomplishments for this quarter have included the elimination of the 100-kHz background signal and the procurement of non-switching power supplies for the CAMAC crate. The 100-kHz background signal, first observed at Argonne National Laboratory on November 30, 1983, and subsequently observed at GARD, appears to have been caused by faulty electrical connections in the signal conditioner module. When the analog signal path wiring was firmly secured and connections were resoldered, the anomalous signal disappeared.

New power supplies were purchased for the CAMAC crate to replace the switching supplies originally provided by the vendor. These samples have been tested and are being hardened for field transport.

(2) Software Accomplishments

Software accomplishments for this quarter have included the establishment of a precise test procedure for correlogram computation, the writing of a new correlation subroutine, and the discovery and elimination of "bugs" in the operator interaction routines. The leak detector's internal function generator was enhanced to include exponential enveloping and linear frequency modulation capabilities. With the aid of the latter, functions with characteristic correlogram patterns were generated and used as data sets for testing the IEEE FFT-based correlation routines. Autocorrelograms were computed as expected, but cross-correlograms rarely yielded the expected results. However, FORTRAN programs computing the straightforward time domain solution for the same data set yielded the expected results.

Because time domain computations written in FORTRAN take so long to execute (5 minutes in our test case) and because the time expenditure in analyzing the IEEE correlator insufficiency was felt to be unpredictable at best and prohibitive at worst, a time domain correlation routine callable from a FORTRAN program was written in 68000 assembler language. This routine has been tested and found to give excellent results. It also executes in one-quarter of the time required by the IEEE FFT-based correlator.

Minor software "bugs" that were discovered and fixed included the inability of the operator to specify display limits when selecting a display of channel 2 data and inhibition of explicit plotting of exterma in high-resolution graphic displays.

(3) Improvement of Data Transfer

A serious bottleneck in the processing of ALD data is in the transfer of the raw data from the transient signal recorders in the CAMAC crate to the host computer system. Currently, the communications link consists of a Kinetic Systems Model 3989 RS-232 crate controller interfaced to our Dual Systems 83/20 computer system through a Dual SIO/DMA Intelligent Four-Port Serial I/O board.

The main problems we face are as follows: (1) the serial I/O board allows direct memory access (DMA) transfer on output only; on input, the host CPU must transfer the data one byte at a time into primary memory; and (2) since the host computer's operating system is a multiuser, multitasking system, we are allotted only small "time slices" in which to accomplish the transfer. Apparently, the duration of one such time slice is not sufficient to allow the transfer of an entire block of data from the transient signal recorders to the host computer.

These factors forced us to resort to a clumsy, programmed I/O type of data transfer. The communications protocol implemented by the CAMAC crate controller requires that to receive one raw datum (in the single-byte transfer mode), we must send about 12 bytes to the controller and then sort the datum out of approximately 23 bytes the controller sends back. Thus, to get one datum, we must transfer roughly 35 bytes.

In our breadboard system, we typically transfer a block of 2 kilobytes after each data acquisition interval. Assuming that the transfer rate is 9600 bits/s (or 960 bytes/s), and ignoring the overhead involved in internal housekeeping that the host CPU must perform between each single-byte transfer, this amounts to a transfer time of

$$\frac{(35 \text{ bytes/datum})\ (2048 \text{ data points})}{(960 \text{ bytes/s})}$$

$\simeq$ 75 s/2-kilobyte data block.

The actual transfer time, if housekeeping is considered, is about 2 min. At this point, the delay is an inconvenience. Eventually the system will transfer up to 16 kilobytes per acquisition interval, and the resulting 16-min transfer time would be intolerable.

To overcome these problems, we have decided to use a bit-parallel rather than RS-232 byte serial interface. A parallel interface is, with proper handshaking, inherently faster than a serial interface. A brief investigation of the commercially available systems for parallel interfacing of a CAMAC crate controller to an IEEE-696-standard backplane computer showed these to be generally too expensive and too inflexible for our needs.

For this reason, we intend to add a parallel port to the existing (serial interface) crate controller. The crate controller PROM firmware will be partially rewritten to support parallel transfers. In addition, we will design an I/O channel controller for the host computer system. This controller will have the ability to drive the host's buses on both output and input operations. Since the controller will have complete control of the host system's resources during CAMAC crate I/O operations, the interference from the host's operating system will be completely avoided. Using the CAMAC block transfer protocol, we will be able to transfer an entire block of data at one time, without concern for operating-system housekeeping activities.

The following example indicates that the above approach should provide a marked improvement in the data transfer rate. Table 1.2 shows execution times for a series of code segments executed by the CPU in the crate controller during block data transfers to the S-100 parallel interface card.

TABLE 1.2. Execution Time for Transfer of Data from Crate Controller to S-100 Interface

	Code	No. of Machine Cycles	Execution Time, μs (using 5-μHz clock)	Comments
Test Ø	LDA CRATE_STATUS	13	2.6	Fetch status
	AMI CMASK	7	1.4	Test bits
	JM STOP	10	2.0	If sign bit is set, time to stop
	JNZ TEST Ø	10	2.0	If some other bit is set, data not ready
	LDA DATA_YTE	13	2.6	Fetch byte
	MOV B,A	5	1.0	Save
Test 1	LDA PORT_STATUS	13	2.6	Wait until port is ready
	ANI PMASK	7	1.4	
	JNZ TEST 1	10	2.0	
	MOV A,B	5	1.0	Then send byte
	STA PORT_OUT	13	2.6	
	JMP TEST Ø	10	2.0	
STOP	...	___	___	
	TOTAL	116	23.2 μs	

If none of the loops is executed more than once for each byte transferred (i.e., if the data source on the CAMAC dataway always has a datum each time its status is polled, and if the S-100 interface is always able to immediately accept a datum from the crate controller), then the transfer rate should be $1/23.2 \times 10^{-6}$ s, or about 43 kilobytes/s.

The crate-controller code segment shown in Table 1.2 is for a polled status mode operation; i.e., the CPU examines the status byte of the data source and fetches a datum whenever it is ready. The crate controller actually operates in an interrupt-driven mode. A "first-in, first-out" buffer of data from the CAMAC dataway is maintained, and some additional housekeeping must be performed to prevent buffer overflow. This housekeeping will adversely affect the data transfer rate, but will not change its order of magnitude.

Additional efforts to speed up the data processing are being applied in the area of special-purpose signal processing hardware. As it now stands, the transfer of acoustic leak data from the transient signal recorder to S-100 RAM is the single most time-consuming operation in the entire data reduction process. This situation will change appreciably when we have modified the CAMAC crate controller-to-S-100 bus interface so that data can be transferred in parallel rather than serially; a 50-to-1 improvement in transfer time is expected. At that point, the main cause of delay will become the correlation algorithm itself.

We have implemented the time-domain correlation algorithm in Motorola MC68000 assembly language; its execution time for processing 1-kilobyte arrays is approximately 30 s. Because the MC68000 was designed to be a general-purpose microprocessor, it is not particularly efficient in carrying out digital signal processing (DSP) computations. For example, it has no special instructions for performing a sum-of-products (or multiply-accumulate) operation on an array of data, an operation that is fundamental to many DSP procedures.

To get exceptional performance in a DSP system, one has traditionally needed to use an array processor, designed with bipolar bit-slice components. Bit-slice components are, essentially, the functional units of a microprocessor [arithmetic logic unit (ALU), microprogram sequencer, control store, etc.], separated into distinct packages. This segregation allows the logic designer to create a customized instruction set. Operations that are computationally feasible only by means of multiple instruction

sequences on a general-purpose machine can be implemented in single instructions on a bit-slice microprocessor. This great flexibility has its price: Bit-slice machines are costly to develop and use, can be difficult to debug, and consume more power than MOS microprocessors.

In the past few years, however, semiconductor manufacturers have introduced single-chip digital signal processors. These are less expensive and easier to use than the bit-slice machines, although they are, for the most part, slower in execution. One notable exception is the Texas Instruments TMS32010. This device features a 200-ns cycle time and can execute most of its instructions in a single cycle. For example, a 16 x 16-bit signed integer multiplication can be performed in 200 ns. This enables the TMS32010 to compute a 64-point discrete Fourier transform (DFT) in about 600 ms. (Compare the typical execution time of the equivalent operations in an 8-MHz MC68000: 10 ms for a multiplication and about 10 mm/s for the 64-point DFT, with an efficient assembly language program.)

Other features of the TMS32010 include a modified Harvard architecture (permitting overlap of instruction fetch and execution), a 32-bit ALU/accumulator, a barrel shifter, and 288 bytes of on-chip read/write/memory. The TMS32010 can address an additional 4096 bytes of external read/write/memory and has eight 16-bit I/O ports. At first glance, a 4096-word memory seems miniscule, but because of the richness of the instruction set, programs are typically compact.

Texas Instruments provides excellent support for this product. Currently, the company is marketing an evaluation module (EVM), which is a self-contained, single-board computer with a monitor, a text editor, an assembler, a reverse assembler, and a software debugging tool, all in ROM. The EVM has two RS-232 serial ports and an EPROM programmer for creating firmware for a target system. The EVM can serve as a stand-alone development system or may be interfaced to a host computer, such as our Dual Systems 83/20. The host can provide sophisticated design tools whose implementation would not have been possible in the stand-alone system. Whether used in a stand-alone or peripheral mode, the EVM has the capability of being used as an in-circuit emulator when it comes time to debug firmware for a target system.

In summary, the TMS32010 appears to be a practical and economical way to speed up our computation of the cross-correlation. Additionally, any digital preprocessing of the raw acoustic leak signal to compensate for phase distortion introduced by the propagation medium, transducer nonlinearities, etc. may be efficiently and flexibly programmed into a TMS32010 subsystem.

c. Evaluation of Moisture-sensitive Tape

Additional tests have been carried out to help assess the effectiveness of moisture-sensitive tape for leak detection. Tapes were supplied by Techmark. Figure 1.6 shows a schematic representation of the facility used for these tests. Leaks are simulated by feeding water through a copper tube to the surface of a 10-in. Schedule 80 pipe. The tapes are located at three positions on the bottom of the pipe, which is tilted approximately 1° as indicated. The pipe is wrapped with either reflective insulation or "soft" insulation (Nu-Kon). The "soft" insulation allows water vapor to penetrate to its outer surface and severely limits the useful range of the tape. Table 1.3 shows the response time of the tape under various experimental conditions. With Nu-Kon in place and the tape placed directly below the leak (test 10), a 0.05-gal/min leak could be detected in about 12 min. With the tape 1 m away (test 11), the leak could not be detected. However, when the reflective insulation was used (test 7) with the same combination of leak and tape positions as in test 11, the leak was detected in about 10 min. The relative positions of leak and tape on a slightly tilted pipe can have a significant effect on the response time, as indicated by the data from tests 1-3. In this case, the tape was able to detect a 0.01-gal/min leak in about 60 min when it was 1 m downstream of the leak, but it did not detect the leak even after 150 min from a location 1 m upstream of the leak. As indicated in tests 5 and 7, however, larger leaks can be detected upstream over these relatively short distances. The analysis of these results suggests that moisture-sensitive tape may be useful for the detection of leaks in reactors. Under the right conditions, the tapes can detect leaks of the order of 0.01 gal/min. The tapes, however, will be significantly more effective in systems that employ reflective insulation. Despite the sensitive

nature of the tapes, they do not provide any quantitative data other than the location at which the system has been triggered. A large leak a long distance from the tape could cause the same response as a small leak at a short distance.

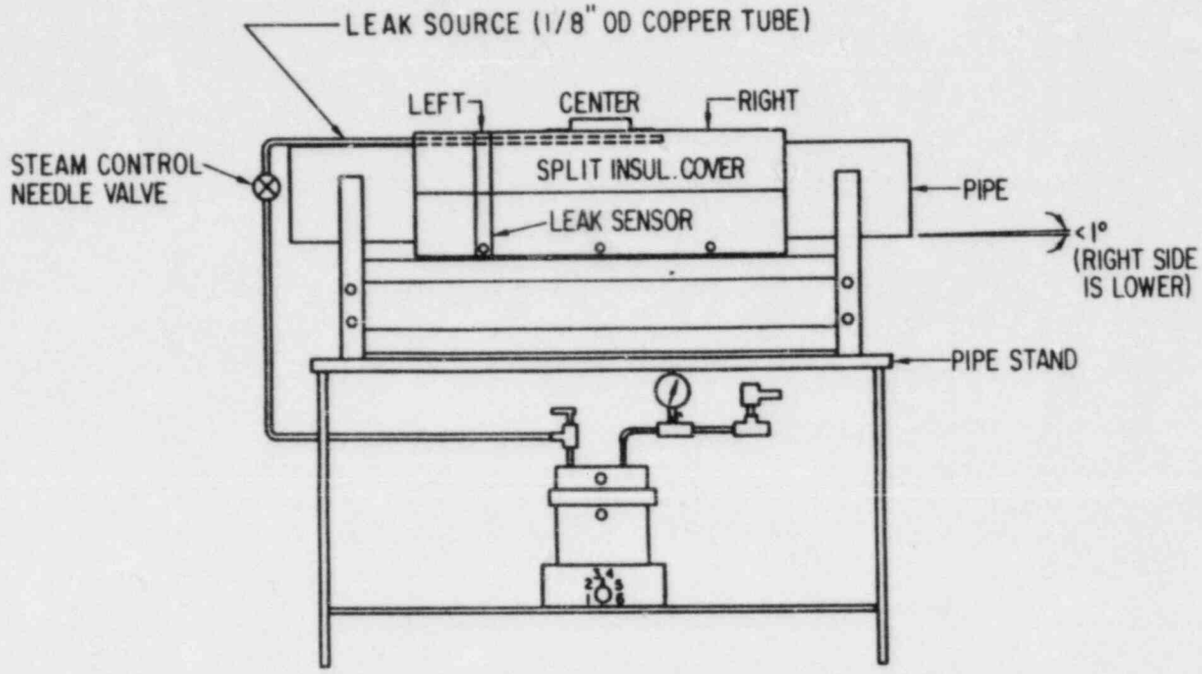

Fig. 1.6. Schematic Representation of Facility Used to Evaluate Moisture-Sensitive Tape. The leak source is placed at one of the indicated positions along the top of the pipe; the leak sensor is placed at one of the three corresponding positions along the bottom. Conversion factor: 1 in. = 2.54 cm.

TABLE 1.3. Response of Moisture-sensitive Tape to Small Leaks

Test	Tape Location[a]	Leak Location[a,b]	Type of Insulation[c]	Flow Rate, gal/min[d]	Water Temperature, °F[d]	Water Pressure, psi[d]	Response Time, min
1	center	center	R	0.01	500	1000	3.8
2	right	center	R	0.01	500	1000	60.2
3	left	center	R	0.01	500	1000	>150.0
4	center	right	R	0.01	500	1000	>270.0
5	center	right	R	0.05	480	770	9.7
6	left	right	R	0.01	500	1000	>270.0
7	left	right	R	0.05	480	770	10.5
8	center	left	R	0.05	500	800	0.3
9	right	left	R	0.05	500	800	0.5
10	left	left	S	0.05	450	900	12.0
11	left	right	S	0.05	500	1000	>65.0

[a] See Fig. 1.6.

[b] Right end of pipe was lower than left (1° tilt).

[c] R = reflective insulation; S = soft insulation (Nu-Kon).

[d] Conversion factors: 1 gal/min = 3800 cm^2/min; °C = (°F - 32)/1.8; 1 psi = 7 x 10^3 Pa.

B. Analysis of Sensitization (J. Y. Park)

1. Introduction

The microstructural changes resulting from thermal exposure, which produce susceptibility to intergranular corrosion, are collectively known as sensitization. It is one of the major causative factors in the IGSCC of austenitic stainless steels in LWR environments. Under normal isothermal heat treatments, sensitization of austenitic stainless steels such as Types 304 and 316 occurs in the temperature range of about 500 to 850°C. However, Type 304 SS may be sensitized at temperatures below this range if carbide nuclei are present at grain boundaries. This low-temperature sensitization (LTS) phenomenon in Type 304 SS has been demonstrated in laboratory experiments in the temperature range from 350 to 500°C. Extrapolations of this behavior to plant operating temperatures (288°C) yield estimated times ranging from 10 to 1000 years for significant LTS to occur. These wide variations have been attributed to differences in the amounts of strain, dislocation densities, and/or impurity element contents of the materials, but with the current level of understanding, the susceptibility to LTS of arbitrary heats of material cannot be assessed.

It is also not clear that the susceptibility to IGSCC produced by long, relatively low-temperature thermal aging can be adequately assessed by conventional measures of the degree of sensitization (DOS), such as the electrochemical potentiokinetic reactivation (EPR) technique or ASTM A262 Practices A through E. These tests have been developed and qualified primarily on the basis of the IGSCC susceptibility produced by high-temperature furnace sensitization or welding.

The objectives of this subtask are to establish the importance of LTS of materials under long-term reactor operating conditions and to evaluate the effect of thermomechanical history on the correlation of IGSCC susceptibility with tests such as the EPR technique and ASTM A262 Practices A through E.

2. Technical Progress

Investigations of the effect of plastic strain on the sensitization behavior of Type 304 SS have been continued. Type 304 SS specimens (Heat No. 10285) were heat treated at 1050°C for 0.5 h and at 700°C for 10 minutes in order to nucleate carbide precipitates, and were then plastically deformed to produce a 5.3% strain. The deformed specimens were aged at 450-600°C, along with control specimens without deformation. The DOS was measured by the EPR method after short-term aging. The results are summarized in Table 1.4. Although the results are limited to short-term aging, the specimens with plastic deformation do show larger EPR values than those without deformation. The increase in EPR value due to deformation is larger for higher aging temperatures (600°C/24 h vs 500°C/100 h). Because of slow sensitization kinetics, it will take longer aging times to see significant effect at low temperatures. Experiments for different aging conditions, amount of plastic strain, and heats of material are in progress. Additional Type 304 SS specimens (Heat Nos. 10285 and 53319) were heat treated at 1050°C for 0.5 h and at 700°C for 10 minutes, and plastically deformed for 0, 2, 5, and 10%. These specimens will be aged at 289, 315, 350 and 400°C.

Low-temperature aging of the specimens from 4-in.-diameter Type 304 SS (Heat No. 53319) pipe weldments with the IHSI, CRC, HSW, and LPHSW treatments is continuing. Since the weldments were sensitized rather severely during welding, as reported earlier,[3] the effect of further LTS may not be fully revealed. ASTM A262-E tests were performed on the HSW specimen after low-temperature aging at 500°C/24 h. The beneficial effect of HSW still remained; intergranular penetration in the HAZ was five times smaller (0.03 cm or 0.01 in.) for HSW than that (0.13 cm or 0.05 in.) for conventional or IHSI-treated weldments.

Scanning transmission electron microscopy (STEM) was performed on Type 304 SS (Heat No. 10285). Specimens were furnace-sensitized at 650°C for 4 h, and the EPR value was 11 C/cm^2. STEM specimens were prepared by jet electropolishing of a thin disk in an electrolyte of 30 v/o HNO_3 plus 70 v/o methanol at 20 V dc, 24 mA/mm^2, and -15 to -20°C. Figure 1.7 shows a grain boundary with carbide precipitates. A depleted chromium

TABLE 1.4. Effect of Plastic Strain on Sensitization of Type 304 SS (Heat No. 10285)

Aging Heat Treatment[a]	EPR, C/cm^2	
	$\varepsilon = 0$	$\varepsilon = 5.3\%$
No aging	2	2
450°C/1000 h	4	4
500°C/100 h	4	5
500°C/240 h	5	6
550°C/24 h	6	8
600°C/24 h	16	20

[a]Specimens were heat treated at 1050°C for 0.5 h and at 700°C for 10 min prior to plastic strain, and then aged.

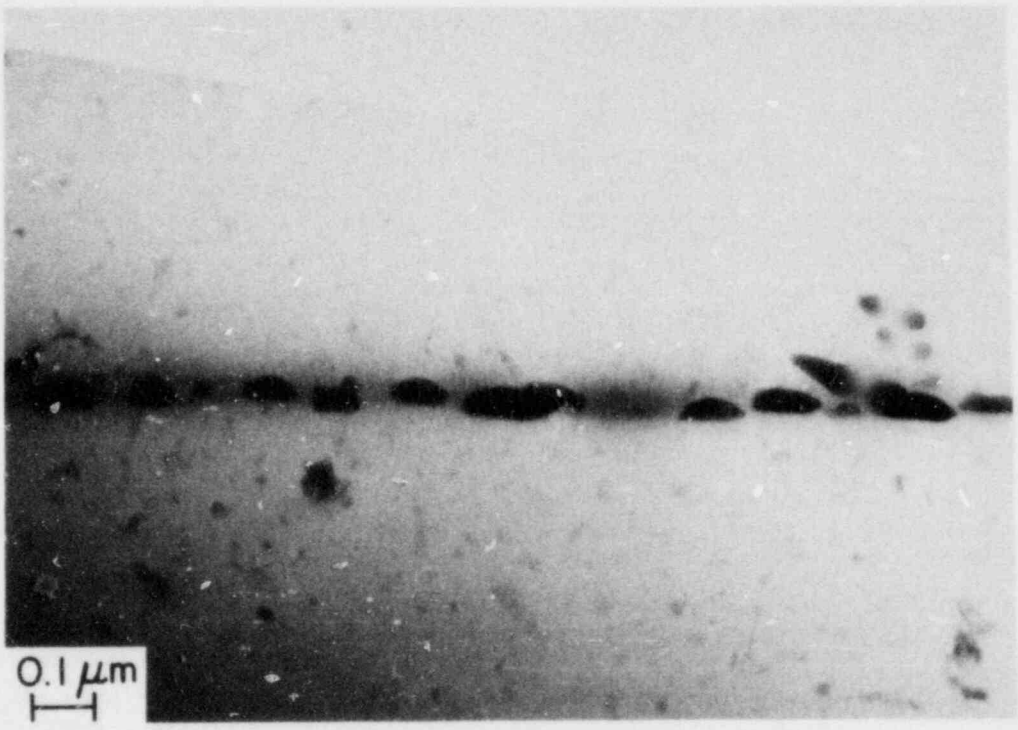

Fig. 1.7. Scanning Transmission Electron Micrograph of Type 304 SS Specimen.

concentration of 15.7 wt % (compared to a bulk chromium concentration of 18.3 wt %) was observed adjacent to the grain boundary. At about 0.15 μm from the grain boundary, the chromium concentration was 17.6 wt %, which is close to the bulk value. At carbide precipitates, up to 39.6 wt % chromium was obtained. These concentrations are averages over the sampling volume, obtained with a 200-Å-diameter electron beam at 100 kV. Further STEM studies are planned for specimens sensitized by different thermomechanical treatments, particularly LTS. The results from STEM and CERT, EPR, and ASTM A262-E tests will be compared.

A specimen of Type 316NG SS (Heat No. P91576) was heat treated at 700°C for 240 h, and a CERT test was performed in high-purity water with 8 ppm dissolved oxygen at 289°C at a nominal strain rate of 5×10^{-7} s^{-1}. The specimen failed in a predominantly ductile fracture mode with a uniform elongation of 25% (Fig. 1.8). A few small areas of brittle transgranular fracture at the surface of the specimen (maximum depth 0.3 mm and about 0.5% of total fracture surface area) were evident; however, intergranular cracking was not observed. Even after this severe heat treatment, the EPR value of the specimen was 4 C/cm^2, which is somewhat higher than the proposed critical value (2 C/cm^2) for IGSCC. The results confirm that the nuclear grade material is very resistant to sensitization and to IGSCC in a high-purity water environment. A duplicate test as well as tests at other heat treatment conditions will be performed.

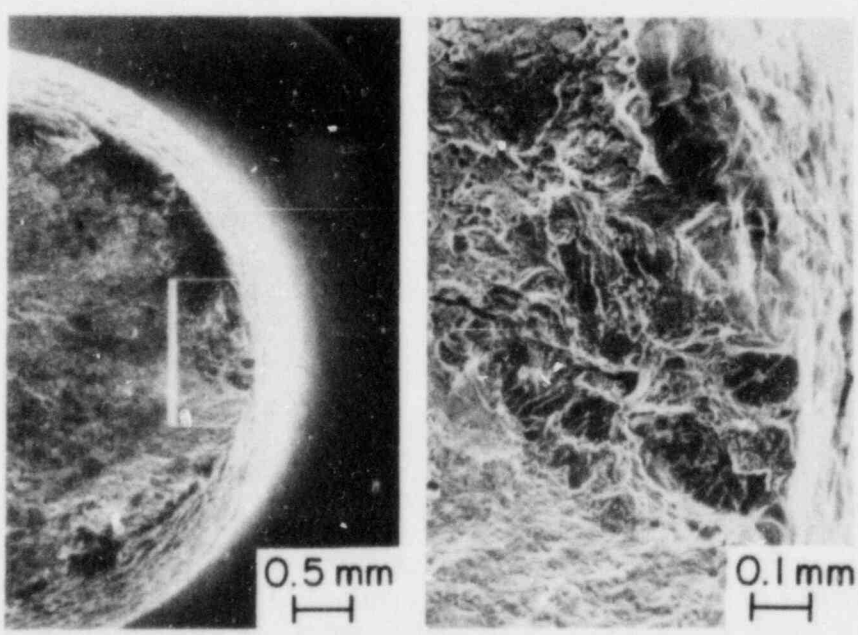

Fig. 1.8

Scanning Electron Micrograph of Type 316NG CERT Specimen.

C. Crack Growth Rate Studies (J. Y. Park and W. J. Shack)

1. Introduction

The early instances of IGSCC in operating BWRs generally occurred in small pipes, and the response to the detection of IGSCC was generally to repair or replace the cracked piping immediately. It is now clear that for reactors with standard Type 304 SS piping material, cracking can occur anywhere in the recirculation system, including the main recirculation line. Because of the severe economic consequences of long forced outages for repair or replacement, the utilities will consider other approaches for dealing with cracked pipe. The possibilities include continued operation and monitoring for any subsequent growth for an indefinite period, continued operation and monitoring until a repair can be scheduled to minimize outage, and immediate repair and replacement.

Understanding crack growth behavior is, of course, important for other reasons besides assessing the safety implications of flawed piping. A better understanding would permit a more rational extrapolation of laboratory test results to the prediction of behavior in operating plants. Current work on the measurement of crack growth rates seeks to characterize these rates in terms of the linear elastic fracture mechanics (LEFM) stress intensity as well as the level of sensitization and the amount of oxygen present in the coolant. The work in this subtask is aimed at a systematic evaluation of the validity of the use of LEFM to predict IGSCC growth. The capability of data obtained under one type of loading history to predict crack growth under a different loading history will be investigated. The effect of flaw geometry on crack propagation rates will also be considered.

2. Technical Progress

Crack growth rate tests have continued for Type 304 SS (Heat No. 10285) 1TCT specimens C-09, -11, and -17 in water with 8 ppm oxygen at 289°C and 8.3 MPa (1200 psi). The current series of tests will establish (at a fixed K) the effect of load ratio R and frequency f on the growth rate, and whether these effects can be understood in terms of the crack-tip strain

rate. The specimens had been furnace heat treated for 700°C/10 min, with a subsequent additional treatment of 450°C/146 h, 450°C/250 h, or 500°C/24 h. The EPR values of companion test coupons were 8, 15, and 4 C/cm^2 for SPC C-09, C-17, and C-11, respectively. Growth rates at maximum stress intensities (K_{max}) ranging from 28 to 38 $MPa \cdot m^{\frac{1}{2}}$; R = 0.5-0.94 and 1; and f = 0, 1×10^{-3}, 2×10^{-3}, and 1×10^{-1} Hz have been reported previously.[4] Sawtooth waveforms with an unloading time of 5 s were used for the cyclic-loading tests. The crack length was continuously monitored by the compliance method with an in-situ clip gage. During the current reporting period, additional tests were carried out at R = 0.95, f = 2×10^{-3} Hz, and K_{max} = 35-39 $MPa \cdot m^{\frac{1}{2}}$. Figure 1.9 shows crack length vs test time for the three specimens. Interruptions or changes in the test conditions (R, f, or K value) occurred at times I through XXI. Average crack propagation rates were obtained by least-squares linear regression analysis for each test condition, and the results, along with those reported previously,[4] are summarized in Table 1.5. For this heat of material and these sensitization conditions, propagation rates are not accelerated by superposed vibrational loads (R = 0.95) compared with the rates under constant load. In fact, the rates decrease slightly. The crack lengths for specimens C-09 and C-17 appeared to decrease beyond interruption IX (Fig. 1.9); this suggested that the clip gages had begun to malfunction. Therefore, average crack propagation rates were not calculated for specimen C-09, or for specimen C-17 beyond interruption IX.

Ford[5] has proposed that the crack growth rate is proportional to the square root of the crack-tip strain rate, i.e.,

$$\dot{a}_{IGSCC} = A \, \dot{\varepsilon}_T^{\,n} \, . \qquad (1.2)$$

As discussed in Section I.D below, this relation is consistent with data obtained from CERT tests at different strain rates. Analysis of the fracture mechanics crack growth tests requires an expression for the crack-tip strain rate. Under constant applied loads, the crack-tip strain rate is determined by the time-dependent plastic deformation, i.e., creep, near the crack tip. For cyclic applied loads of sufficiently high frequency (and sufficiently low R values), the strains are imposed by the external

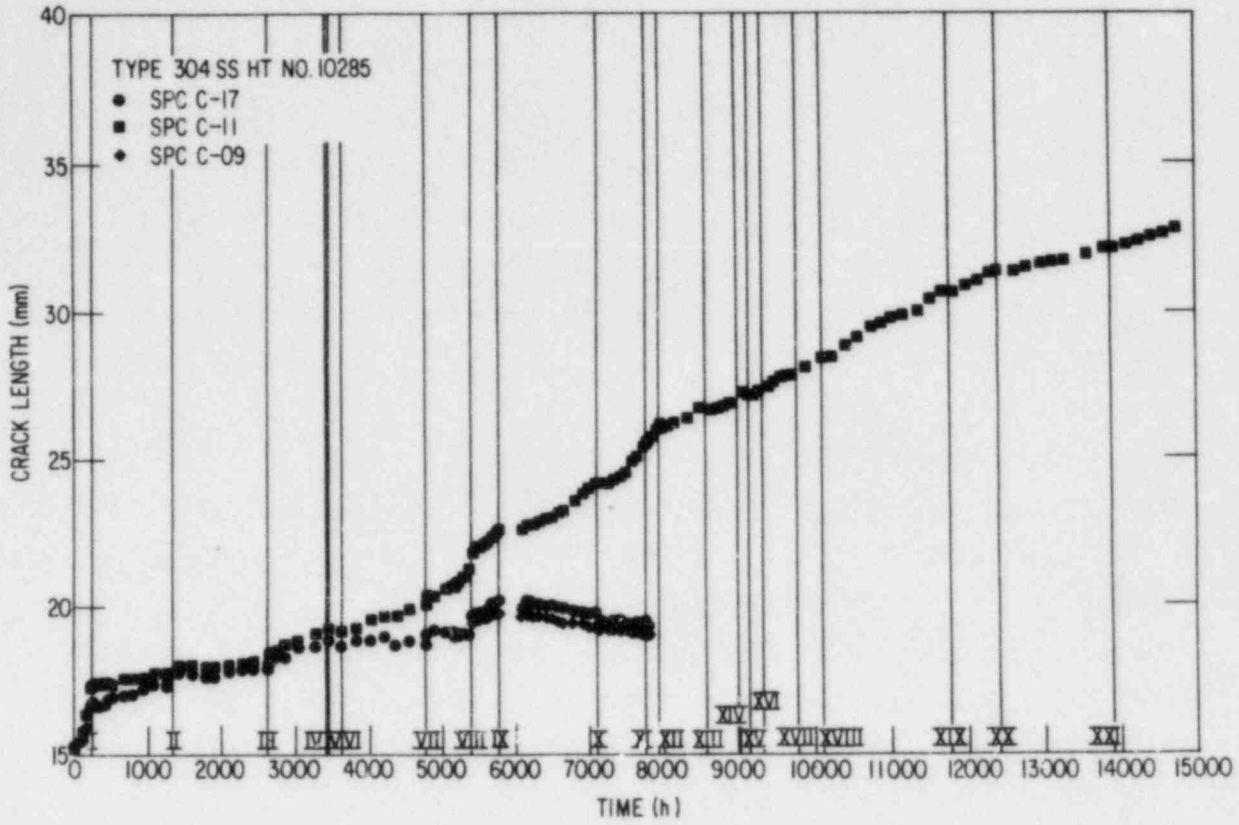

Fig. 1.9. Plots of Crack Length vs Time for Heat No. 10285 Specimens.

loading mechanism. Estimates of the crack-tip strain rates in this case can be obtained from LEFM. Scott and Truswell[6] have suggested a relation of the form

$$\dot{\varepsilon}_T = - 1/T \ln [1 - (1 - R)^2/2], \qquad (1.3)$$

where T is the rise time for the tensile portion of the load cycle. Related expressions for crack-tip strains in fatigue have been proposed by Rice[7] and others. Equation (1.2), since it neglects constant-load creep, predicts $\dot{\varepsilon}_T = 0$ for the constant-load case. It also predicts that the crack-tip strain rate is independent of the value K and hence, together with Eq. (1.1), predicts that the crack growth rate is independent of K. This prediction is contradicted by many experimental observations. Estimates of the crack-tip strain rate obtained from Eq. (1.2) are included in Table 1.5 for the tests on Heat No. 10285 where both R and f are varied. Figure 1.10 shows the crack-tip strain rate vs crack growth rate. As reported earlier,

TABLE 1.5. Crack Propagation Rates in Type 304 SS Specimens (Heat No. 10285) Sensitized to Two Different Levels and Tested in 289°C Water with 8 ppm O_2

f, Hz	R	$\dot{\varepsilon}_T$, s^{-1} [(a)]	K_{max}, MPa·$m^{\frac{1}{2}}$	$\dot{a}$, m/s
		EPR = 4 C/cm^2		
0	1	-	33-34	1.2×10^{-10}
0	1	-	36-37	2.9×10^{-10}
0	1	-	37-38	4.5×10^{-10}
1×10^{-3}	0.5	1.4×10^{-4}	31-32	2.6×10^{-10}
2×10^{-3}	0.5	2.7×10^{-4}	30-31	8.9×10^{-10}
2×10^{-3}	0.5	2.7×10^{-4}	30-33	3.4×10^{-9}
2×10^{-3}	0.6	1.7×10^{-4}	32-33	6.6×10^{-10}
2×10^{-3}	0.7	9.3×10^{-5}	30-31	3.4×10^{-10}
2×10^{-3}	0.7	9.3×10^{-5}	32-33	5.9×10^{-10}
2×10^{-3}	0.79	4.5×10^{-5}	31-32	5.5×10^{-10}
2×10^{-3}	0.79	4.5×10^{-5}	34-36	5.4×10^{-10}
2×10^{-3}	0.8	4.1×10^{-5}	29-32	7.4×10^{-10}
2×10^{-3}	0.8	4.1×10^{-5}	30-31	4.4×10^{-10}
1×10^{-1}	0.94	1.8×10^{-4}	30-31	3.1×10^{-10}
1×10^{-1}	0.94	1.8×10^{-4}	31-32	1.9×10^{-10}
2×10^{-3}	0.95	2.5×10^{-6}	35-36	1.7×10^{-10}
2×10^{-3}	0.95	2.5×10^{-6}	36-37	1.5×10^{-10}
2×10^{-3}	0.95	2.5×10^{-6}	38-39	2.0×10^{-10}
		EPR = 15 C/cm^2		
0	1	-	32-33	2.2×10^{-10}
2×10^{-3}	0.5	2.7×10^{-4}	30-32	2.8×10^{-9}
2×10^{-3}	0.6	1.7×10^{-4}	28-29	5.6×10^{-10}
1×10^{-1}	0.94	1.8×10^{-4}	30	2.1×10^{-10}

[a] $\dot{\varepsilon}_T = -1/T \ln [1 - (1 - R)^2/2]$.

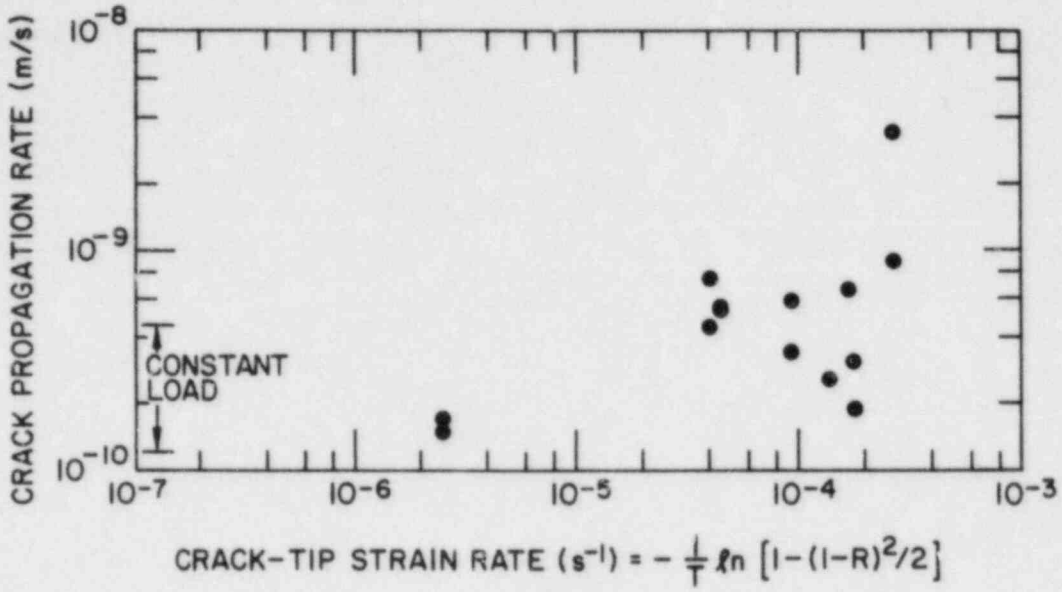

Fig. 1.10. Crack Propagation Rate vs Crack-Tip Strain Rate for Type 304 SS (Heat No. 10285).

no significant correlation can be established between the propagation rate and the estimate of crack-tip strain rate. The correlation is being re-examined with an alternative estimate of crack-tip strain rate based on LEFM with an additional semi-empirical term for constant-load creep deformation at the tip. The crack growth rate tests are continuing with R = 0.95, f = 2 x 10^{-3} Hz, and K_{max} = 39 MPa·$m^{\frac{1}{2}}$ for a longer crack length.

Electrical potential drop methods for crack length measurement have been studied. The sensitivity and stability of the A.C. system was improved. Room temperature tests show a sensitivity of 1.2 V/in. of crack extension, a crack length uncertainty due to temperature changes of less than 6.6 x 10^{-3} cm/°C (2.6 x 10^{-3} in./°C), and a stability of 2.5 x 10^{-3} cm/day (±1 x 10^{-3} in./day). The next tests will be fatigue crack growth tests in high-purity water at 289°C to calibrate the ac potential system.

D. Evaluation of Nonenvironmental Corrective Actions (P. S. Maiya and W. J. Shack)

1. Introduction

The fundamental premise of the current efforts to prevent IGSCC in BWR piping is that IGSCC involves a complex interaction among material susceptibility (sensitization), the stresses acting on the material, and the environment; and that suitable alteration or variation of these parameters can produce immunity to IGSCC. Nonenvironmental corrective actions seek to mitigate either the material susceptibility or the state of stress on the inside surface of the weldment. They include techniques for improving the margin against IGSCC of a susceptible material like Type 304 SS and the identification of alternative materials that are inherently more resistant to IGSCC.

The objective of the current work is an independent assessment of the proposed remedies developed by the utilities and the vendors. Additional testing and research has been carried out to eliminate gaps in the existing data base on alternative materials and fabrication and to develop a better understanding of the relation between the existing laboratory results and satisfactory in-reactor operating performance. Current efforts in this task include additional screening tests for alternative materials and studies of the residual stress distributions associated with weld overlays.

2. Technical Progress

a. Impurity and Strain Rate Effects

CERT tests are continuing on Types 316NG (Heat No. P91576), 316 (Heat No. 0590019), and 304 SS (Heat No. 53319) in oxygenated water (0.2 and 8 ppm O_2) with or without Cl^- and SO_4^{2-} impurities. Specimens are tested in the solution-annealed (1050°C/0.5 h) and solution-annealed and aged (600-700°/2-24 h) conditions. The impurity levels in the initial studies were chosen to be consistent with the operating limits under off-normal

conditions; currently, the impurity levels are within the limits recommended by Reg. Guide 1.56 for normal reactor operating conditions. The tests were conducted at strain rates between 10^{-5} and 10^{-8} s^{-1}. SCC susceptibility has been quantified in terms of CERT parameters such as average crack growth rate, time to failure, and maximum crack length.

As has been discussed in earlier reports,[8,9] although Type 316NG SS is extremely resistant to IGSCC, it can exhibit TGSCC susceptibility in water chemistries consistent with Reg. Guide 1.56 (e.g., 0.2 ppm O_2 + 0.1 ppm SO_4^{2-}). However, the average crack growth rate, $\dot{a}_{av}$, is lower than the intergranular crack growth rates observed in sensitized Types 304 and 316 SS in the same environments.

The effect of oxygen on the relative SCC susceptibility of Types 304, 316, and 316NG SS in water containing 0.1 ppm SO_4^{2-} for several heat treatments and strain rates is shown in Table 1.6. When the dissolved oxygen level decreases from 8 to 0.2 ppm, $\dot{a}_{av}$ (IGSCC) decreases by a factor of 3 for Type 304 SS (EPR = 24 C/cm^2) and by a factor of 2 for Type 316 SS (EPR = 17 C/cm^2), but $\dot{a}_{av}$ (TGSCC) for 316NG SS remains unaffected. These results suggest that TGSCC in 316NG is less sensitive to dissolved oxygen levels than IGSCC in conventional materials, at least over the range considered.

In tests at dissolved oxygen levels typical of BWRs ($\sim$0.2 ppm) and at impurity levels consistent with current water chemistry limits, the transgranular crack growth rates in Type 316NG SS are approximately a factor of 5 slower than the intergranular crack growth rates in Type 304 SS and approximately a factor of 3 slower than those in Type 316 SS when the data are compared at the same strain rate (the estimated $\dot{a}_{av}$ for Type 316 SS at 1×10^{-6} s^{-1} is 4.3×10^{-7} cm/s). Thus, the order-of-magnitude difference in crack growth rates between Types 316NG and 316 SS observed in a more aggressive environment with 8 ppm O_2 and 0.5 ppm Cl^- is significantly reduced in environments more characteristic of reactors.

TABLE 1.6. Effect of Oxygen on the Relative Susceptibility of Types 304, 316, and 316NG SS Tested in 289°C Water with 0.1 ppm SO_4^{2-} and 0.2 or 8 ppm O_2

Material	Heat Treatment[a]	$\dot{\varepsilon}$, s^{-1}	$\dot{a}_{av}$, cm/s	
			0.2 ppm O_2	8 ppm O_2
Type 304	SA + 600°C/24 h	1.0×10^{-6}	7.26×10^{-7}	2.16×10^{-6} 2.13×10^{-6}
Type 316	SA + 650°C/24 h	2.0×10^{-6}	5.23×10^{-7} 5.27×10^{-7}	1.0×10^{-6}
Type 316NG	SA + 650°C/24 h	1.0×10^{-6}	1.4×10^{-7}	1.5×10^{-7}

[a]SA = solution annealed.

In a previous report,[9] we discussed the development of a phenomenological model for IGSCC susceptibility, which describes the effects of the applied strain rate on IGSCC. In the strain-rate regime where the susceptibility to IGSCC increases with a decrease in strain rate, the model gives simple power-law correlations between $\dot{\varepsilon}$ and parameters such as $\dot{a}_{av}$ and time to failure. The model is based on an estimate of the crack-tip strain obtained by use of a J-integral approach, the slip-dissolution model of Ford,[10] and a J-integral fracture criterion. Since the slip-dissolution model does not distinguish between IGSCC and TGSCC, the results observed for Type 316NG SS should also be consistent with the model.

Since a detailed description of the model has been reported previously,[9,11] we outline only the essential ingredients and show the comparison between the results of the analysis and CERT results on TGSCC in Type 316NG SS. For a fully plastic material containing a crack in a uniform strain field, the crack-tip strain rate is given by[9,11]

$$\dot{\varepsilon}_T = \frac{\dot{\varepsilon}}{\varepsilon} + \frac{\dot{a}}{a} , \qquad (1.4)$$

where ε and $\dot{\varepsilon}$ are the nominal strain and strain rate, respectively, and a and $\dot{a}$ are the crack length and crack growth rate, respectively. Using the slip-dissolution model proposed by Ford, one obtains the following relationship between the crack growth rate and the crack-tip strain rate or the nominal strain rate:

$$\dot{a} = A_T \left(\frac{\dot{a}}{a} + \frac{\dot{\varepsilon}}{\varepsilon} \right)^{0.5} , \tag{1.5}$$

where A_T is a constant. The exact solution of Eq. (1.5) for CERT tests is

$$a = A_T \sqrt{6t} . \tag{1.6}$$

Defining $a = a_f$ and $t = t_f$ at failure, Eq. (1.6) becomes

$$a_f = A t_f^{0.5} . \tag{1.7}$$

The experimental results observed for Types 316 and 316NG SS are in good agreement with Eq. (1.7), as can be seen from Fig. 1.11, in which the time to failure has been corrected for a small crack initiation time t_o (i.e., $t_o << t_f$). Equation (1.7) is not in itself sufficient to determine t_f; an additional fracture criterion is required. In the model, we assume that the failure of the specimen occurs when the J-integral approaches the value J_c, which can be related to ε_f and a_f as follows:

$$J_c = C \varepsilon_f^{n+1} a_f , \tag{1.8}$$

where J_C depends on the material and geometry but is independent of $\dot{\varepsilon}$, C is a material parameter related to plastic modulus, and ε_f is the strain at failure ($\sim \dot{\varepsilon} t_f$). A log-log plot of a_f as a function of ε_f (Fig. 1.12) yields a straight line (within the limits of experimental scatter) with a

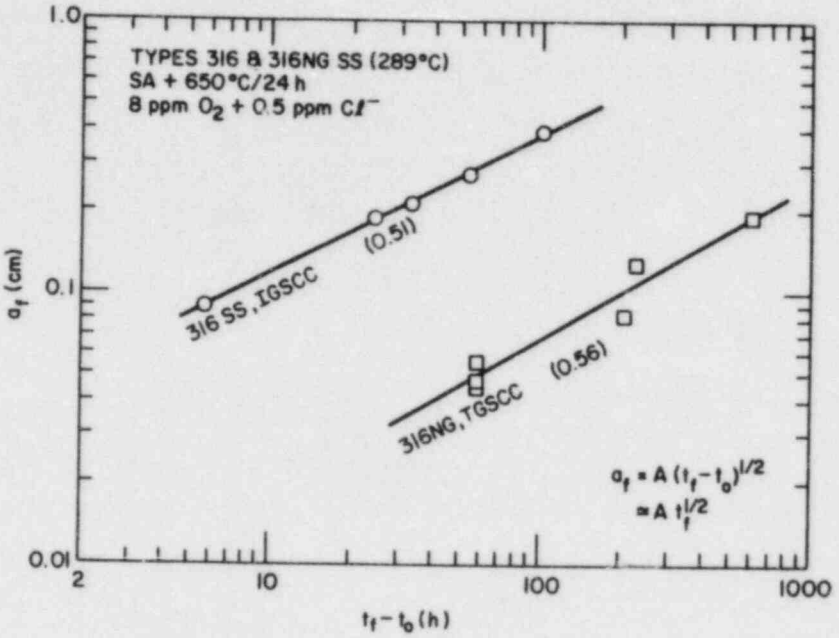

Fig. 1.11. Log-Log Plots of Crack Length at Failure (a_f) vs Failure Time (Corrected for Crack Initiation Time) in Tests Conducted at Different Strain Rates.

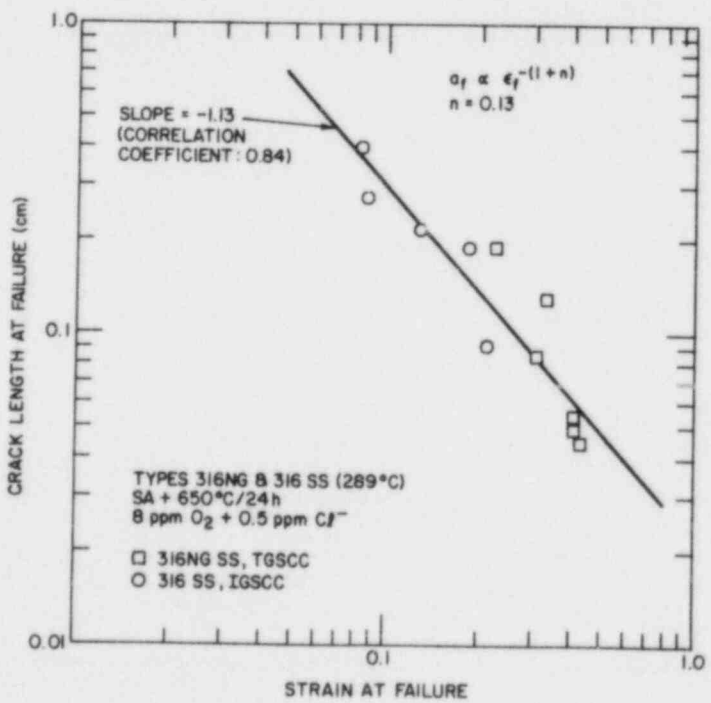

Fig. 1.12. Log-Log Plot of Crack Length at Failure (a_f) vs Strain at Failure (ε_f).

slope equal to -1.13. From this slope, the value of n is found to be about 0.13. (Higher values of power law exponent are usually quoted for stainless steel. However, they are based on a description of the stress-strain behavior over a wide range of strains; $n \simeq 0.13$ is a fairly typical value at large strains [near fracture] and is in good agreement with the value determined from a true-stress/true-strain analysis of the data for large strains.) Since n is small, Eq. (1.8) can be simplified to

$$J_c = C\varepsilon_f a_f \ . \tag{1.9}$$

The data for Types 316NG and 316 SS in Fig. (1.12) can be combined since the fracture-characterizing parameter J_C (or, more specifically, J_C/C) is approximately the same for the two materials, as can be seen from Table 1.7. Since $\varepsilon_f \simeq \dot{\varepsilon} t_f$ and $\dot{a} \simeq a_f/t_f$, Eqs. (1.8) and (1.9) can be combined to derive correlations between the SCC (both IGSCC and TGSCC) susceptibility parameters and the strain rate, as follows:

$$\varepsilon_f = (J_c/AC)^{2/3}\ \dot{\varepsilon}^{1/3} \ , \tag{1.10}$$

$$a_f = A(J_c/AC)^{1/3}\ \dot{\varepsilon}^{-1/3} \ , \tag{1.11}$$

$$t_f = (J_c/AC)^{2/3}\ \dot{\varepsilon}^{-2/3} \ , \text{ and} \tag{1.12}$$

$$\dot{a}_{av} = A(AC/J_c)^{1/3}\ \dot{\varepsilon}^{1/3} \ . \tag{1.13}$$

As for the case of IGSCC, good agreement is obtained between the results of the analysis and CERT results on TGSCC for Type 316NG SS over a fairly wide range of strain rates. As shown in Figs. 1.13 and 1.14, respectively, log-log plots of $\dot{a}_{av}$ and t_f as a function of $\dot{\varepsilon}$ yield straight lines with slopes that are in good agreement with the strain rate exponents predicted by Eqs. (1.13) and (1.12), respectively.

TABLE 1.7. Values of J_c/C (cm) for Types 316 and 316NG SS Tested at Different Strain Rates in 289°C Water with 8 ppm O_2 and 0.5 ppm Cl^-

$\dot{\epsilon}$, s^{-1}	Type 316 SS	Type 316NG SS
1×10^{-5}	0.0193	-
2×10^{-6}	0.0355	0.0193 0.0224 0.0195
1×10^{-6}	0.0279	-
4×10^{-7}	0.0241	0.0442 0.0257
2×10^{-7}	0.0332	-
1×10^{-7}	-	0.0437
	0.028 ± 0.007[a]	0.029 ± 0.01[a]

[a] $(J_c/C)_{av}$.

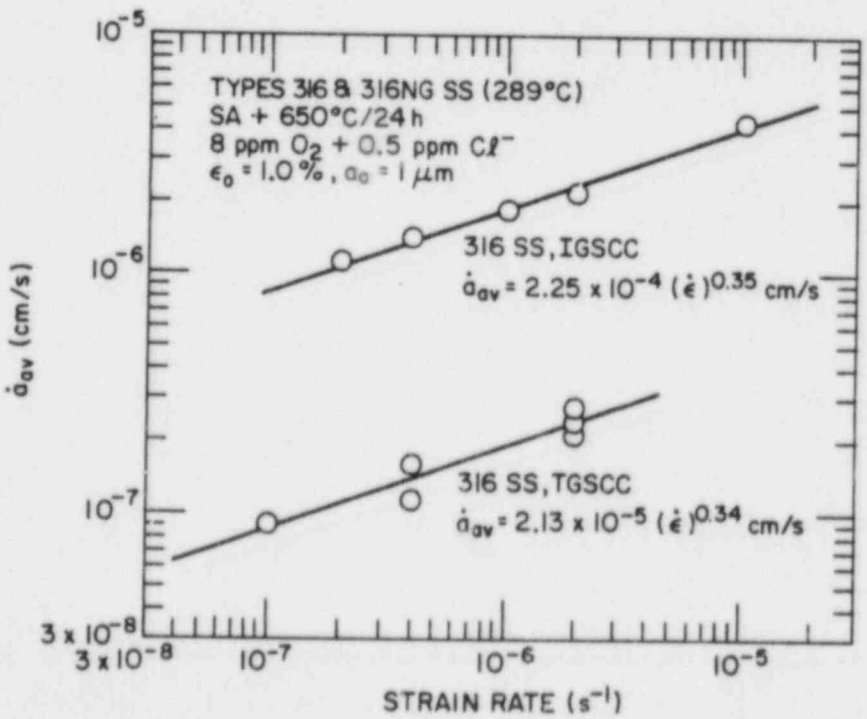

Fig. 1.13. Correlation between Average IGSCC or TGSCC Growth Rate ($\dot{a}_{av}$) and Strain Rate ($\dot{\epsilon}$).

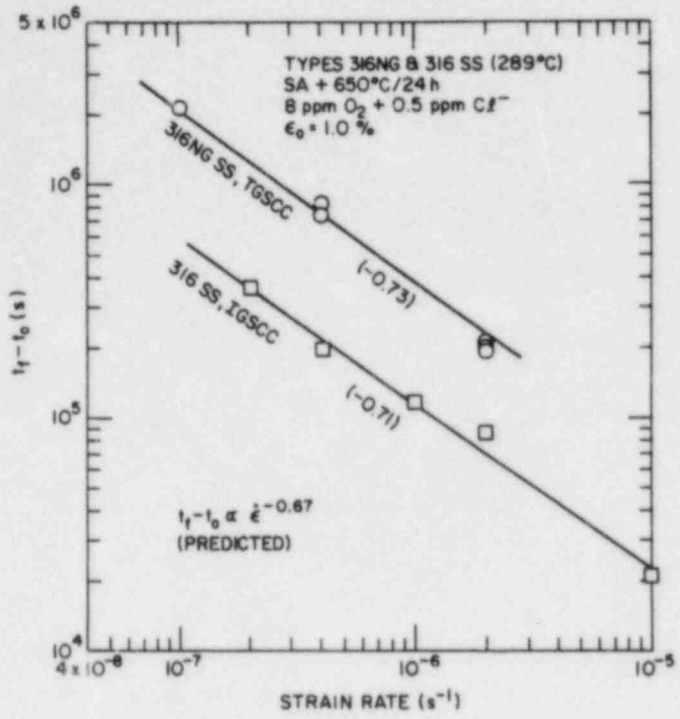

Fig. 1.14

Correlation between Failure Time and Strain Rate for Stress Corrosion Cracks (IGSCC and TGSCC).

An average crack-tip strain rate, $\bar{\dot{\epsilon}}_T$, can be defined as follows:

$$\bar{\dot{\epsilon}}_T = \frac{1}{t_f - t_o} \int_{t_o}^{t_f} \dot{\epsilon}_T dt \ . \tag{1.14}$$

9,11

Substituting from Eq. (1.4) and performing the integration, one obtains

$$\bar{\dot{\epsilon}}_T = \frac{1}{t_f - t_o} \left[\ln \frac{\epsilon_f}{\epsilon_o} + \ln \frac{a_f}{a_o} \right] \ . \tag{1.15}$$

As shown in Fig. 1.15, the average crack growth rate is proportional to the square root of the average crack-tip strain rate for both TGSCC and IGSCC.

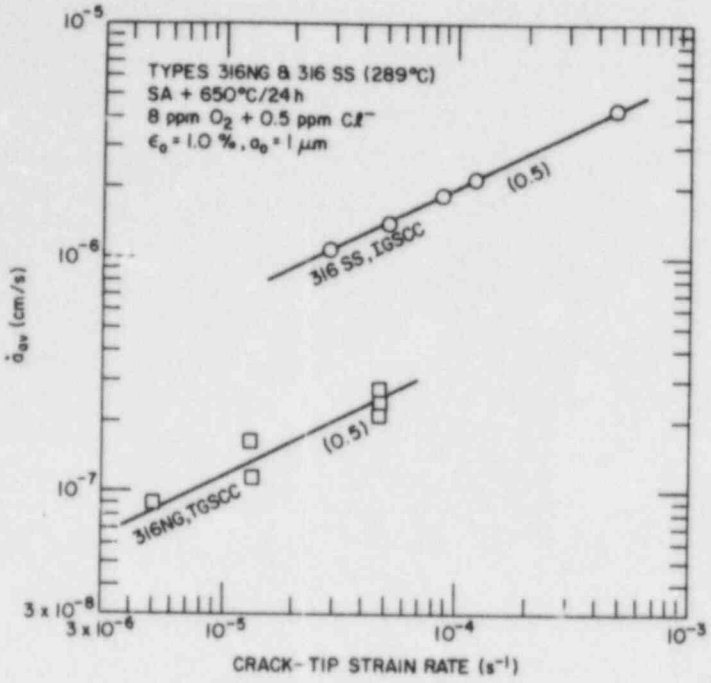

Fig. 1.15

Correlation between Average IGSCC or TGSCC Growth Rate and Average Crack-Tip Strain Rate.

Additional experiments are being performed in reactor-type environments over a wide range of strain rates to determine the relative susceptibility to TGSCC of solution-annealed Types 304 and 316NG SS. Also, experiments are being planned to delineate the role of impurities insofar as TGSCC susceptibility is concerned, and additional heats of 316NG SS are being tested to evaluate heat-to-heat variations in cracking susceptibility.

b. Stress/Strain/Strain-Rate Relations for Sensitized Materials

Stress relaxation experiments are being performed to determine the stress/strain/strain-rate relations of Types 304 and 316 SS for different material conditions (e.g., solution annealed, sensitized). These constitutive equations are required in order to use laboratory results obtained under idealized loading histories (CERT, pipe, constant load tests, etc.) to predict behavior under the loading histories encountered under reactor operating conditions. Measurements have been made on Type 316 SS (Heat No. 0590019) and Type 304 SS (Heat No. 53319) at temperatures of 28 to 289°C over a wide range of strain rates (10^{-4} to 10^{-10} s^{-1}) at different

plastic strains (~0.5-8.0%). Experiments on the materials in the as-received, solution-annealed, and solution-annealed and sensitized conditions at 600-650°C/24-50 h have been completed at 28°C, and plans are under way to perform similar experiments on Type 304 SS at 289°C. The results of the analysis for Type 316 SS showed that the constitutive equation[12] governing the glide friction-controlled flow, namely,

$$\dot{\varepsilon} = \dot{a}^* \left(\frac{\sigma - \sigma^*}{G} \right)^M \tag{1.16}$$

or

$$\sigma = \sigma^* + \left(\frac{G^M}{\dot{a}^*} \right)^{1/M} (\dot{\varepsilon})^{1/M} \tag{1.17}$$

(where $\dot{a}^*$ is the glide friction rate parameter, σ is the stress, σ^* is the hardness, G is the shear modulus, and M and m are constants), described the data obtained at non-elastic strains >1.0% fairly well over a wide range of strain rates. The data obtained for $\varepsilon_i > 1.5\%$ (where ε_i = initial non-elastic strain prior to relaxation) can be fit by assuming that M is approximately constant over a range of strains between 1.5 and 8.0%, while permitting $\dot{a}^*$ over the same range of strains to vary by more than an order of magnitude. However, the assumption of a constant $(G^M/\dot{a}^*)^{1/M}$ in Eq. (1.17) describes the data equally well.[11]

One of the assumptions in the use of Eq. (1.16) is the constancy of the hardness parameter σ^* and the rate constant $\dot{a}^*$ during the relaxation process. As can be seen from Fig. 1.16, the change in strain during a test is small when $\varepsilon_i > 1.5\%$, but it can be when $\varepsilon_i < 1.0\%$. In addition, strain-aging effects in austenitic stainless steels can be significant at low temperatures. Recently, the possibility of changing coefficients in Eq. (1.16) as a result of effects associated with strain aging has been discussed by Hannula and Li.[13] To obtain better insight into the constitutive equation, the stress relaxation data obtained for 316 SS at 28°C at strains between 0.5-8% have been reexamined. Again, the best fit of the data is obtained by assuming that M is approximately constant (M = 14 ± 0.7) but that $\dot{a}^*$ is not a constant.

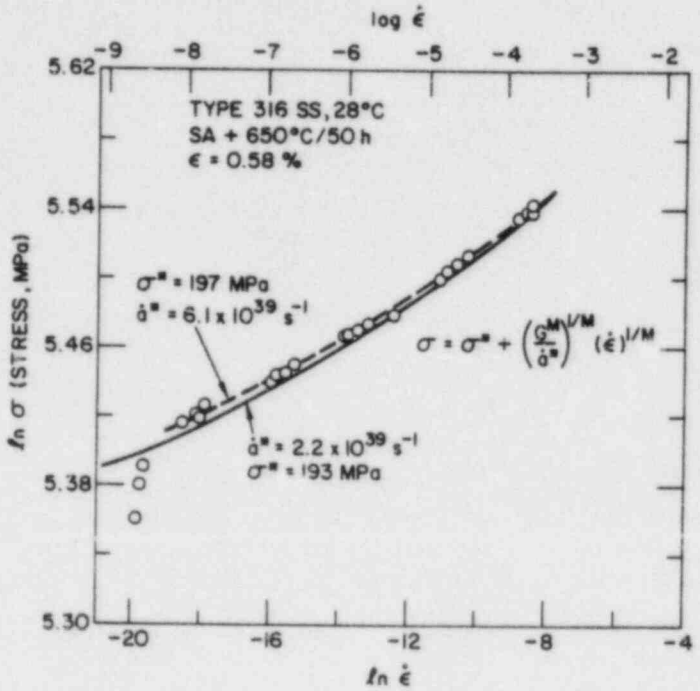

Fig. 1.16. Stress Relaxation Behavior at Low Strains.

To examine whether $\dot{a}^*$ varies systematically with σ^* in different relaxation tests, M was held constant at 14, and the values of $\dot{a}^*$ and σ^* were determined. The results are shown in Table 1.8. The value of $\dot{a}^*$ decreases systematically with an increase in σ^*. The relation between $\dot{a}^*$ and σ^* can be described by a power law, as can be seen from Fig. 1.17, and the variations in the values of the coefficients can be interpreted in a qualitative manner[13] in terms of the dislocation density and mobility, both of which are affected by non-elastic strains and strain aging effects in these materials. The data obtained at $\dot{\epsilon} > 10^{-8}$ s^{-1} for $\epsilon_i = 0.58\%$ can be described well by Eq. (1.16). However, there appears to be some anomalous behavior at $\dot{\epsilon} < 10^{-8}$ s^{-1} (see Fig. 1.18). Attempts to force a fit of the data at $\dot{\epsilon} < 10^{-8}$ resulted in a decrease in the value of $\dot{a}^*$ from 6 x 10^{39} to 3 x 10^{39} s^{-1}. The difference in the relaxation behavior at $\dot{\epsilon} > 10^{-8}$ s^{-1} and at $\dot{\epsilon} < 10^{-8}$ s^{-1} cannot be attributed to temperature variation and appears to be a real effect.

TABLE 1.8. Stress Relaxation Data for Solution-annealed and Aged Type 316 SS Tested at 28°C

ϵ, %	σ_i, MPa	σ^*, MPa	$\dot{a}^*$, s^{-1}
0.58-0.67[a]	257	193	6.1×10^{39}
1.77-1.84	284	224	5.6×10^{39}
2.91-2.99	313	249	1.6×10^{39}
3.79-3.86	342	279	1.6×10^{39}
5.80-5.88	375	305	4.3×10^{38}
7.38-7.46	408	334	1.5×10^{38}

[a]Data obtained for $\dot{\epsilon} < 10^{-8}$ are not considered (see the text).

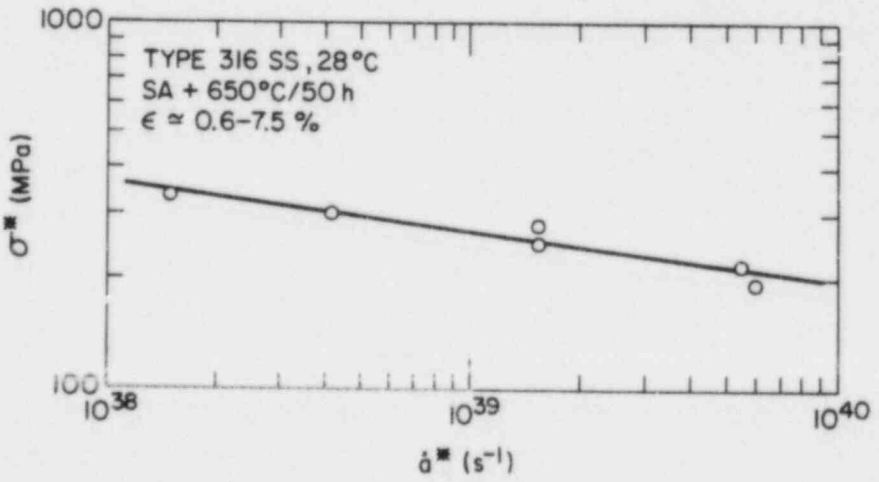

Fig. 1.17. Correlation between Hardness (σ^*) and Glide Friction Rate Parameter ($\dot{a}^*$) over a Wide Range of Non-Elastic Strains.

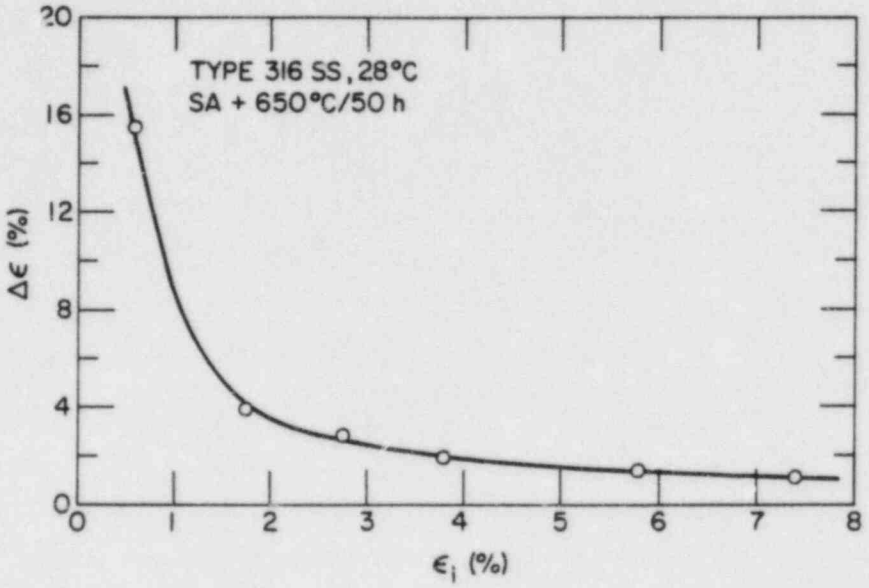

Fig. 1.18. Change in Non-Elastic Strain vs Initial Non-Elastic Strain for Different Stress Relaxation Runs.

c. Measurement of Residual Stresses Produced by Weld Overlays

Inner-surface and throughwall axial residual stresses have been measured on the minioverlay mock-up supplied by Georgia Power and NUTECH for analysis. The weldment was fabricated from 12-in. Schedule 100 pipe by use of overlay welding procedures identical with those used in the repairs on the Hatch reactors. Different weld-prep geometries were used on the two sides of the weld. One was a long, smooth geometry typical of that used in Hatch 1, and the other was a short, angular geometry typical of that used in Hatch 2. Measurements were made at seven axial locations on the side with the long weld-prep geometry and six axial locations on the side with the short weld-prep geometry. The axial locations are indicated in Fig. 1.19. The inner-surface stresses were examined at four azimuths, and throughwall stresses were measured at one azimuth (45°). (Stresses were not measured at all the intended locations, since several gauges were lost during the strain relief process.) Miniature 60° strain-gauge rosettes (Micro-Measurements EA-09-030YB-120) with an active length of 0.76 mm (30 mils) were used.

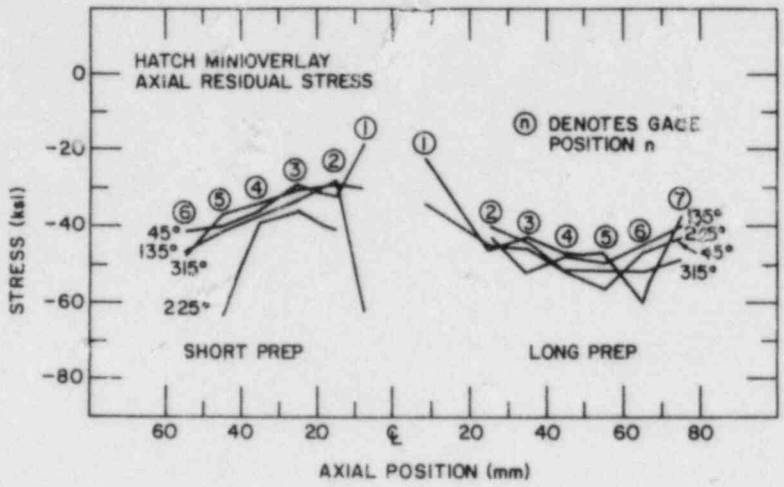

Fig. 1.19. Axial Residual Stresses on the Inner Surface at Four Azimuths of the Minioverlay Mock-Up Weldment.

After the complete weldment was instrumented, full-thickness specimens 63 mm wide and 340 mm long were cut from the weldment at the four azimuthal positions where the strain gauges were mounted. The stress changes measured on the inner and outer surfaces during this process can be used to calculate the net forces and moments acting on the specimens before they were cut from the complete weldment. However, they are not accurate measures of the actual stresses on the inner and outer surfaces, since substantial self-equilibrating stresses remain in the full-thickness specimens. To determine the actual stresses on the inner surface, a thin slab (3 mm thick) was removed from the inner surface of each specimen by electrical discharge machining. This provides almost complete stress relief for the gauges on the inner surface.

To determine the throughwall distribution of stresses in the weldment, thin layers of material were removed from the inner surface by milling. The resultant strain relief measured by the gauges mounted on the outer surface of the weldment was used to compute the throughwall stress distribution. A detailed discussion of the experimental procedures and analysis used was given in Ref. 14.

For both weld prep geometries, the overlay was very successful in inducing compressive residual stresses on the inner surface of the weldment, as shown in Figs. 1.19 and 1.20. The measured results are in general agreement with the finite element predictions supplied by NUTECH; the residual stresses show a general decrease with distance from the weld fusion line, with the compressive residual stresses reaching a peak at the end of the overlay. However, the measured residual stresses on the inner surface are significantly more compressive than those predicted by the calculations. The finite-element calculations also show some very rapid oscillations near the weld fusion line. The experimental results do show more scatter near the fusion line, which is consistent with this prediction, but it is difficult to resolve stress gradients on this scale.

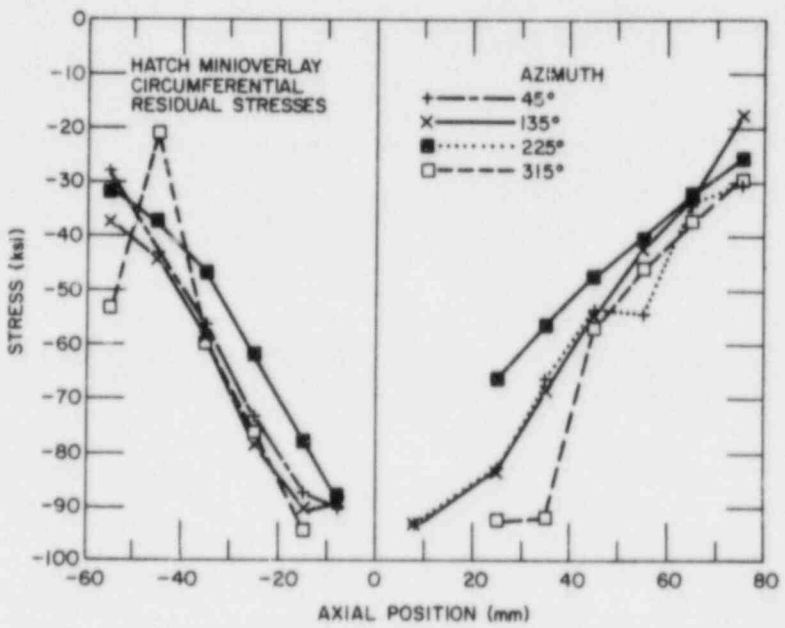

Fig. 1.20. Circumferential Residual Stresses on the Inner Surface at Four Azimuths of the Minioverlay Mock-Up Weldment.

In Figs. 1.21-1.29, the throughwall residual stresses are plotted in terms of a nondimensional depth. For gauge positions 1-4, the depth is nondimensionalized with respect to the total thickness, i.e., wall plus overlay; at gauge position 6, there is no overlay, and the depths are nondimensionalized with respect to the wall thickness. As expected, the stresses are strongly compressive on the inner portion of the wall and tensile on the outer portion. For reasons that are not completely clear,

the data for the outer half of the wall on the side of the pipe with the short weld-prep geometry are unreliable. Readings from the gauges oscillated widely; it may be that the protective coating on the gauges on that side of the weld failed. Therefore, Figs. 1.26-1.29 show only the data for the inner half of the wall. Again, the trends are roughly similar to the finite-element results except that the stresses start out more compressive on the inner surface. The experimental results also show some curvature near the inner and outer surfaces that is not apparent in the finite-element results.

These results should not be interpreted to mean that the overlay will be effective for cracks roughly halfway through the wall and ineffective for deeper cracks. As indicated by the finite-element results reported in Ref. 15, the presence of a crack strongly perturbs the stresses produced by the overlay process. These results do confirm the analytical predictions of strongly compressive stress fields produced on the inner surface by the overlay, but other types of tests are needed to verify the predicted stress fields at crack tips.

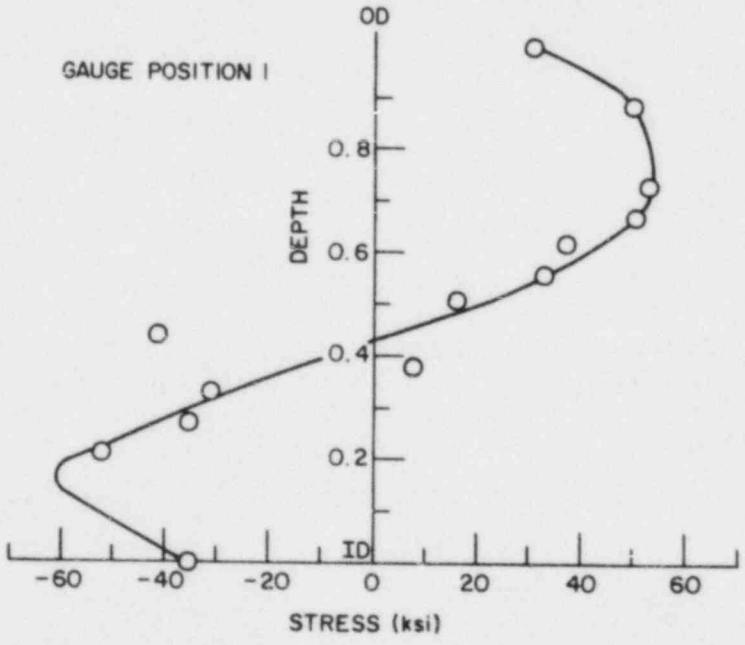

Fig. 1.21. Throughwall Axial Residual Stress at Gauge Position 1 on the Long Weld-Prep Geometry Side of the Minioverlay Mock-Up Weldment.

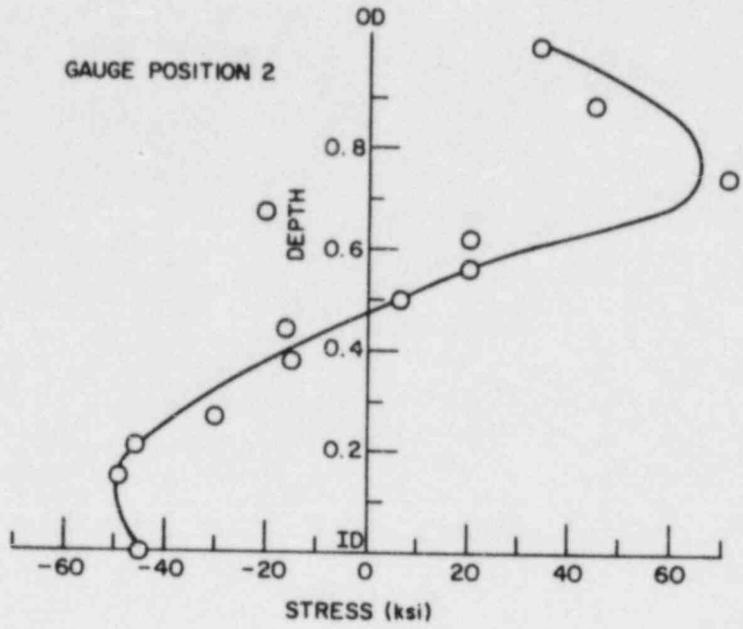

Fig. 1.22. Throughwall Axial Residual Stress at Gauge Position 2 on the Long Weld-Prep Geometry Side of the Minioverlay Mock-Up Weldment.

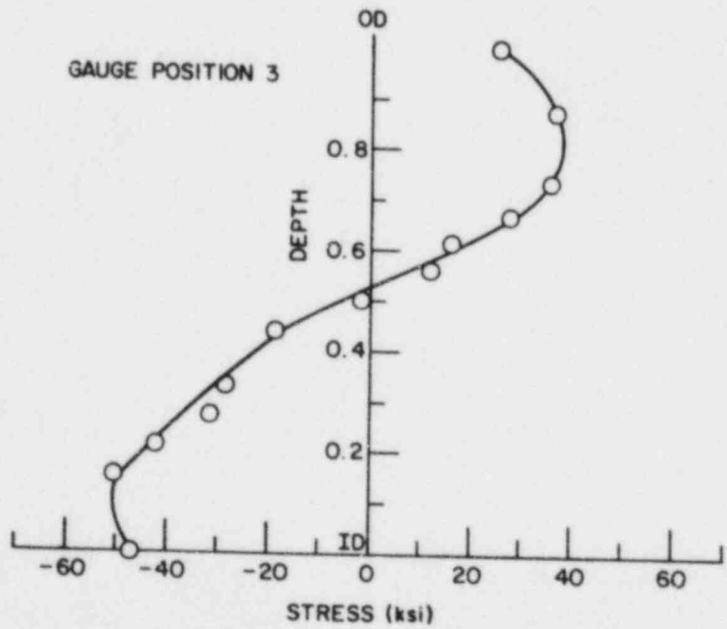

Fig. 1.23. Throughwall Axial Residual Stress at Gauge Position 3 on the Long Weld-Prep Geometry Side of the Minioverlay Mock-Up Weldment.

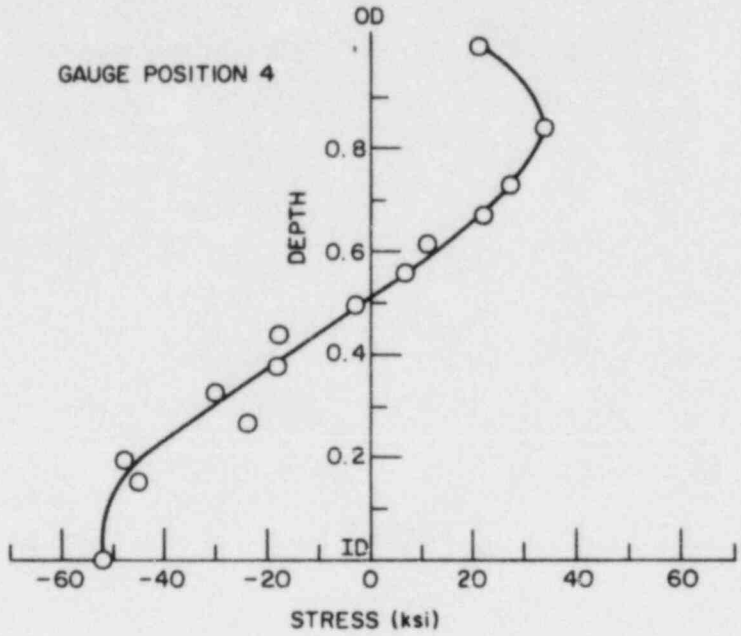

Fig. 1.24. Throughwall Axial Residual Stress at Gauge Position 4 on the Long Weld-Prep Geometry Side of the Minioverlay Mock-Up Weldment.

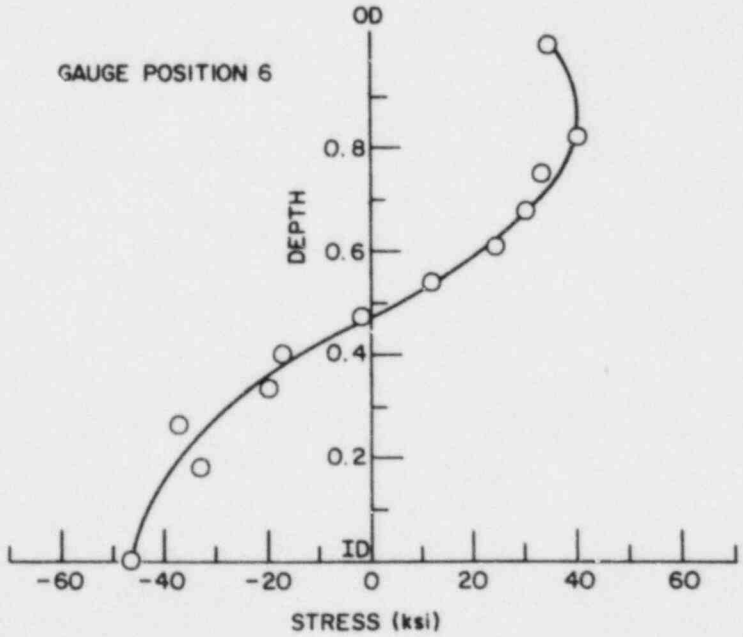

Fig. 1.25. Throughwall Axial Residual Stress at Gauge Position 6 on the Long Weld-Prep Geometry Side of the Minioverlay Mock-Up Weldment.

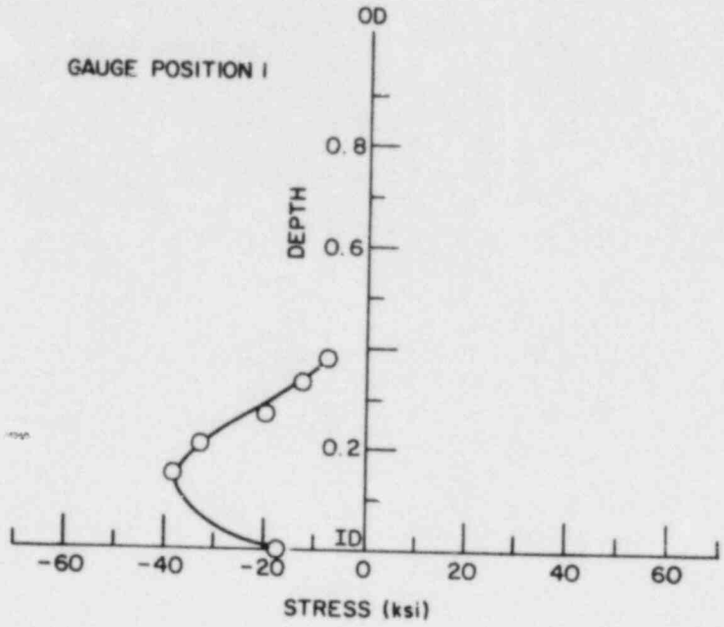

Fig. 1.26. Throughwall Axial Residual Stress at Gauge Position 1 on the Short Weld-Prep Geometry Side of the Minioverlay Mock-Up Weldment.

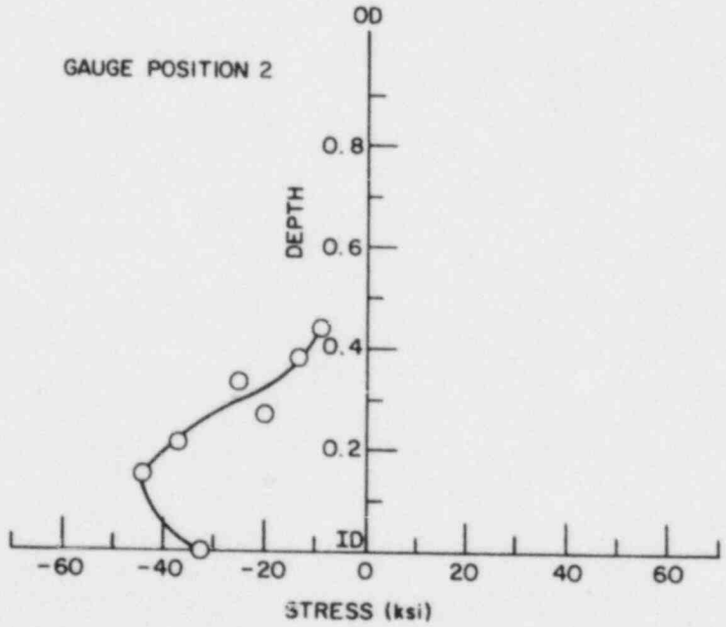

Fig. 1.27. Throughwall Axial Residual Stress at Gauge Position 2 on the Short Weld-Prep Geometry Side of the Minioverlay Mock-Up Weldment.

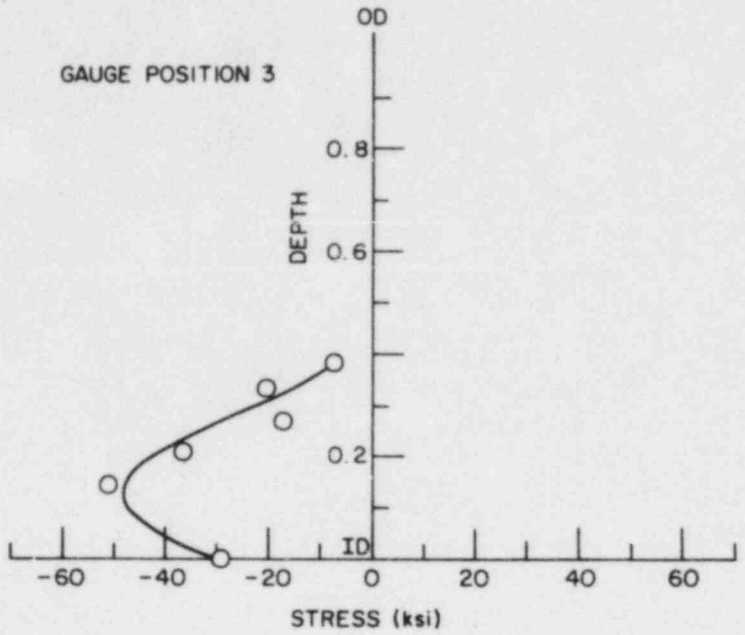

Fig. 1.28. Throughwall Axial Residual Stress at Gauge Position 3 on the Short Weld-Prep Geometry Side of the Minioverlay Mock-Up Weldment.

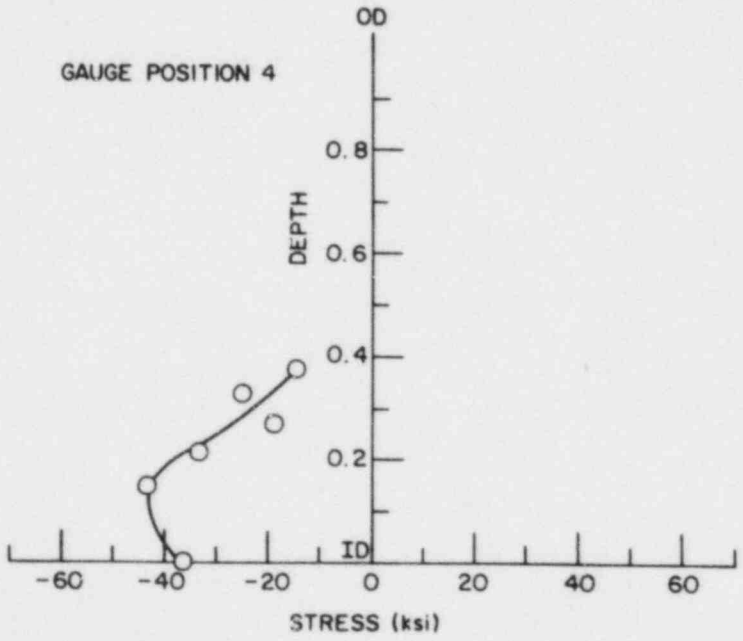

Fig. 1.29. Throughwall Axial Residual Stress at Gauge Position 4 on the Short Weld-Prep Geometry Side of the Minioverlay Mock-Up Weldment.

E. Evaluation of Environmental Corrective Actions (W. E. Ruther, W. K. Soppet, and T. F. Kassner)

1. Introduction

The potential effectiveness of proposed actions to solve or mitigate the problem of IGSCC in BWR piping and safe ends through modifications of the water chemistry is being evaluated. Although the reactor coolant environment has a profound influence on the performance and reliability of nuclear power-plant components, the synergistic effects of oxygen (produced by radiolytic decomposition of the water) and impurities (e.g., H_2SO_4 from decomposition of ion exchange resins during periodic intrusions into the primary system) on the IGSCC susceptibility and crack growth properties of sensitized Type 304 SS have not been investigated adequately. Also, it is not clear whether the potential benefits associated with small additions of hydrogen to the coolant can be realized in the presence of impurities within the normal operating limits of pH (5.6 to 8.6 at 25°C) and specific conductance ($\leq$1 μS/cm at 25°C) of the reactor coolant water.

During this reporting period, additional results have been obtained from constant-extension-rate-tensile (CERT) tests on a reference heat of Type 304 SS. The influence of the degree of sensitization of the material on the SCC susceptibility has been evaluated over a wider range in 289°C water containing 0.2 and 1.0 ppm dissolved oxygen without and with 0.1 ppm sulfate as H_2SO_4. This information supplements results reported previously[16-18] pertaining to the influence of water quality on the SCC behavior of this heat of material in the lightly (EPR = 2 C/cm^2) and moderately (EPR = 20 C/cm^2) sensitized conditions. Information on the rate of intergranular and transgranular crack propagation obtained from the CERT specimens was correlated with the open-circuit corrosion potential of Type 304 SS, which was determined in each experiment, as well as the dissolved oxygen concentration of the feedwater for several conductivity values in the range of $\lesssim$0.2 to 70 μS/cm. The influence of water chemistry transients that involve the dissolved oxygen and sulfate concentration of the feedwater on the crack growth behavior of the steel under low-frequency, moderate-stress-intensity, and high-load-ratio (R) loading also is being evaluated at 289°C.

2. Influence of the Degree of Sensitization on the SCC Susceptibility of Type 304 SS in Simulated BWR-Quality Water

The influence of dissolved oxygen, hydrogen, and sulfate (as H_2SO_4) on the SCC susceptibility of Type 304 SS sensitized to EPR values of 2 and 20 C/cm^2 has been investigated in considerable detail at 289°C and a strain rate of 1 x 10^{-6} s^{-1}. Depending on the dissolved oxygen and sulfate concentration of the feedwater, the SCC susceptibility in terms of the time to failure and fracture morphology of the specimens differed considerably. To obtain better perspective on the role of the environment and the degree of sensitization on the SCC behavior of the steel, a series of CERT experiments was performed in 289°C water containing 0.2 and 1.0 ppm dissolved oxygen without and with 0.1 ppm sulfate as H_2SO_4. The specimens were solution annealed for 0.5 h at 1050°C and water quenched (EPR = 0 C/cm^2) and then heat treated for 0.25, 0.67, 2, 12, and 24 h at 700°C to produce EPR values of 3, 8, 14, 20, and 30 C/cm^2, respectively. Specimens that received an LTS heat treatment at 500°C for 24 h after an initial treatment at 700°C for 0.25 h had an EPR value of 2 C/cm^2 based on numerous measurements. The relationship between the degree of sensitization in terms of the reactivation charge (EPR value) determined by the EPR technique[19,20] and the heat treatment time at 700°C is shown in Fig. 1.30 for heat number 30956.

Results of CERT experiments on specimens with different heat treatments corresponding to EPR values between 0 and 30 C/cm^2 are given in Table 1.9 and are plotted in Figs. 1.31 and 1.32 for dissolved oxygen concentrations in the feedwater of 0.2 and 1.0 ppm, respectively. The curves in Fig. 1.31 indicate the highest degree of IGSCC susceptibility at a sensitization of ~8 C/cm^2 and a decrease in susceptibility for higher levels of sensitization in both the high-purity water and water with 0.1 ppm sulfate at a dissolved oxygen concentration of 0.2 ppm. In the impurity environment, the specimen with the LTS heat treatment exhibited maximum IGSCC susceptibility, whereas the fracture mode was transgranular in high-purity water. For a dissolved oxygen concentration of 1 ppm, the curves in Fig. 1.32 indicate that the degree of sensitization has a relatively small effect on the degree of IGSCC susceptibility over the range of EPR values between ~2 and 30 C/cm^2. The premise that higher levels of sensitization are indicative of greater

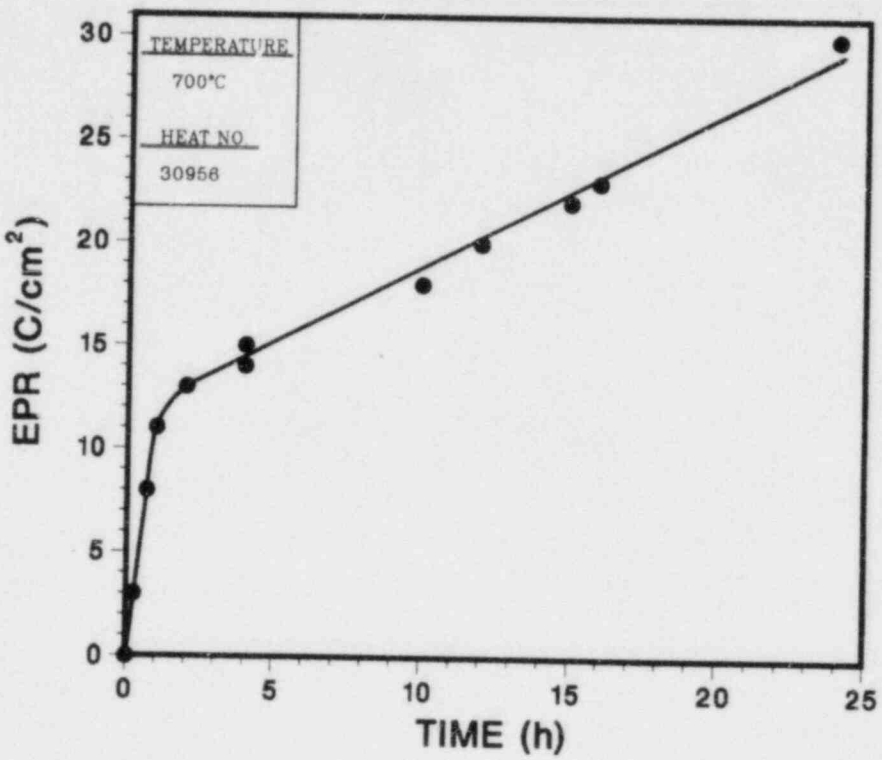

Fig. 1.30. Degree of Sensitization of Type 304 SS from Reactivation Charge Measurements by the Electrochemical Potentiokinetic Reactivation (EPR) Technique as a Function of Heat Treatment Time at 700°C.

TABLE 1.9. Influence of the Degree of Sensitization (EPR Value) on the SCC Susceptibility of Type 304 SS Specimens[a] (Heat No. 30956) in 289°C Water Containing 0.2 and 1.0 ppm Dissolved Oxygen with and without 0.1 ppm Sulfate (as H_2SO_4)

Test No.[b]	EPR, C/cm^2	Feedwater Chemistry				Failure Time, h	Maximum Stress, MPa	Total Elong., %	Reduction in Area, %	Fracture Morphology[c]
		Oxygen, ppm	Sulfate, ppm	Cond., µS/cm	pH at 25°C					
73	30	0.96	0	0.12	6.24	85	468	31	33	0.55D, 0.45G_3
70	20	0.92	0	0.07	6.41	84	447	30	34	0.71D, 0.29I
86	8	0.95	0	0.16	6.20	78	396	28	47	0.33D, 0.67I
77	3	0.87	0	0.11	6.25	91	463	33	49	0.46D, 0.54G_3
71	2[d]	0.87	0	0.13	6.29	69	393	25	27	0.40D, 0.60G_3
90	2[d]	0.99	0	0.11	6.14	71	400	26	42	0.42D, 0.58G_3
72	0	0.91	0	0.10	6.24	144	518	52	53	0.58D, 0.42T
80	30	0.99	0.1	0.89	5.77	60	354	21	27	0.21D, 0.79I
81	20	1.07	0.1	0.90	5.73	50	319	18	20	0.30D, 0.70I
82	8	1.04	0.1	0.89	5.76	39	266	14	16	0.23D, 0.77I
78	3	0.94	0.1	0.88	5.71	62	371	22	25	0.35D, 0.65G_3
79	2[d]	0.98	0.1	0.88	5.72	50	325	18	29	0.18D, 0.82G_3
89	0	1.07	0.1	0.89	5.71	133	521	48	56	0.79D, 0.21T
75	30	0.18[e]	0	0.10	6.26	143	516	51	62	0.81D, 0.19T
8	20	0.20	0	0.20	6.80	119	512	42	45	0.32D, 0.68G_1
87	8	0.23	0	0.09	6.20	100	411	36	46	0.42D, 0.58G_3
76	3	0.19	0	0.14	6.35	158	525	57	76	1.00D
2	2[d]	0.25	0	0.20	6.80	143	492	50	52	0.69D, 0.31T
83	30	0.23	0.1	0.90	5.73	65	389	23	31	0.46D, 0.54I
13	20	0.22	0.1	0.90	5.80	78	439	27	37	0.38D, 0.43T, 0.19I
85	8	0.26	0.1	0.90	5.75	49	325	18	21	0.31D, 0.69I
84	3	0.26	0.1	0.90	5.73	68	419	25	26	0.38D, 0.62G_3
17	2[d]	0.18	0.1	0.90	5.80	49	315	18	10	0.08D, 0.06G_3, 0.86I
88	0	0.26	0.1	0.89	5.78	152	517	55	67	1.00D

[a]Specimens were exposed to the environment for ~20 h at 289°C before straining at a rate of 1 x 10^{-6} s^{-1}.

[b]Specimens were solution annealed for 0.5 h at 1050°C and water quenched (EPR = 0 C/cm^2) and then heat treated at 700°C for 0.25, 0.67, 2, 12, and 24 h to produce EPR values of 3, 8, 14, 20, and 30 C/cm^2, respectively.

[c]Ductile (D), transgranular (T), granulated (G), intergranular (I), in terms of the fraction of the reduced cross-sectional area. Characterization of the fracture surface morphologies is in accordance with the illustrations and definitions provided in Alternate Alloys for BWR Pipe Applications: Sixth Semiannual Progress Report, April-September 1980, General Electric Company Report NEDC-23750-8, pp. 5-70 to 5-81.

[d]Specimens received a low-temperature-sensitization (LTS) heat treatment at 500°C for 24 h after an initial treatment at 700°C for 0.25 h.

[e]Feedwater contained 2.0 ppm dissolved hydrogen.

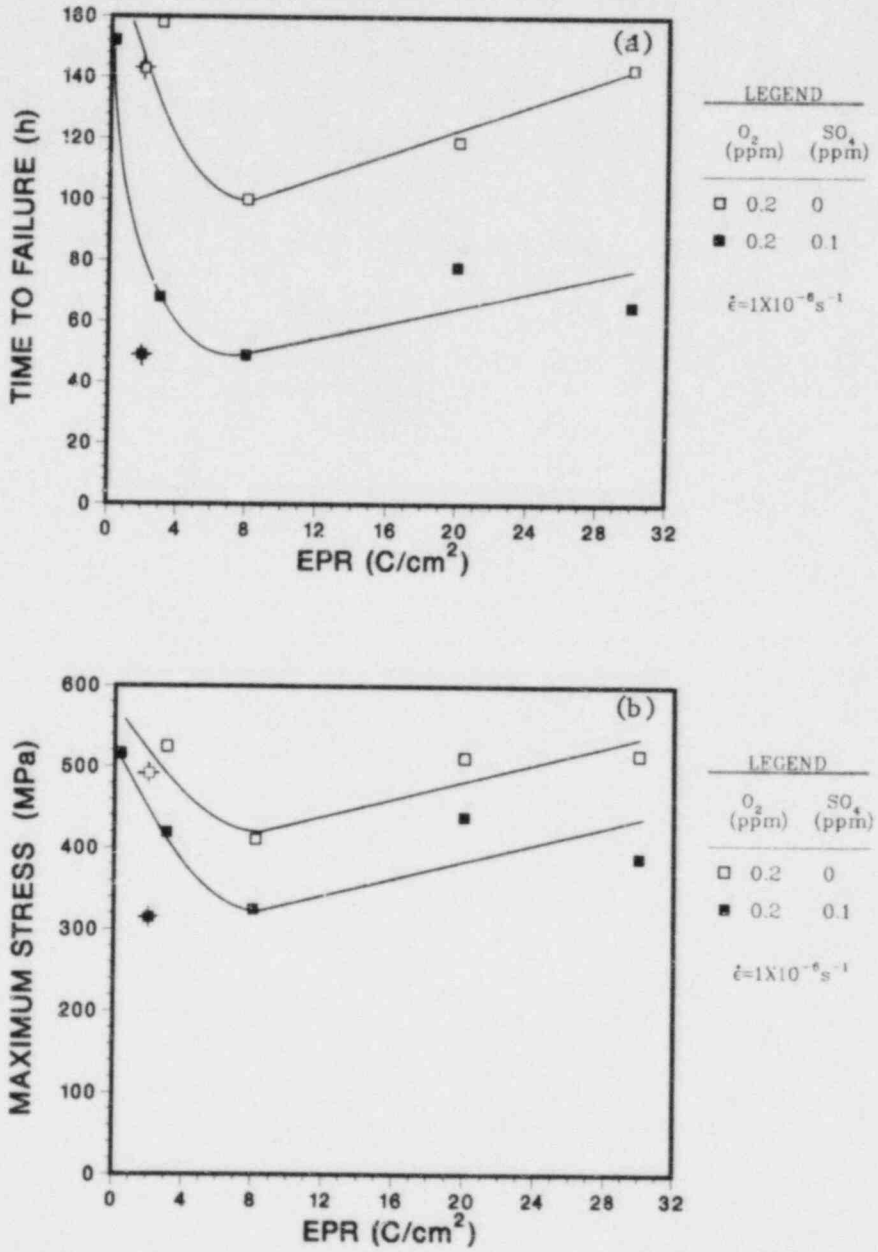

Fig. 1.31. Influence of Degree of Sensitization in Terms of the Reactivation Charge (EPR) Value on the Time to Failure (a) and Maximum Stress (b) of Type 304 SS from CERT Experiments at a Strain Rate of 1×10^{-6} s^{-1} in 289°C Water Containing 0.2 ppm Dissolved Oxygen and 0 and 0.1 ppm Sulfate as H_2SO_4. The accented symbols denote specimens with a low-temperature sensitization heat treatment.

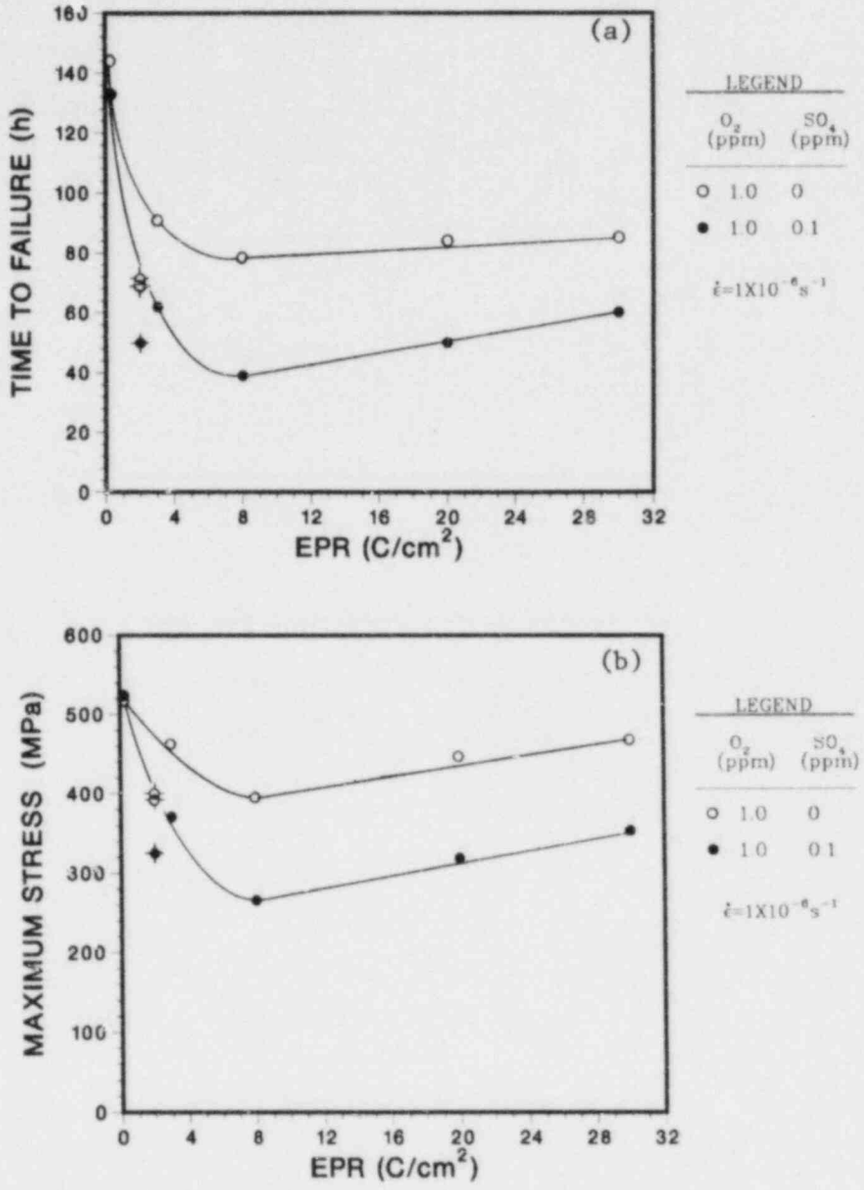

Fig. 1.32. Influence of Degree of Sensitization in Terms of the Reactivation Charge (EPR) Value on the Time to Failure (a) and Maximum Stress (b) of Type 304 SS from CERT Experiments at a Strain Rate of 1×10^{-6} s^{-1} in 289°C Water Containing 1.0 ppm Dissolved Oxygen and 0 and 0.1 ppm Sulfate as H_2SO_4. The accented symbols denote specimens with a low-temperature sensitization heat treatment.

susceptibility to IGSCC is not valid based on these results. The deleterious effect of 0.1 ppm sulfate on IGSCC of sensitized Type 304 SS is evident in both figures, however. The solution-annealed material (EPR = 0 C/cm^2) failed in an entirely ductile manner in high-purity water with 0.2 ppm oxygen and exhibited a ductile plus transgranular failure mode in the other environments.

3. Correlation of Crack Growth Data from CERT Experiments on Sensitized Type 304 SS at 289°C with Dissolved Oxygen Concentration and Conductivity of the Feedwater

The rate of intergranular or transgranular crack growth of the sensitized Type 304 SS has been evaluated from CERT experiments in 289°C water with different concentrations of dissolved oxygen, hydrogen, and sulfate as H_2SO_4. The maximum depth of stress corrosion crack propagation on the fracture surface of each of the CERT specimens was determined from enlarged photomicrographs of known magnification. This information was used with time increments from the onset of yield to the time of maximum load on the load versus time curve to obtain a crack growth rate. A schematic of a typical load-time curve and a fracture surface that illustrates the clear demarkation between the intergranular (dark) and the ductile (light) failure regions on the surface is shown in Fig. 1.33. The crack growth rate in these experiments was obtained by dividing the maximum radial depth of SCC penetration from the outer surface of the specimen by the time interval denoted by t_c in the figure. The strain or time at which stress corrosion cracks initiate in a CERT test depends on the environment (i.e., the sulfate and dissolved oxygen concentrations) as well as on the temperature.[21] At 288°C, the strain to initiation was between ~5.5 and 2.5% for sensitized Type 304 SS specimens[21] in water with 0.2 ppm dissolved oxygen and conductivities between 0.1 and 55 μS/cm at a strain rate of $\sim 3 \times 10^{-7}$ s^{-1}. Also, it is probable that the onset of ductile failure in the central region of the specimen in our experiments occurs at a time prior to the point of maximum load based on the decrease in the amplitude and the eventual disappearance of the serrations on the load-time curve as the point of maximum load is approached. Thus, the actual stress corrosion crack growth rates may be somewhat higher than the values reported in Tables 1.10 to 1.13 with information on the degree of sensitization of the material, feedwater chemistry, fracture mode, and the electrochemical potentials of Type 304 SS and platinum electrodes at 289°C.

TABLE 1.10. Crack Growth Rates Obtained from CERT Experiments on Sensitized Type 304 SS Specimens[a] (Heat No. 30956) in 289°C Water ($\lesssim$0.2 μS/cm) with Different Dissolved Oxygen and Hydrogen Concentrations

Run No.	EPR,[b] C/cm^2	Feedwater Chemistry: Oxygen, ppm	Hydrogen, ppm	Sulfate, ppm	pH at 25°C	Cond., μS/cm	Potentials: Type 304 SS, mV(SHE)	Pt, mV(SHE)	SCC Growth Rate,[c] mm·h^{-1}	m·s^{-1}	Fracture Morphology[d]
1	2	7.3	0	0	6.80	0.30	155	-	2.6×10^{-2}	7.2×10^{-9}	I
90		0.99	0	0	6.14	0.11	137	192	3.3×10^{-2}	9.2×10^{-9}	G_3
71		0.87	0	0	6.29	0.08	143	242	4.4×10^{-2}	1.2×10^{-8}	G_3
2		0.25	0	0	6.80	0.20	-268	-	7.9×10^{-3}	2.2×10^{-9}	T
41		0.20	0.5	0.01	6.10	0.20	-120	-455	2.3×10^{-2}	6.4×10^{-9}	I
18		0.19	0	0.01	6.20	0.20	8	8	2.4×10^{-2}	6.7×10^{-9}	G_3
31		0.13	0.5	0	6.40	0.20	-145	-415	1.1×10^{-2}	3.1×10^{-9}	I
45		0.06	0.5	0	6.10	0.10	-502	-514	7.4×10^{-3}	2.1×10^{-9}	T
4		0.05	0	0	6.80	0.10	-550	-558	9.2×10^{-3}	2.5×10^{-9}	T
43		0.03	0.5	0.01	6.10	0.20	-320	-390	8.3×10^{-3}	2.3×10^{-9}	T
33		0.03	0.3	0	6.60	0.10	-320	-350	9.8×10^{-3}	2.7×10^{-9}	T
77	3	0.87	0	0	6.25	0.11	112	213	2.3×10^{-2}	6.4×10^{-9}	G_3
76	3	0.19	0	0	6.35	0.14	25	94	0	0	D
86	8	0.95	0	0	6.20	0.16	135	225	3.5×10^{-2}	9.7×10^{-9}	I
87	8	0.23	0	0	6.20	0.09	88	94	3.2×10^{-2}	8.9×10^{-9}	G_3
9	20	8.0	0	0	6.10	0.20	171	243	6.0×10^{-2}	1.7×10^{-8}	I
70		0.92	0	0	6.41	0.07	133	229	2.5×10^{-2}	7.0×10^{-9}	I
8		0.20	0	0	6.80	0.20	-	-	1.8×10^{-2}	5.0×10^{-9}	G_1
32		0.18	0.4	0	6.60	0.20	-75	-375	-	-	I
74		0.08	2.0	0	6.30	0.10	-411	-431	1.0×10^{-2}	2.8×10^{-9}	T
46		0.07	0.5	0	6.30	0.10	-510	-520	7.3×10^{-3}	2.0×10^{-9}	T
24		0.03	0	0	6.30	0.10	-470	-362	1.1×10^{-2}	3.1×10^{-9}	T
34		0.03	0.1	0	6.50	0.10	-510	-520	1.0×10^{-2}	2.8×10^{-9}	T
44		0.02	0.5	0.01	6.10	0.20	-460	-475	9.5×10^{-3}	2.6×10^{-9}	T
73	30	0.96	0	0	6.24	0.12	134	239	2.7×10^{-2}	7.5×10^{-9}	G_3
75	30	0.15	2.0	0	6.26	0.10	-13	-114	1.5×10^{-2}	4.2×10^{-9}	T

[a]Specimens were exposed to the environment for 720 h at 289°C before straining at a rate of 1×10^{-6} s^{-1}.

[b]Heat treatment conditions that correspond to the degree of sensitization determined by the electrochemical potentiokinetic reactivation (EPR) technique (reactivation change values, C/cm^2) are as follows: 700°C/0.25 h plus 500°C/24 h, EPR = 2 C/cm^2; 700°C/0.25 h, EPR = 3 C/cm^2; 700°C/0.67 h, EPR = 8 C/cm^2; 700°C/12 h, EPR = 20 C/cm^2; and 700°C/24 h, EPR = 30 C/cm^2.

[c]SCC growth rates are based on measurement of depth of the longest crack in an enlarged micrograph of the fracture surface and the time period from the onset of yield to the point of maximum load on the tensile curve.

[d]Ductile (D), transgranular (T), granulated (G), and intergranular (I) characterization of the fracture surface morphologies in accordance with the illustrations and definitions provided in Alternate Alloys for BWR Applications: Sixth Semiannual Progress Report, April-September 1980, General Electric Company Report NEDC-23750-8, pp. 5-70 to 5-81.

TABLE 1.11. Crack Growth Rates Obtained from CERT Experiments on Sensitized Type 304 SS Specimens[a] (Heat No. 30956) in 289°C Water (~0.9 μS/cm) with 0.1 ppm Sulfate as H_2SO_4 and Different Dissolved Oxygen and Hydrogen Concentrations

Run No.	EPR,[b] C/cm^2	Feedwater Chemistry					Potentials		SCC Growth Rate,[c]		Fracture Morphology[d]
		Oxygen, ppm	Hydrogen, ppm	Sulfate, ppm	pH at 25°C	Cond., μS/cm	Type 304 SS, mV(SHE)	Pt, mV(SHE)	mm·h^{-1}	m·s^{-1}	
22	2	7.0	0	0.1	5.80	0.90	185	290	1.4×10^{-1}	3.9×10^{-8}	I
79		0.98	0		5.72	0.88	145	241	6.4×10^{-2}	1.8×10^{-8}	G_3
16		0.18	0		5.80	0.90	15	-85	1.2×10^{-2}	3.3×10^{-9}	I
17		0.18	0		5.80	0.90	19	-10	8.3×10^{-2}	2.3×10^{-8}	I
35		0.18	0.6		5.80	0.80	-480	-470	3.7×10^{-2}	1.1×10^{-8}	I
25		0.08	0		5.80	0.80	-472	-372	-	-	G_3
47		0.07	0.5		5.80	0.90	-485	-500	1.3×10^{-2}	3.6×10^{-9}	T
37		0.05	0.5		5.80	0.80	-490	-520	1.5×10^{-2}	4.2×10^{-9}	T
20		0.03	0		5.80	0.80	-265	-395	7.8×10^{-3}	2.2×10^{-9}	T
59		0.03	0.5		5.80	0.80	-535	-525	1.2×10^{-2}	3.3×10^{-9}	T
68		<0.005[e]	2.0		8.40	1.10	-573	-575	5.9×10^{-3}	1.6×10^{-9}	T
78	3	0.94	0	0.1	5.71	0.88	148	248	3.8×10^{-2}	1.1×10^{-8}	G_3
84	3	0.26	0	0.1	5.73	0.90	97	190	2.6×10^{-2}	7.2×10^{-9}	G_3
82	8	1.04	0	0.1	5.76	0.89	151	245	9.3×10^{-2}	2.6×10^{-8}	I
85	8	0.26	0	0.1	5.75	0.90	95	196	7.3×10^{-2}	2.0×10^{-8}	I
23	20	7.0	0	0.1	5.80	0.90	175	274	7.6×10^{-2}	2.1×10^{-8}	I
81		1.07	0		5.73	0.90	150	243	5.4×10^{-2}	1.5×10^{-8}	I
13		0.22	0		5.80	0.90	-66	-239	2.8×10^{-2}	7.8×10^{-9}	I
14		0.20	0		5.30	0.80	20	2	2.3×10^{-2}	6.4×10^{-9}	I
36		0.20	0.5		5.80	0.90	-130	-368	2.3×10^{-2}	6.4×10^{-9}	I
26		0.08	0		5.80	0.80	-132	-312	2.8×10^{-2}	7.8×10^{-9}	I
38		0.05	0.5		5.80	0.80	-520	-	1.2×10^{-2}	3.3×10^{-9}	T
15		0.03	0		5.80	0.90	-250	-410	1.5×10^{-2}	4.2×10^{-9}	G_1
69		<0.005[e]	2.0		8.50	1.0	-586	-582	5.7×10^{-3}	1.6×10^{-9}	T
80	30	0.99	0	0.1	5.77	0.89	139	229	5.8×10^{-2}	1.6×10^{-8}	I
83	30	0.23	0	0.1	5.73	0.90	83	82	4.6×10^{-2}	1.3×10^{-8}	I

[a]Specimens were exposed to the environment for ~20 h at 289°C before straining at a rate of 1×10^{-6} s^{-1}.

[b]Heat treatment conditions that correspond to the degree of sensitization determined by the electrochemical potentiokinetic reactivation (EPR) technique (reactivation change values, C/cm^2) are as follows: 700°C/0.25 h plus 500°C/24 h, EPR = 2 C/cm^2; 700°C/0.25 h, EPR = 3 C/cm^2; 700°C/0.67 h, EPR = 8 C/cm^2; 700°C/12 h, EPR = 20 C/cm^2; and 700°C/24 h, EPR = 30 C/cm^2.

[c]SCC growth rates are based on measurement of depth of the longest crack in an enlarged micrograph of the fracture surface and the time period from the onset of yield to the point of maximum load on the tensile curve.

[d]Transgranular (T), granulated (G), and intergranular (I) characterization of the fracture surface morphologies in accordance with the illustrations and definitions provided in Alternate Alloys for BWR Applications: Sixth Semiannual Progress Report, April-September 1980, General Electric Company Report NEDC-23750-8, pp. 5-70 to 5-81.

[e]Hydrazine added to the feedwater to reduce the dissolved oxygen concentration to <0.005 ppm.

TABLE 1.12. Crack Growth Rates Obtained from CERT Experiments on Sensitized Type 304 SS Specimens[a] (Heat No. 30956) in 289°C Water (~8 μS/cm) with 1.0 ppm Sulfate as H_2SO_4 and Different Dissolved Oxygen and Hydrogen Concentrations

Run No.	EPR,[b] C/cm^2	Feedwater Chemistry: Oxygen, ppm	Hydrogen, ppm	Sulfate, ppm	pH at 25°C	Cond., μS/cm	Potentials: Type 304 SS, mV(SHE)	Pt, mV(SHE)	SCC Growth Rate,[c] $mm \cdot h^{-1}$	$m \cdot s^{-1}$	Fracture Morphology[d]
28	2	8.6	0	1.0	4.80	9.0	180	250	9.4×10^{-2}	2.6×10^{-8}	I
19		0.20	0		4.80	9.0	-75	-75	1.2×10^{-1}	3.3×10^{-8}	I
39		0.20	0.5		4.80	8.0	-	-360	9.6×10^{-2}	2.7×10^{-8}	I
10		0.03	0		4.70	8.0	-205	-450	1.5×10^{-2}	4.2×10^{-9}	G_3
49		0.03	0.5		4.80	8.0	-450	-470	1.8×10^{-2}	5.0×10^{-9}	G_2
60		0.01	2.0		4.80	8.3	-496	-515	1.4×10^{-2}	3.9×10^{-9}	G_2
67		<0.005[e]	2.0		8.9	4.4	-572	-606	8.0×10^{-3}	2.2×10^{-9}	T
27	20	7.0	0	1.0	4.80	9.0	-	-	4.6×10^{-2}	1.3×10^{-9}	I
21		0.21	0		4.80	9.0	100	198	5.0×10^{-2}	1.4×10^{-9}	I
40		0.20	0.5		4.80	8.0	-50	-340	5.7×10^{-2}	1.6×10^{-9}	I
11		0.05	0		4.70	8.0	-	-420	1.0×10^{-2}	2.8×10^{-9}	G_3
50		0.03	0.5		4.80	8.0	-450	-475	1.2×10^{-2}	3.3×10^{-9}	G_2
61		0.02	2.0		4.80	8.3	-516	-518	1.1×10^{-2}	3.1×10^{-9}	G_2
66		<0.005[e]	2.0		8.9	4.4	-584	-624	1.5×10^{-2}	4.2×10^{-9}	T

[a]Specimens were exposed to the environment for ~20 h at 289°C before straining at a rate of 1×10^{-6} s^{-1}.

[b]Heat treatment conditions that correspond to the degree of sensitization determined by the electrochemical potentiokinetic reactivation (EPR) technique (reactivation change values, C/cm^2) are as follows: 700°C/0.25 h plus 500°C/24 h, EPR = 2 C/cm^2; and 700°C/12 h, EPR = 20 C/cm^2.

[c]SCC growth rates are based on measurement of depth of the longest crack in an enlarged micrograph of the fracture surface and the time period from the onset of yield to the point of maximum load on the tensile curve.

[d]Transgranular (T), granulated (G), and intergranular (I) characterization of the fracture surface morphologies in accordance with the illustrations and definitions provided in Alternate Alloys for BWR Applications: Sixth Semiannual Progress Report, April-September 1980, General Electric Company Report NEDC-23750-8, pp. 5-70 to 5-81.

[e]Hydrazine added to the feedwater to reduce the dissolved oxygen concentration to <0.005 ppm.

TABLE 1.13. Crack Growth Rates Obtained from CERT Experiments on Sensitized Type 304 SS Specimens[a] (Heat No. 30956) in 289°C Water (~70μS/cm) with 10 ppm Sulfate as H_2SO_4 and Different Dissolved Oxygen and Hydrogen Concentrations

Run No.	EPR,[b] C/cm^2	Feedwater Chemistry: Oxygen, ppm	Hydrogen, ppm	Sulfate, ppm	pH at 25°C	Cond., μS/cm	Potentials: Type 304 SS, mV(SHE)	Pt, mV(SHE)	SCC Growth Rate,[c] mm·h^{-1}	m·s^{-1}	Fracture Morphology[d]
30	2	8.0	0	10.0	3.8	80.0	230	325	7.5×10^{-2}	2.1×10^{-8}	I
57		0.25	0.5			71.0	-375	-325	4.8×10^{-2}	1.3×10^{-8}	G_3
56		0.21	0			71.0	-70	-110	7.7×10^{-2}	2.1×10^{-8}	G_3
53		0.03	0			71.0	-405	-365	4.0×10^{-2}	1.1×10^{-8}	I
51		0.03	0.5			71.0	-	-	3.0×10^{-2}	8.4×10^{-9}	G_3
62		0.03	2.0			71.5	-419	-416	5.7×10^{-2}	1.6×10^{-8}	G_3
64		<0.005[e]	2.0		4.3	26.0	-512	-556	1.6×10^{-2}	4.5×10^{-9}	G_2
29	20	8.0	0	10.0	3.8	80.0	222	306	6.2×10^{-2}	1.7×10^{-8}	I
58		0.23	0.5			71.0	-387	-370	3.7×10^{-2}	1.0×10^{-8}	G_3
55		0.20	0			71.0	-360	-320	5.5×10^{-2}	1.5×10^{-8}	I
63		0.03	2.0			71.5	-424	-423	4.8×10^{-2}	1.3×10^{-8}	I
52		0.03	0.5			69.0	-410	-415	3.8×10^{-2}	1.1×10^{-8}	I
54		0.03	0			71.0	-410	-365	5.6×10^{-2}	1.6×10^{-8}	I
65		<0.005[e]	2.0		4.4	26.0	-468	-534	3.2×10^{-2}	8.9×10^{-9}	I

[a]Specimens were exposed to the environment for ~20 h at 289°C before straining at a rate of 1×10^{-6} s^{-1}.

[b]Heat treatment conditions that correspond to the degree of sensitization determined by the electrochemical potentiokinetic reactivation (EPR) technique (reactivation change values, C/cm^2) are as follows: 700°C/0.25 h plus 500°C/24 h, EPR = 2 C/cm^2; and 700°C/12 h, EPR = 20 C/cm^2.

[c]SCC growth rates are based on measurement of depth of the longest crack in an enlarged micrograph of the fracture surface and the time period from the onset of yield to the point of maximum load on the tensile curve.

[d]Granulated (G) and intergranular (I) characterization of the fracture surface morphologies in accordance with the illustrations and definitions provided in Alternate Alloys for BWR Applications: Sixth Semiannual Progress Report, April-September 1980, General Electric Company Report NEDC-23750-8, pp. 5-70 to 5-81.

[e]Hydrazine added to the feedwater to reduce the dissolved oxygen concentration to <0.005 ppm.

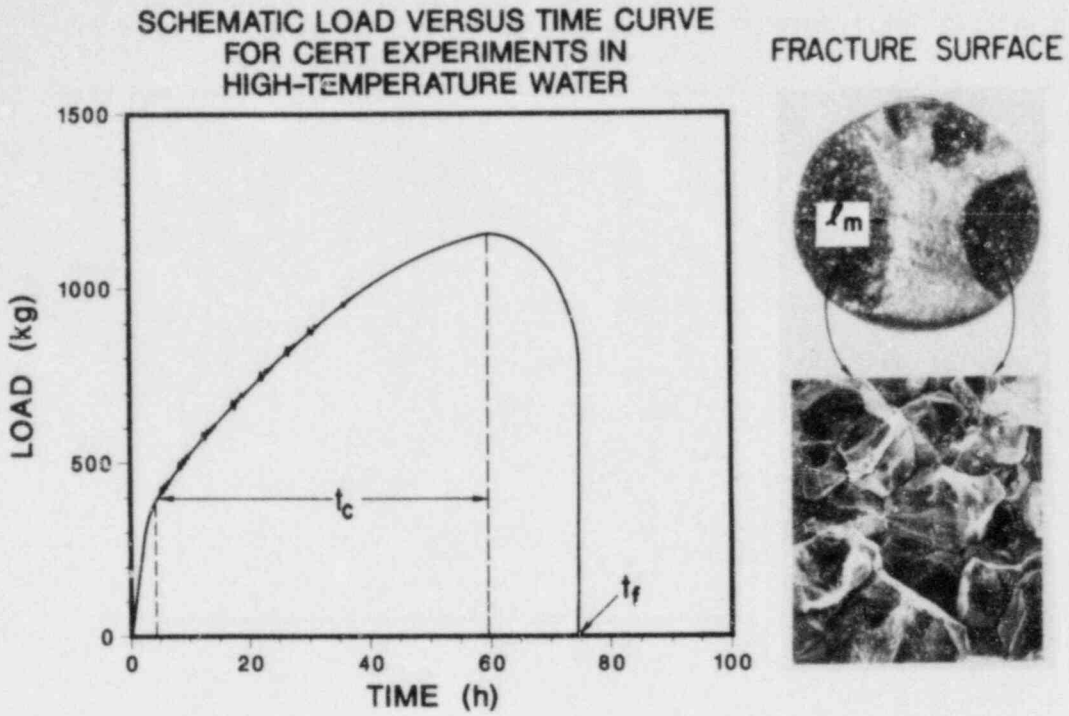

Fig. 1.33. Information from the Load versus Time Curve and the Fracture Surface of CERT Specimens to Determine the SCC Growth Rate.

The dependence of the crack growth rate on the dissolved oxygen concentration of the water is shown in Fig. 1.34 for conductivity values of $\lesssim$0.2, 0.9, 8, and 70 μS/cm. Conductivity values of $\lesssim$0.2 μS/cm in Table 1.10 correspond to high-purity water, and the higher values in Tables 1.11 to 1.13 were obtained by H_2SO_4 additions to the feedwater for sulfate concentrations of 0.1, 1, and 10 ppm, respectively. The crack growth rates exhibit a sigmoidal dependence on the dissolved oxygen concentration in the logarithmic plots for conductivity values of $\leq$8 μS/cm [Fig. 1.34(a)-(c)], in which the rates are relatively independent of oxygen concentration above ~0.2 ppm and below ~0.06 ppm, with an abrupt transition from the higher to lower values as the oxygen concentration decreases over the intermediate range. At conductivity values of $\leq$0.2 and ~0.9 μS/cm, the mode of crack growth was intergranular (closed symbols) at dissolved oxygen concentrations $\gtrsim$0.1 ppm and transgranular (open symbols) at lower oxygen concentrations, whereas at 8 μS/cm (1.0 ppm sulfate as H_2SO_4) intergranular crack growth occurred over the entire range of oxygen concentrations (i.e., ~0.01 to

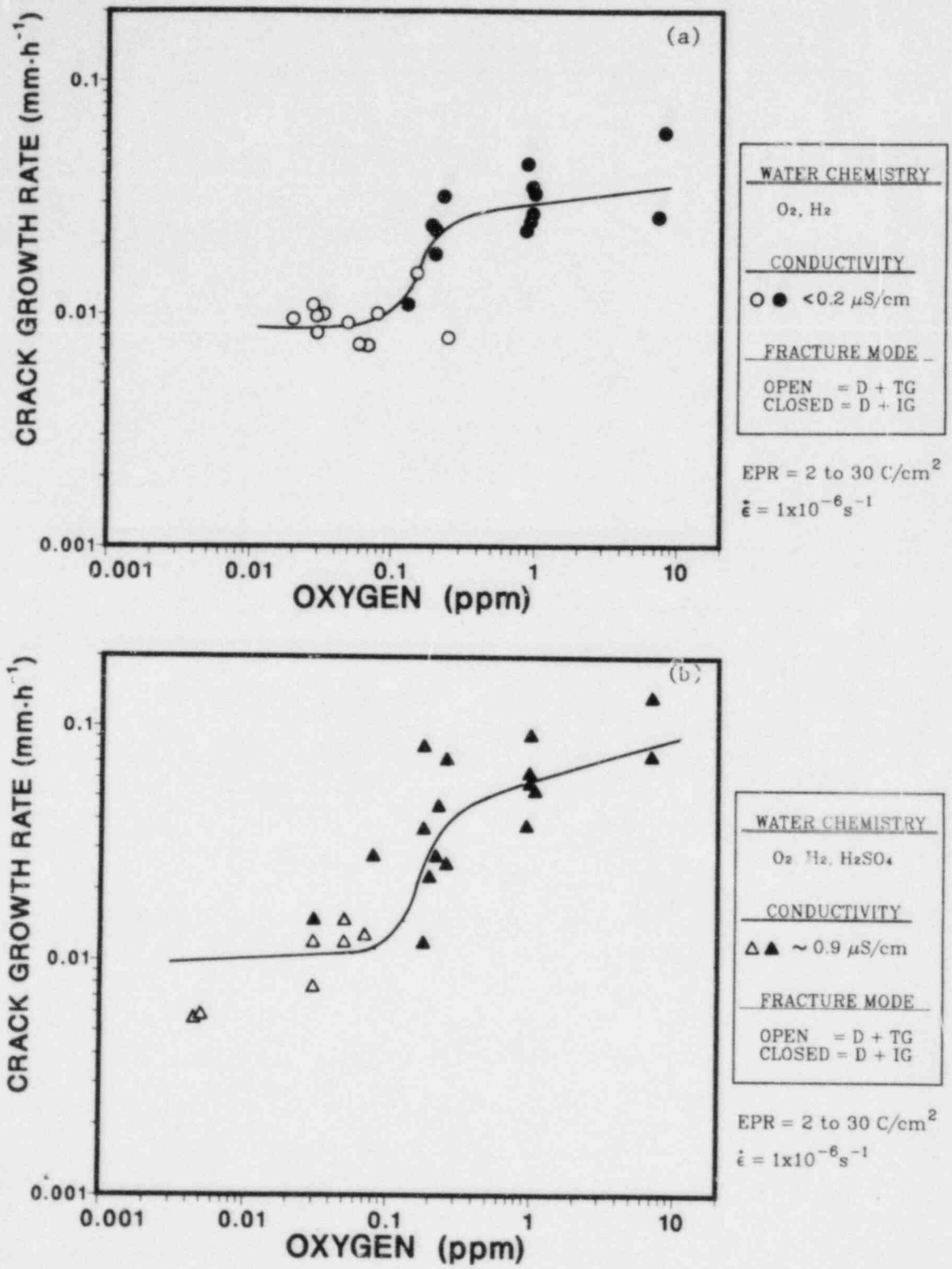

Fig. 1.34. Crack Growth Rate of Sensitized Type 304 SS (EPR = 2 to 30 C/cm^2) from CERT Experiments at 289°C as a Function of the Dissolved Oxygen Concentration in the Feedwater for Conductivity Values of (a) $\leq$0.2, (b) 0.9, (c) 8, and (d) ~70 μS/cm. Conductivity values above ~0.2 μS/cm were obtained by H_2SO_4 additions to the water for sulfate concentrations of 0.1, 1, and 10 ppm. Open and closed symbols denote a transgranular and intergranular fracture mode, respectively.

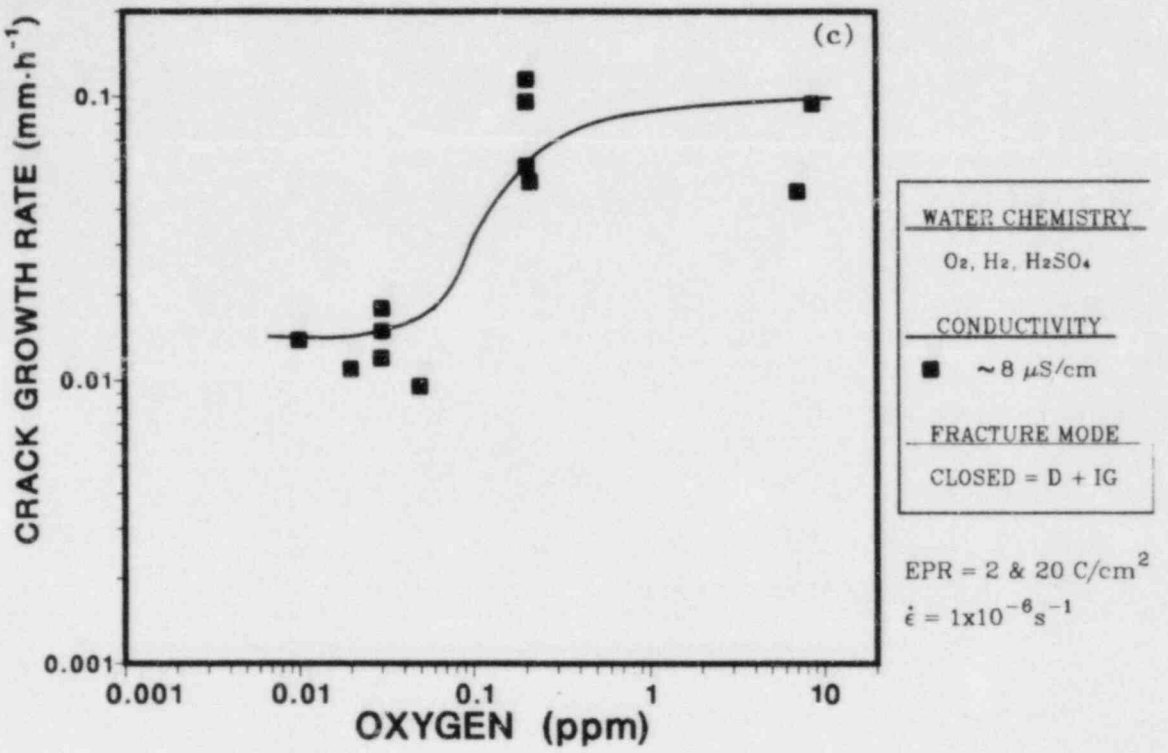

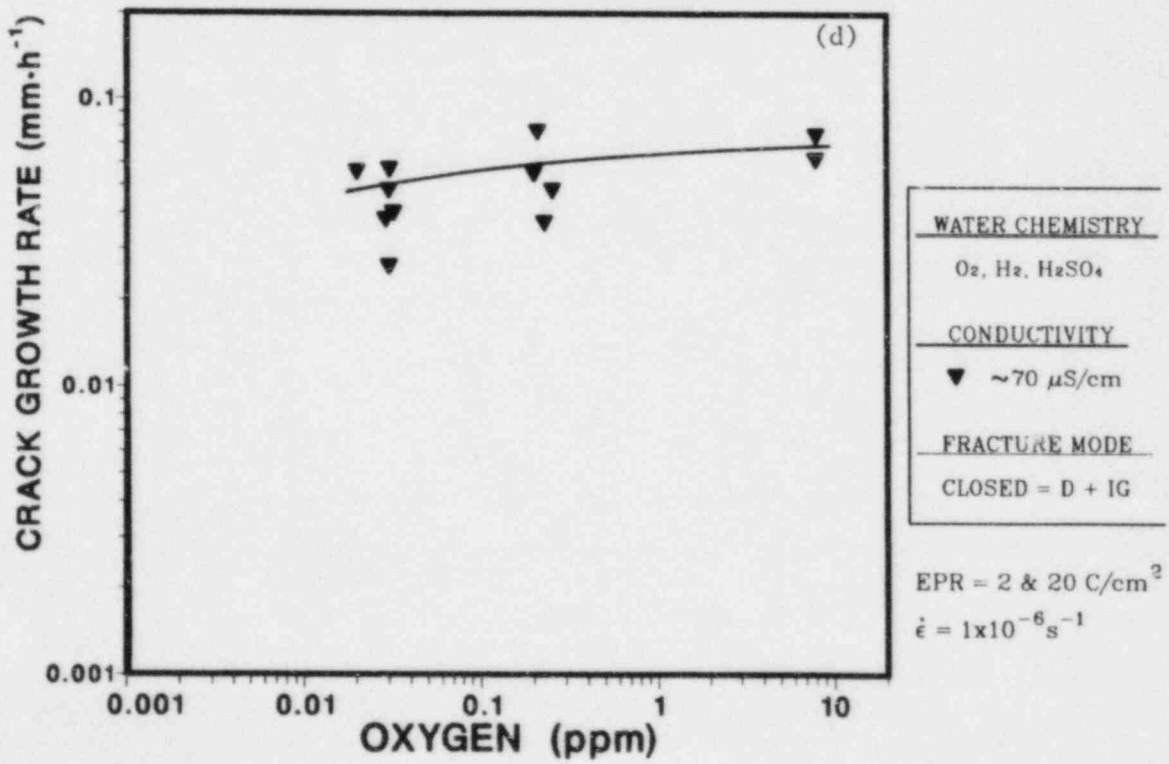

Fig. 1.34. (Contd.)

8 ppm). For a feedwater conductivity of ~70 μS/cm (10 ppm sulfate), the rate of intergranular crack growth was relatively independent of the oxygen concentration over this range.

The results in Fig. 1.34(a) and (b) indicate that SCC propagation rates in sensitized Type 304 SS (EPR = 2 to 30 C/cm^2) will decrease by factors of ~3 and 5 for conductivity values of $\lesssim$0.2 and 0.9 μS/cm, respectively, if the dissolved oxygen concentration of the water decreases from ~0.3 to 0.02 ppm. The higher oxygen level corresponds to normal BWR operation, and the lower value is indicative of continuous hydrogen addition to the feedwater of a BWR, which suppresses radiolysis of water in the reactor core.[22] Conductivity values between ~0.2 and 0.9 μS/cm encompass the range of recirculation loop water during normal BWR operation[23,24] with different types of reactor-water-cleanup systems (viz., deep-bed bead or precoat powdered resin), the maximum percent of feedwater flow through the cleanup system (~1 to 13%), the cation-to-anion volume ratio (deep bed), and water chemistry control procedures (i.e., actual vessel flow rates, operation of more than one loop, backwash regeneration frequency, or resin disposal rather than regeneration).

The actual improvement in the crack growth rate of sensitized Type 304 SS that can be realized by decreasing the oxygen and sulfate concentrations of the water to very low levels is likely to be much greater than the factor of 3 to 5 obtained from the CERT results. A crack growth experiment at 289°C on 1TCT specimens of the same heat of steel with similar levels of sensitization (EPR = 2 and 20 C/cm^2) indicated that for stress intensity values of ~28-30 MPa•m$^{1/2}$, the rate of intergranular crack propagation in the material ceased when the dissolved oxygen concentration of high-purity water decreased from 0.2 to 0.02 ppm (see Sec. E.6). Additional experiments on fracture-mechanics type specimens will further quantify the effect of water chemistry on SCC crack propagation in the steel.

4. Correlation of Crack Growth Data from CERT Experiments on Sensitized Type 304 SS with Open-Circuit Corrosion Potential of the Steel at 289°C and the Conductivity of the Feedwater

During the CERT experiments, the electrochemical potentials of Type 304 SS and a platinum electrode were monitored as a function of time.

The potential measurements were made at 289°C relative to an external 0.1M KCl/AgCl/Ag reference electrode[25] and the values were converted to the standard hydrogen electrode at 289°C.[26] Typical potential-versus-time curves are shown in Fig. 1.35 for different environments. Since a large change in the potentials was observed in low-oxygen environments after heating the autoclave to 289°C, straining of the specimens was initiated after ~20 h in all the experiments to allow the corrosion and redox potentials to approach the steady-state values reported in Tables 1.10 to 1.13. In early experiments, the platinum electrode was not incorporated into the autoclave system. Missing entries in the tables are also due to rather infrequent failure of the high-temperature reference electrode and shorting of the electrodes after installation.

The crack growth rate data at 289°C are plotted in Fig. 1.36 as a function of the open-circuit corrosion potential of Type 304 SS at 289°C determined in each experiment for feedwater conductivity values of $\lesssim$0.2, 0.9, 8, and 70 μS/cm. These values correspond to high-purity water and water with 0.1, 1, and 10 ppm sulfate as H_2SO_4, respectively. For conductivity values of $\lesssim$8 μS/cm, the crack growth rates increase gradually as the corrosion potential increases over the range of -500 mV(SHE) to ~0 mV(SHE), and then increase more rapidly with potential to a value of ~200 mV(SHE). At a conductivity of ~70 μS/cm (10 ppm sulfate as H_2SO_4), the intergranular crack growth rate was virtually independent of the corrosion potential over the range -425 to +225 mV(SHE). "Best-fit" curves in Fig. 1.37 for the dependence of the crack growth rates on the corrosion potential at the four conductivity levels show that for corrosion potentials below ~100 mV(SHE), the crack growth rate increases with conductivity. However, for potentials greater than ~100 mV(SHE), the highest crack growth rates occurred at intermediate conductivity values, viz., ~0.9 and 8 μS/cm. This could be attributed, in part, to the rather high general corrosion rate of the specimens in the 70-μS/cm water, in contrast to more selective corrosion of the chromium-depleted grain boundary region under the less aggressive water-chemistry conditions. Higher corrosion of the facets and edges of the grains was evident in scanning electron micrographs of CERT specimens that were strained to failure in water containing $\gtrsim$1 ppm dissolved oxygen and $\gtrsim$10 ppm sulfate as H_2SO_4.

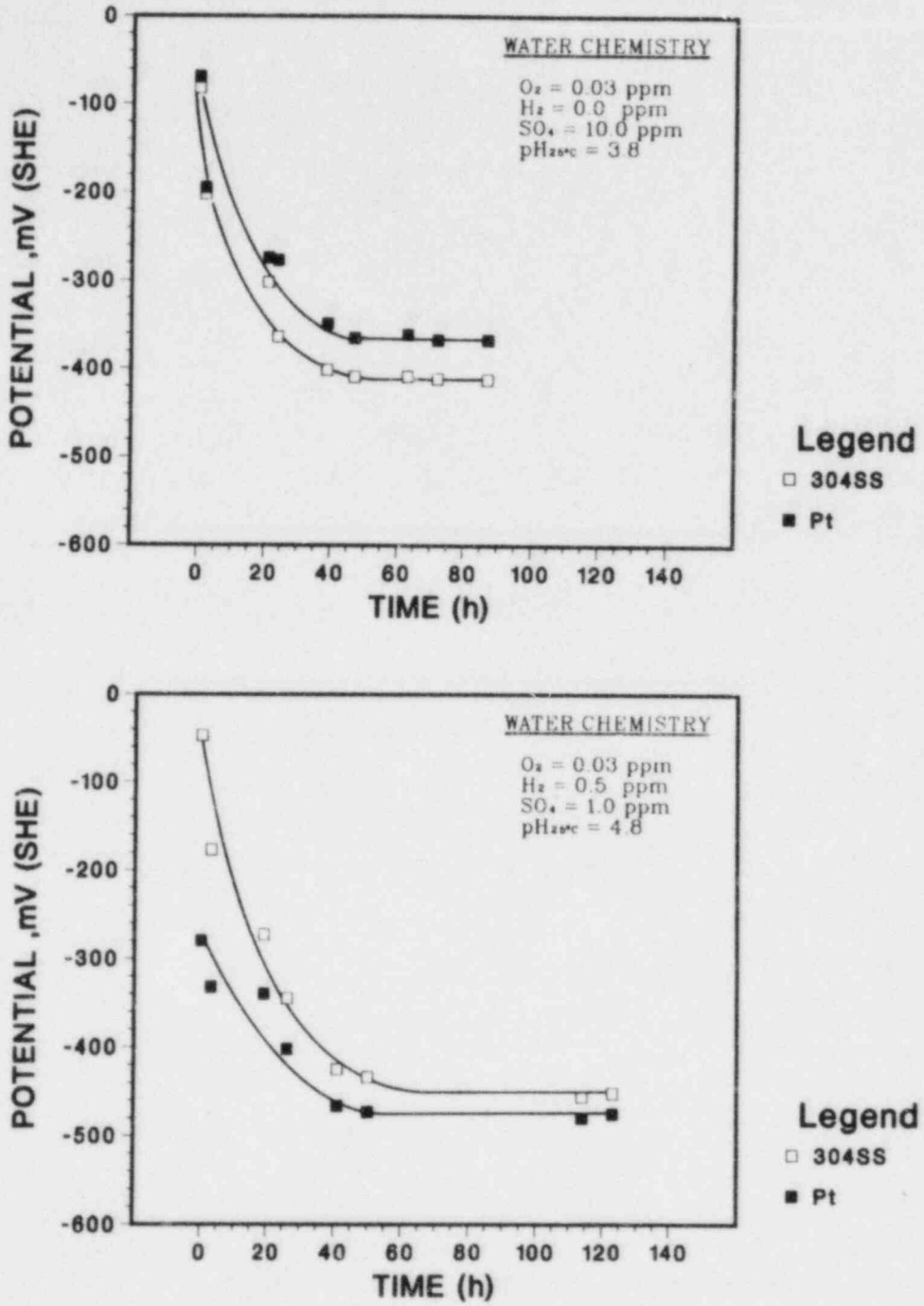

Fig. 1.35. Typical Results for the Time Dependence of the Electrochemical Potential of Type 304 SS and Platinum during CERT Experiments in 289°C Water Containing Dissolved Oxygen, Hydrogen, and Sulfate. Straining of the CERT specimen was initiated after ~20 h when the potentials approached the steady-state values.

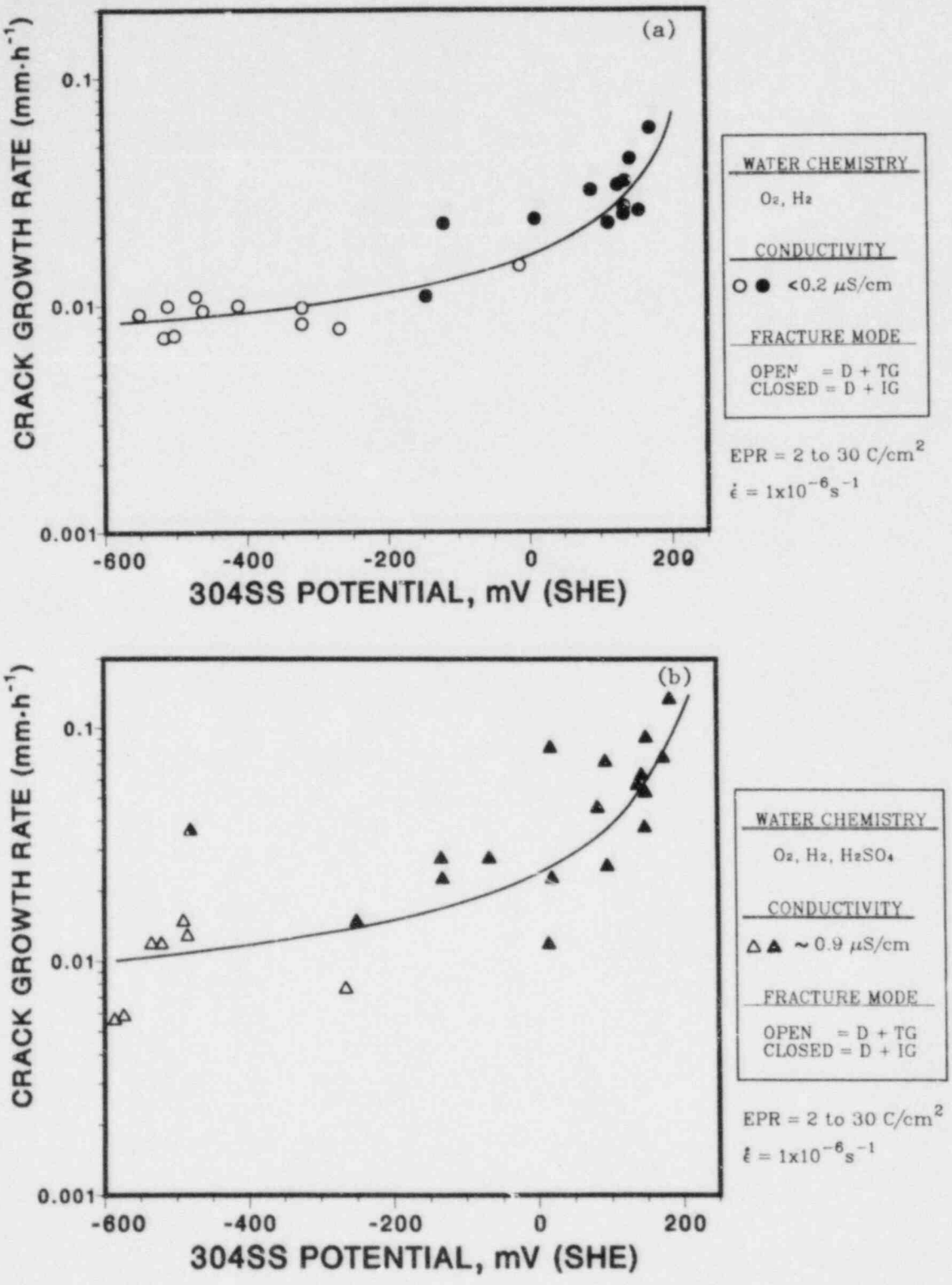

Fig. 1.36. Crack Growth Rate of Sensitized Type 304 SS (EPR = 2 to 30 C/cm^2) from CERT Experiments at 289°C as a Function of the Open Circuit Corrosion Potential of the Steel for Feedwater Conductivity Values of (a) $\leq$0.2, (b) 0.9, (c) 8, and (d) ~70 μS/cm. Conductivity values above ~0.2 μS/cm were obtained by H_2SO_4 additions to the feedwater for sulfate concentrations of 0.1, 1, and 10 ppm. Open and closed symbols denote a transgranular and intergranular fracture mode, respectively.

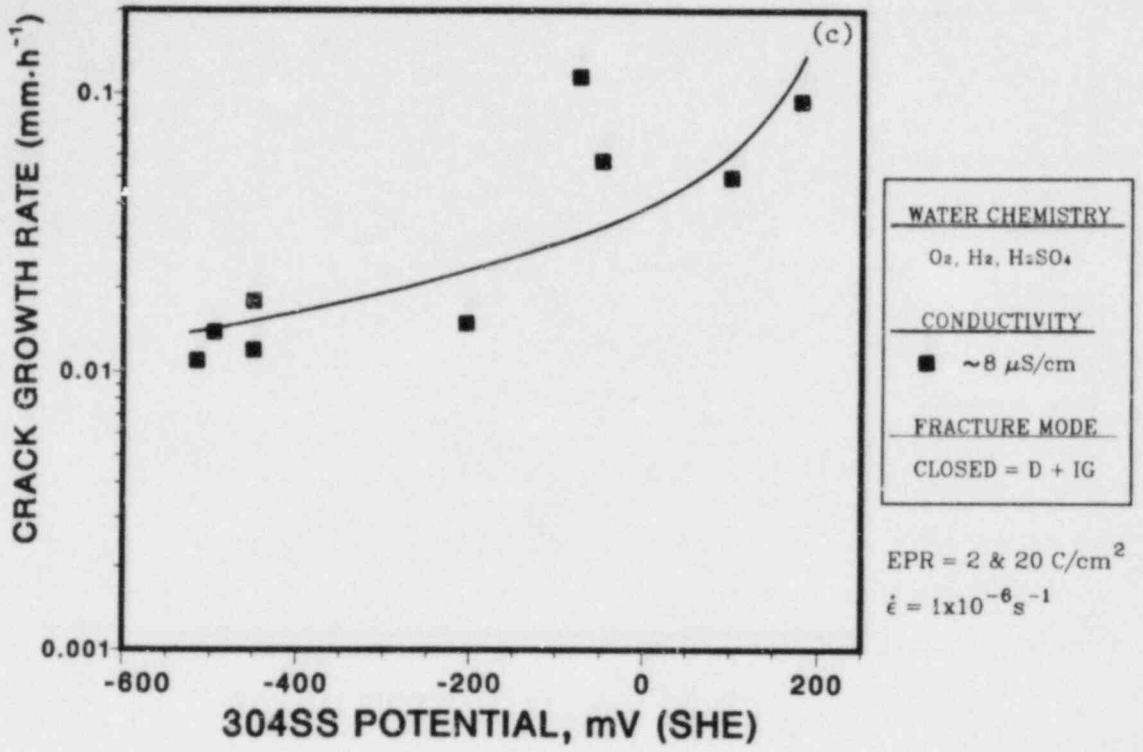

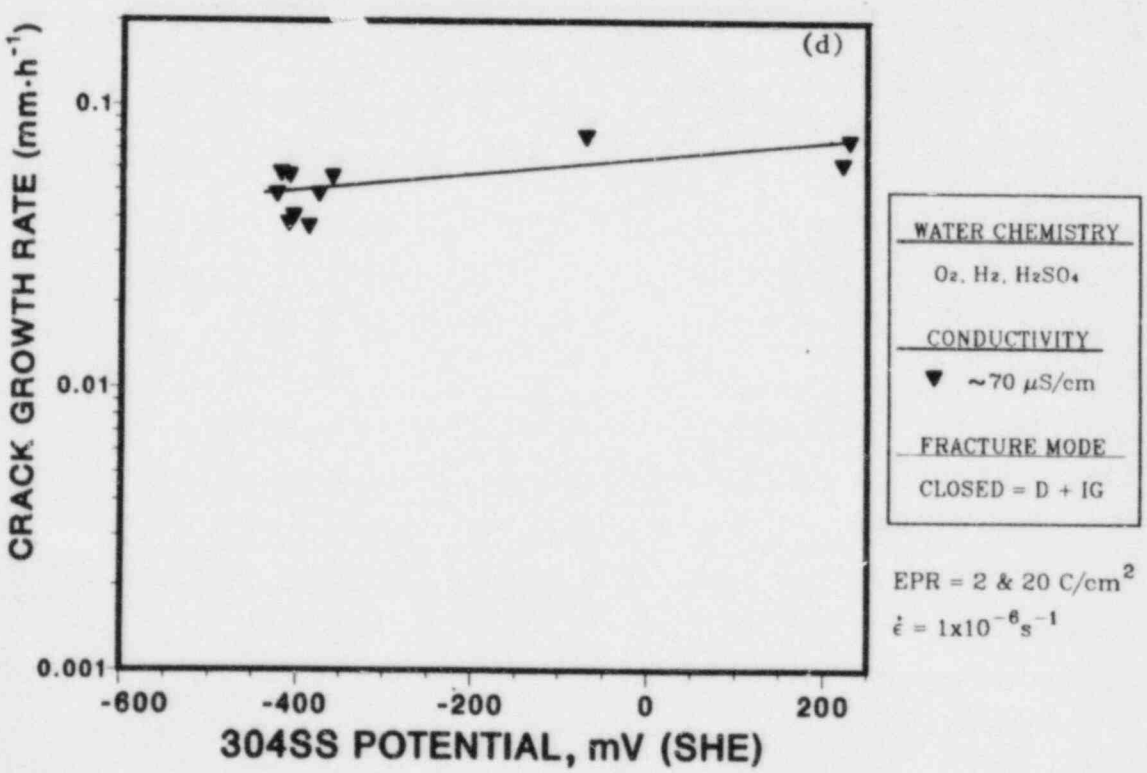

Fig. 1.36. (Contd.)

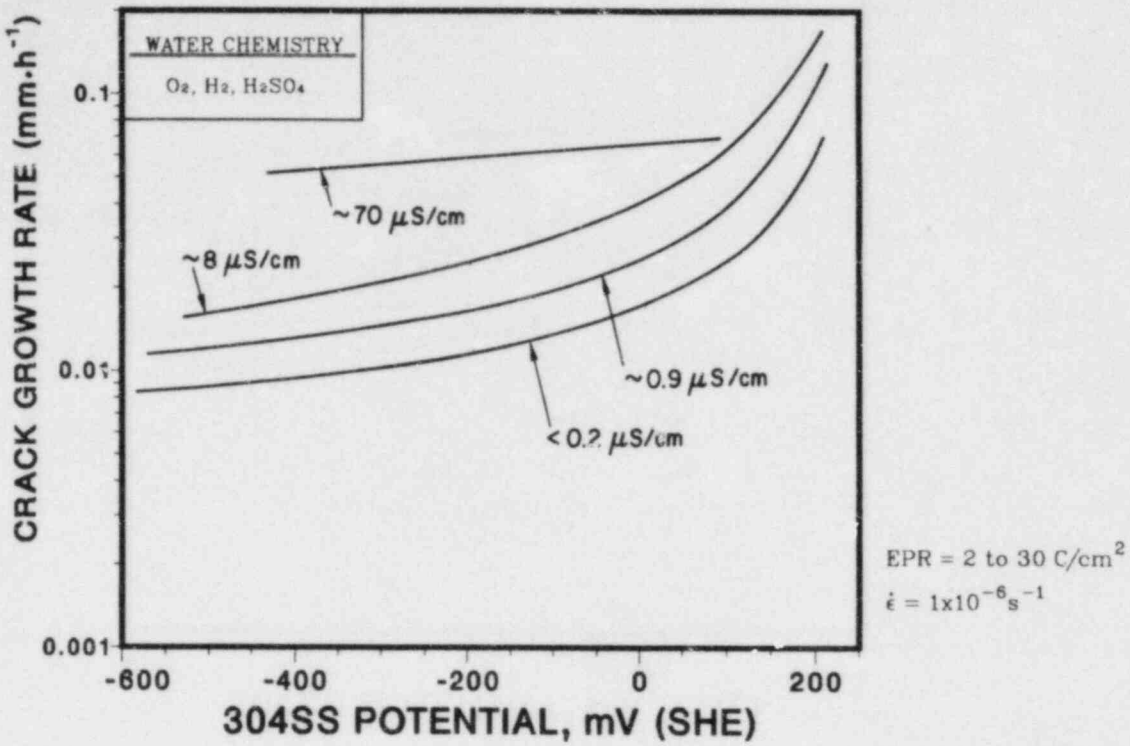

Fig. 1.37. "Best-Fit" Curves for the Dependence of the Crack Growth Rate of Sensitized Type 304 SS (EPR = 2 to 30 C/cm^2) on the Open Circuit Corrosion Potential of the Steel at 289°C in High-Purity Water ($\lesssim$0.2 μS/cm) and in Water Containing 0.1, 1, and 10 ppm Sulfate as H_2SO_4 (~0.9, 8, and 70 μS/cm, respectively). Crack growth rate data were obtained from CERT experiments at 289°C and a strain rate of 1×10^{-6} s^{-1}.

The crack growth rates in Figs. 1.34 and 1.36 (a)-(c) show a clear dependence on the dissolved oxygen concentration of the feedwater and the bulk open-circuit corrosion potential of the steel in the different environments. Since the level of sensitization of the steel and the water chemistry are within the range of interest for BWR piping systems, the present results provide useful insight into the effect of the simulated BWR environments on SCC susceptibility of the steel. For example, the "best-fit" curves in Fig. 1.37 reveal that the crack growth rate of sensitized Type 304 SS under exemplary BWR-water quality conditions [$\lesssim$0.2 μS/cm conductivity, ~0.2 ppm dissolved oxygen, and a corrosion potential of 50 mV(SHE) for stainless steel at 289°C] is only slightly greater than that associated with alternative hydrogen-water chemistry conditions with less than optimal impurity control for sulfur species [viz., ~0.9 μS/cm conductivity and a corrosion potential of

-350 mV(SHE) at 289°C]. Furthermore, a crack growth rate of 2×10^{-2} mm·h^{-1} from Fig. 1.37 is achieved both under optimal BWR-water quality conditions, as noted above, and in water containing 1 ppm sulfate at a low dissolved oxygen concentration [~8 μS/cm conductivity, pH = 4.8, and a corrosion potential of -350 mV(SHE) at 289°C]. This observation is in agreement with crack-growth-rate results[21] from several CERT experiments on welded Type 304 SS specimens that had undergone a low-temperature sensitization heat treatment before straining at a rate of $\sim 3 \times 10^{-7}$ s^{-1} in high-purity water and in water with 0.04 ppm oxygen, 0.125 ppm H_2, and H_2SO_4 at a conductivity of 10 μS/cm. If, however, the pH of the reactor coolant water is outside the range from 5.6 to 8.6 for a period of 72 h, the reactor would be required to shut down under present BWR-water quality limits in Regulatory Guide 1.56.

Comparisons between the material behavior under laboratory and reactor operating conditions are facilitated when both the corrosion potential of the steel at the operating temperature and the chemistry of the water in the recirculation loop of a BWR are known (i.e., the concentration of various ionic species, pH, dissolved oxygen concentration, and conductivity). This type of information is now being obtained for a number of operating BWRs.

From a mechanistic viewpoint, it is well known that the solution chemistry[27-29] and the electrochemical conditions[30-38] at the tip of a pit, a crevice, or an advancing stress corrosion crack can be quite different from those of the bulk solution. Various models have been developed to calculate the electrode potential and the concentration of ionic species within a stress corrosion crack.[30-38] In general, these models predict that the potential at the crack tip is more negative than that at the mouth of the crack for anodic applied potentials, although the potential drop is small near the free corrosion potential of the steel. Also, the concentration of dissolved oxygen decreases markedly at the crack tip,[28] whereas the concentrations of metal cations and the hydrogen ion increase relative to the bulk solution. Thus, the dependence of the crack growth rates on the bulk solution chemistry and open-circuit corrosion potential depicted in Figs. 1.34 and 1.36, respectively, may not be entirely characteristic of the dependence based on crack tip values. This does not present a problem in the interpretation or applicability of our results since the CERT experiments were <u>not</u> performed in

concentrated solutions or under external applied potentials to accelerate IGSCC. Therefore, detailed analytical models for the crack growth process based on the stress intensity and various electrochemical parameters that are controlled by the environment as well as the composition and structure of the material at the crack path (e.g., the sensitized grain boundary) are not necessary to extrapolate the present results to the dilute BWR service environment. However, the relationship between the mechanical loading inherent in the CERT test and actual reactor loading conditions does require further consideration.

5. Relationship between the Corrosion Potential of Type 304 SS at 289°C and the Dissolved Oxygen Concentration of the Water with Different Sulfate Concentrations

The relationship between the open-circuit corrosion potential of Type 304 SS and the dissolved oxygen in the feedwater for different sulfate concentrations or conductivity values can be obtained from the results in Tables 1.10 to 1.13. The steady-state corrosion potentials determined during the CERT experiments are plotted in Fig. 1.38 as a function of dissolved oxygen concentrations for high-purity water (<0.2 μS/cm) and for conductivity values of ~0.9, 8, and 70 μS/cm. The curves at each conductivity value exhibit the characteristic sigmoidal shape that has been reported by several investigators.[39-41] The dashed line in each figure at low oxygen concentrations denotes the minimum potential for the hydrogen evolution reaction ($2H^+ + 2e^- = H_2$) at the different pH values for a dissolved hydrogen concentration of 2 ppm. The potential values were obtained from the expression

$$E_{289°C}(SHE) = -0.1113 \cdot pH_{289°C} - 0.0557 \log \frac{C_H}{C_H^o}, \qquad (1.17)$$

where C_H^o is the solubility of hydrogen in the water at 289°C (viz., 7.55 ppm)[42] and C_H is the concentration of hydrogen in the feedwater (2.0 ppm). The $pH_{289°C}$ values for high-purity water and water containing 0.1, 1, and 10 ppm sulfate as H_2SO_4 are 5.63, 5.49, 4.95, and 4.00, respectively, based on information on the dissociation of water[43] and the second dissociation constant of sulfuric acid[44] at high temperature.

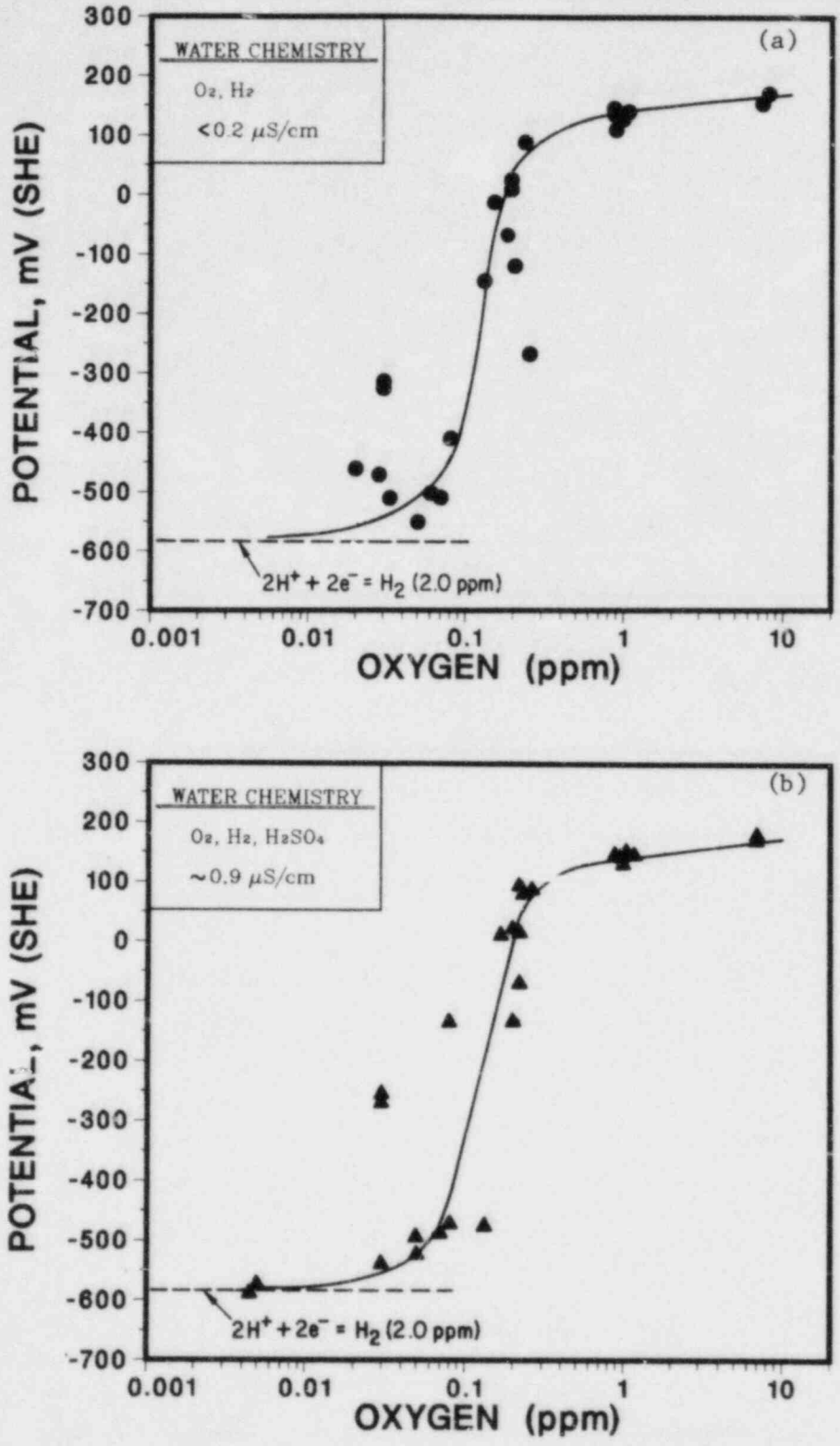

Fig. 1.38. Steady-State Open-Circuit Corrosion Potential of Type 304 SS during Individual CERT Experiments at 289°C versus the Dissolved Oxygen Concentration in the Feedwater for Conductivity Values of (a) $\lesssim$0.2, (b) 0.9, (c) 8, and (d) ~70 μS/cm. Conductivity values above ~0.2 μS/cm were obtained by H_2SO_4 additions to the feedwater for sulfate concentrations of 0.1, 1, and 10 ppm (0.9, 8, and 70 μS/cm, respectively).

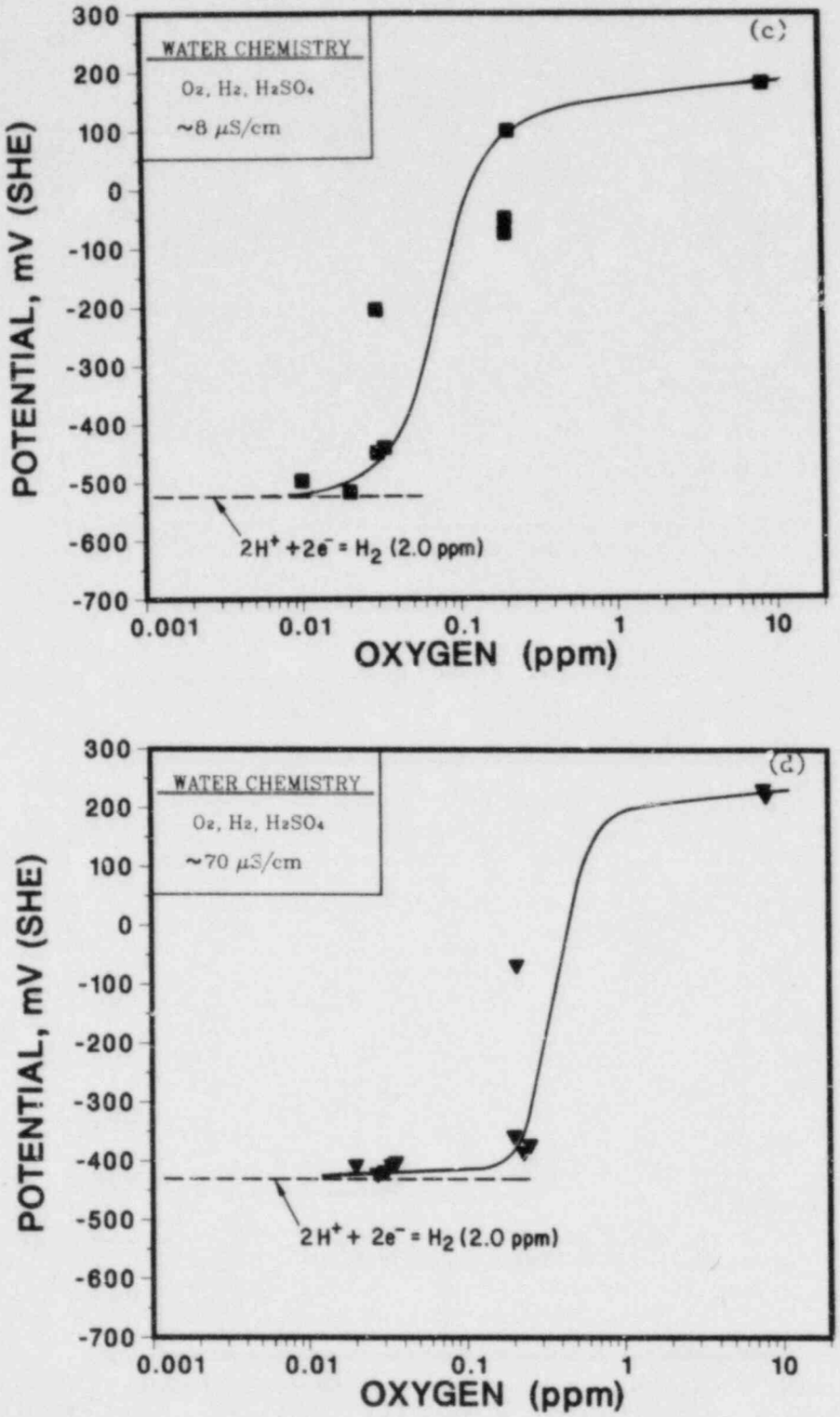

Fig. 1.38. (Contd.)

It is evident from these results that the corrosion potential of the steel was very close to the potential for the cathodic reduction of hydrogen ions for dissolved oxygen concentrations of $\lesssim$0.03 ppm. These potentials are associated with transgranular stress corrosion cracking in the sensitized steel in high-purity water ($\lesssim$0.2 μS/cm) and in water with ~0.1 ppm sulfate as H_2SO_4 (~0.9 μS/cm). The corrosion potentials in Fig. 1.38 corresponding to a dissolved oxygen concentration of 8 ppm are ~225 mV below the redox potential for the reaction $O_2 + 4H^+ + 4e^- = 2H_2O$ at 289°C from the expression

$$E_{289°C} = 1.021 - 0.1113\ pH_{289°C} + 0.0278 \log \frac{C_o}{C_o^o}, \qquad (1.18)$$

where C_o^o is the solubility of oxygen in the water at 289°C (viz., 113 ppm) and C_o is the dissolved oxygen concentration in the feedwater. The relative position of the "best-fit" pH versus potential curves in Fig. 1.39(a) at high and low dissolved oxygen concentrations are consistent with the dependence of the limiting redox potentials on pH at 289°C. These curves provide a rationale for the envelope of the corrosion potential versus dissolved oxygen data in Fig. 1.39(b) for the CERT experiments in 289°C water with different concentrations of oxygen, hydrogen, and sulfate as H_2SO_4.

6. Crack Growth Results on Type 304 SS in Simulated BWR-Quality Water at 289°C

To further investigate the effects of dissolved oxygen and impurities, viz., H_2SO_4 from decomposition of ion exchange resins, on the crack growth properties of Type 304 SS, tests are in progress on fracture-mechanics type specimens of the same heat of steel as in the CERT experiments. Three 1TCT specimens of the material in the solution-annealed and sensitized conditions (EPR = 0, 2, and 20 C/cm^2) were connected in series and stressed at an R value of 0.95 under a positive sawtooth waveform at a frequency of 8×10^{-2} Hz. The loading in the initial phases of the experiment established the influence of K_{max} over the range of ~30 to 50 MPa·m$^{1/2}$ on the steady-state crack growth rates in water with 0.2 ppm dissolved oxygen and 0.1 ppm sulfate as H_2SO_4.[16] At this point in the test (~1600 h), sulfate was not added to the

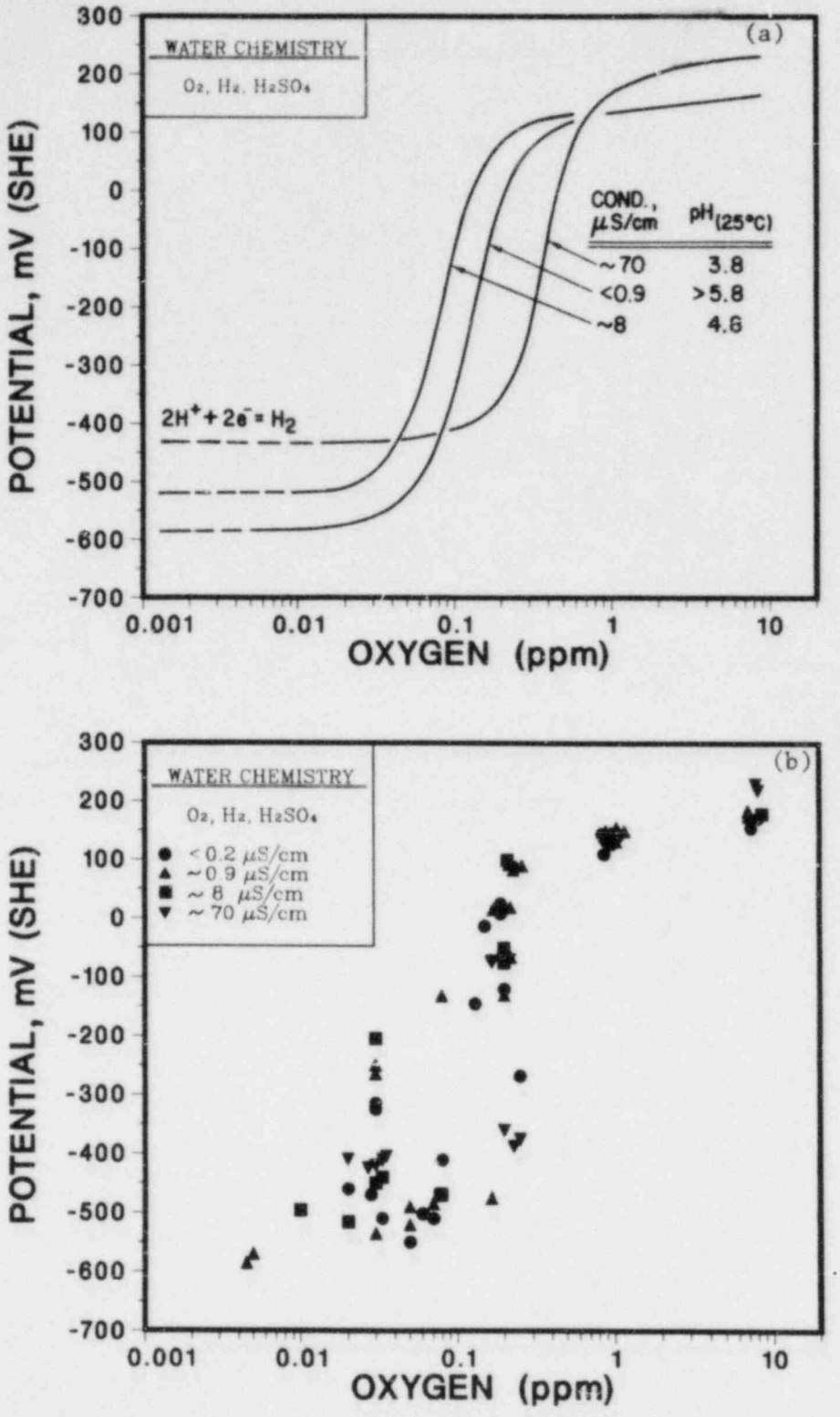

Fig. 1.39. Open-Circuit Corrosion Potential of Type 304 SS at 289°C versus Dissolved Oxygen Concentration of the Feedwater: (a) "Best-Fit" Curves for Several Conductivity/pH Values and (b) Summary of the Experimental Data. Dashed lines in (a) represent the minimum potential for the hydrogen evolution reaction at the indicated pH values for 2.0 ppm dissolved hydrogen in the feedwater.

feedwater (high-purity water with 0.2 ppm oxygen), and measurements of the crack length in the three specimens were made over a period of ~1200 h. After this time interval, 0.1 ppm sulfate again was added to the feedwater with 0.2 ppm dissolved oxygen, and crack growth in the specimens was determined over a period of ~370 h.

The results of the crack length measurements as a function of time are shown in Fig. 1.40 for the water chemistry transient in which sulfate was not present in the environment during a 1200-h time interval. The stress intensity values for the lightly sensitized specimen (EPR = 2 C/cm^2) are noted on the figure at different times in the experiment. These values, along with similar information for the other specimens, are given in Table 1.14. The crack growth rates for the time periods in which sulfate was and was not present in the 0.2-ppm oxygen environment are noted in the table for each specimen. It is clear from Fig. 1.40 and Table 1.14 that removal of sulfate had virtually no effect on crack growth in the solution-annealed (EPR = 0) and moderately sensitized (EPR = 20 C/cm^2) specimens. The crack growth rate of the lightly sensitized specimen decreased by a factor of ~4 over a ~600-h period after sulfate was removed from the feedwater; however, the rate increased to the initial value over the next 600 h in the high-purity water environment. A further increase in the crack growth rate occurred at ~7300 h when sulfate was added to the feedwater. Since the actual crack length in the EPR = 2 C/cm^2 specimen was between ~9 and 13 mm during the transient water-chemistry experiment, the stress intensity factor increased from ~49 to 63 $MPa \cdot m^{1/2}$, which has some effect on the growth rate over the duration of the test. Under constant water chemistry (0.2 ppm oxygen and 0.1 ppm sulfate), the dependence of the crack growth rate on maximum stress intensity is given by the relation[16] $CGR\ (mm \cdot h^{-1}) = 4 \times 10^{-10}\ (K_{max})^{4.0}$. For example, an increase in the stress intensity factor from 53 to 59 $MPa \cdot m^{1/2}$ during the time period when no sulfate was present in the water would account for a factor of 1.5 increase in the crack growth rate from the beginning to the end of this period. The crack growth rate during the last half of this period was a factor of three higher than that during the initial phase with no sulfate in the feedwater. If we assume that the initial decrease in the crack growth rate was due to the change in crack tip chemistry associated with the removal

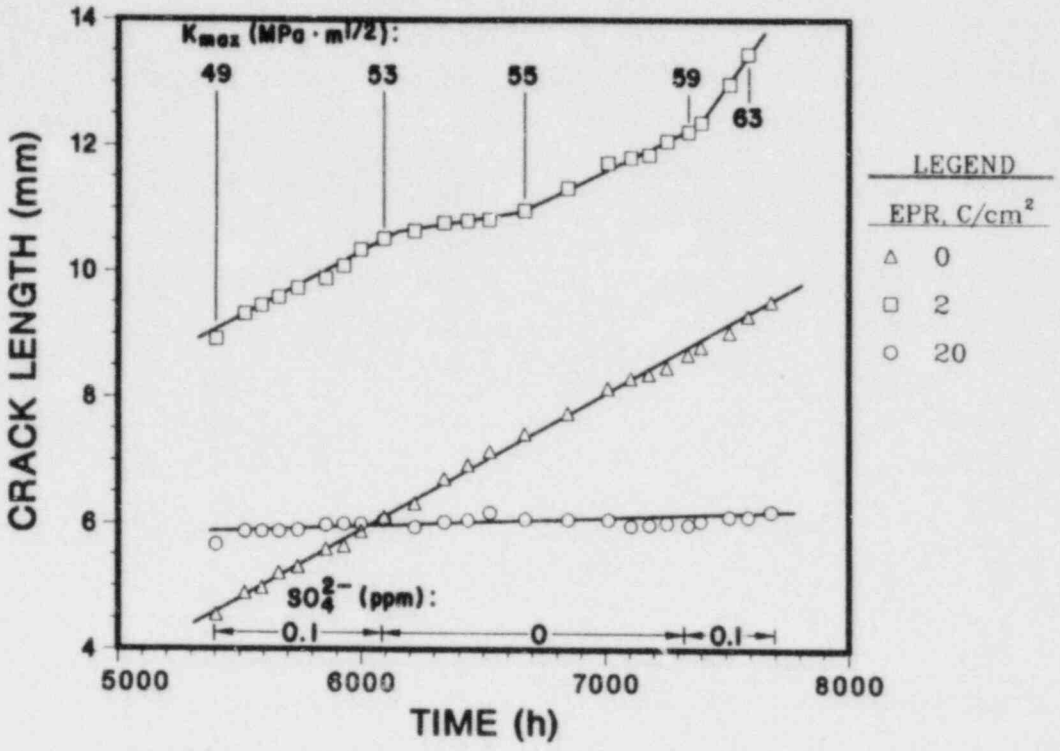

Fig. 1.40. Crack Length versus Time for 1TCT Specimens of Solution-annealed (EPR = 0) and Sensitized (EPR = 2 and 20 C/cm^2) Type 304 SS in 289°C Water Containing 0.2 ppm Dissolved Oxygen and 0.1 ppm Sulfate as H_2SO_4, Except for an Intermediate Period with High-Purity Water. The loading conditions for the positive sawtooth waveform with a slow loading time (12 s) and a rapid unloading (1 s) are as follows: stress ratio R = 0.95, frequency = 8 x 10^{-2} Hz, and K_{max} = 49 to 63 MPa·$m^{1/2}$ for the specimen with the largest crack.

TABLE 1.14. Crack Growth Results for Type 304 SS Specimens[a] at 289°C during an Experiment[b] in Which 0.1 ppm Sulfate Was Removed from and Reintroduced to the Feedwater Containing 0.2 ppm Dissolved Oxygen

	Water Chemistry			Specimen #7 (EPR = 0 C/cm^2)			Specimen #9 (EPR = 2 C/cm^2)			Specimen #8 (EPR = 20 C/cm^2)		
Time, h	Oxygen,[c] ppm	Sulfate, ppm	Cond., µS/cm	Crack Length, mm	K_{max}, MPa·m$^{1/2}$	Growth Rate, mm·h^{-1}	Crack Length, mm	K_{max}, MPa·m$^{1/2}$	Growth Rate, mm·h^{-1}	Crack Length, mm	K_{max}, MPa·m$^{1/2}$	Growth Rate, mm·h^{-1}
5404	0.21	0.1	0.88	4.55	38.9	-	8.92	48.7	-	5.66	41.2	-
6096	0.21	0.1	0.92	6.10	42.1	2.2×10^{-3}	10.52	53.2	2.3×10^{-3}	6.05	42.0	5.6×10^{-4}
6221	0.25	0	0.11	6.32	42.6	-	10.64	53.6	-	5.94	41.8	-
6527	0.26	0	0.12	7.14	44.4	2.7×10^{-3}	10.82	54.2	5.9×10^{-4}	6.17	42.1	7.5×10^{-4}
6672	0.21	0	0.17	7.42	45.1	-	10.97	54.6	-	6.07	42.1	-
7345	0.25	0	0.25	8.69	48.2	1.9×10^{-3}	12.22	58.7	1.9×10^{-3}	5.99	41.9	~0
7397	0.25	0.1	0.91	8.81	48.2	-	12.37	58.7	-	6.05	41.9	-
7590	0.25	0.1	1.04	9.30	49.8	2.5×10^{-3}	13.46	63.4	5.6×10^{-3}	6.12	42.2	3.6×10^{-4}

[a]Compact tension specimens (1TCT) from Heat No. 30956 were solution annealed at 1050°C for 0.5 h (EPR = 0), sensitized at 700°C for 12 h (EPR = 20 cm^2), and 700°C for 0.25 h plus 500°C for 24 h (EPR = 2 C/cm^2).

[b]The load ratio and frequency of the positive sawtooth waveform were 0.95 and 8×10^{-2} Hz, respectively.

[c]Effluent dissolved oxygen concentration based on thallium column conductometric measurements. Feedwater oxygen concentration was approximately a factor of two higher to compensate for oxygen depletion caused by corrosion of the autoclave system.

of sulfate from the bulk water, it is possible that sulfate or perhaps other sulfur species slowly desorbed from the oxide on the walls of the crack, migrated to the crack tip zone, and subsequently influenced the crack growth process.

Qualitatively, the effect of sulfate in the crack growth experiment under cyclic loading is consistent with crack growth information from CERT tests on the EPR = 2 and 20 C/cm^2 specimens in water containing ~0.2 ppm dissolved oxygen without and with 0.1 ppm sulfate (Tables 1.10 and 1.11, respectively). Based on a limited number of CERT tests, 0.1 ppm sulfate causes a relatively minor increase (~40%) in the crack growth rate of the moderately sensitized material and a factor of ~5 increase in the growth rate of the lightly sensitized steel. Also, the crack growth rate of the latter material is somewhat greater than that of the moderately sensitized steel during CERT tests in the dilute sulfate environment (e.g., ~4.4×10^{-2} versus 2.5×10^{-2} $mm \cdot h^{-1}$, respectively, from the results in Table 1.11).

Figures 1.41-1.43 show the fracture surfaces, the SCC fracture morphology, and the nature of the crack near the crack tip region for specimens with different levels of sensitization (EPR = 0, 2, and 20 C/cm^2, respectively). The 1TCT specimens were sectioned vertically, and half of each specimen was split in the plane of the crack at liquid nitrogen temperature to reveal the SCC fracture surface at low magnification (center micrograph in each figure). The corrosion product film was removed from the fracture surface by the APAC process[45,46] [i.e., by exposure of the specimens for 2 h in a gently boiling alkaline permanganate solution (20% NaOH, 3% $KMnO_4$), hot rinse, and then 2 h in a 20% dibasic ammonium citrate solution] to reveal the morphology of the underlying metal. The intact portion of the specimen that encompassed the crack was polished and etched to corroborate the mode of crack propagation and also to determine if macrobranching of the crack had occurred during the test. Reasonable agreement was obtained between the final crack lengths from compliance measurements and values based on the area of SCC growth in micrographs of the fracture surface (Table 1.15).

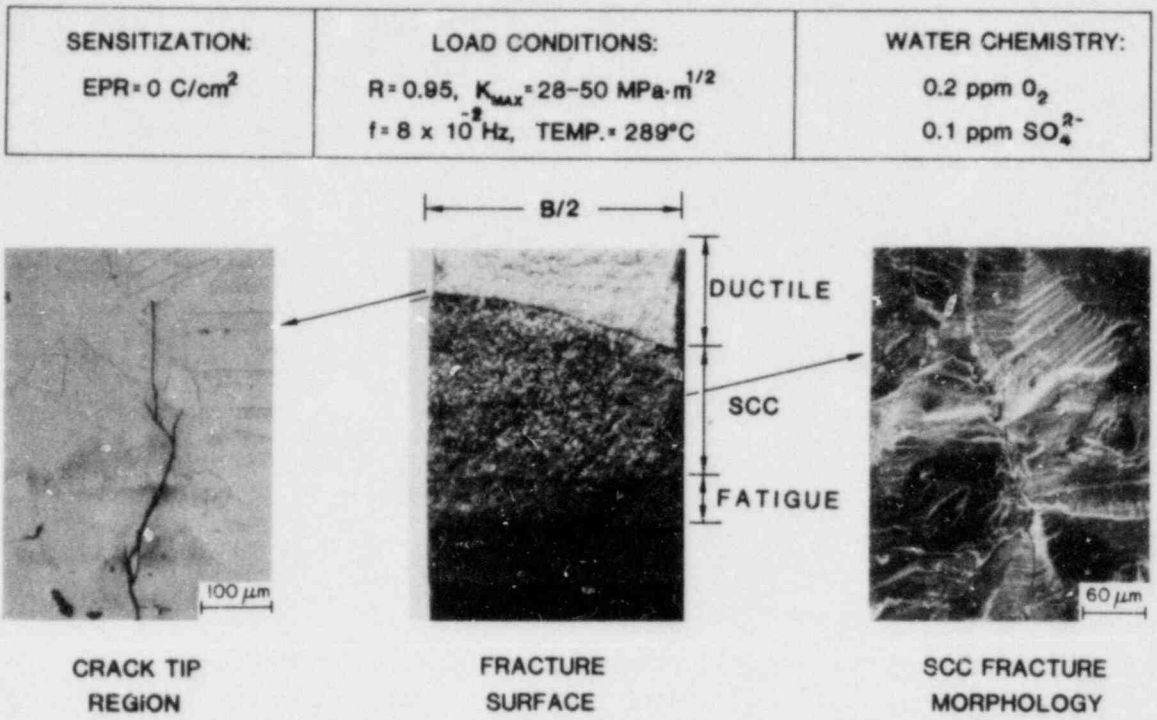

Fig. 1.41. Fracture Surface and SCC Fracture Morphology of Solution-annealed 1TCT Specimen No. 7 of Type 304 SS after a Crack Growth Experiment in 289°C Water with 0.2 ppm Dissolved Oxygen and 0.1 ppm Sulfate.

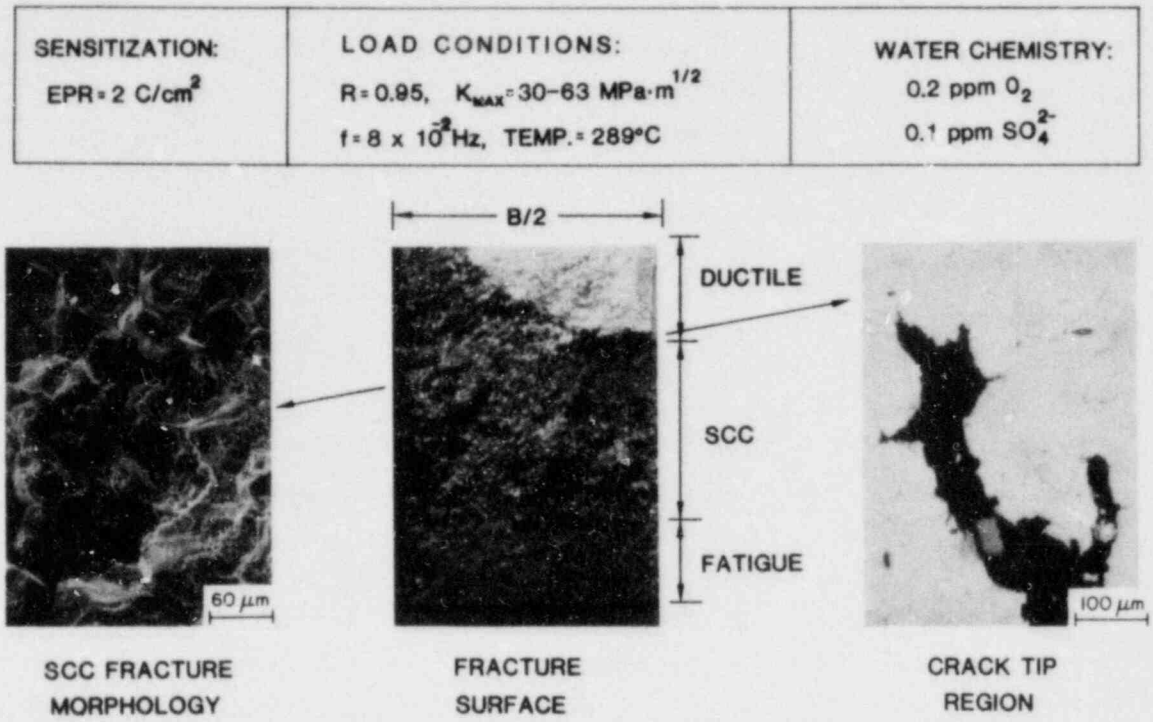

Fig. 1.42. Fracture Surface and SCC Fracture Morphology of Lightly Sensitized 1TCT Specimen No. 9 of Type 304 SS after a Crack Growth Experiment in 289°C Water with 0.2 ppm Dissolved Oxygen and 0.1 ppm Sulfate. The wide crack opening relative to the other specimens resulted from a higher stress intensity at the end of the tests.

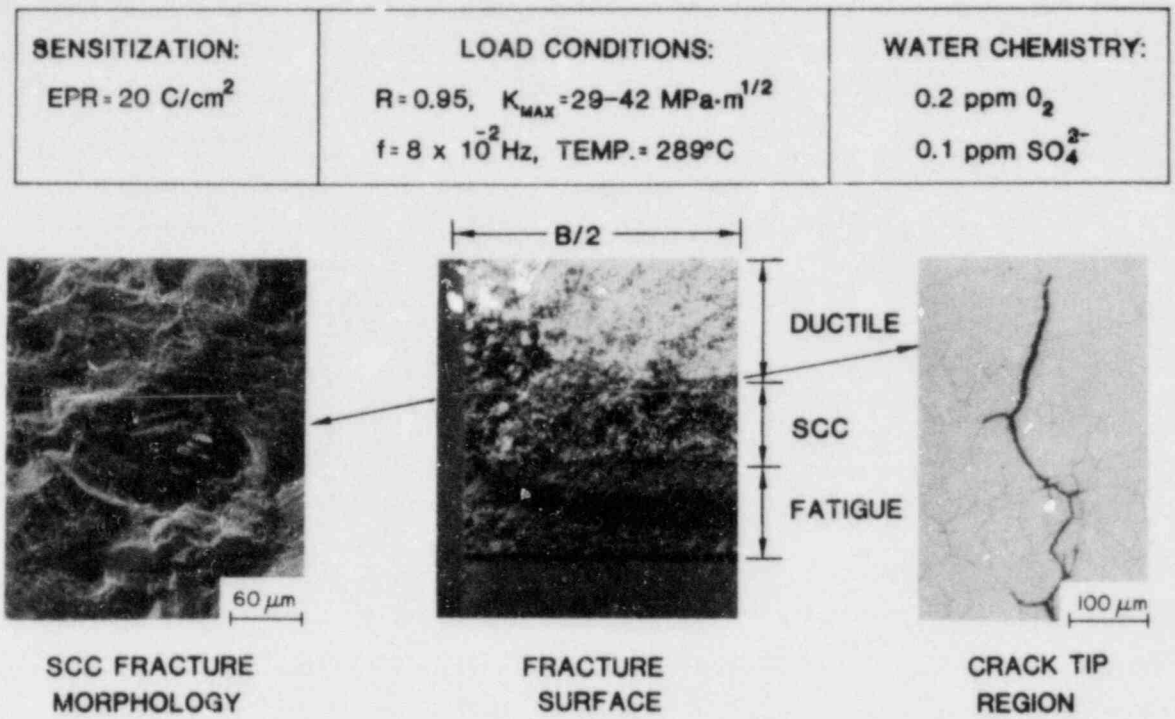

Fig. 1.43. Fracture Surface and SCC Fracture Morphology of Moderately Sensitized 1TCT Specimen No. 8 of Type 304 SS after a Crack Growth Experiment in 289°C Water with 0.2 ppm Dissolved Oxygen and 0.1 ppm Sulfate.

TABLE 1.15. Comparison of Crack Length from Compliance Measurements with Values Based on the Area of SCC Growth in the Fracture Surface

Specimen Number	Final Crack Length by Compliance, mm	Crack Length by SCC Area, mm
7 (EPR = 0)	9.5	9.2
8 (EPR = 20 C/cm^2)	6.2	7.6
9 (EPR = 2 C/cm^2)	13.8	14.0

The fracture surface morphology and the crack path in Fig. 1.41 both indicate that the mode of crack propagation was transgranular in the solution annealed material (EPR = 0). The micrographs in Figs. 1.42 and 1.43 for the lightly and moderately sensitized specimens reveal intergranular cracking. The intergranular nature of the crack is more evident in the lightly sensitized material (Fig. 1.42), which, as mentioned previously, exhibits a high degree of IGSCC susceptibility in CERT experiments in 289°C water with 0.2 ppm dissolved oxygen and 0.1 ppm sulfate.

Macrobranching of the cracks was not observed; however, some curvature of the crack front is evident in the three specimens. The thumbnail-type of crack front in the solution-annealed specimen (Fig. 1.41) is typical of the crack curvature that has been observed during fatigue crack growth of austenitic stainless steels in air[47] and for carbon steels (SA 333-Gr6 and SA 508-2) in simulated BWR[48] and PWR[49] environments at 288°C. In the case of the sensitized specimens (Figs. 1.42 and 1.43), crack advance was more rapid at the side surface of the specimens under the high-R, low-ΔK loading. This type of behavior has been reported for sensitized Type 304 SS in high-purity water[50,51] and in water with the same dissolved oxygen and sulfate concentrations as in our experiment under similar loading conditions at 288°C.[21] Accelerated intergranular crack advance at the side region of compact tension specimens has been rationalized on the basis of diffusion dominated crack growth[16] where the diffusion path for ions to or away from the crack tip is shortest near the edge of the specimen.

The effect of dissolved oxygen concentration of high-purity water on the crack growth properties of Type 304 SS was evaluated in a similar experiment at 289°C in which three 1TCT specimens (EPR = 0, 2, and 20 C/cm^2) were connected in series and stressed at an R value of 0.95 and a frequency of 8×10^{-2} Hz under a positive sawtooth waveform. As in the previous experiment, the specimens were fatigue precracked in air at 289°C to facilitate the initiation of stress corrosion cracks during exposure to the high-temperature water environment.

The crack length as a function of time is shown in Fig. 1.44 for the three specimens in which the dissolved oxygen concentration of the water was decreased from 0.2 to 0.02 ppm at ~960 h and then returned to the initial concentration at ~1600 h. The curves clearly indicate that crack growth in the

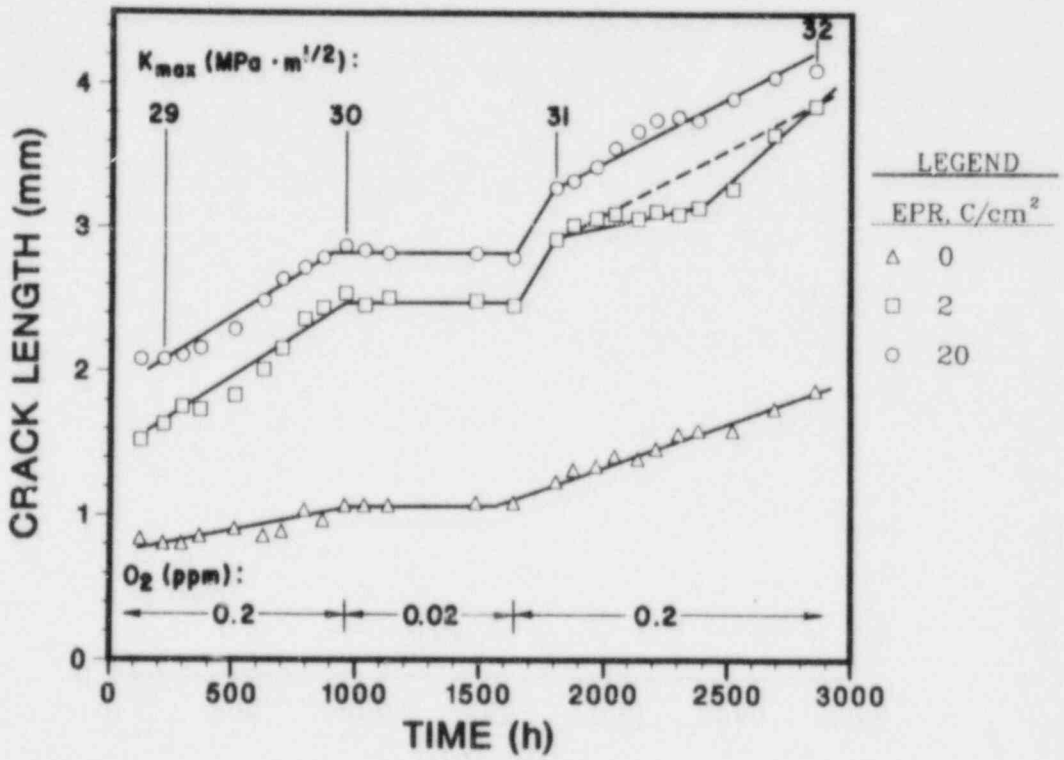

Fig. 1.44. Crack Length versus Time for 1TCT Specimens of Solution-annealed (EPR = 0) and Sensitized (EPR = 2 and 20 C/cm^2) Type 304 SS in 289°C Water Containing 0.2 ppm Dissolved Oxygen, with an Intermediate Period in Which the Oxygen Concentration Was Decreased to 0.02 ppm. The loading conditions for the positive sawtooth waveform with a slow loading time (12 s) and rapid unloading (1 s) are as follows: stress ratio R = 0.95, frequency = 8×10^{-2} Hz, and K_{max} = 29 to 32 MPa·m$^{1/2}$ for the specimen with the largest crack.

three specimens virtually ceased over the ~600-h time interval at the low dissolved oxygen concentration. The crack lengths, stress intensity values, and crack growth rates from the time periods at the different dissolved oxygen concentrations in the water during the transient are given in Table 1.16. Crack growth in the three specimens resumed at approximately the initial rates after the dissolved oxygen concentration was increased to the 0.2 ppm value. In this experiment, the material in the lightly and moderately sensitized conditions exhibited similar behavior during the transient. This is consistent with the results of the CERT experiments in high-purity water in Table 1.10, which indicate that the intergranular crack propagation rates of specimens sensitized to EPR values of 2 and 20 C/cm^2 are similar in water with 0.2 ppm dissolved oxygen (e.g., ~1.2×10^{-2} and 1.8×10^{-2} $mm \cdot h^{-1}$). The rate of transgranular crack propagation at a dissolved oxygen concentration of ~0.02 ppm is the same (~1×10^{-2} $mm \cdot h^{-1}$) for both levels of sensitization of the material. In summary, the CERT experiments in Table 1.10 indicate that the crack propagation rate is not strongly dependent on the degree of sensitization of the steel in either environment and that although the mode of crack propagation is intergranular at the higher oxygen concentration and transgranular at the lower concentration, the crack growth rates are of the same magnitude. Thus, the CERT experiments conducted at a given dissolved oxygen concentration of the feedwater provide only limited information on the SCC behavior of steel under transient water chemistry conditions. Crack growth experiments on fracture-mechanics type specimens can provide the necessary information; however, the time period involved in these tests is quite long. A comparison of the actual crack growth rates determined in the CERT tests at a strain rate of 1×10^{-6} s^{-1} with the values obtained from the fracture mechanics specimens at a K_{max} of 30 $MPa \cdot m^{1/2}$, a frequency of 8×10^{-2}, and a load ratio of 0.95 for a positive sawtooth waveform reveals the following. For the lightly sensitized material (EPR = 2 C/cm^2), the crack growth rates obtained from the CERT tests in high-purity water and in water with 0.1 ppm sulfate as H_2SO_4 are factors of ~10 and 100 higher than the corresponding values determined in the experiments under cyclic loading at a K_{max} of ~30 $MPa \cdot m^{1/2}$, R = 0.95, and a frequency of 8×10^{-2} Hz. A more detailed analysis of the crack growth results under the two loading modes will be made on the basis of the calculated crack-tip strain rates and crack length, which may influence water chemistry at the crack tip.

TABLE 1.16. Crack Growth Results for Type 304 SS Specimens[a] during an Experiment[b] in Which the Dissolved Oxygen Concentration of the Feedwater Was Decreased from 0.2 to 0.02 ppm and Then Returned to the Initial Value

	Water Chemistry		Specimen #22 (EPR = 0 C/cm^2)			Specimen #20 (EPR = 2 C/cm^2)			Specimen #21 (EPR = 20 C/cm^2)		
Time, h	Oxygen,[c] ppm	Cond., µS/cm	Crack Length, mm	K_{max}, MPa·m$^{1/2}$	Growth Rate, mm·h^{-1}	Crack Length, mm	K_{max}, MPa·m$^{1/2}$	Growth Rate, mm·h^{-1}	Crack Length, mm	K_{max}, MPa·m$^{1/2}$	Growth Rate, mm·h^{-1}
218	0.16	0.10	0.81	26.9	-	1.63	28.0	-	2.08	28.7	-
960	0.23	0.11	1.07	27.3	3.5×10^{-4}	2.54	29.3	1.2×10^{-3}	2.87	29.9	1.1×10^{-3}
1037	<0.02	0.10	1.07	27.3	-	2.46	29.3	-	2.84	29.9	-
1637	<0.02	0.09	1.09	27.3	~0	2.46	29.3	~0	2.79	29.8	~0
1807	0.24	0.10	1.24	27.5	-	2.92	30.0	-	3.28	30.5	-
2304	0.32	0.16	1.57	28.0	6.6×10^{-4}	3.10	30.3	1.6×10^{-4}	3.78	31.3	1.0×10^{-3}
2382	0.21	0.13	1.60	28.0	-	3.15	30.3	-	3.76	31.3	-
2856	0.25	0.14	1.88	28.4	5.9×10^{-4}	3.86	31.5	[d] 1.5×10^{-3}	4.11	31.9	[d] 7.4×10^{-4}

[a] Compact tension specimens (1TCT) from heat 30956 were solution annealed at 1050°C for 0.5 h (EPR = 0), sensitized at 700°C for 12 h (EPR = 20 C/cm^2), and 700°C for 0.25 h plus 500°C for 24 h (EPR = 2 C/cm^2).

[b] The load ratio and frequency of the positive sawtooth waveform were 0.95 and 8×10^{-2} Hz, respectively.

[c] Effluent dissolved oxygen concentration based on thallium column conductometric measurements. Feedwater oxygen concentration at the 0.2 ppm level was approximately a factor of ~3 higher to compensate for oxygen depletion caused by corrosion of the autoclave system.

[d] Average crack growth rates over the 1049-h period with 0.2 ppm dissolved oxygen in the feedwater were 9.0×10^{-4} and 7.9×10^{-4} mm·h^{-1}, for the EPR = 2 and 20 C/cm^2 material, respectively.

F. References for Chapter I

1. "Standard for Light Water Power Reactor Coolant Pressure Boundary Leak Detection," ISA Standard S67.03, ANS Standard N41.21 (1978).

2. D. S. Kupperman, T. N. Claytor, and R. Groenwald, "Acoustic Leak Detection and Ultrasonic Crack Detection," in Proc. of the USNRC Eleventh Water Reactor Safety Research Information Meeting, U.S. Nuclear Regulatory Commission, Washington, D. C., NUREG/CR-0048, Vol. 4 (1984), pp. 20-40.

3. J. Y. Park, in Materials Science and Technology Division Light-Water-Reactor Safety Research Program: Quarterly Progress Report, January-March 1983, NUREG/CR-3689 Vol. I, ANL-83-35 Vol. I (April 1984), pp. 24-29.

4. J. Y. Park and W. J. Shack, in Materials Science and Technology Division Light-Water-Reactor Safety Research Program: Quarterly Progress Report, April-June 1983, NUREG/CR-3689 Vol. II, ANL-83-35 Vol. II (June 1984), pp. 18-21.

5. F. P. Ford, A Mechanism of Environmentally Controlled Crack-Growth of Structural Steels in High-Temperature Water, General Electric Co. Report 81-CRD-125 (August 1981).

6. P. M. Scott and A. E. Truswell, "Corrosion Fatigue Crack Growth in Reactor Pressure Vessel Steels in PWR Primary Water," in Aspects of Fracture Mechanics in Pressure Vessels and Piping, PVP Vol. 58, American Society of Mechanical Engineers, New York (1982), pp. 271-301.

7. J. R. Rice, "Mechanics of Crack Tip Deformation and Extension by Fatigue," in Fatigue Crack Propagation, ASTM STP 415, American Society for Testing and Materials, Philadelphia (1967), pp. 247-309.

8. P. S. Maiya and W. J. Shack, in Materials Science and Technology Division Light-Water-Reactor Safety Research Program: Quarterly Progress Report, January-March 1983, NUREG/CR-3689 Vol. I, ANL-83-35 Vol. I (April 1984), pp. 34-46.

9. P. S. Maiya and W. J. Shack, in Environmentally Assisted Cracking in Light Water Reactors: Annual Report, October 1982-September 1983, NUREG/CR-3806, ANL-84-36 (June 1984), pp. 58-100.

10. F. P. Ford, "Mechanisms of Stress Corrosion Cracking," in Aspects of Fracture Mechanics in Pressure Vessels and Piping, PVP Vol. 58, American Society of Mechanical Engineers, New York (1982), pp. 229-269.

11. P. S. Maiya and W. J. Shack, "Effects of Nominal and Crack-Tip Strain Rate on IGSCC Susceptibility in CERT Tests," Proceedings of the Symposium on Localized Chemistry and Mechanics in Environment-Assisted Fracture, TMS-AIME Fall Mtg., Philadelphia, PA, October 3-6, 1983 (in press).

12. E. W. Hart, Constitutive Relations for the Non-elastic Deformation of Metals, J. Eng. Mater. Technol. 93 (3), 193 (1976).

13. S. P. Hannula and C. Y. Li, Repeated Load Relaxations of Type 316 Austenitic Stainless Steel, Scripta Metall. 18, 225-229 (1984).

14. W. J. Shack, Measurement of Throughwall Residual Stresses in Large-Diameter Type 304 Stainless Steel Piping Butt Weldments, ANL-82-15 (1982).

15. Ref. 9, pp. 83-92.

16. W. E. Ruther, W. K. Soppet, and T. F. Kassner, in Materials Science and Technology Division Light-Water Reactor Safety Research Program: Quarterly Progress Report, January-March 1983, NUREG/CR-3689 Vol. I, ANL-83-35 Vol. I (April 1984), pp. 47-59.

17. W. E. Ruther, W. K. Soppet, and T. F. Kassner, in Materials Science and Technology Division Light-Water Reactor Safety Research Program: Quarterly Progress Report, April-June 1983, NUREG/CR-3689 Vol. II, ANL-83-85 Vol. II (May 1984), pp. 32-58.

18. W. E. Ruther, W. K. Soppet, G. Ayrault, and T. F. Kassner, Effect of Sulfuric Acid, Oxygen, and Hydrogen in High-Temperature Water on Stress Corrosion Cracking of Sensitized Type 304 Stainless Steel, to be published, Corrosion 40 (1984).

19. W. L. Clarke et al., Detection of Sensitization in Stainless Steel Using Electrochemical Techniques, General Electric Company Report GEAP-21382, August 1976.

20. W. L. Clarke, R. L. Cowen, and W. L. Walker, "Comparative Methods for Measuring Degree of Sensitization of Stainless Steels," Intergranular Corrosion of Stainless Alloys, ASTM STP 656, R. F. Steigerwald, ed., American Society for Testing and Materials, Philadelphia (1978), pp. 99-132.

21. P. L. Andresen, The Effects of Aqueous Impurities on Intergranular Stress Corrosion Cracking of Sensitized Type 304 Stainless Steel, EPRI Final Report NP-3384 (November 1983).

22. E. L. Burley, Oxygen Suppression in Boiling Water Reactors - Phase 2 Final Report, General Electric Company, NEDC-23856-7, DOE/ET/43203-47 (October 1982).

23. R. H. Asay, J. Blok, and J. H. Holloway, Water Quality in Boiling Water Reactors, EPRI Final Report, NP-1603 (November 1980).

24. A. D. Miller, Water Chemistry Characterizations of a Boiling Water Reactor, Nucl. Technol. 37(2), 111-117 (1978).

25. P. L. Andresen, Innovations in Experimental Techniques for Testing in High-Temperature Aqueous Environments, General Electric CRD Report 81CRD088 (May 1981).

26. D. D. Macdonald, A. C. Scott, and P. Wentrcek, External Reference Electrodes for Use in High-Temperature Aqueous Systems, J. Electrochem. Soc. 126(6), 908-911 (1979).

27. J. W. Oldfield and W. H. Sutton, Crevice Corrosion of Stainless Steels-I A Mathematical Model, Br. Corros. J. 13(1), 13-22 (1978).

28. A. Turnbull, A Theoretical Evaluation of the Influence of Mechanical Variables on the Concentration of Oxygen in a Corrosion Fatigue Crack, Corros. Sci. 22(9), 877-893 (1982).

29. D. F. Taylor and M. Silverman, Some Effects of Electrolyte Composition and Heat Treatment on the Aqueous Crevice Corrosion of Alloy 600 and Type 304 Stainless Steel at 288°C, Corrosion 36(9), 447-458 (1980).

30. J. G. Hines, On the Propagation of Stress Corrosion Cracks in Metals, Corros. Sci. 1, 21-48 (1961).

31. T. R. Beck and E. A. Grens, III, An Electrochemical Mass Transport-Kinetic Model for Stress Corrosion Cracking of Titanium, J. Electrochem. Soc. 116(2), 177-184 (1969).

32. G. J. Bignold, Electrochemical Aspects of Stress Corrosion of Steels in Alkaline Solutions, Corrosion 28(8), 307-312 (1972).

33. H. W. Pickering and R. P. Frankenthal, On the Mechanism of Localized Corrosion of Iron and Stainless Steel, J. Electrochem. Soc. 119(10), 1297-1304 (1972).

34. G. Faita, F. Mazza, and G. Bianchi, Role of Water and Ionic Solvation in Localized Corrosion Phenomena, in Localized Corrosion, NACE, Houston (1974), pp. 34-44.

35. P. Doig and P. E. J. Flewitt, An Electrochemical Model for Intergranular Stress Corrosion Cracking in Iron-Nickel Alloys, in Mechanisms of Environment Sensitive Cracking of Materials, The Metals Society, London, (1977), pp. 113-124.

36. P. Doig and P. E. J. Flewitt, Limitations of Potentiostatic Control in Stress Corrosion Crack Growth Measurements, Met. Trans. 9A, 357-362 (1978).

37. R. Alkire and D. Siitari, The Location of Cathodic Reaction during Localized Corrosion, J. Electrochem. Soc. 126(1), 15-22 (1979).

38. A. Turnbull and J. G. N. Thomas, A Model of Crack Electrochemistry for Steels in the Active State Based on Mass Transport by Diffusion and Ion Migration, J. Electrochem. Soc. 129(7), 1412-1422 (1982).

39. M. E. Indig and A. R. McIlree, High-Temperature Electrochemical Studies of Stress Corrosion of Type 304 Stainless Steel, Corrosion 35(7), 288-295 (1979).

40. S. Szklarska-Smialowska and G. Cragnolino, Stress Corrosion Cracking of Sensitized Type 304 Stainless Steel in Oxygenated Pure Water at Elevated Temperatures (Review), Corrosion 36(12), 653-665 (1980).

41. P. E. Morris, Evaluation of the Effects of Heat Treatment on the Passive Behavior of Ni-Cr-Fe Alloys in High-Temperature Water, EPRI Report NP-1884 (June 1981).

42. D. M. Himmelblau, Solubilities of Inert Gases in Water, 0°C to Near the Critical Point of Water, J. Chem. and Engr. Data 5(1), 10-15 (1960).

43. F. H. Sweeton, R. E. Mesmer, and C. F. Baes, Jr., Acidity Measurements at Elevated Temperatures; VII Dissociation of Water, J. Solution Chem. 3(3), 191-214 (1974).

44. W. L. Marshall and E. V. Jones, Second Dissociation Constant of Sulfuric Acid from 25 to 350°C Evaluated from Solubilities of Calcium Sulfate in Sulfuric Acid Solutions, J. Phys. Chem. 70(12), 4028-4040 (1966).

45. M. T. Jones, Reactor Technology Report No. 14, KAPL 2000-11 (1960).

46. W. E. Ruther and S. Greenberg, Corrosion of Steels and Nickel Alloys in Superheated Steam, J. Electrochem. Soc. 111(10), 1116-1121 (1964).

47. C. Amzallag, P. Rabbe, C. Bathias, D. Benoit, and M. Truchon, "Influence of Various Parameters on the Determination of the Fatigue Crack Arrest Threshold," in Fatigue Crack Growth Measurement and Data Analysis, ASTM STP-738, S. J. Hudak, Jr. and R. J. Bucci, eds. (1981), pp. 29-44.

48. D. Weinstein, BWR Environmental Cracking Margins for Carbon Steel Piping, EPRI Final Report NP-2406 (May 1982).

49. W. A. Van Der Sluys, Corrosion Fatigue Characterization of Reactor Pressure Vessel Steels, EPRI Interim Report NP-2775 (December 1982).

50. D. H. Hale et al., The Growth and Stability of Stress Corrosion Cracks in Large-Diameter BWR Piping Volume 2: Appendixes, EPRI Final Report NP-2472 (July 1982).

51. J. Y. Park and W. J. Shack, Intergranular Crack Propagation Rates in Sensitized Type 304 Stainless Steel in an Oxygenated Water Environment, ANL-83-93 (December 1983).

II. TRANSIENT FUEL RESPONSE AND FISSION PRODUCT RELEASE

Principal Investigator:
J. Rest

A. Description of FASTGRASS-VFP Theory

FASTGRASS-VFP[1-3] is a mechanistic computer model for predicting the behavior of fission gas and volatile fission products (VFPs) in solid UO_2-based fuels during steady-state and transient conditions. The model accounts for the effects of a number of processes on both the distribution of fission products within the fuel and the amount released. These processes include fission product generation; gas bubble nucleation and re-solution; bubble migration and coalescence; interaction between I, Cs, CsI, and fission gas bubbles; chemical reaction between I, Cs, and fuel; channel formation on grain faces; interlinked porosity on grain edges; and microcracking. The present version of the theory models the fission gases Xe and Kr; the volatiles I and Cs; and the major VFP reaction products, CsI, Cs_2MoO_4, and Cs_2UO_4. Including the latter two reaction products can alter the Cs and CsI release predictions by up to 10%.[2] Fission products released from the fuel are assumed to reach the pellet surface by successively migrating from the grain interiors to grain faces and then to the grain edges, with subsequent transport through a network of interconnected tunnels and as-fabricated porosity.

The approach to modeling VFP chemistry in FASTGRASS-VFP is to assume that the kinetics of the relevant reactions occur fast enough for a quasi equilibrium to be maintained. The following reactions are considered to dominate I and Cs release characteristics:

$$C_s + I \longrightarrow CsI;\quad 2Cs + UO_2 + O_2 \longrightarrow Cs_2UO_4;\ \text{and}\ 2Cs + Mo + 2O_2 \longrightarrow Cs_2MoO_4.$$

The model for the VFP chemistry is based on the analysis of Tam et al., which employs the laws of mass balance and mass action[4]; the values used for partial pressure of oxygen are calculated from the model of Blackburn[5] for stoichiometric $UO_{2.0}$.

FASTGRASS-VFP has recently been used in the interpretation of fission gas, iodine, and cesium release from (1) irradiated high-burnup LWR fuel in a flowing steam atmosphere during high-temperature, in-cell heating tests performed at Oak Ridge National Laboratory (ORNL) and (2) trace-irradiated LWR fuel during severe-fuel-damage (SFD) tests performed in the PBF Reactor in Idaho. The results of the analyses demonstrate that intragranular fission product behavior during both types of tests can be interpreted in terms of a grain-growth/grain-boundary-sweeping mechanism that enhances the flow of fission products from within the grains to the grain boundaries. Basically, the model assumes that small intragranular bubbles (consisting, in general, of Xe, Kr, I, Cs, and CsI), and gaseous and VFP atoms in the path of a growing grain, are swept up by grain boundary adhesive forces. Such grain boundary sweeping provides another mechanism for the collection of fission products at grain faces and edges.

At temperatures of about 1900 K,[6] atomic mobilities in UO_2 result in an enhanced migration of atoms from the convex to the concave side of a curved boundary. The atoms move toward the concave side of the boundary because in that location, they are surrounded by a somewhat larger number of neighboring atoms and thereby exhibit a lower effective energy state. The net result of this atomic motion is shrinkage of small grains with predominantly convex surfaces and growth of larger grains with concave surfaces.

Speight and Greenwood[7] have proposed a grain growth theory which includes the sweeping of entrapped microbubbles by the front of an advancing grain boundary. The basic postulate of their theory is that small bubbles exert a minimal drag force on an advancing grain surface and thus are swept along with the moving boundary, while large bubbles detach from the advancing surface because of their higher drag. To assess the efficiency of bubble sweeping, they compared the magnitude of the force exerted by the bubble on the boundary, i.e.,

$$F_b = \pi R_b \sigma_{gb} \sin 2\phi \quad , \tag{2.1}$$

with the adhesive effects of the interfacial surface tensions, i.e.,

$$F_{gb} = \frac{2\sigma_{gb}}{R_c} \pi R_{gb}^2 \quad , \tag{2.2}$$

where R_b = bubble radius, R_c = radius of curvature of the grain, R_{gb} = characteristic distance of bubble spacing, σ_{gb} = grain boundary surface tension, and ϕ = angle of contact between the bubble and the boundary.

Because of the complex nature of the phenomena involved in experiments simulating severe accidents (oxidation, as well as liquefaction and/or melting, of the fuel; and oxidation and melting of the cladding), a simpler approach to describing grain-growth/grain-boundary-sweeping than that described above was initially incorporated into the FASTGRASS-VFP theory. Since atoms are removed from lattice positions in the crystal structure of the grain, the grain growth process is thermally activated, and varies according to an Arrhenius-type relation[6]:

$$D_t^2 = D_o^2 + A \exp(-Q/RT)t \quad , \tag{2.3}$$

where A = a proportionality constant (cm^2/s), D_t = grain size at time t (cm), D_o = initial grain size (cm), Q = activation energy (cal), R = gas constant (1.987 cal/mole K), T = temperature (K), and t = time (s).

Fuel stoichiometry can have a pronounced effect on atomic mobilities in UO_2 fuel and thus on grain growth kinetics. Data[8] on the diffusivity of ^{133}Xe in UO_{2+x} as a function of fuel stoichiometric condition show that increased levels of oxygen in solution in UO_2 lead to observed increases in the diffusivity of ^{133}Xe and ^{85}Kr. For example, a change from $UO_{2.0}$ to $UO_{2.12}$ can increase the diffusivity of ^{133}Xe by more than two orders of magnitude. Thus, the stoichiometry of the oxide can have a significant impact on atomic mobility and grain growth characteristics. Indeed, for the highly oxidizing environment of fuel exposed to steam flow at elevated temperatures, UO_2 can be expected to become hyperstoichiometric during the course of a severe-core-damage accident.

To account for such oxidation effects, two grain-growth models are employed in the present version of FASTGRASS-VFP.

Stoichiometric $UO_{2.00}$ (Nominal Grain Growth):

$$\frac{dD_t}{dt} = k/D_t \tag{2.4}$$

where $k = 1.46 \times 10^{-4} \exp(-32100/T)$, cm^2/s.

Hyperstoichiometric UO_{2+x} (Enhanced Grain Growth):

$$\frac{dD_t}{dt} = k/D_t \tag{2.5}$$

where $k = 3.5 \times 10^{-5} \exp(-22150/T)$, cm^2/s.

The grain growth laws shown in Eqs. 2.4 and 2.5 have been expressed in differential form rather than the integral form of Eq. 2.3. The grain growth law for stoichiometric fuel is based upon the findings of Malen et al.[9] For hyperstoichiometric (oxidized) fuel, the activation energy is decreased proportionately to the difference in activation energy between UO_2 and UO_{2+x} reported by Turnbull.[10] The preexponential factor in Eq. 2.5 was determined by the requirement that the integrated intragranular fission gas release as calculated by FASTGRASS-VFP must be consistent with measured total (end-of-test) release values for SFD-ST. Equation 2.4 is assumed to be operative at all temperatures, whereas Eq. 2.5 is invoked, when appropriate, for temperatures exceeding 1900 K.

As the boundary moves, the rate $\frac{dC_{gb}}{dt}$ at which fission products are swept up by the moving boundary is proportional to the rate of change of the volume of the grain; i.e., from Eqs. 2.4 and 2.5,

$$\frac{dC_{gb}}{dt} = \frac{\pi e C_I D_t^2}{2} \frac{dD_t}{dt} = \frac{\pi e k C_I D_t}{2\Delta t}, \tag{2.6}$$

where C_I is the intragranular concentration of the fission product, Δt is the time increment over which k can be assumed to remain approximately constant, and e is a factor that describes the grain boundary sweeping efficiency. The factor e includes the effects of bubble pulloff, as described by Eqs. 2.1 and 2.2, and atomic vibrational and minimum energy effects. The value of e is assumed to be unity for the fission gases, I, and CsI (in bubbles), and 0.6

for atomic Cs. The lower value of e for Cs is consistent with the high chemical affinity of Cs for UO_2, other fission products, and metallic inclusions. Equation 2.6 is one term in the overall equation for dC_I/dt (e.g., see Ref. 3).

B. Fission Product Behavior in High-Burnup Fuel During ORNL In-Cell Heating Tests

Figures 2.1 and 2.2 show FASTGRASS-VFP predictions of fission gas and Cs release for ORNL tests HI-1 and HI-3[11] and compare them with the corresponding measured quantities. Tests HI-1 and HI-3 were conducted for 30 min at 1673 K and 20 min at 2273 ± 50 K, respectively, within a flowing steam environment. The fuel specimens were 20-cm-long sections of H. B. Robinson fuel rod irradiated to 28,000 MWd/MTU. In order to assess correctly the state of the fuel prior to the test, a thermally and mechanically coupled model consisting of FASTGRASS-VFP and the LIFE-LWR fuel behavior code was used for the in-reactor irradiation period.[3] The total gas released during the irradiation was about 0.2%.

The stoichiometric grain growth law (Eq. 2.4) was used for both test simulations: This resulted in predictions of no grain growth for HI-1 and a 26-45% increase in grain size for HI-3. These grain growth predictions are consistent with microscopic observations. Figure 2.3 shows scanning electron micrographs of H. B. Robinson fuel specimens before and after test HI-3; the grain size before transient heating was approximately 4.2 μm, whereas post-test examination indicates an ~50% increase in grain size. More detailed microscopic results are presented in Ref. 12.

Very little fission gas and Cs release occurred during HI-1 (Fig. 2.1). Two curves for predicted Cs release are shown in Fig. 2.1b; these correspond to two different values of Cs diffusivity. The relatively high release predictions were based on the Cs diffusivities reported by Matzke[13], while the low release predictions were based on the assumption that the diffusivities are the same for Cs as for Xe (D_{Xe} is based on the data of Cornell[14]). The Cs diffusivities used in earlier studies[1,2] (based on the work of Oi and Takagi, as discussed in Refs. 1 and 2) result in Cs release predictions for

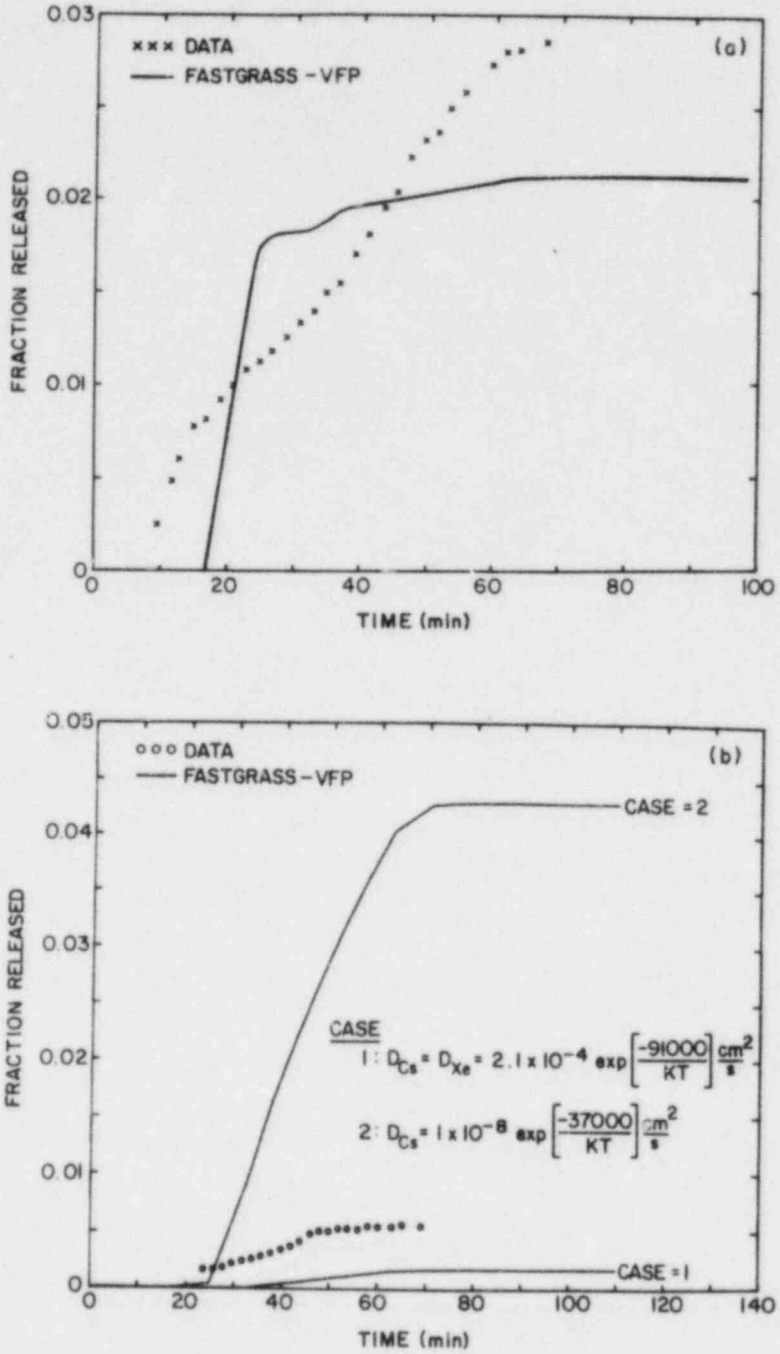

Fig. 2.1. FASTGRASS-VFP Predictions of (a) Fission Gas and (b) Cesium Release During ORNL Test HI-1, Compared with Measured Values. In (b), predictions are given for two values of the cesium diffusion coefficient.

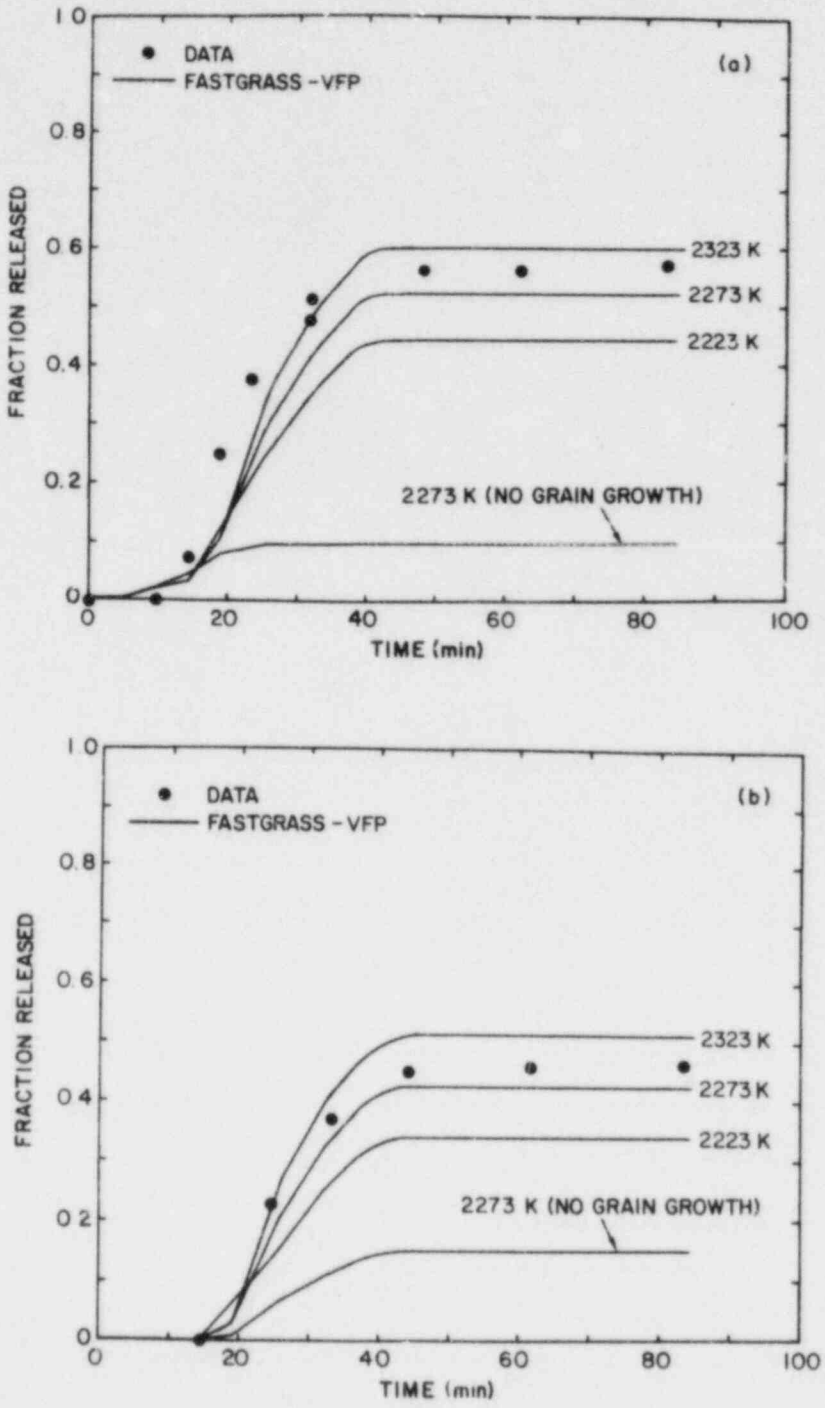

Fig. 2.2. FASTGRASS-VFP Predictions of (a) Fission Gas and (b) Cesium Release During ORNL Test HI-3, Compared with Measured Values.

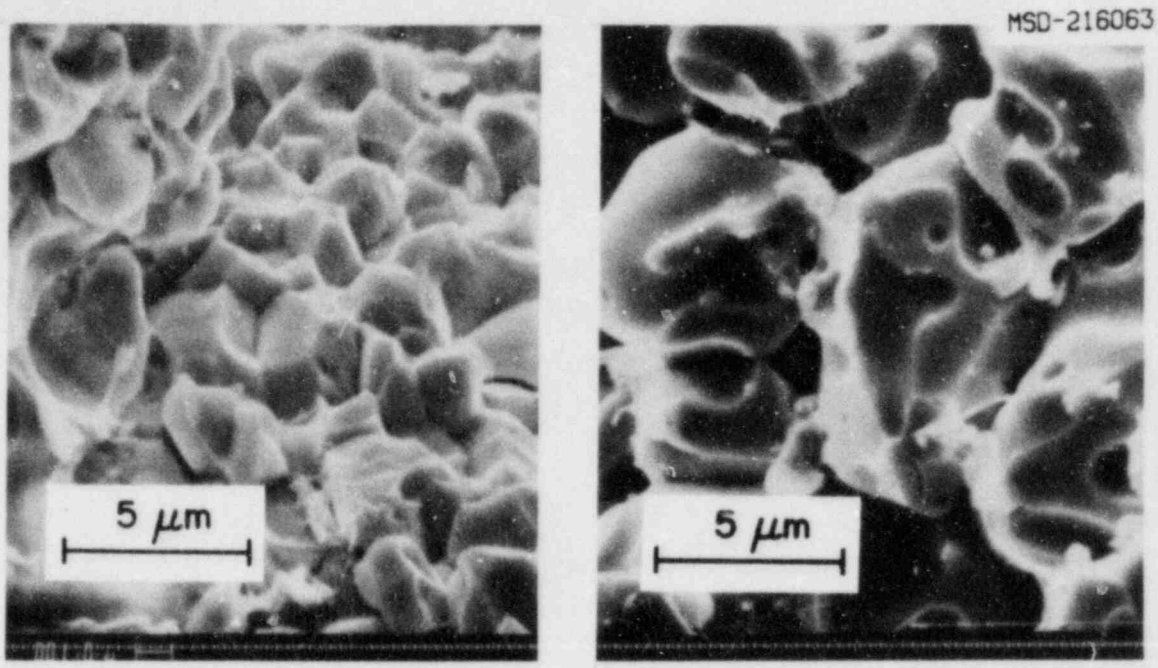

Untested; 5000X

5000X

Fig. 2.3. Scanning Electron Micrographs of H. B. Robinson Fuel (left) Before and (right) After ORNL Test HI-3.

test HI-1 which are a factor of ~3 larger than those obtained with the diffusivities reported by Matzke. As the effects of chemical trapping are included in the FASTGRASS-VFP calculations (i.e., CsI, Cs_2MoO_4, and Cs_2UO_4 reaction products), and as the relatively low HI-1 test temperatures preclude any appreciable grain growth, the predicted D_{Cs} dependence of fission product release during the test should be physically realistic. The results shown in Fig. 2.1b suggest that equating D_{Cs} with D_{Xe} is the most reasonable assumption. Consequently, this value of D_{Cs} is used in all subsequent calculations.

In order to reflect the reported experimental uncertainty in temperature for test HI-3, each part of Fig. 2.2 includes three predicted curves, which correspond to test temperatures of 2273 ± 50 K. Also shown in Fig. 2.2 are the predictions of the theory in the absence of grain growth. On the basis of the good agreement between theory and data for fission gas and Cs release when a grain-growth/grain-boundary-sweeping mechanism is operative (Fig. 2.2), and the agreement between predicted and observed end-of-test grain size, it is concluded that grain boundary sweeping of fission products is a key mechanism

for moving fission products from within the grains to the grain boundaries under HI-3 test conditions.

This position is further supported by the agreement between the FASTGRASS-VFP results for fission gas and Cs release and the data for test HI-4[11] shown in Fig. 2.4. The fuel specimen for test HI-4 consisted of a 20.3-cm-long fuel segment from a rod which had been irradiated in the Peach Bottom-2 reactor to about 10,100 MWd/MTU. Again, FASTGRASS-VFP/LIFE-LWR was used to simulate the irradiation period prior to the transient test. About 9% fission gas release occurred from this rod during the irradiation. Test HI-4 consisted of 20 min at a temperature of 2073 ± 50 K in a flowing steam-helium atmosphere. With the stoichiometric grain growth law (Eq. 2.4), and assuming an initial grain size of 6 μm, the theory predicts an ~10% increase in grain size. Again, this grain growth prediction is consistent with microscopic observations.[12]

It should be noted that whereas partial oxidation of the cladding was observed after tests HI-3 and HI-4 , no visual evidence of appreciable fuel oxidation was detected.[12] This result is consistent with the use of the stoichiometric grain growth law within FASTGRASS-VFP for HI-1, HI-3, and HI-4 test conditions.

Figure 2.5 shows FASTGRASS-VFP predictions of fission gas and Cs release for test HI-2.[11] The HI-2 test specimen was similar to those used in tests HI-I and HI-3. Test HI-2 was conducted for 20 min at about 1973 K in flowing steam. Metallographic examination[11,12] of the tested fuel specimen revealed extensive fractures in the cladding, essentially complete oxidation to ZrO_2, and evidence of fuel-cladding interaction. Thus, it seems likely that fuel oxidation did occur during test HI-2, in contrast to tests HI-1, HI-3, and HI-4. Each part of Fig 2.5 shows predicted curves obtained with both the stoichiometric ("nominal", grain growth law of Eq. 2.4 and the hyperstoichiometric ("enhanced") grain growth law of Eq. 2.5. Although FASTGRASS-VFP tends to overpredict fission gas and Cs release when the hyperstoichiometric grain growth law is invoked, the agreement is better than that obtained with

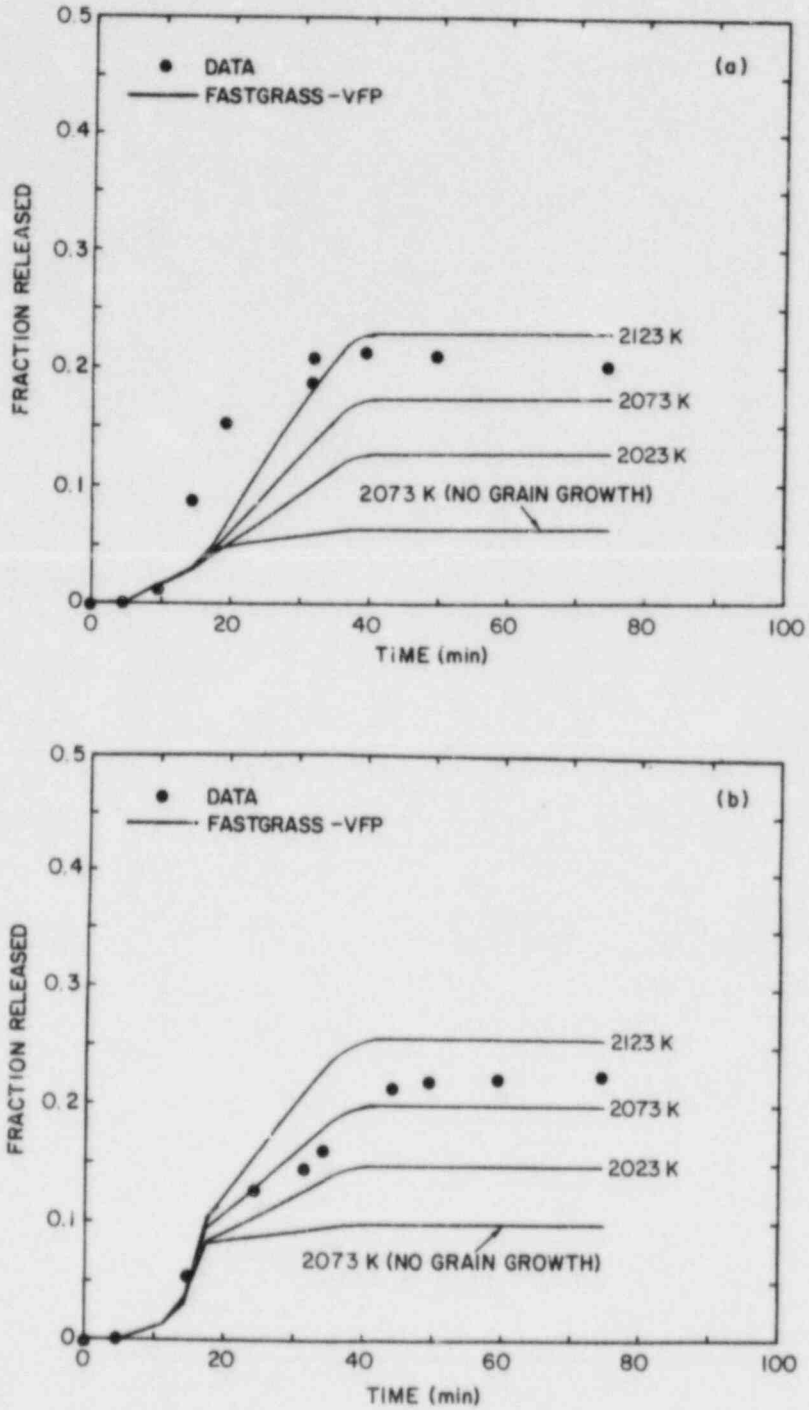

Fig. 2.4. FASTGRASS-VFP Predictions of (a) Fission Gas and (b) Cesium Release During ORNL Test HI-4, Compared with the Measured Values.

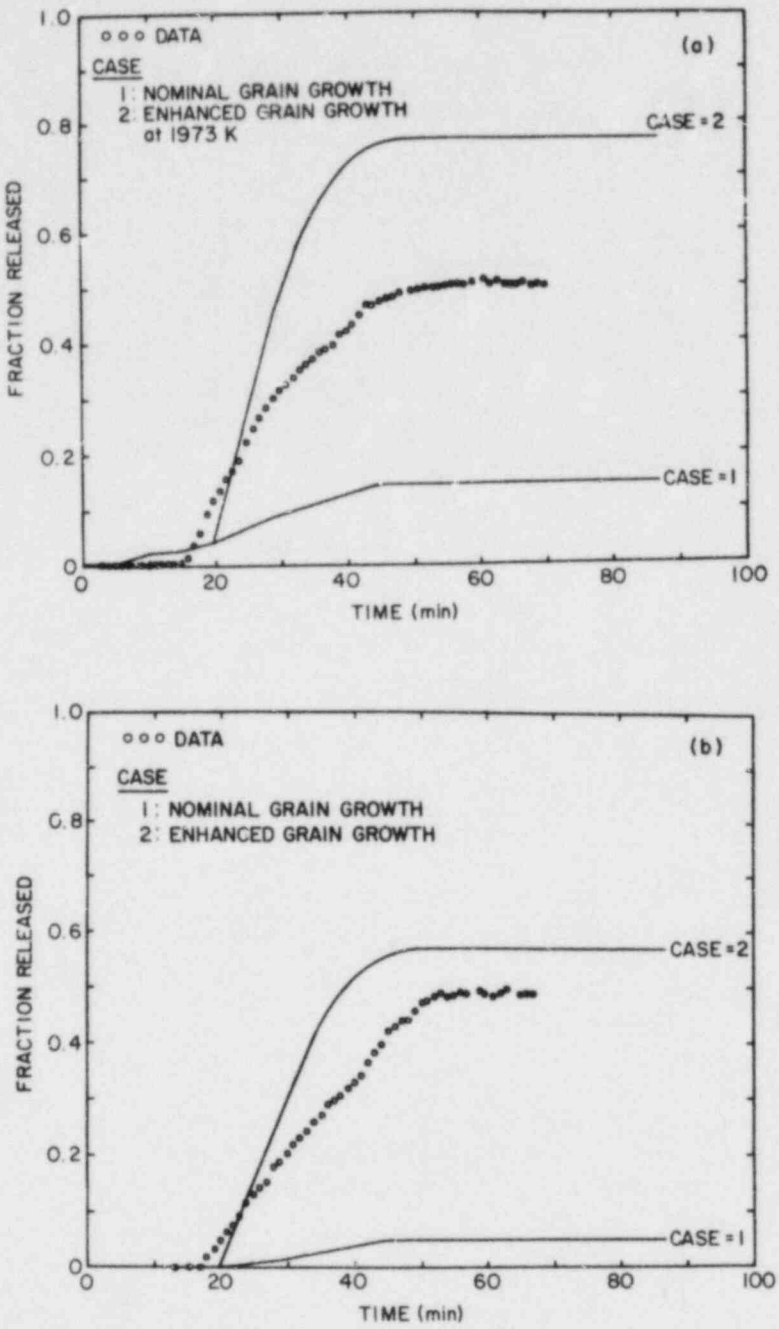

Fig. 2.5. FASTGRASS-VFP Predictions of (a) Fission Gas and (b) Cesium Release During ORNL Test HI-2, Compared with the Measured Values.

the stoichiometric law. Thus, both the experimental results available to date and the FASTGRASS-VFP analysis (Fig. 2.5) indicate that the UO_2 diffusivities were enhanced to some extent during test HI-2 owing to UO_2 oxidation to UO_{2+x}.

C. Fission Product Behavior in Trace-irradiated Fuel During SFD Tests in the PBF Reactor

The SFD-ST experiment[15] consisted of a 32-rod bundle of PWR-type fuel rods, 0.91 m long and enclosed in an insulated shroud. The bundle was subjected to a slow heatup (~2 h) in an oxygen-rich environment to about 1400 K in the lower part of the fuel bundle and about 1800 K in the upper portion of the bundle and then rapid heatup (~10 min) to 2400 K, followed by a rapid quench and coolant reflood. Considerable cladding oxidation and melting, fuel liquefaction, and fuel fragmentation occurred. The SFD 1-1 test[15] also consisted of a 32-rod bundle, but the temperature transient consisted of a rapid heatup (~30 min) in a steam-starved environment to 2400 K followed by a slow cooldown (~20 min) without a rapid quench. The effective burnup levels for SFD-ST and SFD 1-1 are 88.9 and 79.1 MWd/MTU, respectively.

In Fig. 2.6, the measured fission gas release rates for SFD-ST are compared with the release rates predicted by FASTGRASS-VFP on the basis of both the stoichiometric (nominal) and hyperstoichiometric (enhanced) grain growth correlations. The enhanced grain growth law, which is assumed to be activated at fuel temperatures $\geq$1900 K, gives rise to a release rate curve that simulates the ST data quite well, whereas the nominal correlation gives release rates that are approximately an order of magnitude below the data at fuel temperatures >1900 K. Such differences in predicted release characteristics due to grain-growth/grain-boundary-sweeping effects are further illustrated in Fig. 2.7, which shows intragranular fission gas retention during SFD-ST as predicted by FASTGRASS-VFP. If nominal grain growth occurs, the majority of the fission gas is predicted to remain entrapped within the grain interior, with a total fractional retention of greater than 80% even as fuel temperatures approach 2400 K. However, if the grain growth is enhanced owing to fuel oxidation, a much larger fraction of the intragranular gas is swept to grain boundaries, with only 20% retention within grains at fuel temperatures of ~2400 K. Such predictions clearly illustrate the important influence of

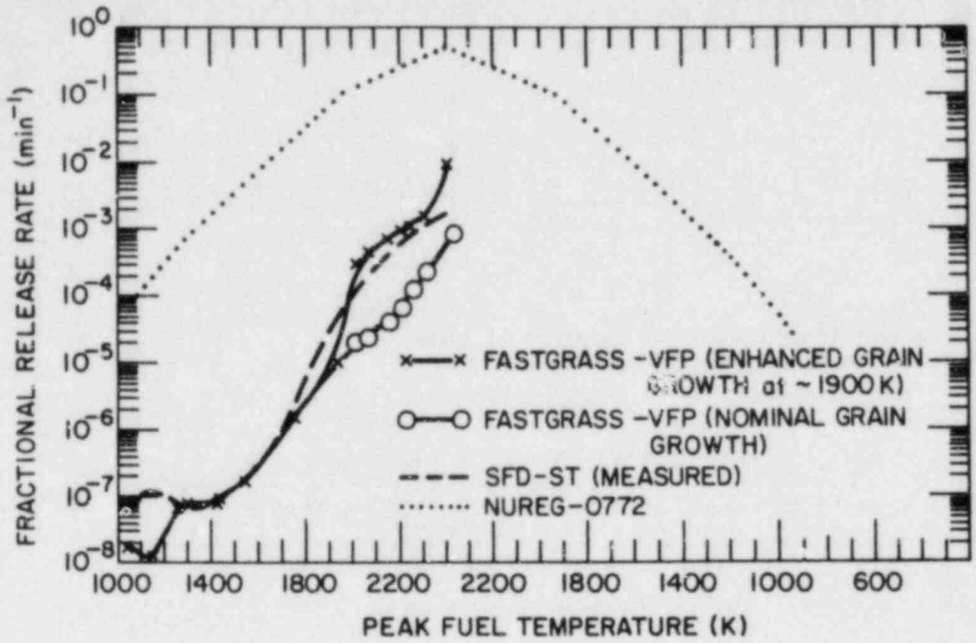

Fig. 2.6. FASTGRASS-VFP Predictions of Fission Gas Release Rates for the SFD-ST Experiment, Compared with the Measured Values and Those Obtained from NUREG-0772.

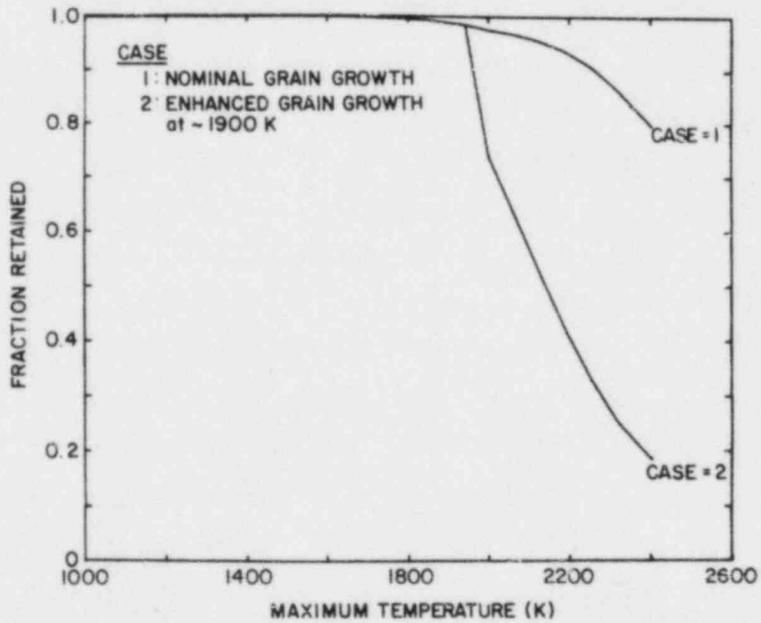

Fig. 2.7. FASTGRASS-VFP Predictions of Fission Gas Retained Intragranularly at the Hottest Node During the SFD-ST Experiment, Just Prior to Quench.

the grain-growth/sweeping process on the morphology and attendant release behavior of gaseous and volatile fission products. Since the steam flow conditions of the SFD-ST scoping test produced an oxidizing environment, the enhanced grain growth law appears appropriate for this analysis. The analysis is also consistent with the fuel-oxidation-enhanced grain growth noted in the PBF-SFD scoping test,[15] where both U_4O_9 precipitates and a substantial increase in grain size were noted upon post-test fuel examination.

In Table 2.1, FASTGRASS-VFP predictions for fission product release during SFD-ST are compared with the measured values. The calculations shown in Table 2.1 were made by assuming that the requench provided the appropriate mechanisms (e.g., fuel fracturing) for the release of the majority of the fission products predicted to be on the grain boundaries. (FASTGRASS-VFP does not currently contain a model for requench-induced processes, e.g., grain boundary fracturing.)

TABLE 2.1. FASTGRASS-VFP Predictions of Fission Product Release During the SFD-ST Test, Compared with the Measured Values

Fission Product	Fraction Released	
	FASTGRASS-VFP Calculation	Collection Tank Measurement
Xe	0.47	~0.50
Cs	0.34	~0.32
I	0.47	~0.49

The agreement between the theory and the data shown in Table 2.1 is very good. The theory predicts that in the absence of a requench (and fuel liquefaction), very little fission product release would have occurred during SFD-ST. The reason for this result is that owing to the low concentrations of fission gas in this trace-irradiated, low-burnup fuel, very little interconnection of fission gas bubbles is predicted to occur on the grain faces and along the grain edges. This is in contrast to the ORNL transient tests on

high-burnup fuel described earlier. The relatively high concentration of fission gas in the high-burnup fuel enables a high degree of bubble interconnection to occur, with subsequent venting of the retained fission products.

In Fig. 2.8, the measured fission gas release rates for the SFD 1-1 test are compared with the release rates predicted by FASTGRASS-VFP for two values of the maximum fuel temperature. The FASTGRASS-VFP predictions are based on the stoichiometric (nominal) grain growth law for fuel temperatures <1900 K and the hyperstoichiometric (enhanced) grain growth correlation for temperatures ≥1900 K. The predicted release rates are seen to increase dramatically upon the initiation of grain-growth-induced sweeping of entrapped intragranular bubbles to grain boundaries. Without such grain-growth-induced sweeping, little gas release is predicted for such low-burnup fuel. It is of particular interest to note that the hyperstoichiometric grain growth law for equiaxed grain growth simulates the test data rather well. Such calculations clearly illustrate the point that for low-burnup fuel, the majority of the fission products remain trapped within the grain interior until elevated temperatures cause sweeping of fission products to grain surfaces and open pores.

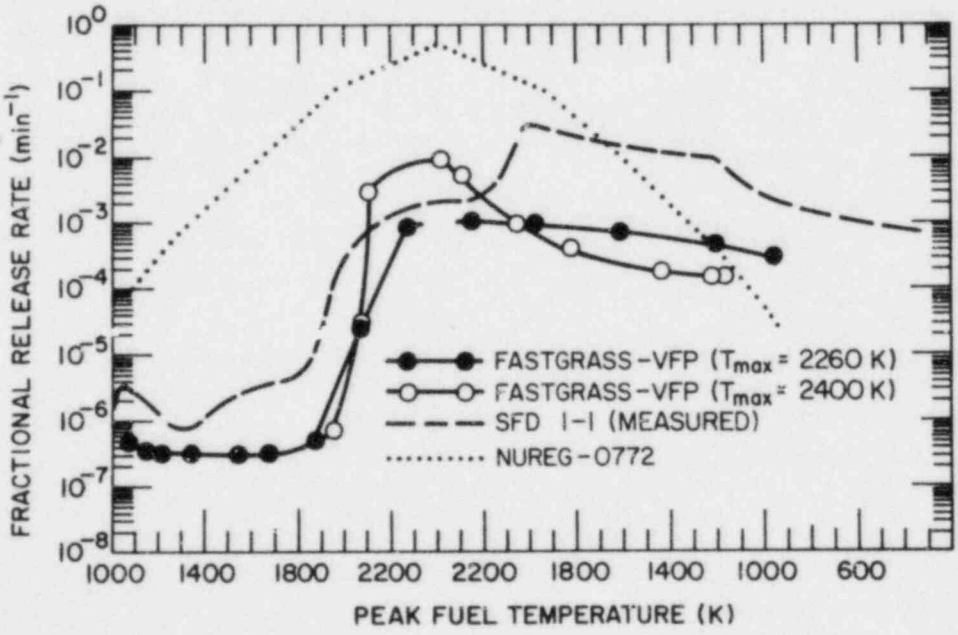

Fig. 2.8. FASTGRASS-VFP Predictions of Fission Gas Release Rates for the SFD 1-1 Experiment, Compared with the Measured Values and Those Obtained from NUREG-0772.

Although the initial release characteristics are modeled fairly well by FASTGRASS-VFP, the total fractional release for the SFD 1-1 test is underpredicted by an order of magnitude (i.e., 2% total predicted release versus ≈20% measured release for the test). This is attributed to the fact that during grain growth, the fission gases are predicted to be swept to grain boundaries, where the majority of such gas is trapped. Owing to the absence of quench-induced grain separation in the SFD 1-1 test, and the fact that FASTGRASS-VFP does not currently model the gas release that accompanies fuel liquefaction[16], the model predicts gas accumulation at grain surfaces. In actuality the following morphology sequence, leading to fission product release for the SFD 1-1 test, appears probable: (1) initial high gas retention within individual grains due to entrapment of gaseous fission products as individual atoms or intragranular microbubbles, with negligible gas release; (2) grain-growth-induced intragranular microbubble sweeping to grain boundaries at temperatures above ~1900 K, with gas accumulation at grain boundaries and initiation of slow gas release; and (3) destruction of the grain boundary structure by fuel liquefaction (not currently modeled in FASTGRASS-VFP), with attendant rapid gas release.

This suggested sequence of events is supported by the FASTGRASS-VFP prediction of retained intragranular gas at the hottest fuel node in test SFD 1-1 (T_{max} = 2260 K) in the absence of fuel liquefaction, shown in Fig. 2.9. Again, the predictions are based on the stoichiometric (nominal) grain growth law for temperatures <1900 K and the hyperstoichiometric (enhanced) grain growth law for temperatures ≥1900 K. For the situation of fuel-oxidation-enhanced grain growth, a large fraction of the intragranular gas is swept to grain boundaries, with only ~25% retention within grains at fuel temperatures of ~2200 K.

Figures 2.6 and 2.8 also shown fission gas release rates as a function of fuel temperature for the SFD-ST and SFD 1-1 tests, respectively, as calculated from the temperature correlations given in NUREG-0772.[17] As indicated earlier, the FASTGRASS-VFP-predicted and measured release rates agree quite well; however, these rates are about 4 orders of magnitude lower than the predicted rates based upon the NUREG-0772 temperature correlations. This

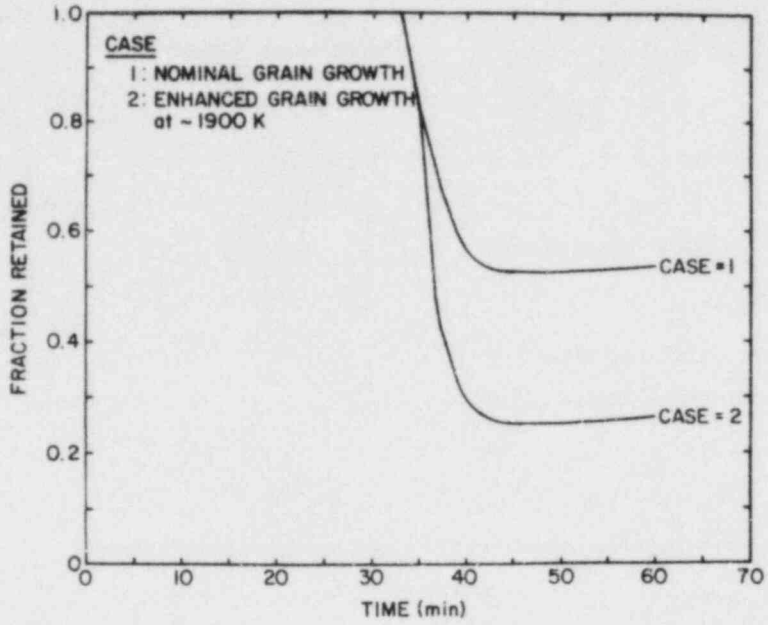

Fig. 2.9. FASTGRASS-VFP Predictions of Fission Gas Retained Intragranularly at the Hottest Node During the SFD 1-1 Experiment, in the Absence of Fuel Liquefaction.

discrepancy is due, in part, to the fission product morphology characteristics of the trace-irradiated fuel employed in the SFD-ST and SFD 1-1 tests. The NUREG-0772 correlations were developed primarily from release experience for medium- to high-burnup fuel under relatively isothermal test conditions; in contrast, the SFD-ST and SFD 1-1 tests were non-isothermal, and the fuel used in these tests was essentially fresh (except for the development of a small inventory of fission products at an effective burnup level of approximately 0.0089 atom-percent). FASTGRASS-VFP analyses indicate that for trace-irradiated fuel, the vast majority of both fission gases and volatiles (I and Cs) are still retained within the interior of individual grains either as individual atoms or as newly nucleated intragranular microbubbles. FASTGRASS-VFP calculations indicate that such morphology will exist until grain growth causes the sweeping of intragranular microbubbles to grain boundaries. Since grain growth normally requires fuel temperatures in excess of 1900 K, significant release during the heatup phase of these PBF/SFD tests is precluded. Only when temperatures above 1900 K cause destruction of the grain boundary structure (by eutectic fuel melting and/or quench induced processes such as grain boundary fracturing) is significant release predicted for such low-burnup fuel.

D. Conclusions

The results of the FASTGRASS-VFP analysis indicate that for the SFD-ST and SFD 1-1 tests, the sequence of events leading to fission product release appears to be as follows: (1) initial high fission product retention within individual grains due to entrapment of fission products as individual atoms or intragranular microbubbles, with negligible release; (2) grain-growth-induced intragranular atomic and microbubble sweeping to grain boundaries at temperatures in excess of 1900 K, with attendant bubble growth and gas accumulation at the grain boundaries and initiation of slow gas and VFP release; (3) destruction of the grain boundary structure via fuel liquefaction and/or quench-induced processes (e.g., grain-boundary fracturing), with attendant rapid intergranular gas release.

FASTGRASS-VFP theory correctly predicts the fission product behavior of high-burnup fuel during the ORNL high-temperature heating tests. The results of the analysis indicate that a grain-growth/grain-boundary-sweeping mechanism is responsible for the relatively large intragranular fission product release predicted to occur during the majority of these tests. FASTGRASS-VFP-predicted grain sizes for tests HI-1, HI-3, and HI-4 are in reasonable agreement with grain growth observations made on the tested fuel. The measured grain growth for the high-burnup fuel used in these ORNL high-temperature heating tests is substantially less than the observed grain growth for the PBF tests on trace-irradiated fuel. This result is consistent with the predictions of the Speight-Greenwood theory for grain-growth/grain-boundary-sweeping in that the accumulation of fission products on the grain boundaries of high-burnup fuel retards grain boundary movement. (The Speight-Greenwood theory has been incorporated into the FASTGRASS-VFP Theory. Results of this combined theory will be presented elsewhere.)

The results of FASTGRASS-VFP analyses indicate the inappropriateness of extrapolating the NUREG-0772 correlations, which are based primarily upon medium- to high-burnup data, to determine release characteristics for the trace-irradiated fuel employed in the PBF tests. This is because at extremely low burnup, there does not exist a sufficient inventory of fission gases to precipitate the development of a network of interconnected porosity necessary

for gas release from the fuel interior to the pellet surface. Only upon initiation of enhanced grain growth at elevated temperatures (≥1900 K), and destruction of the grain boundary structure by liquefaction and/or quench-induced processes, would significant release be expected for these low-burnup conditions.

E. References for Chapter II

1. J. Rest, "Volatile Fission-Product Source Term Evaluation Using the FASTGRASS Computer Code," in Proc. Int. Mtg. on Thermal Nuclear Reactor Safety, Chicago, IL, August 29-September 2, 1982, NUREG/CP-0027, Vol. 1 (February 1983), pp. 111-121.

2. J. Rest, Evaluation of Volatile and Gaseous Fission Product Behavior in Water Reactor Fuel Under Normal and Severe Core Accident Conditions, Nucl. Technol. 61(1), 33-48 (April 1983).

3. J. Rest, An Improved Model for Fission Product Behavior in Nuclear Fuel Under Normal and Accident Conditions, J. Nucl. Mater., in press, 1984.

4. S. W. Tam, P. E. Blackburn, and C. E. Johnson, "Effect of Core Chemistry on Fission Product Release," Proc. Int. Mtg. on Thermal Nuclear Reactor Safety, Chicago, IL, August 29-September 2, 1982, NUREG/CP-0027, Vol. 1 (February 1983), pp. 101-110.

5. P. E. Blackburn, Fuels and Materials Chemistry Annual Report, 1975, Argonne National Laboratory Report ANL-75-48, pp. 14-15.

6. D. R. Olander, Fundamental Aspects of Nuclear Reactor Fuel Elements, U. S. Energy Research and Development Administration, Washington, DC (1976).

7. M. V. Speight and G. W. Greenwood, Grain Boundary Mobility and Its Effects in Materials Containing Inert Gases, Philos. Mag. 9, 683 (1964).

8. J. Belle, Uranium Dioxide, U. S. Government Printing Office, Washington, DC (1961), pp. 512-515.

9. K. Malen, "Migration of ^{131}I in Fuel Rods with Burnups of 5-30 MWd/kg U Reirradiated at Powers of 40-60 kW/m for up to 5 Days," Proc. Specialists' Meeting on Internal Fuel Rod Chemistry, IWGFPT/3, International Atomic Energy Agency, Vienna (1979), p. 57.

10. J. A. Turnbull, A Review of Rare Gas Diffusion in Uranium Dioxide, unpublished work, 1972.

11. M. F. Osborne et al., "Fission Product Release from Irradiated Fuel Under Accident Conditions," paper to be presented at the Topical Mtg. on Fission Product Behavior and Source Term Research, Snowbird, Utah, July 15-19, 1984.

12. R. V. Strain, "Fission Product Release From Irradiated LWR Fuel Under Accident Conditions," paper to be presented at the Topical Mtg. on Fission Product Behavior and Source Term Research, Snowbird, Utah, July 15-19, 1984.

13. Hj. Matzke, The Release of Some Non-Gaseous Fission Products from CaF_2, UO_2, and ThO_2, J. Nucl. Mater. 25, 209-221 (1967).

14. R. M. Cornell, The Growth of Gas Bubbles in Irradiated Uranium Dioxide, Philos. Mag. 19, 539 (1969).

15. D. J. Osetek, R. R. Hobbins, K. Vinjamuri, and A. W. Cronenberg, "Fission Product Behavior During the First Two PBF Severe Fuel Damage Tests," paper to be presented at the Topical Mtg. on Fission Product Behavior and Source Term Research, Snowbird, Utah, July 15-19, 1984.

16. A. W. Cronenberg et al., "An Assessment of Liquefaction Induced I, Cs, and Te Release from Low and High Burnup Fuel," Proc. Int. Mtg. on Light Water Reactor Severe Accident Evaluation, Cambridge, MA, August 28-September 1, 1983, American Nuclear Society, La Grange Park, IL (1983), Vol. I, pp. 4.5-1 to 4.5-8.

17. U. S. Nuclear Regulatory Commission, Technical Basis for Estimating Fission Product Behavior During LWR Accidents, NUREG-0772 (June 1981).

III. CLAD PROPERTIES FOR CODE VERIFICATION

Principal Investigators:
H. M. Chung, F. L. Yaggee, and T. F. Kassner

The Zircaloy cladding of fuel rods in light-water-cooled reactors is susceptible to local breach-type failures, commonly known as pellet-cladding interaction (PCI) failures, during power transients after the fuel has achieved sufficiently high burnup. As a result of the high burnup, the gap between the UO_2 fuel pellets and the cladding is closed and highly localized stress is believed to be imposed on the cladding by differential thermal expansion of the cracked fuel and cladding during power transients. In addition to the localized stress, a high-burnup fuel cladding is also characterized by high-density radiation-induced defects (RID), mechanical constraints imposed by pellet-cladding friction, compositional changes (e.g., oxygen and hydrogen uptake associated with in-service corrosion), and geometrical changes due to creep-down and bowing. It is possible that synergistic effects involving more than one of the above factors influence the deformation and fracture of the in-reactor fuel cladding, e.g., strain aging associated with impurity or alloying elements, irradiation- or stress-induced segregation of the elements and subsequent formation of nonequilibrium phases. Although mechanisms of stress-corrosion-cracking (SCC) associated with volatile fission products such as I and liquid-metal-embrittlement (LME) associated with an element such as Cd have been well established for local breach-type failures of irradiated and unirradiated Zircaloy cladding under out-of-reactor simulation conditions, conclusive evidence of these processes is not yet available for in-reactor PCI failures. Consequently, to provide a better understanding of the PCI phenomenon, we have undertaken a mechanistic study of the deformation and fracture behavior of actual power-reactor fuel cladding discharged after a high burnup.

In this program, the effect of temperature, strain rate, and stress localization on the deformation and fracture characteristics of Zircaloy cladding from spent-fuel rods is being investigated by means of internal gas-pressurization and mandrel-loading experiments in the absence of simulated fission product species. The deformed and fractured specimens of spent-fuel

cladding are then being examined by optical microscopy, scanning electron microscopy (SEM), transmission electron microscopy (TEM), and high voltage electron microscopy (HVEM). The results of microstructural and fracture-property investigations will be used to develop a failure criterion for the cladding under PCI-type loading conditions. The information will be incorporated into fuel performance codes, which can be used to evaluate the susceptibility of extended-burnup fuel elements in commercial reactors to PCI failures during power transients in later cycles, and to evaluate cladding performance and reliability in new fuel-element designs. An optimization of power ramp procedures to minimize cladding failures would result in a significant decrease in radiation exposure of plant personnel due to background and airborne radioactivity as well as an extension of core life in terms of allowable off-gas radioactivity.

A. SEM Examination of H. B. Robinson Cladding after Fracture by Expanding-Mandrel Loading (H. M. Chung)

1. Introduction

Preliminary test results of H. B. Robinson spent-fuel cladding by expanding-mandrel loading at 292 and 325°C have been reported previously.[1,2] Brittle-type failure was not observed in specimens fractured at 292°C. However, from examinations of four specimens fractured at 325°C, three specimens revealed the brittle-type pseudocleavage feature in the fracture surfaces. One specimen failed in a ductile manner. The results of the fracture surface examinations are summarized in Table 3.1.

2. Ductile Failure

Results of the SEM examination of the 217A2E cladding specimen after fracture at 292°C have been reported previously.[1] The fracture surface showed a ductile fracture morphology. A similar ductile failure was observed for specimen 217B2D, which fractured after 237.8 h under expanding-mandrel loading at 325°C. Crack morphologies near the inner and outer surfaces of the specimen are shown in Figs. 3.1 and 3.2, respectively. An indentation produced by

TABLE 3.1. Summary of Fracture Surface Morphologies Produced in H. B. Robinson Spent-Fuel Cladding[a] by Expanding-Mandrel Loading

Specimen Number	Test Temp., °C	Time at Transient Loading, h	Strain Rate During Transient Loading, s^{-1}	Maximum Mandrel Load, kg	Time under Creep Mode at Max. Load, h	Total Time to Failure, h	Diametral Plastic Strain at OD, %	Failure Mode
217A2C	292	17.1	5×10^{-7}	505	0	-	1.2	Not failed
217A2D	292	5.0	5×10^{-6}	740	0	-	2.4	Not failed
217A2E	292	0.3	5×10^{-5}	772	0	0.3	3.3	Ductile, rupture
217A2F	292	28	5×10^{-7}	775	0	-	1.3	Not failed
217A4C	325	25.5	5×10^{-7}	459	36.0	68.1	4.7	Brittle, pinhole, pseudocleavage
217A4E	325	44.1	2×10^{-7}	845	189.7	223.8	6.0	Brittle, pinhole, pseudocleavage
217A4F	325	-	1×10^{-7}	740	-	91.5	4.7	Brittle, pinhole, pseudocleavage
217B2D	325	-	7×10^{-8}	1016	-	237.8	6.0	Ductile

[a]Fuel burnup 27.7 MWd/kg U, cladding fluence (E > 0.1 MeV) 4.4×10^{21} n/cm^2.

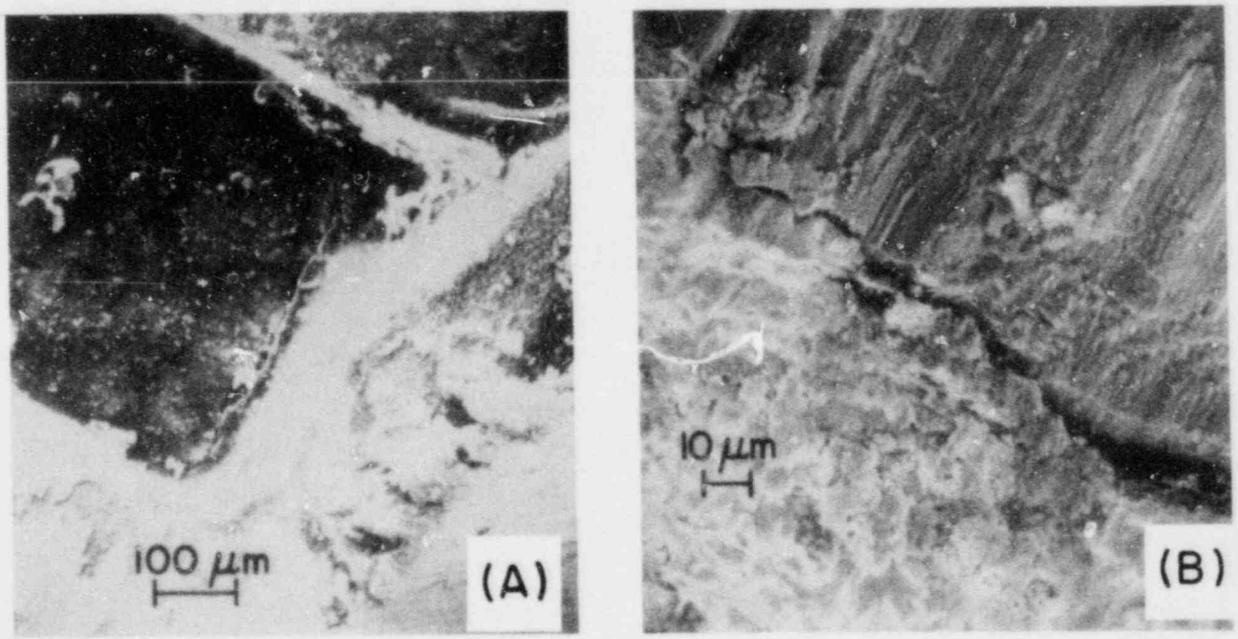

Fig. 3.1. Crack Morphologies of the Inner Surface of Specimen 217B2D after Fracture at 325°C under Expanding-Mandrel Loading. (A) Crack parallel to axial direction located at the edge of the expanding ring; (B) higher magnification of the crack.

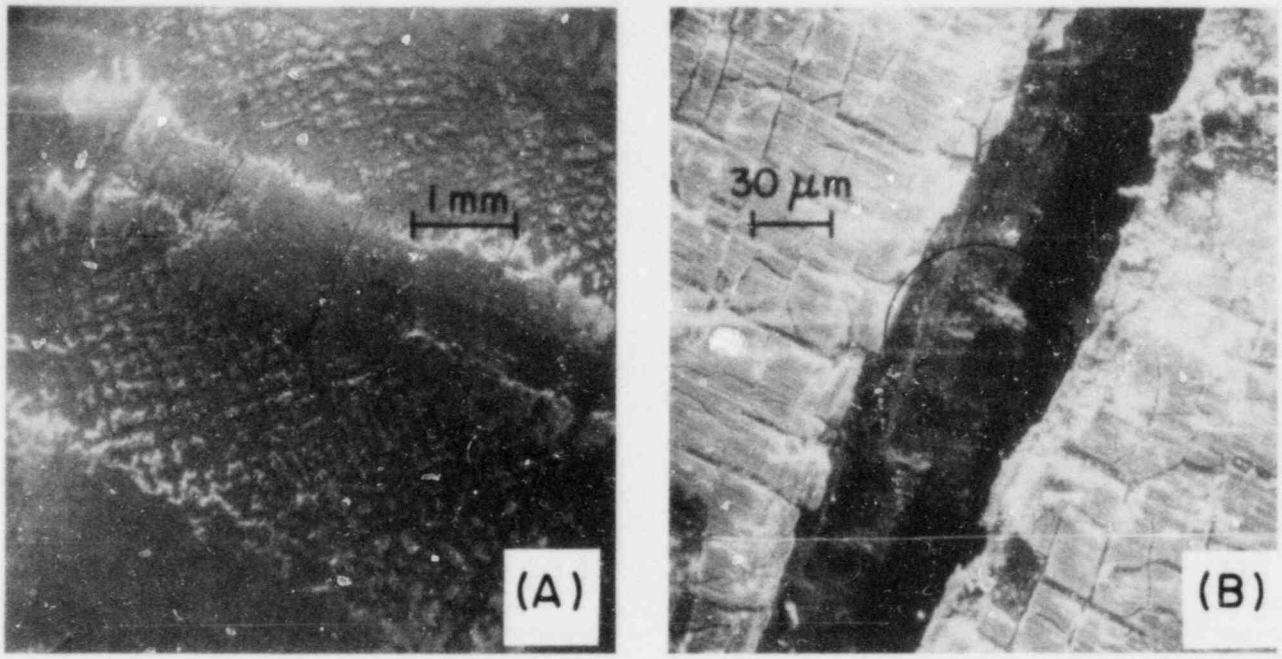

Fig. 3.2. Crack Morphologies of the Outer Surface of Specimen 217B2D after Fracture at 325°C under Expanding-Mandrel Loading. (A) Single pinhole crack located at the axial position of maximum diametral expansion; (B) higher magnification of (A) showing axial and circumferential cracks in the surface oxide layer.

the single ring used in the mandrel-expansion test is visible in Fig. 3.1(A). It appears that the crack initiated at the region where the edge of the expanding split ring deformed the inner surface of the cladding.

Significant deformation in the circumferential and axial directions can be deduced from the morphology of the deformed and cracked surface oxide layer in Fig. 3.2(A) and (B). Deformation in the axial direction appears to be most pronounced in regions immediately above and below the ring, which was used to produce stress localization. However, with the present mandrel-loading apparatus, tight contact (and hence friction) between the expanding-mandrel and cladding inner surface is lost during deformation. As a result, the cladding tube was free to contract in the axial direction. If the tube was constrained in the axial direction (as in the case of a PCI situation), the circumferential expansion (i.e., ~6%) would have been significantly smaller.

Examination of the fracture surface of the 217B2D specimen did not show clear evidence of pseudocleavage features. Characteristic fracture surface morphologies observed near the inner surface and in the middle of the tube wall are shown in Fig. 3.3(A) and (B), respectively. The morphology near the outer surface at higher magnification [i.e., the circled area of Fig. 3.2(B)] is shown in Fig. 3.3(C). The morphologies depicted in Fig. 3.3 are similar to those of specimen 217A2E[1] and indicate that the 217B2D tube failed in a ductile manner.

3. Brittle-type Failures

Results of a preliminary SEM examination of tube 217A4C, deformed and fractured at 325°C at a relatively slow strain rate and at a smaller creep load (see Table 3.1), have been reported previously.[1] Additional results for the specimen are shown in Figs. 3.4 and 3.5. The overall fracture surface near the expanding ring (i.e., at the axial position of maximum ridging) is shown in Fig. 3.4(A), and a strip in the figure is magnified in Fig. 3.4(B). A similar fracture surface away from the expanding ring (i.e., away from the ridge) is shown in Fig. 3.5. The morphologies in Figs. 3.4(B) and 3.5 at high magnification reveal pseudocleavage over a large portion of the fracture surface. However, many "steps" parallel to the axial direction and almost perpendicular to the pseudocleavage plane can be observed, particularly in Fig. 3.5. The morphology of the "steps" was invariably ductile in nature. The overall fracture surface morphology is similar to that of the fracture surface reported by Rosenbaum et al.[3] for a fuel rod which failed during service in the Dresden III reactor (e.g., see Figs. 3.2-17 of Ref. 3). The "steps" of the fracture surface parallel to the axial direction indicate some form of plastic deformation in the axial direction. If the specimen had been constrained in the axial direction, the plastic deformation associated with the "steps" would have been minimal.

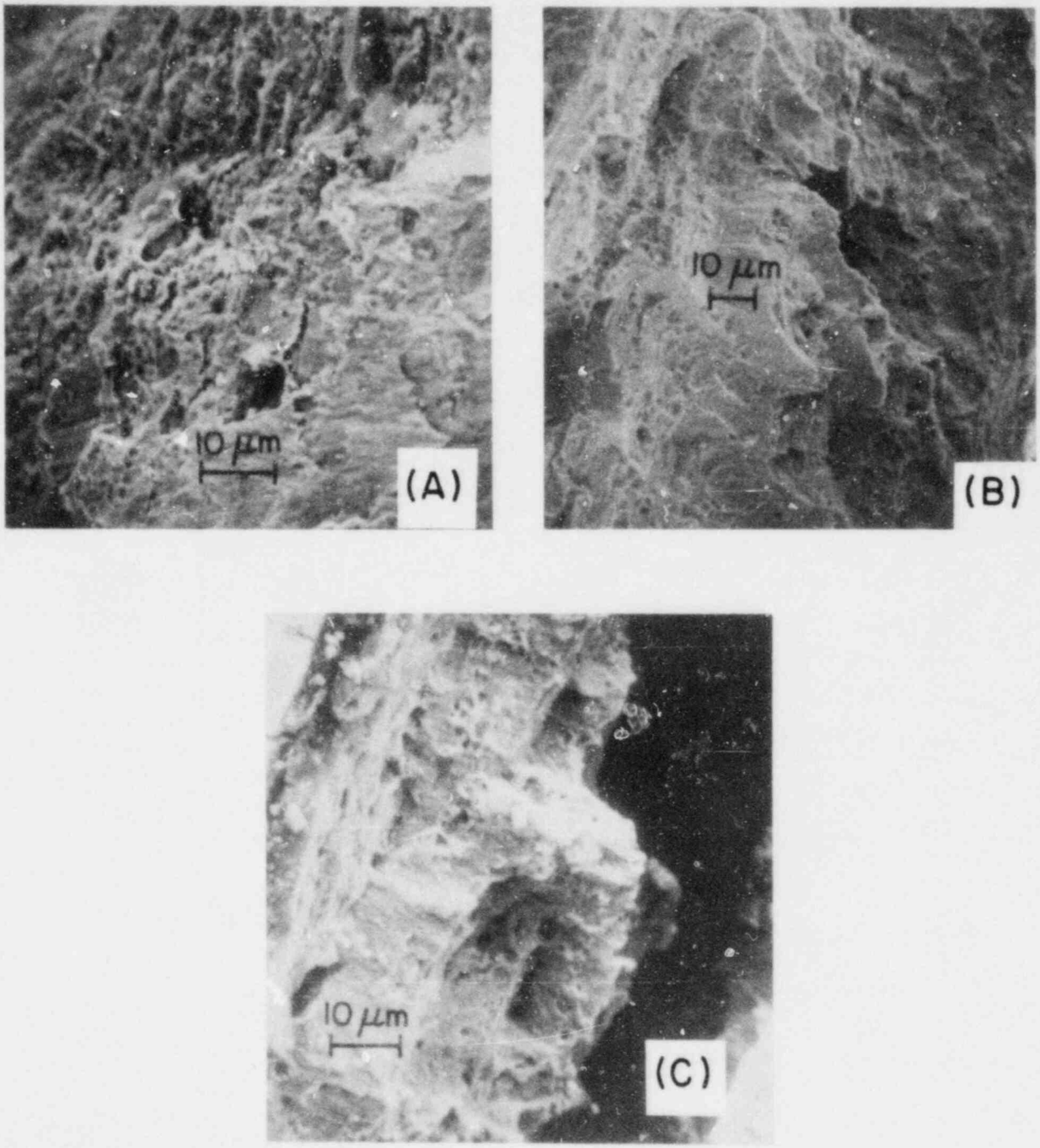

Fig. 3.3. Fracture Surface Morphologies of the 217B2D Specimen. (A) Near the inner surface; (B) middle of cladding wall; (C) near the outer surface. The specimen failed in a ductile manner.

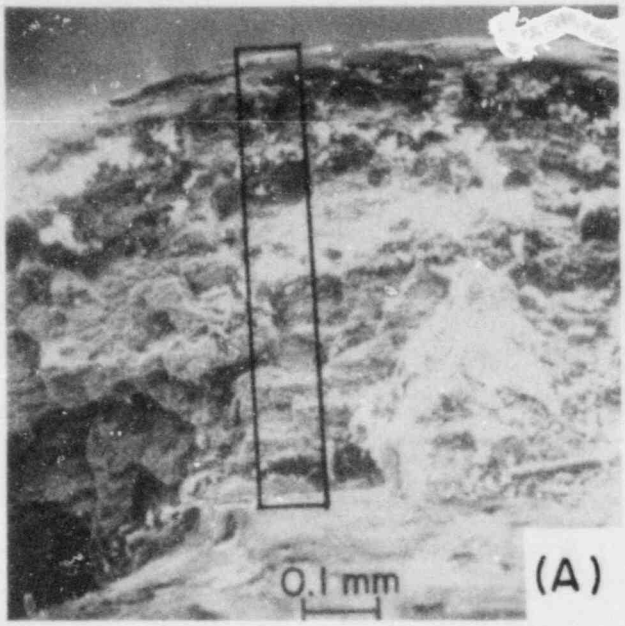

Fig. 3.4
Fracture Surface Morphologies of Specimen 217A4C after Brittle-type Fracture at 325°C under Expanding-Mandrel Loading. (A) Overall fracture surface; (B) higher magnification of the area denoted by the strip in (A) showing pseudo-cleavage.

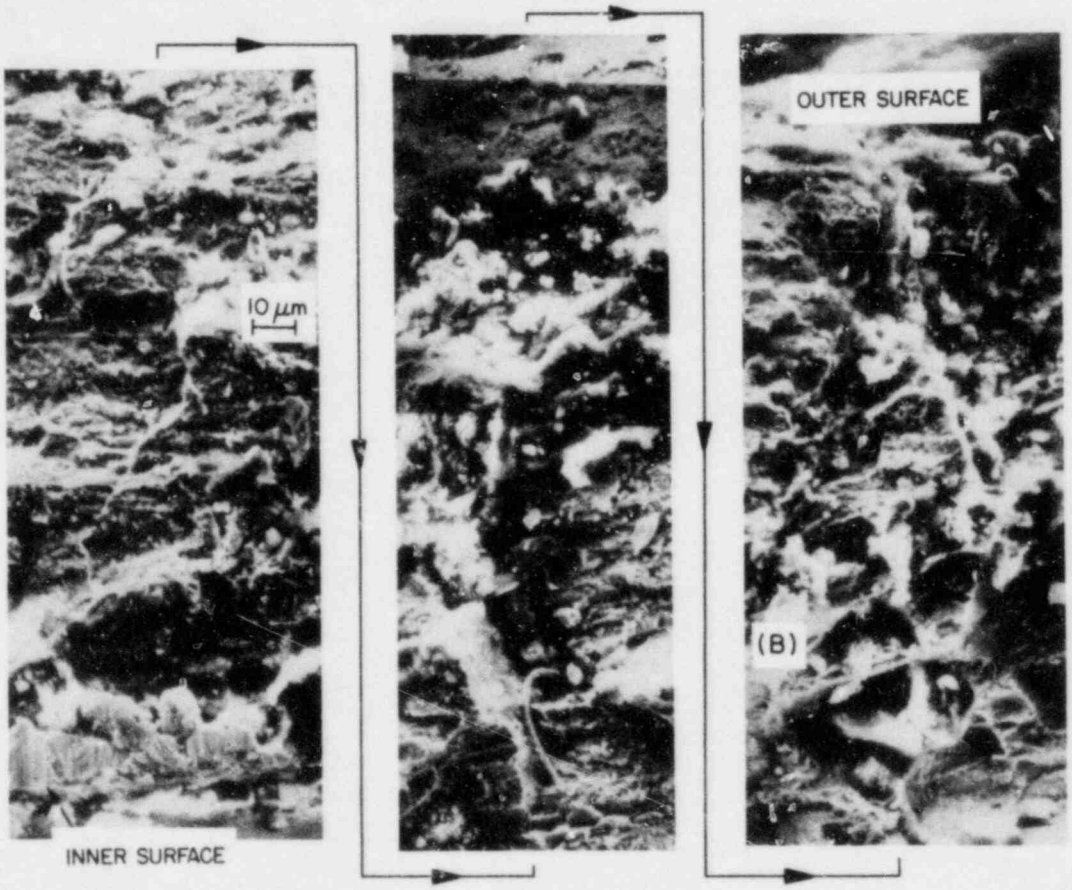

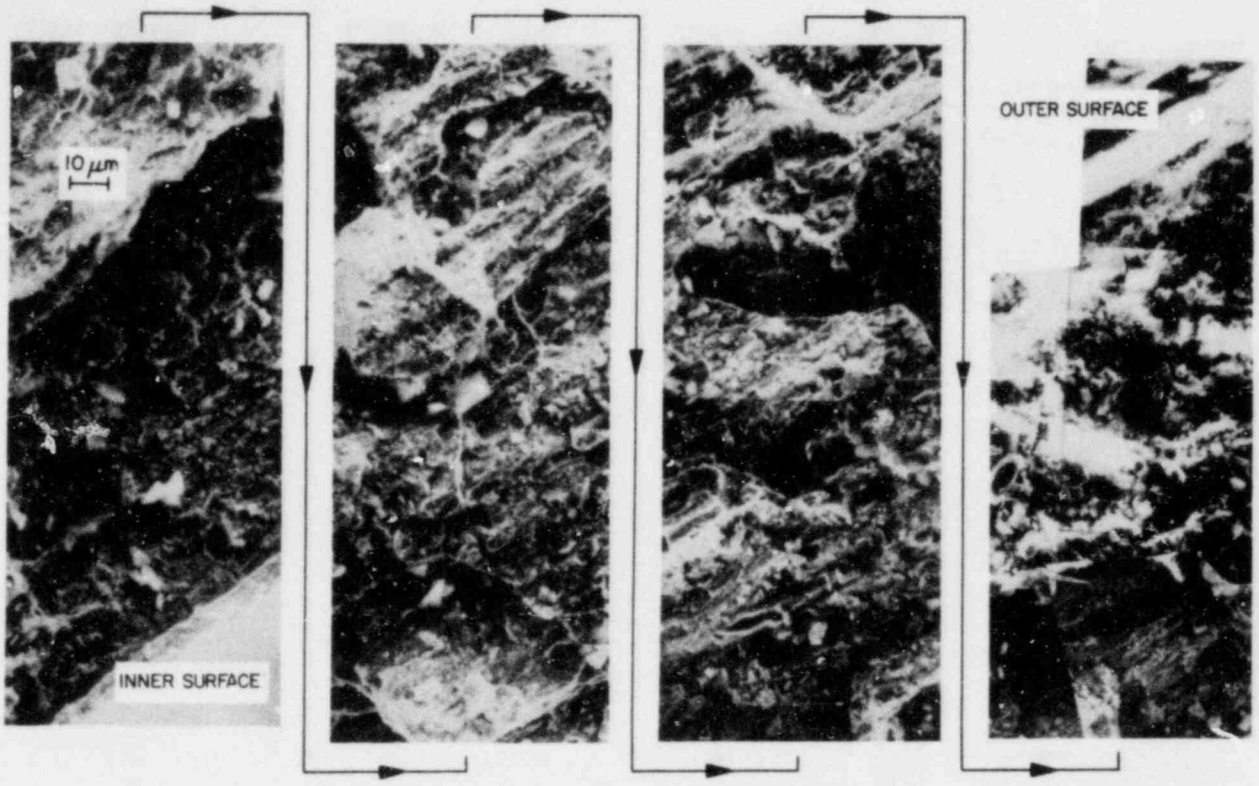

Fig. 3.5. Fracture Surface Morphology Similar to Fig. 3.4(B) away from the Expanding Ring.

Fracture surface morphologies with pseudocleavage features similar to those in Figs. 3.4 and 3.5 are shown in Figs. 3.6 and 3.7 for another tube (217A4E) which fractured after 223.8 h at 325°C. The region of pseudocleavage extends from the inner toward the outer surface of the tube up to ~30% of the wall thickness. Beyond ~30%, only ductile morphology is observed. A composite fracture surface of tube 217A4F similar to Figs. 3.4-3.7 is shown in Fig. 3.8. The 217A4F specimen was also fractured at 325°C under similar strain-rate and loading conditions. In the case of Fig. 3.8(B), the fracture region near the inner surface was accidentally compressed and damaged during preparation of the SEM specimen. As a result, an artifact morphology is evident in that portion (bounded by dark lines) of Fig. 3.8(B).

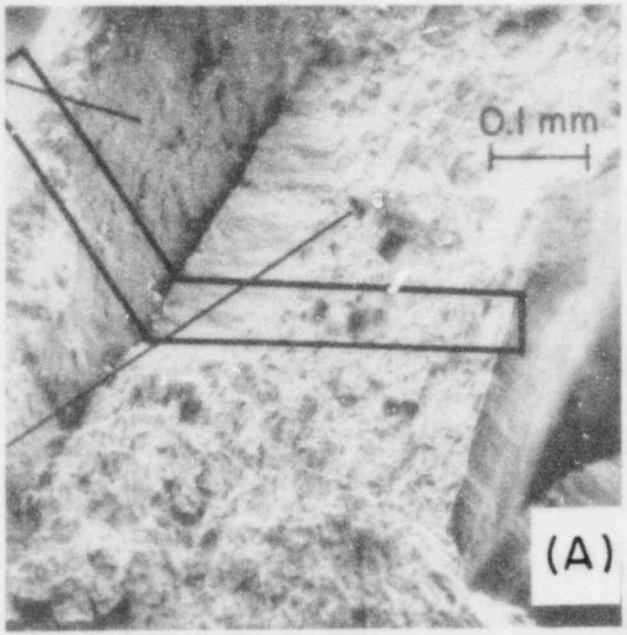

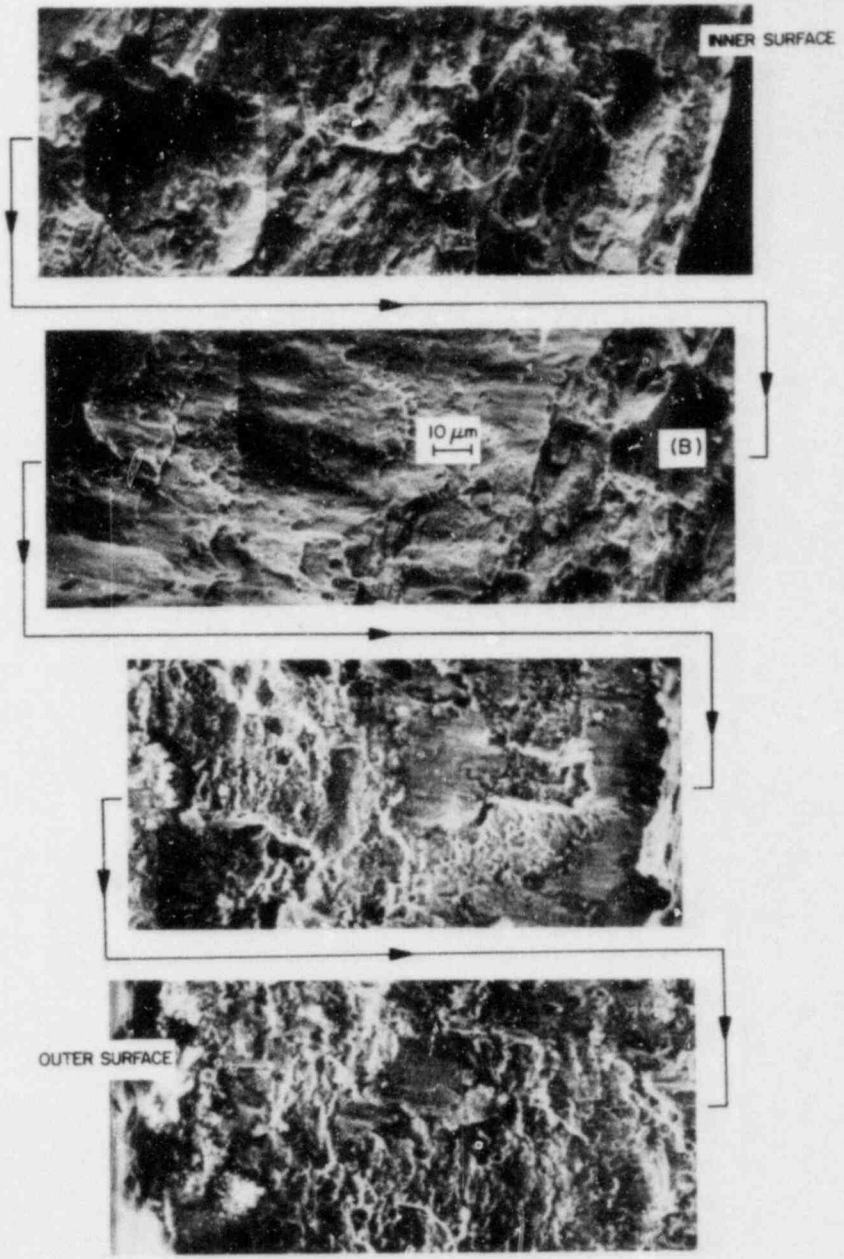

Fig. 3.6
Fracture Surface Morphologies of Specimen 217A4E after Fracture at 325°C under Expanding-Mandrel Loading. (A) Overall fracture surface near the expanding ring; (B) higher magnification of the strip in (A) showing pseudocleavage extending up to ~30% of wall thickness from the inner surface.

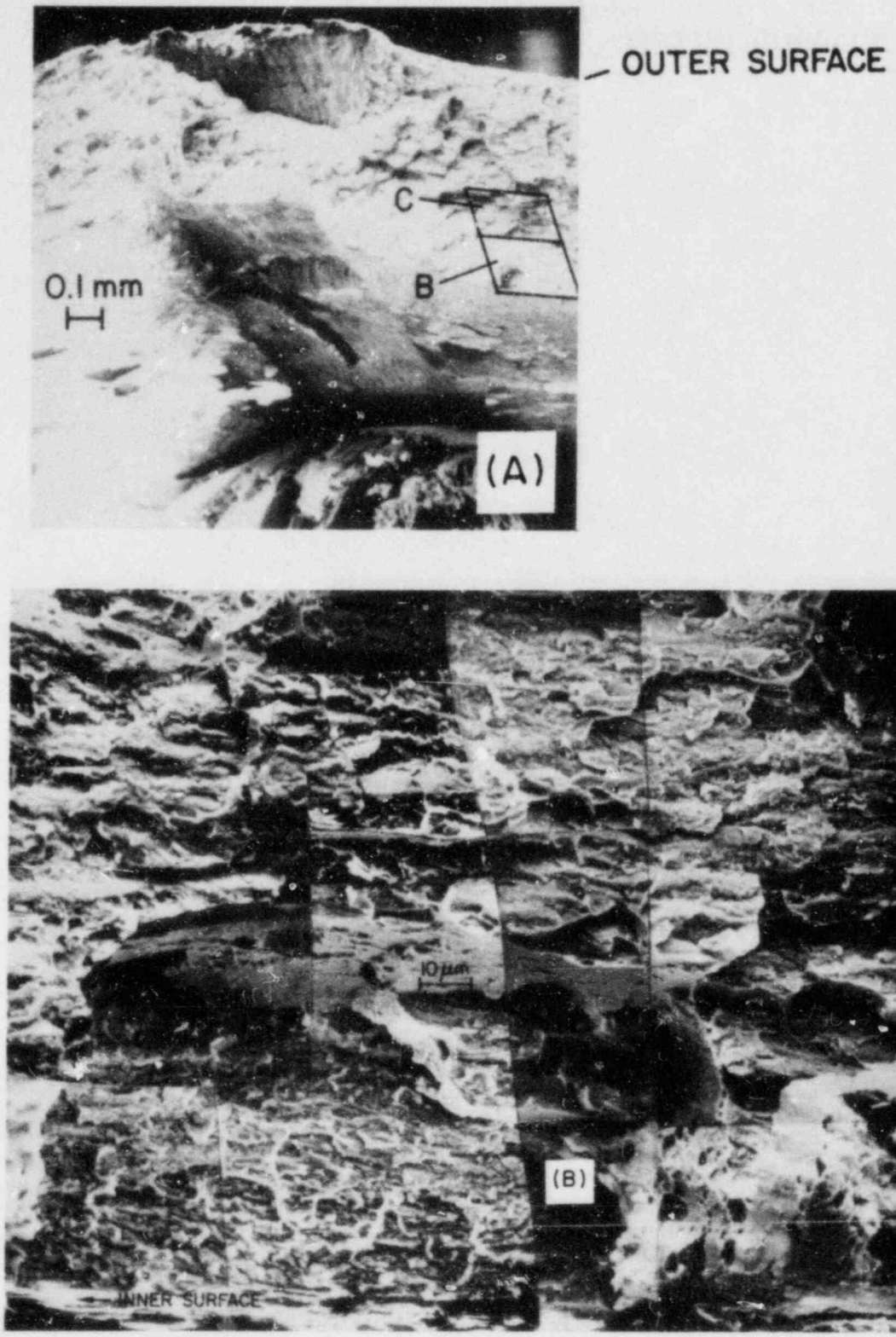

Fig. 3.7. Fracture Surface Morphologies Similar to Fig. 3.6 but away from the Expanding Ring. (A) Overall view of the fracture surface; higher magnifications of the bounded areas B and C are shown in (B) and (C), respectively.

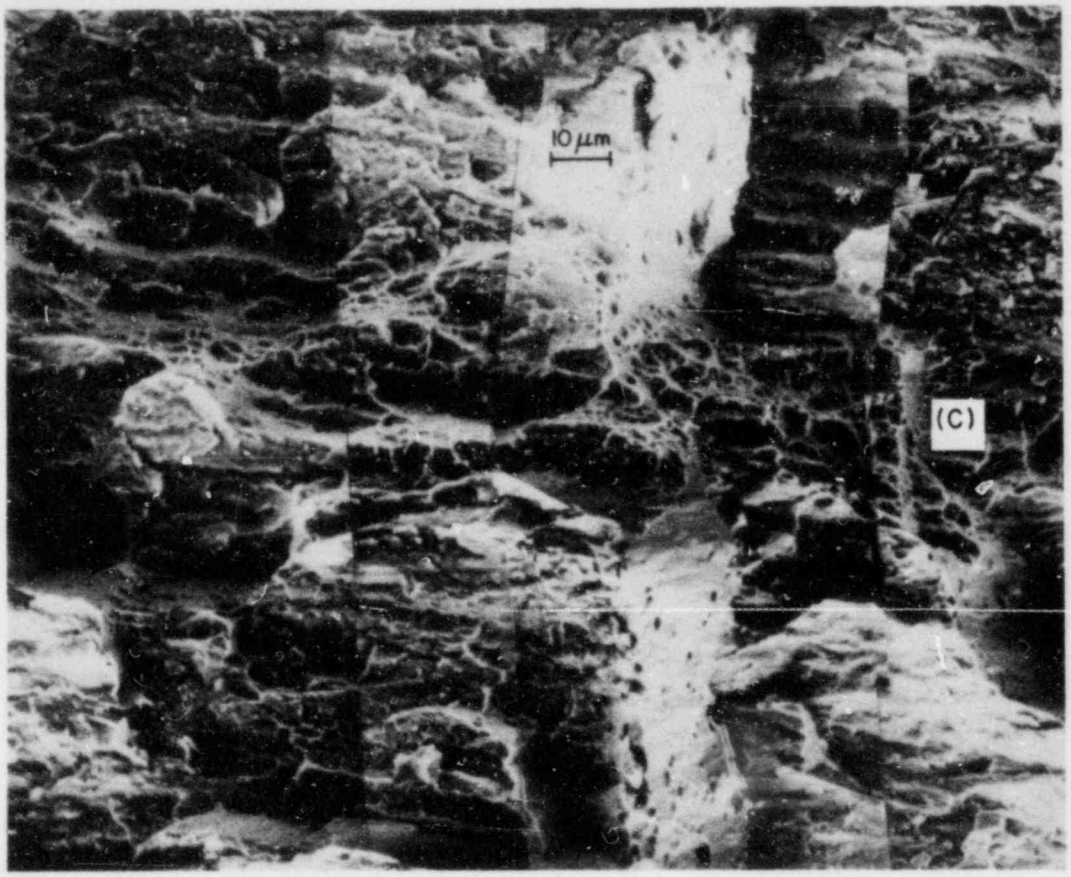

Fig. 3.7. (Contd.)

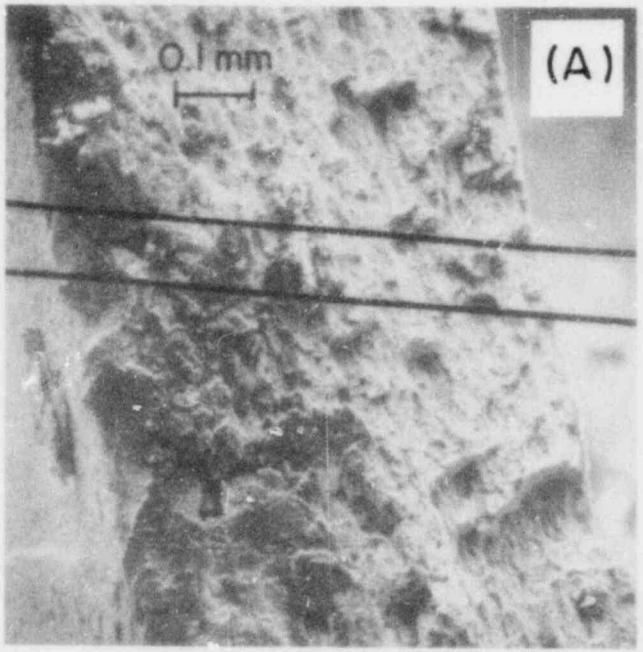

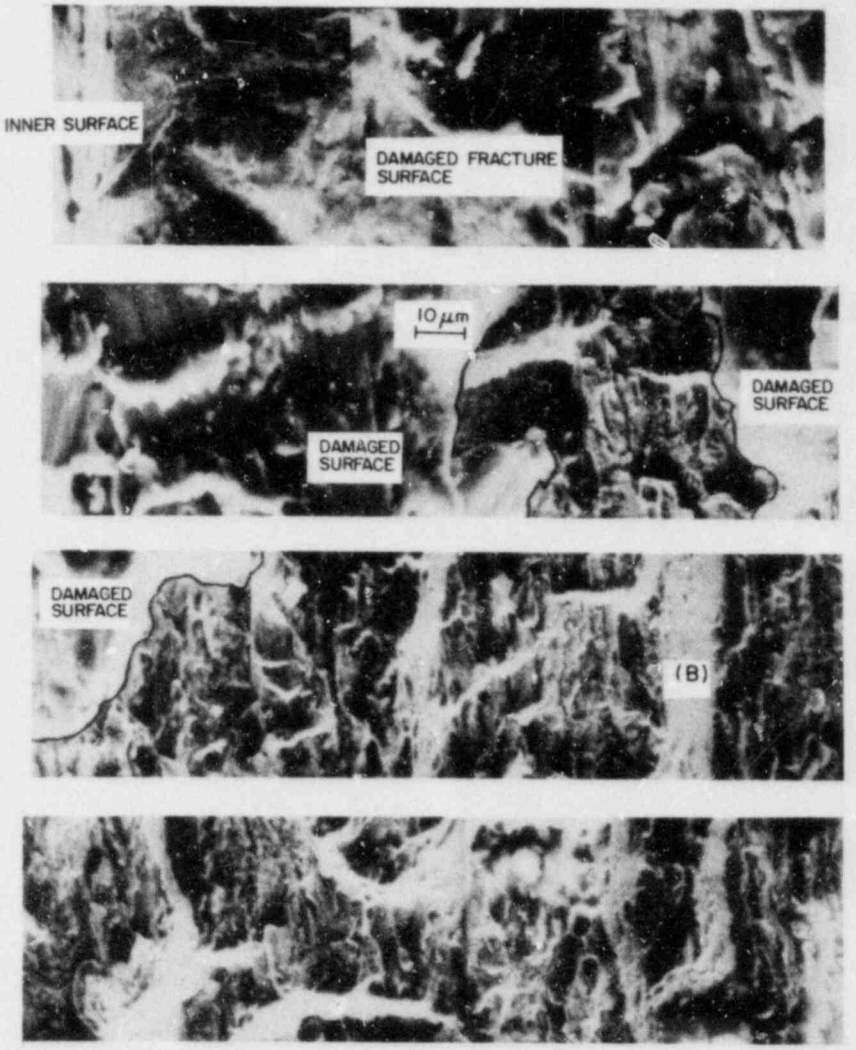

Fig. 3.8
Fracture Surface Morphologies of Specimen 217A4F after Fracture at 325°C under Expanding-Mandrel Loading. (A) Overall view; (B) higher magnification of the strip in (A) showing pseudocleavage mixed with a damaged artifact surface morphology.

B. TEM Examination of Zr_3O Phase Distribution (H. M. Chung)

1. Introduction

Electron-diffraction characteristics of the Zr_3O phase, observed in association with brittle-type failures produced in Big Rock Point and H. B. Robinson spent-fuel cladding, were shown to be identical to those of the α-phase Zircaloy except for the presence of superlattice reflections.[4] Therefore, an analysis of the dark-field images obtained from the superlattice reflections is the best method to determine the morphology and distribution of the phase. The dark-field images are discussed in the present report.

2. Dark-field Morphology of the Zr_3O Phase

The selected area diffraction (SAD) pattern in Fig. 3.9 from Big Rock Point cladding specimen 165AE4B contains Zr_3O superlattice reflections of $(\bar{1}105)_{Zr_3O}$ and $(0\bar{1}16)_{Zr_3O}$. The SAD pattern of Fig. 3.9(E) was obtained from the circled area in the bright-field image of Fig. 3.9(A). Figure 3.9(C) and (D) show the dark-field images produced from the superlattice reflections of $(\bar{1}105)_{Zr_3O}$ and $(0\bar{1}16)_{Zr_3O}$, respectively.

A closer examination of the dark-field morphology with a magnifying glass revealed discrete precipitates of ellipsoidal shape (size $\lesssim$100 Å). The aggregate precipitate virtually forms a continuous phase as shown in the figures. Numerous dislocations decorated by the precipitates were observed near the regions of dense precipitation. The precipitates also form on grain boundaries as denoted by arrows in Fig. 3.9(C) and (D). Grain boundary segregation would be more pronounced if the as-fabricated cladding was fully recrystallized. Similar dark-field morphologies from superlattice reflections of $(21\bar{3}2)_{Zr_3O}$ and $(42\bar{6}4)_{Zr_3O}$ (obtained from a different region of the same thin-foil specimen) are shown in Fig. 3.10. Again, dislocations decorated by the Zr_3O phase can be observed in Fig. 3.10(C) and (D). The dark-field morphologies in Figs. 3.9 and 3.10 reveal that the Zr_3O phase forms primarily in association with dislocation substructures, and to a lesser extent, on grain boundaries.

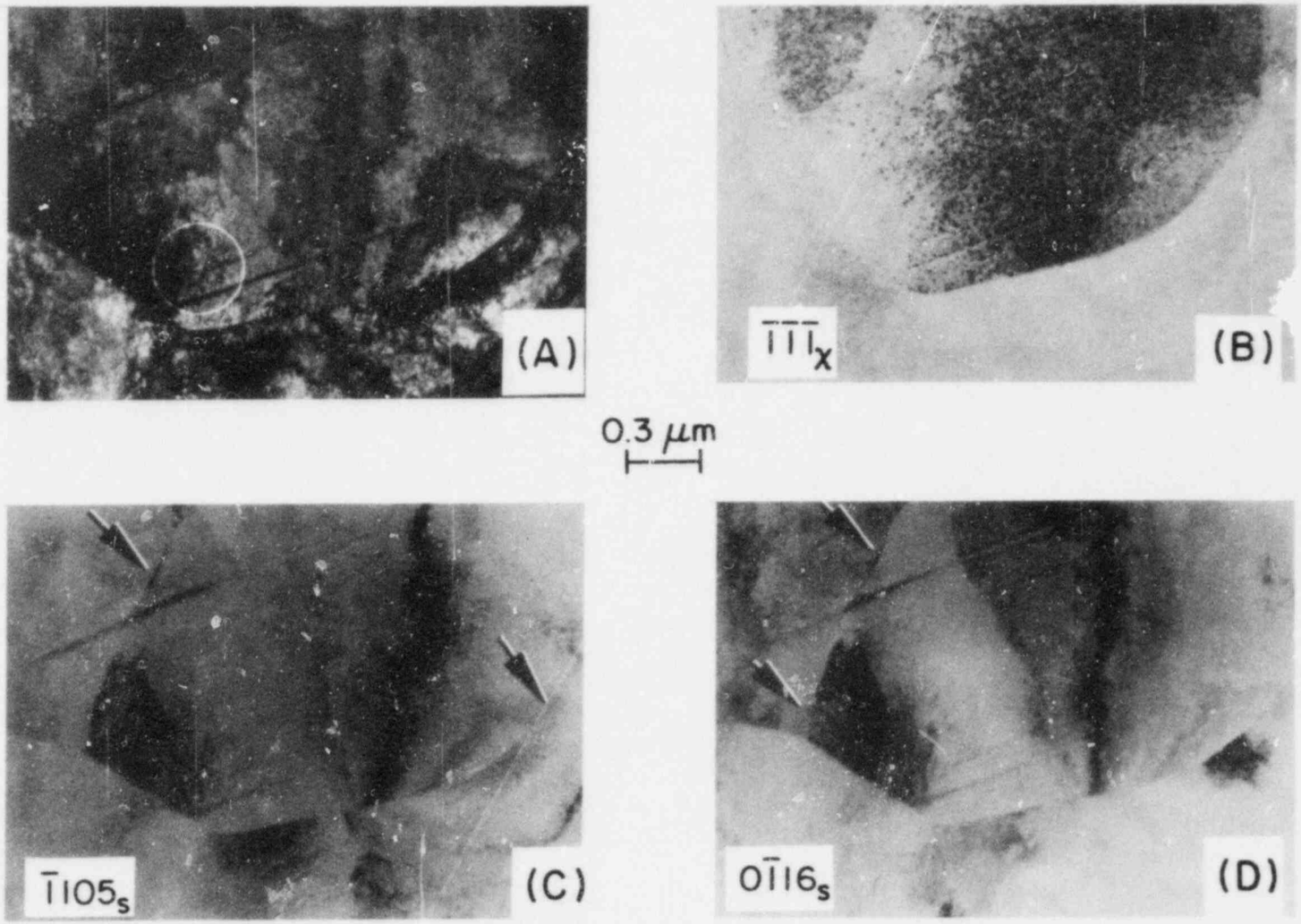

Fig. 3.9. TEM Micrographs of Big Rock Point Cladding Specimen 165AE4B That Failed in a Brittle-type Manner at 325°C under Internal Gas-Pressurization Loading. (A) Bright-field image; (B) dark-field images of $(\bar{1}\bar{1}\bar{1})_\chi$ of artifact surface hydride; (C) $(\bar{1}105)_s$ of the Zr_3O phase; (D) $(0\bar{1}16)_s$ of the Zr_3O phase; (E) indexed SAD pattern of the circled area of (A). Subscripts α, s, χ, and D used in (E) refer to α-Zr matrix, Zr_3O, surface χ-hydride, and double diffraction, respectively. Arrows in (C) and (D) denote the location of the Zr_3O phase on the grain boundaries.

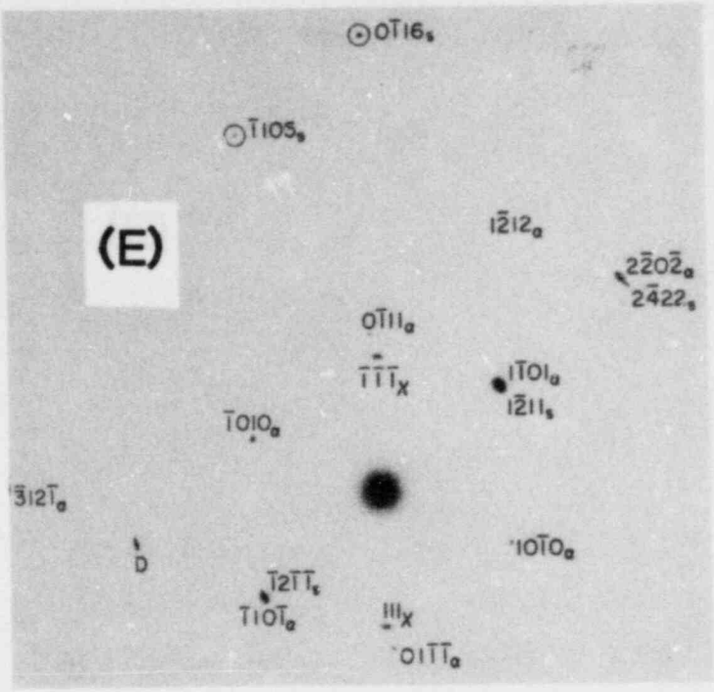
(E)
$\odot 0\bar{1}16_s$
$\odot \bar{1}10\bar{5}_s$
$1\bar{2}12_a$
$2\bar{2}0\bar{2}_a$
$2\bar{4}22_s$
$0\bar{1}11_a$
$\bar{1}\bar{1}\bar{1}_x$
$1\bar{1}01_a$
$1\bar{2}11_s$
$\bar{1}010_a$
$\bar{3}12\bar{1}_a$
D
$10\bar{1}0_a$
$\bar{1}2\bar{1}\bar{1}_s$
$\bar{1}10\bar{1}_a$
$\bar{1}\bar{1}\bar{1}_x$
$01\bar{1}\bar{1}_a$

Fig. 3.9. (Contd.)

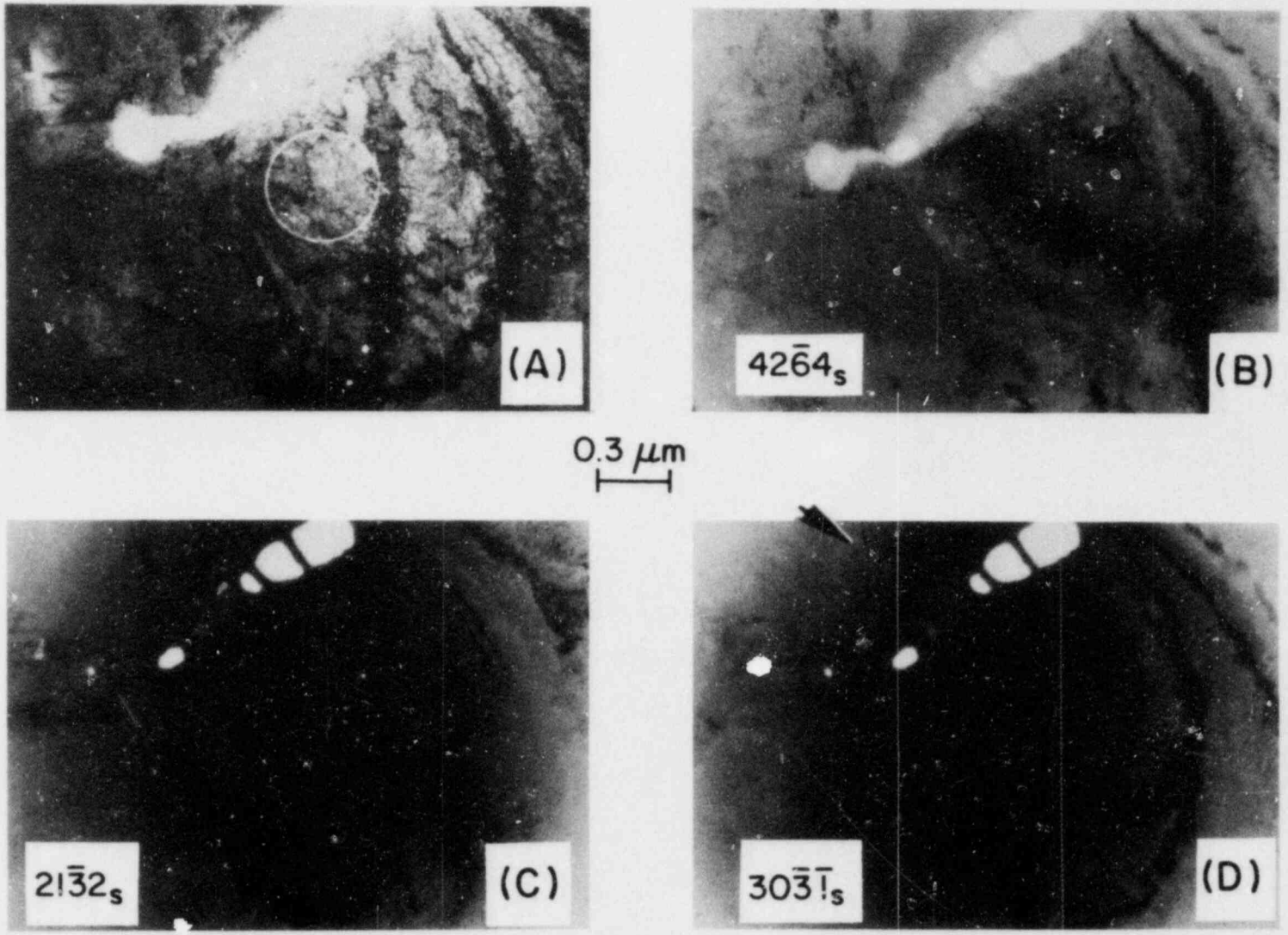

Fig. 3.10. TEM Micrographs Similar to Fig. 3.9. (A) Bright-field; (B) dark-field images of Zr_3O phase $(42\bar{6}4)_s$; (C) $(21\bar{3}2)_s$; (D) $(30\bar{3}\bar{1})_s$; (E) indexed SAD pattern of the circled area of (A). The labeling notations are the same as in Fig. 3.9.

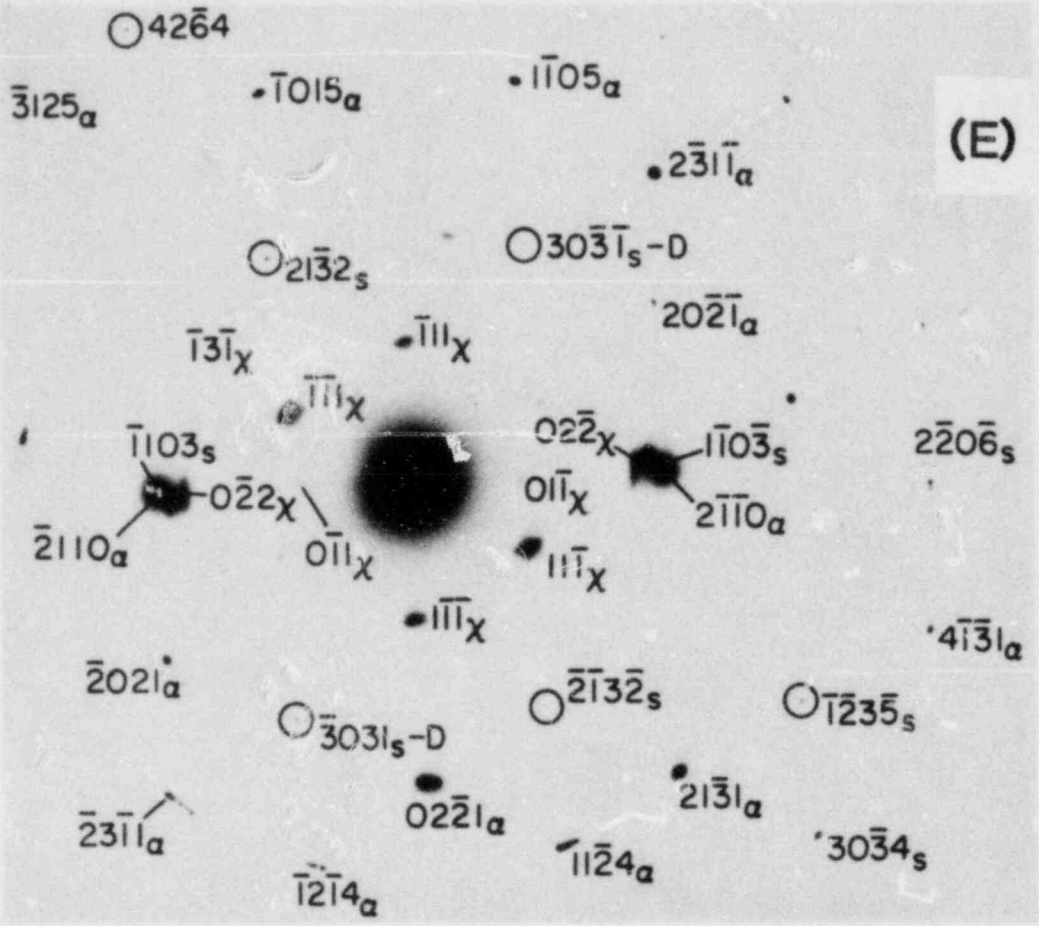

Fig. 3.10. (Contd.)

C. References for Chapter III

1. H. M. Chung, in Materials Science and Technology Division Light-Water-Reactor Safety Research Program: Quarterly Progress Report, April-June 1983, NUREG/CR-3689 Vol II, ANL-83-85, Vol. II, pp. 79-88.

2. H. M. Chung, F. L. Yaggee, and T. F. Kassner, "Fracture Behavior of Zircaloy Spent-Fuel Cladding," in Trans. Eleventh Water Reactor Safety Research Information Meeting, October 24-28, 1983, Gaithersburg, MD, NUREG/CP-0047 Vol. 3, pp. 521-548.

3. H. S. Rosenbaum, U. E. Wolff, and W. L. Bell, "Fractography of Incipient Cracks on Rod KE-2225," in Determination and Microscopic Study on Incipient Defects in Irradiated Power Reactor Fuel Rods, EPRI NP-812, July 1978, Electric Power Research Institute, pp. 3-97 to 3-141.

4. H. M. Chung, in Materials Science and Technology Division Light-Water-Reactor Safety Research Program: Quarterly Progress Report, July-September 1983, NUREG/CR-3689 Vol. III, ANL-83-85 Vol. III, pp. 10-24.

IV. LONG-TERM EMBRITTLEMENT OF CAST DUPLEX STAINLESS STEELS IN LWR SYSTEMS

Principal Investigators:
O. K. Chopra and G. Ayrault

A program is being conducted to investigate the significance of in-service embrittlement of cast duplex stainless steels under light water reactor (LWR) operating conditions, and to evaluate possible remedies to the embrittlement problem for existing and future plants. The existing data on embrittlement of duplex stainless steels and single-phase ferritic steels were reviewed to determine the critical parameters that control the embrittlement phenomenon and to establish the test matrices for microstructural studies and mechanical property measurements.[1,2] The scope of the program includes the following: (1) characterize and correlate the microstructure of in-service reactor components and laboratory-aged material with loss of fracture toughness and identify the mechanism of embrittlement, (2) determine the validity of laboratory-induced embrittlement data for predicting the toughness of component materials after long-term aging at reactor operating temperatures, (3) characterize the loss of fracture toughness in terms of fracture mechanics parameters to provide the data needed to assess the safety significance of embrittlement, and (4) provide additional understanding of the effects of key compositional and metallurgical variables on the kinetics and degree of embrittlement.

Nineteen experimental and six commercial heats of CF-3, -8, and -8M grades of cast stainless steel (ASTM Specification A351 and A451) were procured in different product forms and section thicknesses. The composition of the experimental heats was varied to provide different concentrations of nickel, chromium, carbon, and nitrogen in the material and ferrite contents in the range of 3 to 30 vol %. The outer diameter and wall thickness of the cast pipes range from 0.6 to 0.9 m and 38.1 to 76.2 mm, respectively. Material will be available for Charpy impact tests and microstructural studies over the entire range of compositions. However, it is prohibitively expensive to procure and age material of all compositions for J_R curve testing. Six large experimental heats, in the form of 76-mm-thick slabs, were obtained for these

tests. The test matrices for the microstructural studies and mechanical property measurements were presented in an earlier report.[2]

The kinetics and fracture toughness data generated in this program and from other sources will provide the technical basis to assess the in-service embrittlement of cast stainless steels under LWR operating conditions. Estimates of the degree of embrittlement will be compared with data obtained from examination of material from actual reactor service. Data pertaining to the effects of compositional and metallurgical variables on the embrittlement phenomenon will help to evaluate the possible remedies for existing and future plants.

A. Technical Progress

Characterization of the various cast materials is in progress to determine the chemical composition, ferrite content, hardness, and grain structure. Metallographic evaluation of the morphology and distribution of the ferrite structure and measurements of the ferrite content and hardness of the material from 19 heats of cast keel blocks and six reactor components has been completed. A ferrite scope was used to measure the ferrite content of the castings. The instrument was calibrated with several weld-metal standards (ferrite numbers between 2.4 and 28.1) obtained from the British Welding Institute. The cast materials were examined in the three orientations, i.e., axial, circumferential, and radial planes, as well as different locations, namely, material near the center and the inner and outer surfaces of the pipes, and top (Row 6) and bottom (Row 3) regions of the keel blocks. Orientation of the material had little or no effect on either hardness or ferrite content and morphology. Some differences in hardness and ferrite content were observed for material from different locations of the castings. The chemical composition, hardness, and ferrite content of the various heats of cast stainless steel are given in Table 4.1. The hardness and ferrite content values represent the average for the three orientations.

TABLE 4.1. Chemical Composition, Hardness, and Ferrite Content of the Various Heats of Cast Stainless Steel

Heat	Grade	Composition,[a] wt %							Location	Hardness, R_B	Ferrite Content,[b] %
		Mn	Si	Mo	Cr	Ni	N	C			
						Cast Keel Blocks					
58	CF-8	0.66	1.21	0.29	19.56	10.37	0.040	0.050	Row 3	76.0	3.6
									Row 6	78.2	2.1
57		0.69	1.24	0.28	18.45	8.94	0.041	0.060	Row 3	80.1	5.1
									Row 6	80.3	2.8
54		0.58	1.08	0.31	19.42	8.91	0.073	0.065	Row 3	82.6	1.2
									Row 6	83.9	2.3
53		0.70	1.28	0.35	19.62	8.86	0.045	0.070	Row 3	82.6	9.5
									Row 6	83.6	7.8
56		0.60	1.16	0.30	19.33	8.93	0.031	0.060	Row 3	81.9	11.9
									Row 6	83.1	8.2
59		0.63	1.14	0.26	20.35	8.95	0.040	0.070	Row 3	83.5	14.2
									Row 6	82.8	12.7
61		0.70	1.20	0.27	20.54	8.59	0.060	0.060	Row 3	85.1	13.0
									Row 6	85.5	13.1
60		0.71	1.01	0.26	21.02	8.07	0.050	0.070	Row 3	86.2	20.4
									Row 6	87.2	21.7
50	CF-3	0.67	1.26	0.28	17.63	8.84	0.064	0.019	Row 3	79.6	5.0
									Row 6	80.6	3.7
49		0.66	1.11	0.29	19.32	10.10	0.064	0.022	Row 3	76.1	8.0
									Row 6	77.2	6.3
48		0.67	1.21	0.26	19.42	9.90	0.071	0.016	Row 3	77.6	8.9
									Row 6	78.6	8.5
47		0.65	1.23	0.45	19.67	10.04	0.027	0.018	Row 3	79.0	16.5
									Row 6	80.3	16.2
52		0.63	1.04	0.31	19.51	9.07	0.049	0.021	Row 3	81.4	10.3
									Row 6	81.8	16.7
51		0.66	1.06	0.28	20.36	8.69	0.048	0.023	Row 3	83.7	18.0
									Row 6	83.9	18.0
62	CF-8M	0.84	0.64	2.46	18.38	11.35	0.030	0.070	Row 3	78.2	6.3
									Row 6	78.0	2.6
63		0.69	0.75	2.52	19.39	11.22	0.030	0.050	Row 3	81.0	10.9
									Row 6	82.1	10.0

TABLE 4.1. (Contd.)

Heat	Grade	Composition,[a] wt % Mn	Si	Mo	Cr	Ni	N	C	Location	Hardness, R_B	Ferrite Content,[b] %
66	CF-8M	0.71	0.60	2.36	19.41	9.13	0.030	0.060	Row 3	84.6	19.2
									Row 6	85.8	20.5
65		0.66	0.63	2.53	20.95	9.39	0.060	0.060	Row 3	88.4	21.4
									Row 6	89.5	25.4
64		0.70	0.71	2.41	20.87	9.01	0.030	0.050	Row 3	89.7	
									Row 6	89.7	2
						Cast Components					
C1	CF-8	1.22	1.19	0.64	19.10	9.32	0.041	0.036	O.D.	78.3	2.3
					18.89	9.42			I.D.	80.6	1.7
P1		0.56	1.07	0.04	20.38	8.00	0.053	0.032	O.D.	84.5	27.6
					20.60	8.20			I.D.	85.3	19.5
P3	CF-3	1.04	0.86	0.01	18.93	8.33	0.159	0.020	O.D.	80.6	2.5
					18.85	8.56			I.D.	83.7	0.9
P2		0.72	0.92	0.16	20.20	9.24	0.041	0.020	O.D.	82.4	15.9
					20.20	9.51			I.D.	85.1	13.2
I		0.46	0.80	0.44	20.08	8.50	0.030	0.016	Vane 3	81.1	20.2
					20.20	0.80			Vane 1	82.2	14.3
					20.34	8.64			Shroud	78.1	16.9
					20.20	8.84			Hub	81.0	19.1
P4	CF-8M	1.07	1.02	2.06	19.63	10.00	0.153	0.039	O.D.	83.0	11.1
					19.65	9.99			I.D.	83.2	9.8

[a]Chemical composition of the keel blocks supplied by the vendor.
[b]Ferrite content measured by Ferrite Scope, Auto Test FE, Probe Type FSP-1.

Typical microstructures for the various experimental heats and reactor components are shown in Figs. 4.1-4.8. The ferrite morphology in the static cast keel blocks is different from that in the centrifugally cast pipes. For the same ferrite content, the islands of ferrite in the keel blocks are smaller and have a finer dispersion than in the pipe material. In general, the ferrite morphology is globular for ferrite contents of <5%, lacy for ferrite contents between 5 and 20%, and acicular for material with larger amounts of ferrite. The lacy form of ferrite is characterized by an interlaced network of ferrite islands, whereas the acicular morphology represents fine needle-like ferrite distributed in the austenite matrix. All morphologies have a random arrangement within the casting.

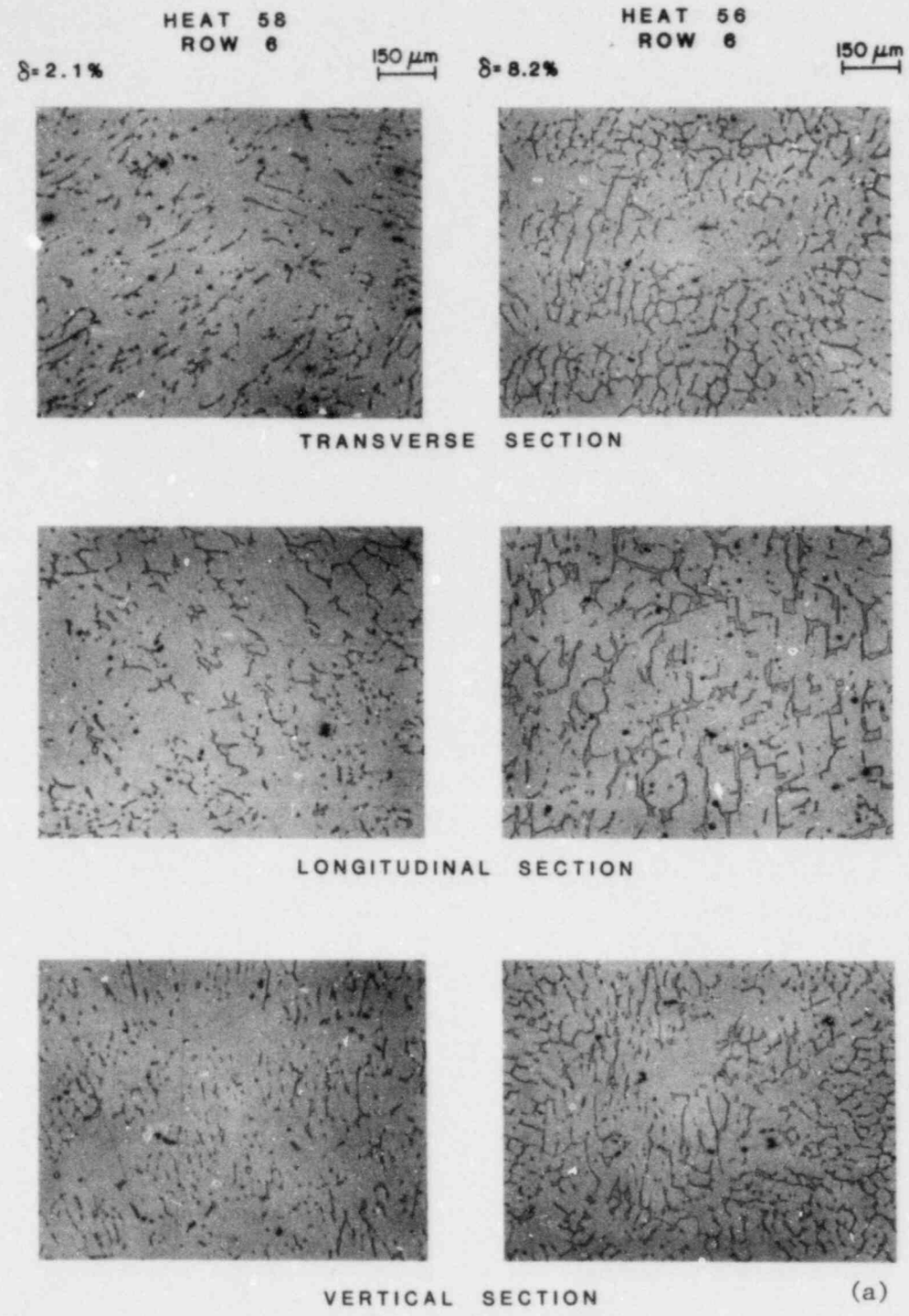

Fig. 4.1. Microstructures Along the Three Orientations of Static Cast Keel Blocks of CF-8 Stainless Steel. (a) and (b) Top section (Row 6) and (c) bottom section (Row 3) of the casting.

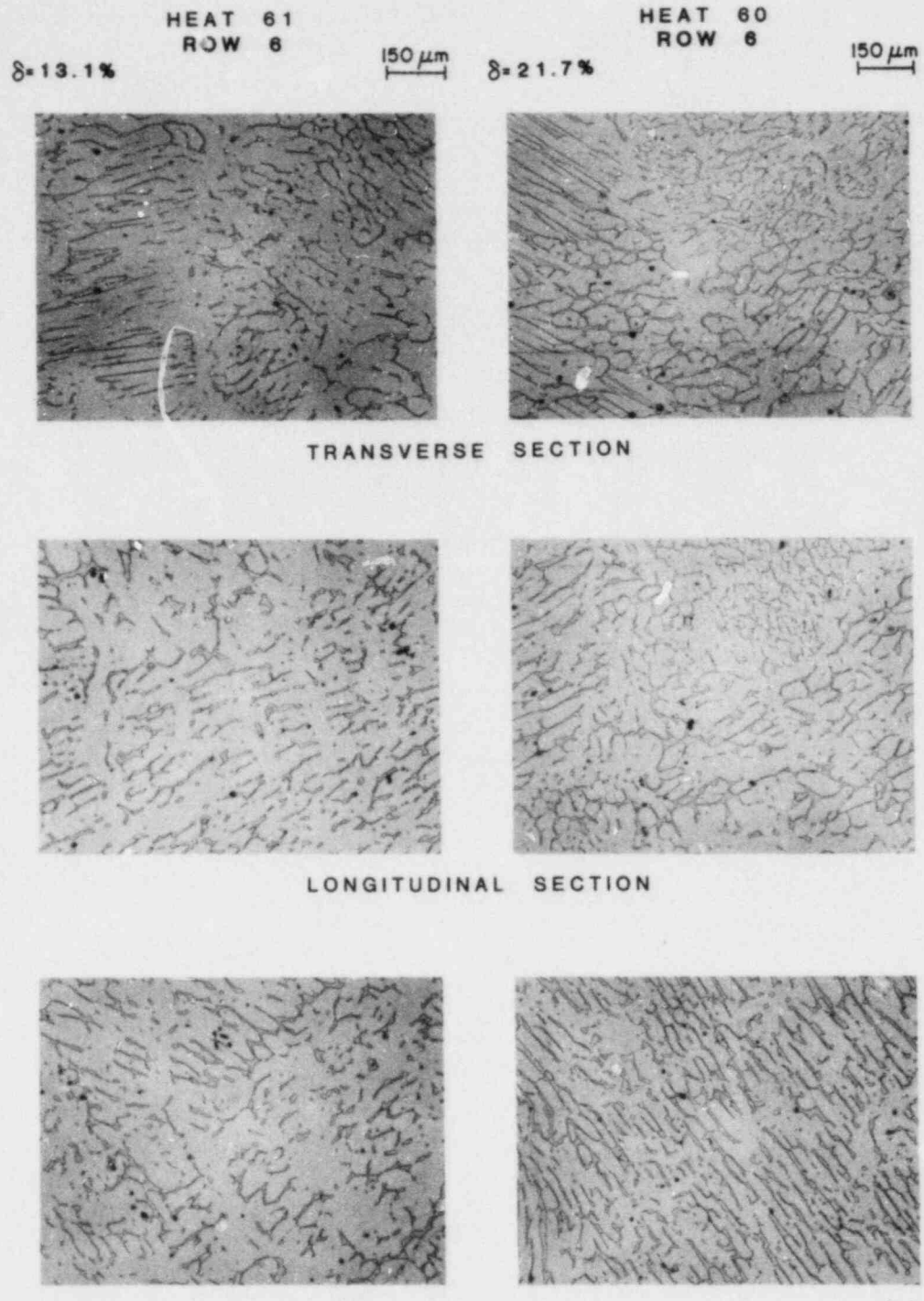
HEAT 61
ROW 6
δ=13.1%
150 μm
HEAT 60
ROW 6
δ=21.7%
150 μm
TRANSVERSE SECTION
LONGITUDINAL SECTION
VERTICAL SECTION
(b)

Fig. 4.1. (Contd.)

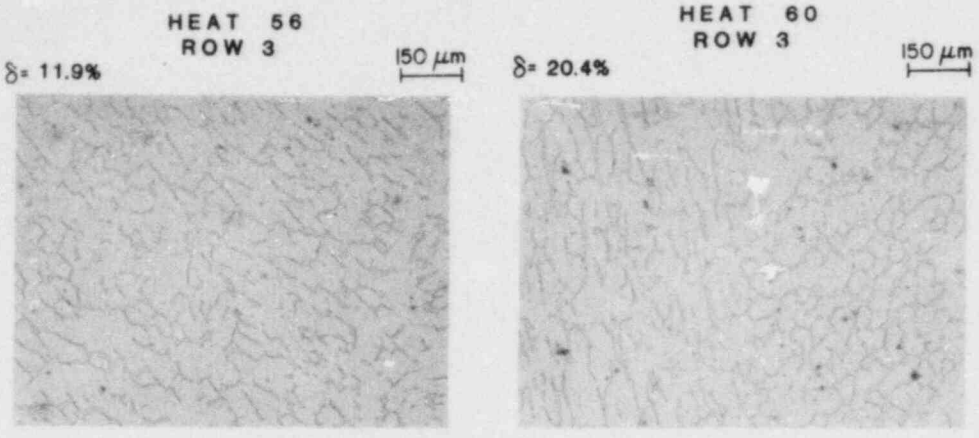

TRANSVERSE SECTION

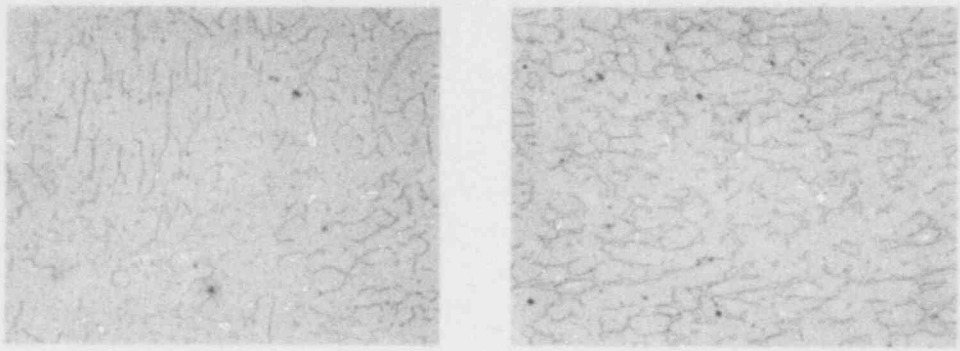

LONGITUDINAL SECTION

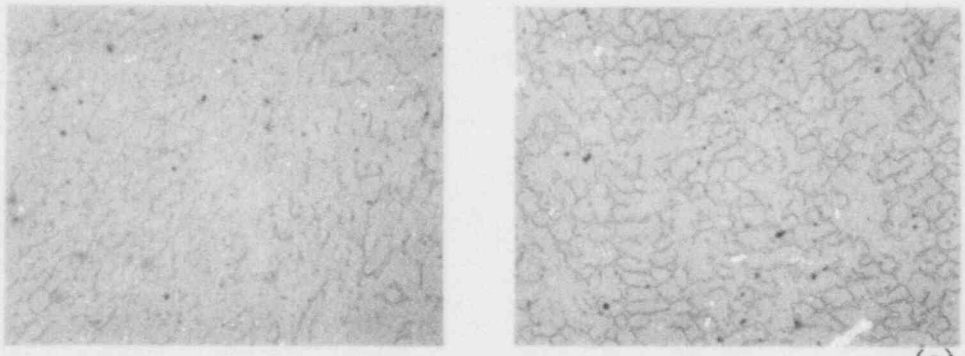

(c)

VERTICAL SECTION

Fig. 4.1. (Contd.)

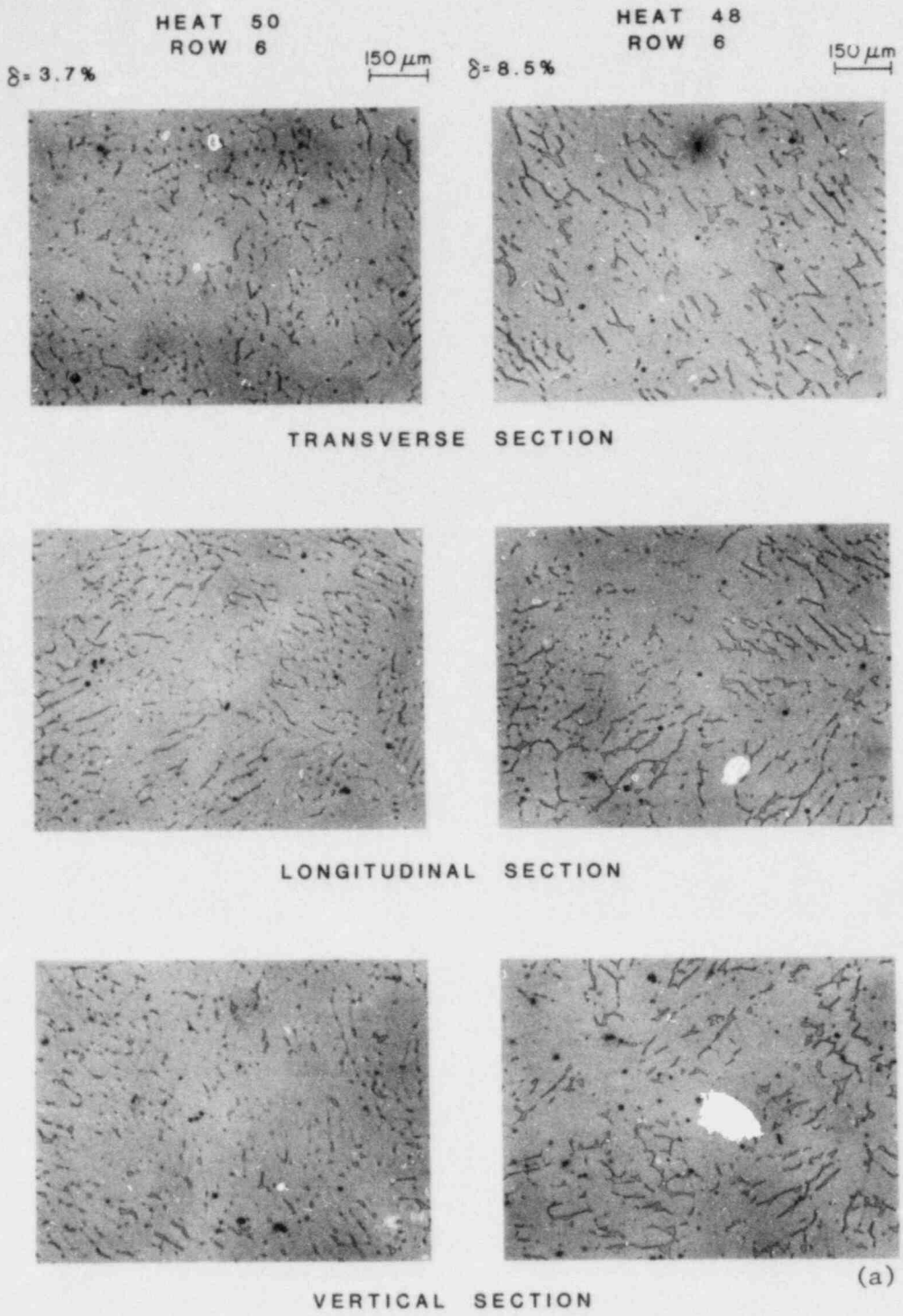

Fig. 4.2. Microstructures Along the Three Orientations of Static Cast Keel Blocks of CF-3 Stainless Steel. (a) and (b) Top section (Row 6) and (c) bottom section (Row 3) of the casting.

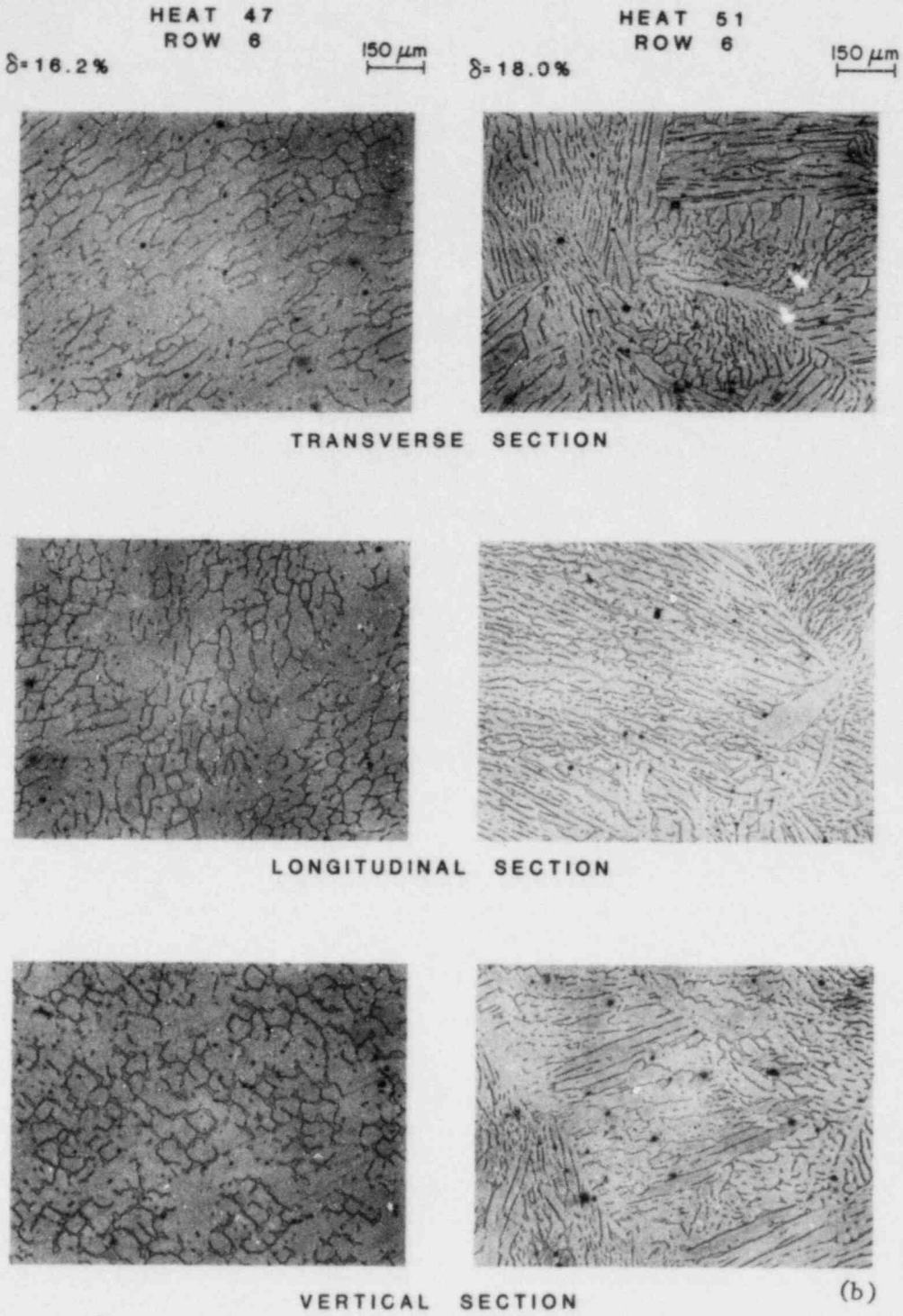
HEAT 47
ROW 6
δ=16.2%
150 μm
HEAT 51
ROW 6
δ=18.0%
150 μm
TRANSVERSE SECTION
LONGITUDINAL SECTION
VERTICAL SECTION
(b)

Fig. 4.2. (Contd.)

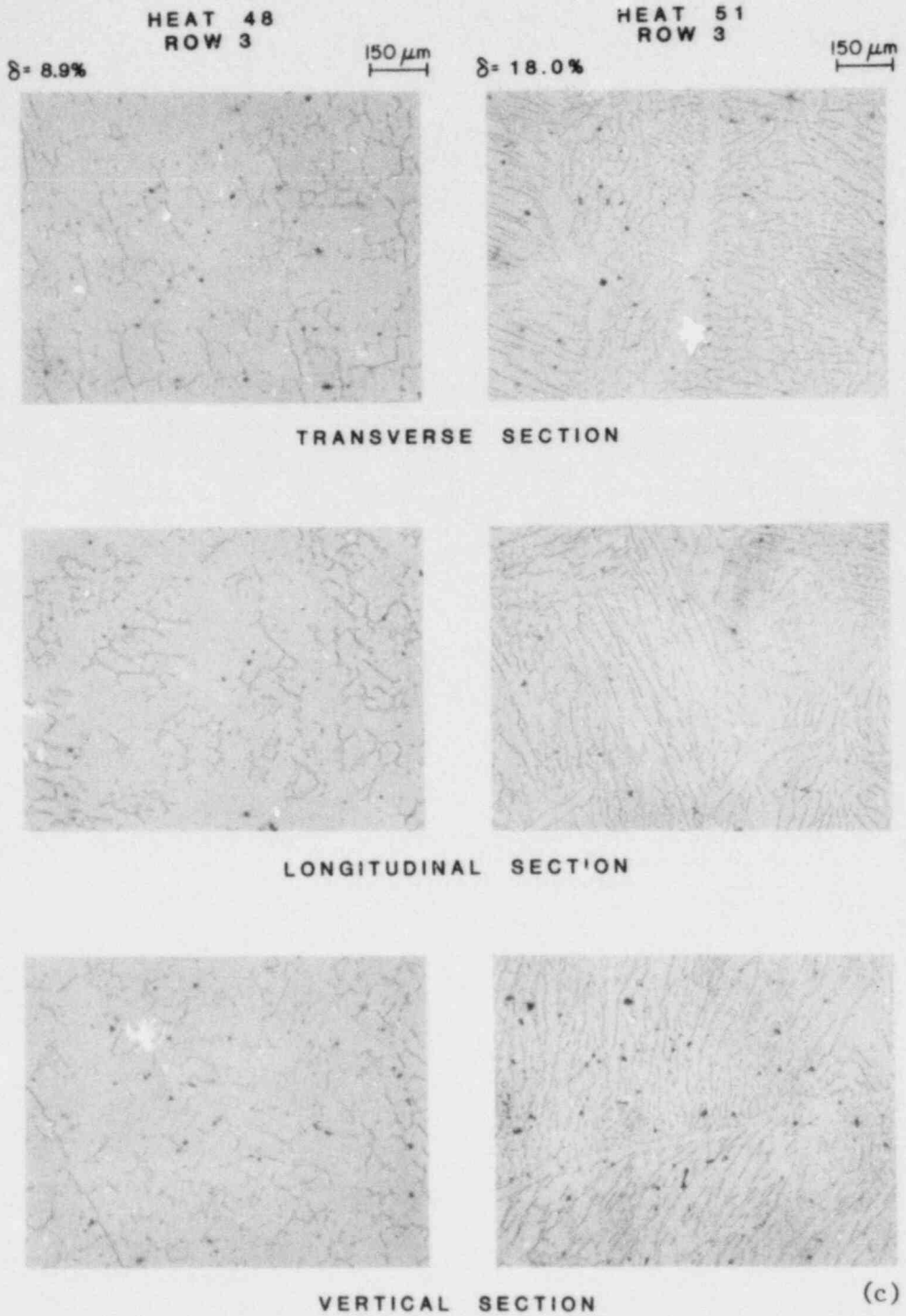
HEAT 48
ROW 3
δ= 8.9%
150 μm
HEAT 51
ROW 3
δ= 18.0%
150 μm
TRANSVERSE SECTION
LONGITUDINAL SECTION
VERTICAL SECTION
(c)

Fig. 4.2. (Contd.)

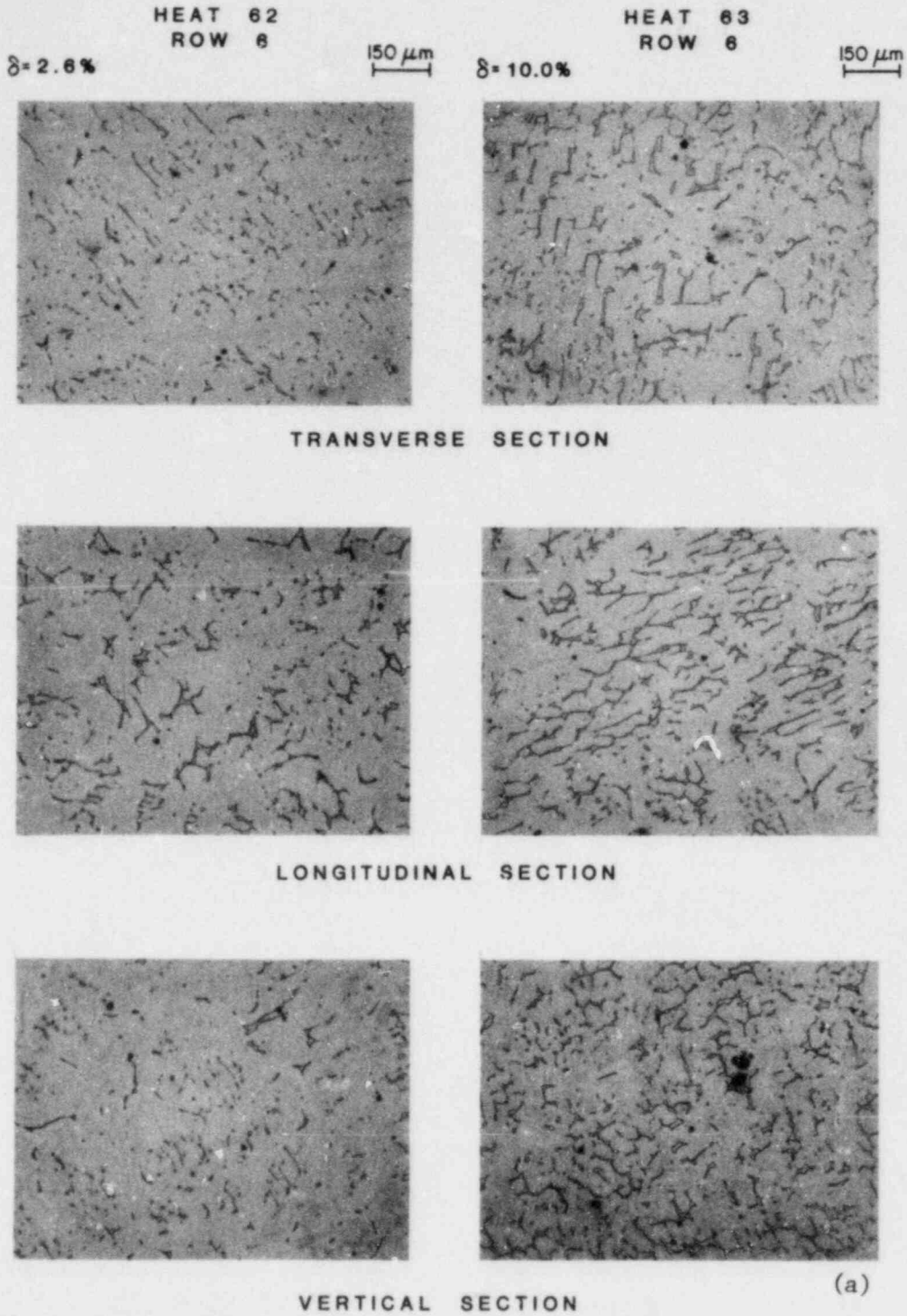

Fig. 4.3. Microstructures Along the Three Orientations of Static Cast Keel Blocks of CF-8M Stainless Steel. (a) and (b) Top region (Row 6) and (c) bottom region (Row 3) of the casting.

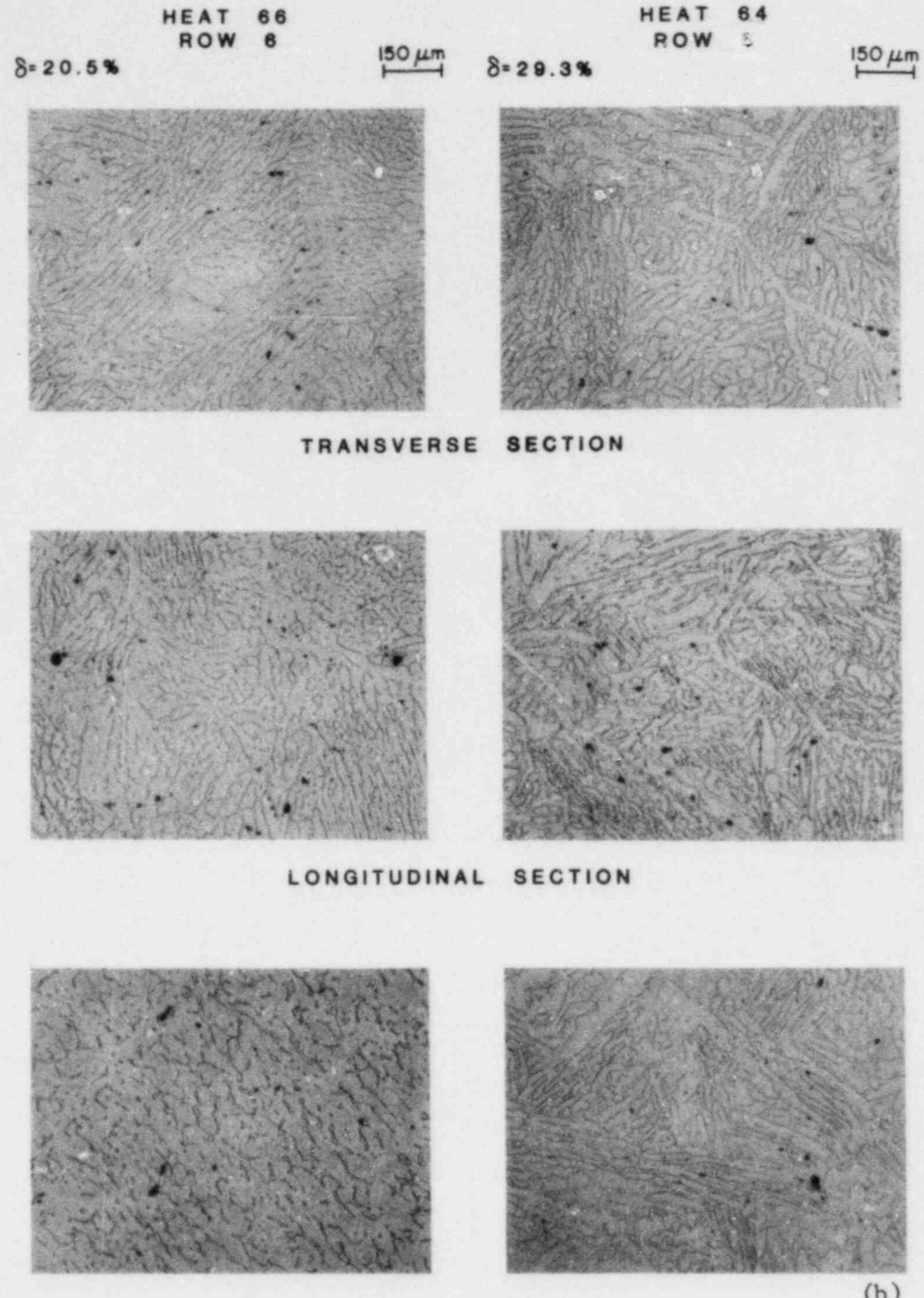
HEAT 66
ROW 6
δ=20.5%
150 μm
HEAT 64
ROW 5
δ=29.3%
150 μm
TRANSVERSE SECTION
LONGITUDINAL SECTION
VERTICAL SECTION
(b)

Fig. 4.3. (Contd.)

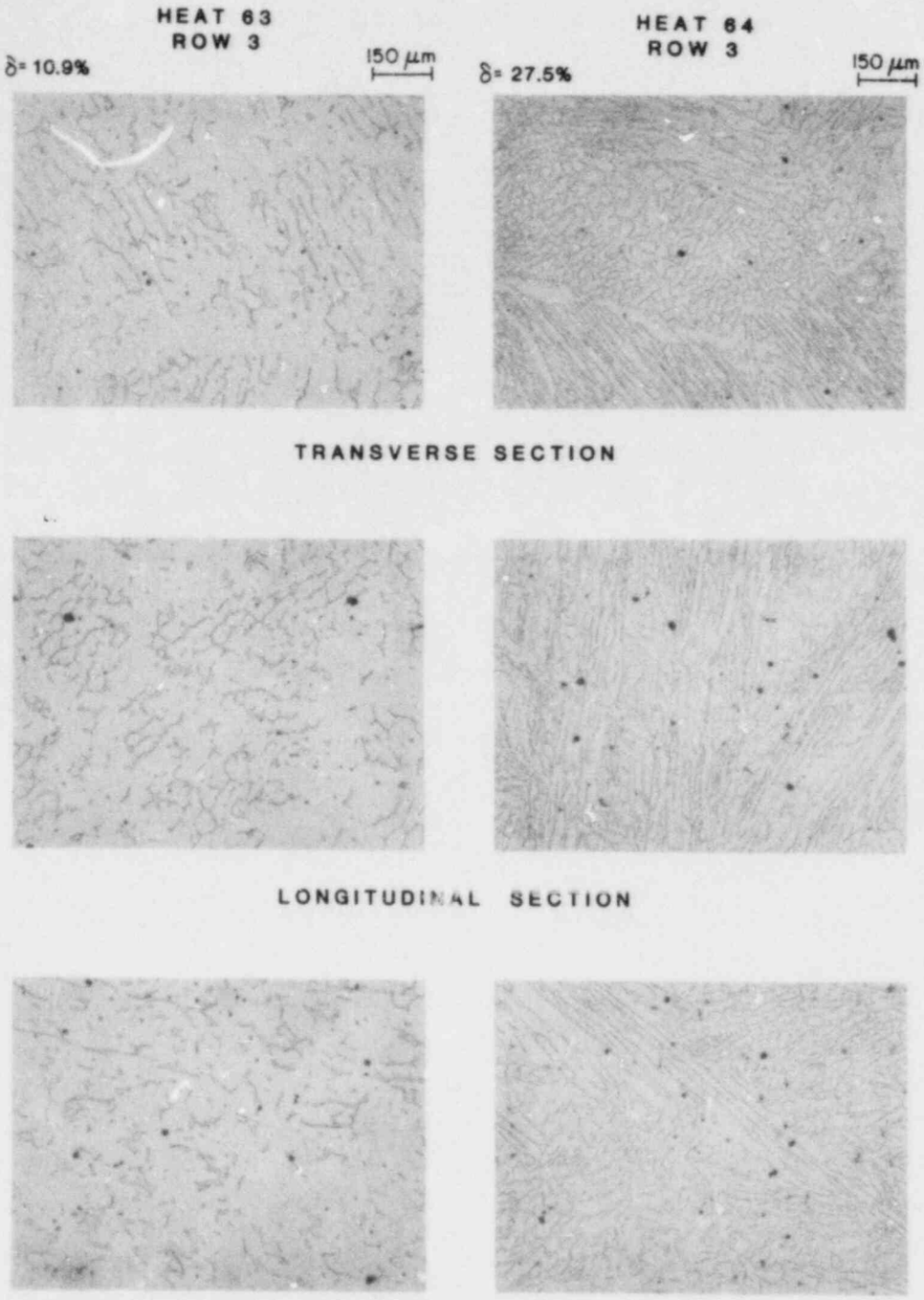
HEAT 63
ROW 3
δ= 10.9%
150 μm
HEAT 64
ROW 3
δ= 27.5%
150 μm
TRANSVERSE SECTION
LONGITUDINAL SECTION
VERTICAL SECTION
(c)

Fig. 4.3. (Contd.)

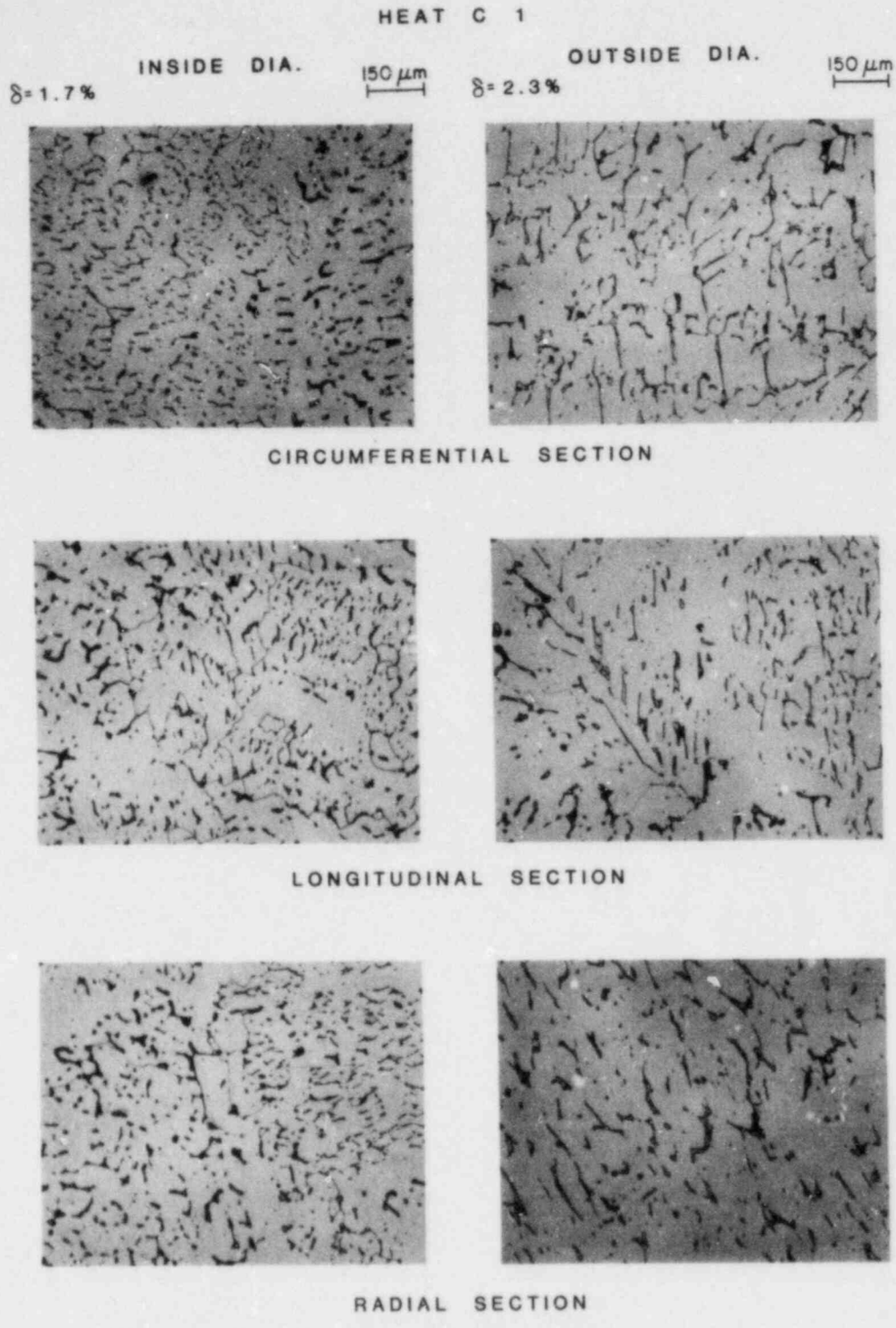

Fig. 4.4. Microstructures Along the Three Orientations of the Static-Cast Pump-Casing Ring of CF-8 Stainless Steel.

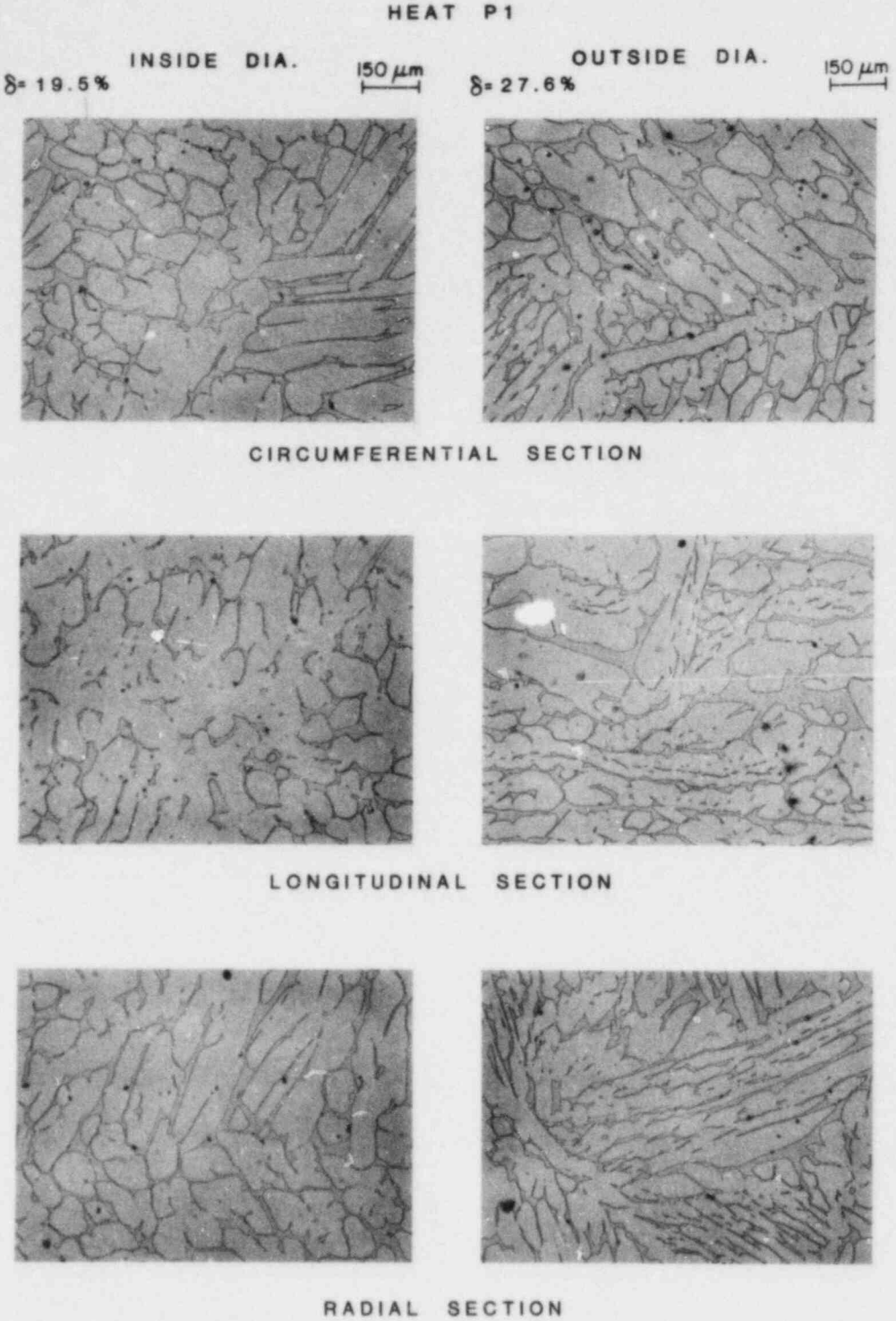

Fig. 4.5. Microstructures Along the Three Orientations of the Centrifugally Cast Pipe of CF-8 Stainless Steel.

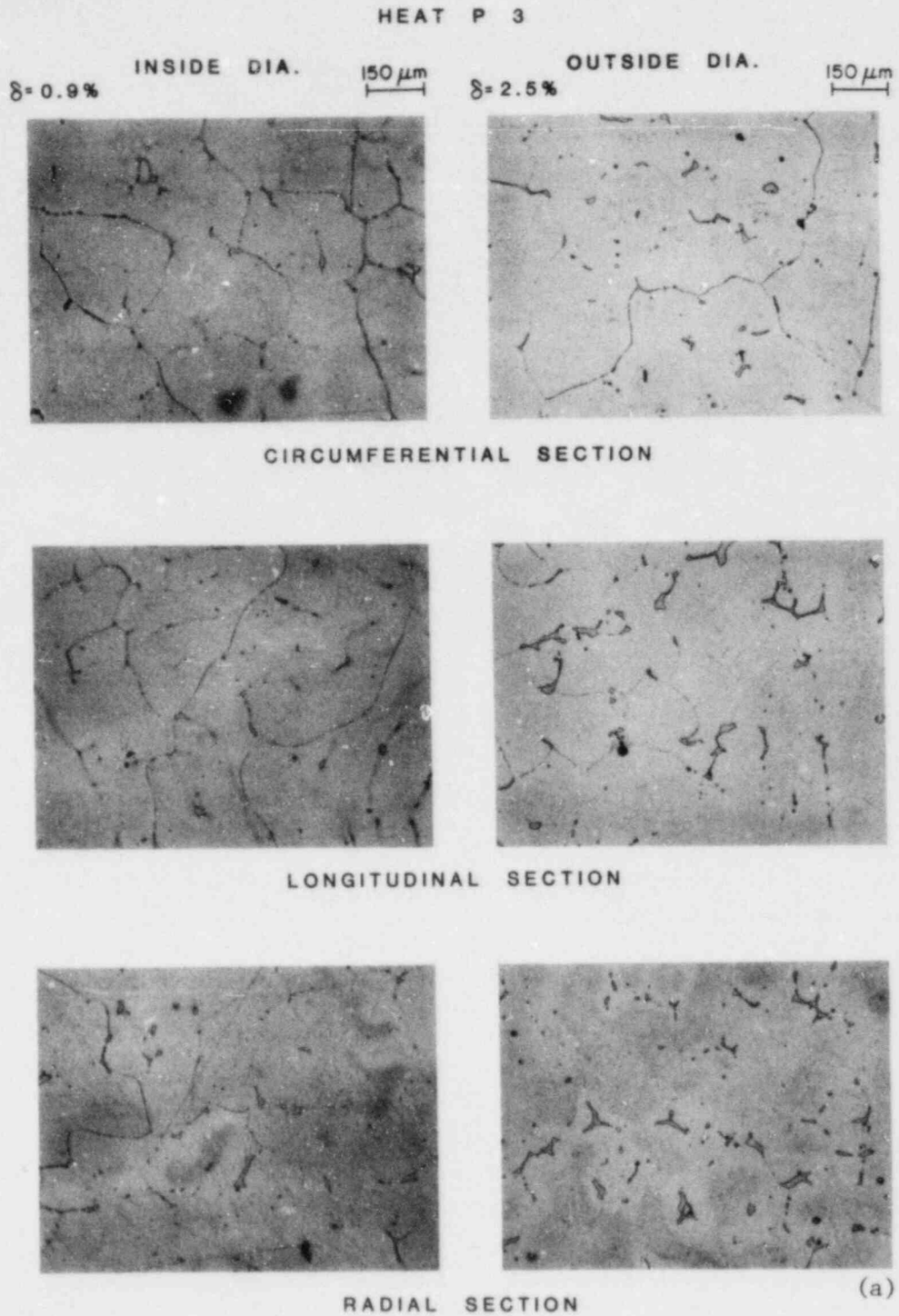

Fig. 4.6. Microstructures Along the Three Orientations of the Centrifugally Cast Pipe of CF-3 Stainless Steel. (a) Heat P3 and (b) heat P2.

HEAT P 2

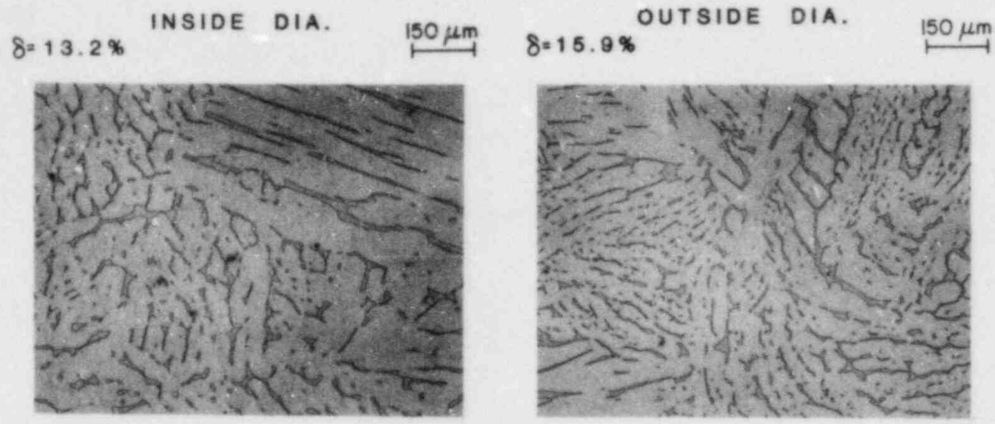

CIRCUMFERENTIAL SECTION

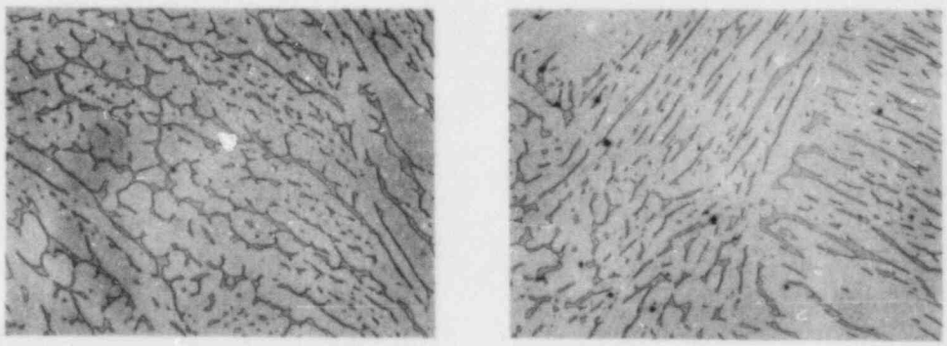

LONGITUDINAL SECTION

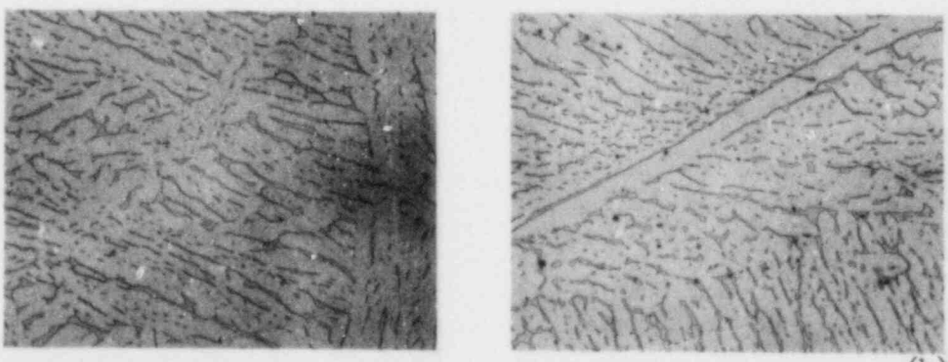

(b)

RADIAL SECTION

Fig. 4.6. (Contd.)

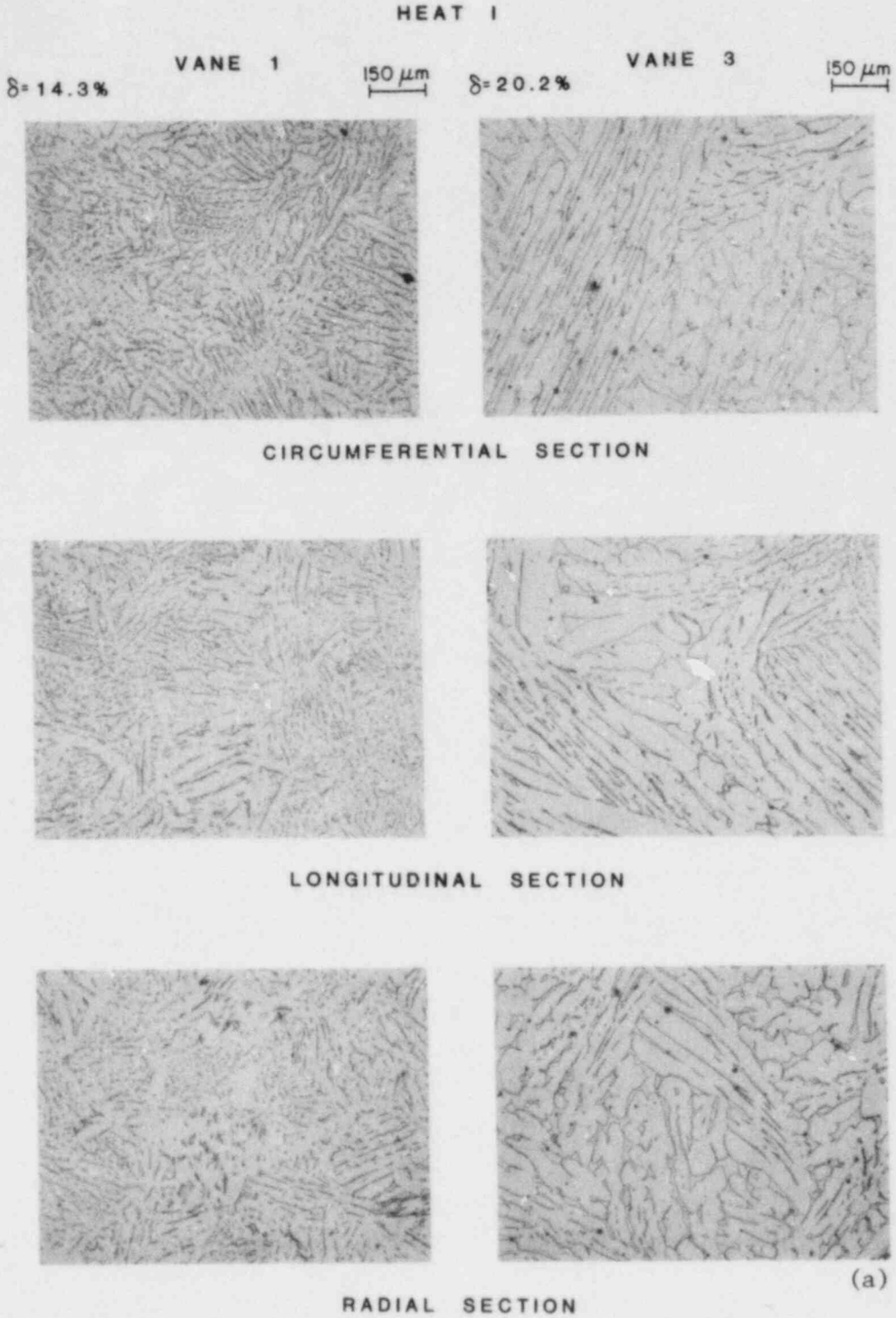

Fig. 4.7. Microstructures Along the Three Orientations of the Static-Cast Pump Impeller of CF-3 Stainless Steel. (a) Vanes and (b) shroud and hub of the impeller.

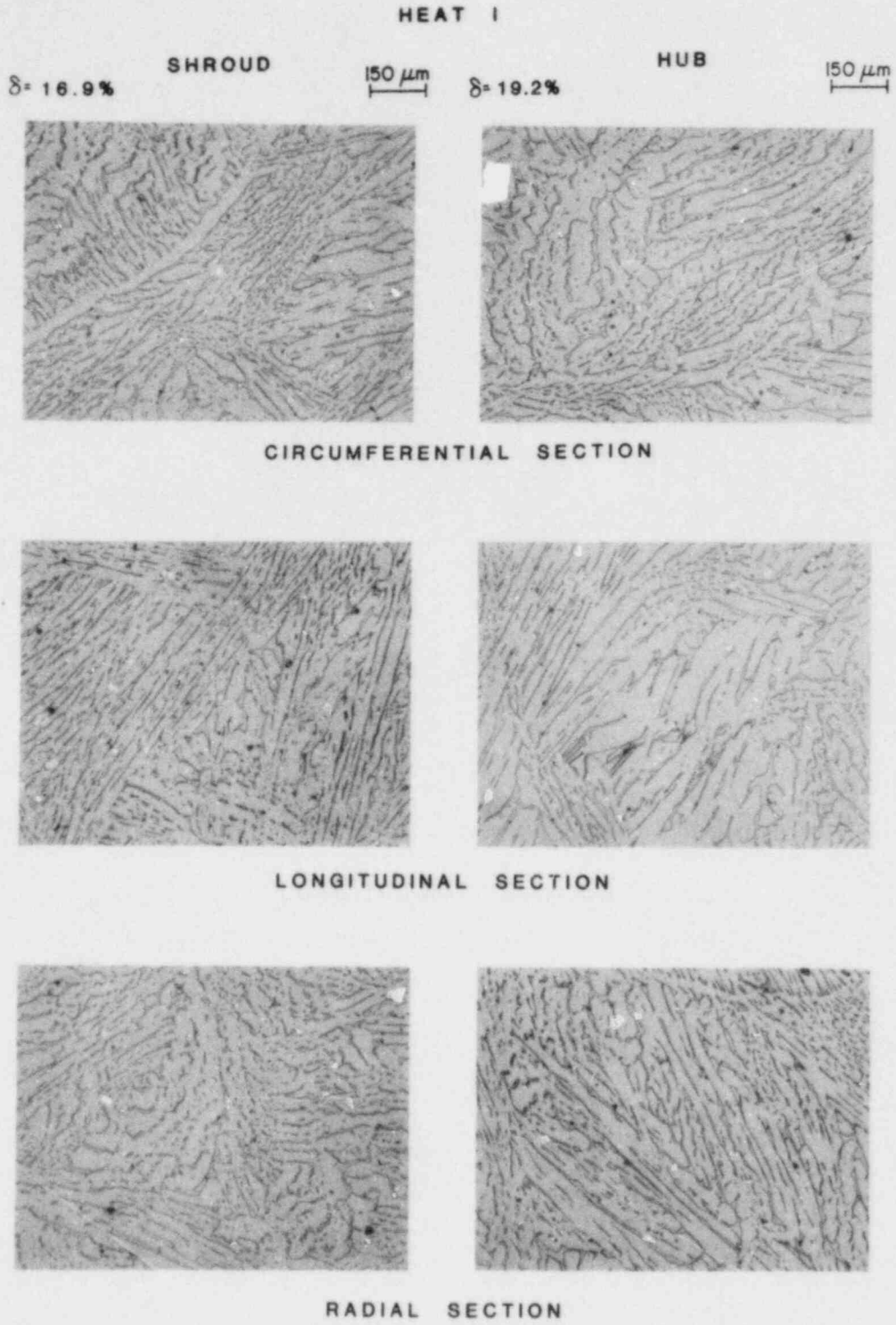
HEAT I
SHROUD
δ= 16.9%
150 μm
HUB
δ= 19.2%
150 μm
CIRCUMFERENTIAL SECTION
LONGITUDINAL SECTION
RADIAL SECTION

Fig. 4.7. (Contd.)

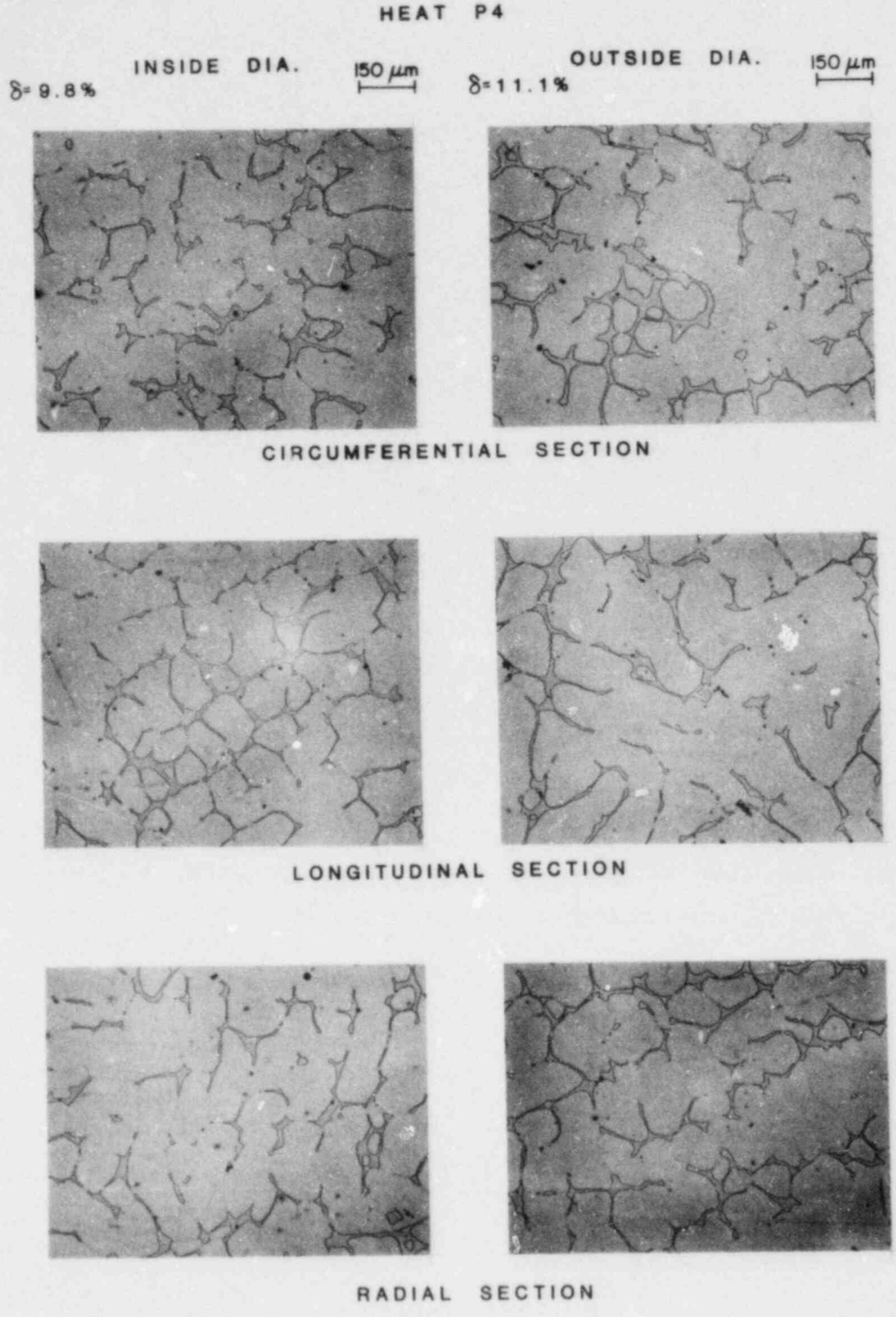

Fig. 4.8. Microstructures Along the Three Orientations of the Centrifugally Cast Pipe of CF-8M Stainless Steel.

Table 4.1 indicates that the ferrite content is lower and hardness is slightly higher toward the inner surface of the various cast pipes. This condition appears to be related to the nickel content in the material, i.e., the concentration of nickel is higher near the inner surface. Differences in hardness and ferrite content are also observed for material from different locations of the static cast keel blocks. Hardness is always higher toward the top of the keel blocks. However, variations in the ferrite content depend on the Cr_{eq}/Ni_{eq} ratio in the material; the ferrite content toward the top of the casting is lower for material with Cr_{eq}/Ni_{eq} <1.13 and higher for material with Cr_{eq}/Ni_{eq} >1.13. Characterization of the grain structure, chemical composition, and microhardness of the ferrite and austenite phases of the materials is in progress. The information will be used to define the compositional and metallurgical conditions that lead to significant embrittlement of the cast duplex stainless steels.

Charpy impact specimen blanks were prepared from keel blocks of the experimental heats and material from the six reactor components. Blanks for the 1-T compact tension specimens were obtained from sections of two centrifugally cast pipes, a static-cast pump-casing ring, and the impeller. The specimens are being aged at 450, 400, 350, 320, and 290°C in muffle furnaces lined with a steel shell to increase the heat capacity of the furnace and to improve the size of the uniform temperature zone. The temperature of the specimens is maintained within ±2°C. The aging times range from 100 to 50,000 h.

Preliminary Charpy impact tests were performed on unaged specimens of the cast material to assess the influence of specimen location and orientation on impact strength. A Dynatup Model 8000A drop-weight impact machine with an instrumented tup and data readout system was used for the tests. The instrumented tup and data readout system were calibrated by means of standard V-notch specimens fabricated from 6061-T6 aluminum and 4340 steel. Aluminum specimens were used to adjust the load limit of the readout instrumentation and the linearity of the calibration was established from results obtained on the 4340 steel specimens. Charpy V-notch specimens (ASTM Specification E-23) were fabricated from cast material from the top and bottom sections of the

keel block. The V-notch was machined in the L-T or L-V orientation.* The specimen location or the orientation of the V-notch had little or no effect on the results. The average value for the various specimens was 258 ± 20 J.

Specimen blanks from two pipe sections (heats P1 and P2) and the pump-casing ring (heat C1) were sent to Materials Engineering Associates (MEA) for J-R curve and tensile tests on the unaged material. Tests will be conducted at room temperature and at 290°C. The orientation of the notch is either L-C or C-L (L-longitudinal and C-circumferential direction of the pipe). The test matrix is given in Table 4.2.

Microstructural evaluation of the aged specimens obtained from George Fischer Co. of Switzerland has continued. The effort was focused on inspection of the specimens from heats 278 (15% ferrite) and 280 (40% ferrite) that were aged for 3000 and 10,000 h at 300 and 350°C. The $M_{23}C_6$-like precipitates were not observed in any of the specimens. Microstructural observations for the different specimens of cast CF-8 stainless steel are given in Table 4.3. The results do not correlate well with the Charpy impact data. Precipitate phases were evident only in specimens that were aged for long times, i.e., 10,000 h at 400°C and 70,000 h at 300, 350, and 400°C. However, for heat 280, a substantial reduction in impact energy (from 250 to 150 J) occurred after 3000 h at 350°C and 10,000 h at 300°C. Furthermore, the impact energy for specimens aged for 3000 h at 400°C is comparable to that in specimens aged for 70,000 h at 300°C. Precipitates were found in the latter specimens but not in those aged for 3000 h at 400°C. It is probable that the precipitate phases are too small to be resolved, yet significant with regard to embrittlement. A correlation of the degradation of mechanical properties with microstructural changes requires a quantitative determination of the precipitates over a substantial volume of the material. An analysis of the aged material by neutron diffraction in the ANL Intense Pulsed Neutron Source (IPNS) is being planned.

---

*L is longitudinal, T is transverse, and V is vertical direction. The first letter designates the direction normal to the crack plane and the second letter the expected direction of crack propagation.

TABLE 4.2. Test Matrix for J-R Curve Determination and Tensile Properties of CF-3 and CF-8 Cast Stainless Steels (Heats P1, P2, and C1)

Test Temp.[a]	J-R Curve		Tensile Test	
	Notch Orientation	Number of Tests	Specimen Orientation	Number of Tests
RT	L-C	2	L	2
290°C	L-C	2	L	2
RT	C-L	1	C	2
290°C	C-L	-	C	2

[a]RT = room temperature.

TABLE 4.3. Precipitate Phases[a] Identified in Thermally Aged Specimens of CF-8 Cast Stainless Steel Obtained from George Fischer Co.

Time, h \ Temp., °C	Heat 280			Heat 278		
	300	350	400	300	350	400
70,000	X	M	M	M	X	M
10,000	-	-	X	-	-	-
3,000	-	-	-	-	-	-

[a]M = $M_{23}C_6$-like precipitate.
X = Precipitate on dislocations not similar to $M_{23}C_6$.

B. References for Chapter IV

1. O. K. Chopra et al., in Materials Science and Technology Division Light-Water-Reactor Safety Research Program: Quarterly Progress Report, October-December 1982, NUREG/CR-2970 Vol. IV, ANL-82-41 Vol. IV (November 1983), pp. 99-110.

2. O. K. Chopra and G. Ayrault, Long-Term Embrittlement of Cast Duplex Stainless Steels in LWR Systems: Annual Report, October 1982-September 1983, NUREG/CR-3857, ANL-84-44 (July 1984).

Distribution for NUREG/CR-3689 Vol. IV (ANL-83-85 Vol. IV)

Internal:

R. Avery
G. Ayrault
M. Blander
F. A. Cafasso
O. K. Chopra
H. M. Chung
T. N. Claytor
L. W. Deitrich
C. E. Dickerman
D. R. Diercks
F. Y. Fradin
E. E. Gruber
D. M. Gruen
P. R. Huebotter
M. Ishii
C. E. Johnson
T. F. Kassner (10)
K. L. Kliewer
D. S. Kupperman
D. J. Lam
Y. Y. Liu
P. A. Lottes
P. S. Maiya
V. A. Maroni
D. K. Moores
K. Natesan
L. A. Neimark
F. A. Nichols
P. R. Okamoto
F. S. Onesto
R. G. Palm
J. Y. Park
R. B. Poeppel
L. E. Rehn
K. J. Reimann
J. Rest (10)
G. S. Rosenberg
W. E. Ruther
W. J. Shack (3)
W. K. Soppet
E. M. Stefanski (2)
R. V. Strain
C. E. Till
H. C. Tsai
R. A. Valentin
A. Villalobos
R. W. Weeks
H. Wiedersich
F. L. Yaggee
R. S. Zeno
ANL Patent Dept.
ANL Contract File
ANL Libraries (3)
TIS Files (6)

External:

NRC, for distribution per R3 and R5 (400)
DOE-TIC (2)
Manager, Chicago Operations Office, DOE
R. Tom, DOE-CH
Materials Science and Technology Division Review Committee:
B. Alcock, U. Toronto
A. Arrott, Simon Fraser U.
R. C. Dynes, Bell Labs., Murray Hill
A. G. Evans, U. California, Berkeley
H. K. Forsen, Bechtel Group, San Francisco
E. Kay, IBM San Jose Research Lab.
B. Maple, U. California, San Diego
P. G. Shewmon, Ohio State U.
J. K. Tien, Columbia U.
J. W. Wilkins, Cornell U.
R. B. Adamson, General Electric Co., Vallecitos Nuclear Center, P. O. Box 460, Pleasanton, Calif. 94566
P. L. Andresen, General Electric Corporate Research and Development, Schenectady, N. Y. 12301
G. A. Arlotto, Office of Nuclear Regulatory Research, USNRC, Washington
D. Atteridge, Battelle Pacific Northwest Lab., P. O. Box 999, Richland, Wash. 99352
W. H. Bamford, Structural Materials Engineering, Westinghouse Electric Corporation, WNES, Box 355, Pittsburgh, Pa. 15230
W. Berry, Battelle-Columbus Labs., 505 King Ave., Columbus, OH 43201
D. L. Burman, Westinghouse PWR Systems Div., P. O. Box 355, Pittsburgh, Pa. 15230
L. K. Chan, Office of Nuclear Regulatory Research, USNRC, Washington
C. Y. Cheng, Office of Nuclear Reactor Regulation, USNRC, Washington
R. A. Clark, Battelle Pacific Northwest Lab., P. O. Box 999, Richland, Wash. 99352

W. J. Collins, Office of Inspection and Enforcement, USNRC, Washington
A. Cowan, Risley Nuclear Power Development Labs., United Kingdom Atomic Energy Authority (Northern Division), Risley, Warrington WA3 6AT, UK
B. Cox, Chalk River Nuclear Labs., AECL, Chalk River, Ont., K0J 1J0, Canada
G. Cragnolino, Dept. of Metallurgical Engineering, Ohio State U., Columbus, OH 43210
D. Cubiciotti, Electric Power Research Inst., P. O. Box 10412, Palo Alto, Calif. 94304
W. H. Cullen, Materials Engineering Associates, Inc., 9700 B. George Palmer Highway, Lanham, Maryland 20706
J. C. Danko, Electric Power Research Inst., P. O. Box 10412, Palo Alto, Calif. 94304
B. J. L. Darlaston, CEGB, Berkeley Nuclear Laboratories, Berkeley, Glos., England
B. J. Elliot, Office of Nuclear Reactor Regulation, USNRC, Washington
R. B. Foulds, Office of Nuclear Reactor Regulation, USNRC, Washington
M. Fox, Fox Enterprises, 7490 Stanford Place, Cupertino, Calif. 95014
Y. S. Garud, S. Levy, Inc., 1901 S. Bascom Ave., Campbell, Calif. 95008
S. M. Gehl, Electric Power Research Inst., P. O. Box 10412, Palo Alto, Calif. 94304
J. H. Gittus, Springfields Nuclear Power Development Labs., U. K. Atomic Energy Authority, Springfields, Salwick, Preston, PR4 ORR, England
W. Gysel, George Fischer, Ltd., Schaffhausen, Switzerland
D. O. Harris, 750 Welch Rd., Palo Alto, Calif. 94304
W. S. Hazelton, Office of Nuclear Reactor Regulation, USNRC, Washington
B. Hemsworth, HM Nuclear Installations Inspectorate, Thames House North, Millbank, London SW1P 42J, England
R. R. Hobbins, EG&G/INEL, 1520 Sawtelle Dr., Idaho Falls, Idaho 83401
W. V. Johnston, Office of Nuclear Reactor Regulation, USNRC, Washington
R. L. Jones, Electric Power Research Inst., P. O. Box 10412, Palo Alto, Calif. 94304
K. R. Jordan, Nuclear Fuel Div., Monroeville Nuclear Center, Westinghouse Electric Corp., Monroeville, Pa. 15146
C. N. Kelber, Office of Nuclear Regulatory Research, USNRC, Washington
E. Kohn, Atomic Energy of Canada Ltd., Sheridan Park Research Community, Mississauga, Ont., Canada L5K 1B2
P. M. Lang, Office of Converter Reactor Deployment, USDOE, Washington, D. C. 20545
D. D. Lanning, Battelle Pacific Northwest Lab., P. O. Box 999, Richland, Wash. 99352
R. A. Lorenz, Oak Ridge National Lab., P. O. Box X, Oak Ridge, Tenn. 37830
P. MacDonald, EG&G/INEL, 1520 Sawtelle Dr., Idaho Falls, Idaho 83401
G. P. Marino, Office of Nuclear Regulatory Research, USNRC, Washington
S. McDonald, Westinghouse Electric Corp., R&D Center, Beulah Rd., Pittsburgh, Pa. 15235
K. R. Merckx, Exxon Nuclear, Inc., 2955 George Washington Way, Richland, Wash. 99352
A. C. Millunzi, Office of Breeder Reactor Programs, USDOE, Washington D. C. 20545
J. Muscara, Office of Nuclear Regulatory Research, USNRC, Washington
D. M. Norris, Electric Power Research Inst., P. O. Box 10412, Palo Alto, Calif. 94304
D. R. O'Boyle, Commonwealth Edison Co., P. O. Box 767, Chicago, Ill. 60690
R. N. Oehlberg, Electric Power Research Inst., P. O. Box 10412, Palo Alto, Calif. 94304

M. F. Osborne, Oak Ridge National Lab., P. O. Box X, Oak Ridge, Tenn. 37830
D. E. Owen, EG&G Idaho, P. O. Box 88, Middletown, Pa. 17057
T. P. Papazoglou, Lynchburg Research Center, Babcock & Wilcox Co., P. O. Box 1260, Lynchburg, Va. 24505
J. T. A. Roberts, Electric Power Research Inst., P. O. Box 10412, Palo Alto, Calif. 94304
E. J. Rowley, Commonwealth Edison Co., P. O. Box 767, Chicago, Ill. 60690
E. F. Rybicki, Dept. of Mechanical Engineering, Univ. of Tulsa, Tulsa, Okla. 74110
H. H. Scott, Office of Nuclear Regulatory Research, USNRC, Washington
C. Z. Serpan, Office of Nuclear Regulatory Research, USNRC, Washington
L. Shao, Office of Nuclear Regulatory Research, USNRC, Washington
V. K. Sikka, Oak Ridge National Laboratory, P. O. Box X, Oak Ridge, TN 37830
R. D. Silver, Office of Nuclear Reactor Regulation, USNRC, Washington
G. Slama, Framatome, Tour FIAT, Cedex 16, 92084, Paris La Defense, France
P. Smerd, Combustion Engineering, Inc., P. O. Box 500, Windsor, Conn. 06095
L. J. Sobon, NUTECH Engineers, 6835 Via del Oro, San Jose, Calif. 95119
A. A. Solomon, School of Nuclear Engineering, Purdue U., West Lafayette, Ind. 47907
H. D. Solomon, General Electric Company, P. O. Box 43, Schenectady, N. Y. 12301
D. M. Stevens, Lynchburg Research Center, Babcock & Wilcox Co., P. O. Box 239, Lynchburg, VA 24505-0239
J. Strosnider, Office of Nuclear Regulatory Research, USNRC, Washington
A. Taboada, Office of Nuclear Regulatory Research, USNRC, Washington
R. Van Houten, Office of Nuclear Regulatory Research, USNRC, Washington
J. R. Weeks, Brookhaven National Lab., Upton, N. Y. 11973
K. R. Wichman, Office of Nuclear Reactor Regulation, USNRC, Washington

NRC FORM 335 (2 84) NRCM 1102 3201, 3202

U.S. NUCLEAR REGULATORY COMMISSION

BIBLIOGRAPHIC DATA SHEET

SEE INSTRUCTIONS ON THE REVERSE

1 REPORT NUMBER (Assigned by TIDC and Vol. No., if any)
NUREG/CR-3689 Vol. IV
ANL-83-85 Vol. IV

2 TITLE AND SUBTITLE
Materials Science and Technology Division Light-Water-Reactor Safety Research Program: Quarterly Progress Report, October-December 1983

3 LEAVE BLANK

4 DATE REPORT COMPLETED
MONTH | YEAR

5 AUTHOR(S)
W. J. Shack et al.

6 DATE REPORT ISSUED
MONTH: September | YEAR: 1984

7 PERFORMING ORGANIZATION NAME AND MAILING ADDRESS (Include Zip Code)
Argonne National Laboratory
9700 South Cass Avenue
Argonne, Illinois 60439

8 PROJECT/TASK/WORK UNIT NUMBER

9 FIN OR GRANT NUMBER
A2016, A2017, A2212, A2243

10 SPONSORING ORGANIZATION NAME AND MAILING ADDRESS (Include Zip Code)
Division of Engineering Technology
Office of Nuclear Regulatory Research
U.S. Nuclear Regulatory Commission
Washington, D. C. 20555

11a TYPE OF REPORT
Technical; quarterly

b PERIOD COVERED (Inclusive dates)
October-December 1983

12 SUPPLEMENTARY NOTES

13 ABSTRACT (200 words or less)

This progress report summarizes the Argonne National Laboratory work performed during October, November, and December 1983 on water reactor safety problems. The research and development areas covered are Environmentally Assisted Cracking in Light Water Reactors, Transient Fuel Response and Fission Product Release, Clad Properties for Code Verification, and Long-Term Embrittlement of Cast Duplex Stainless Steels in LWR Systems.

14 DOCUMENT ANALYSIS a KEYWORDS/DESCRIPTORS
embrittlement cast stainless steel
fission product modeling
fracture irradiated Zircaloy
nondestructive evaluation
pipe cracking
water chemistry

b IDENTIFIERS/OPEN ENDED TERMS

15 AVAILABILITY STATEMENT
unlimited

16 SECURITY CLASSIFICATION
(This page) unclassified
(This report) unclassified

17 NUMBER OF PAGES
167

18 PRICE

501